



Lodz University of Technology

Interdisciplinary Doctoral School

Material Engineering

M.Sc. Eng. Michał Piotrowski

801608

Development of the Fricke Radiochromic Gel Dosimeter for Radiotherapy Dosimetry Applications

Rozwój dozymetru radiochromowego Fricke do zastosowań w
dozymetrii w radioterapii

Doctoral dissertation

Supervisor:
Prof., D.Sc., Ph.D. Marek Kozicki
Department of Mechanical Engineering, Informatics and
Chemistry of Polymer Materials
Faculty of Material Technologies and Textile Design

Lodz, 2025

Acknowledgements

I would like to express my deepest gratitude to the people who supported me in the course of this work.

I would like to express my deepest gratitude to Professor Marek Kozicki for interest me in the three-dimensional gel dosimetry. Throughout the entire period of conducting the research, the Professor supported me with his knowledge and experience and motivated me when difficulties arose (there were quite a few of them). I would like to thank the Professor for teaching me how to prepare scientific articles to meet the standards of strong international journals. I would like to express my special gratitude for his interest in my ideas and giving me a lot of freedom in their implementation. Although most of them were not accurate, it allowed me to perceive myself as a mature scientist.

I would like to thank the members of the DosLab team, Dr. Elżbieta Sąsiadek-Andrzejczak and Dr. Malwina Jaszcak-Kuligowska, for many valuable discussions and, above all, for the fantastic atmosphere accompanying my daily research. I would like to thank Dr. Piotr Maras for all the sample irradiations, which have accumulated quite a lot over the last four years, and also for valuable knowledge in the field of medical physics.

I would like to thank the employees of the Lodz University of Technology who carried out some analyses for me and helped to interpret and describe the obtained results. Professor Zbigniew Stempień for carrying out the analysis of the mechanical strength of gelatin samples, Dr. Radosław Wach for measuring the sol-gel transition temperature of gelatin, and Prof. Małgorzata Szykowska-Jóźwik and Dr. Aleksandra Pawlaczyk for carrying out the quantitative analysis of the metal content using the ICP-OES method.

I would like to thank Professor Panagiotis Papagiannis for his warm (literally, considering the temperatures in Greece in September) welcome during my internship in Athens. The invaluable conversations with the Professor allowed me to better understand the point of view and needs of medical physicists. I would like to thank the members of Professor Papagiannis' team, Professor Evangelos Pantelis for sample irradiation and Associated Professor Elefterios Pappas for valuable ideas on optimizing the conditions for imaging samples using optical computed tomography. Special thanks to M.Sc. Ioanna Grammatikou, who not only performed experiments with me, but also took care of me during my entire stay in Athens, making me feel at home even though I was about 1570 kilometers (straight line distance) from Łódź.

I would like to thank my parents Marzena and Tomasz and my sister Anna for creating the conditions for me to develop and gain knowledge not only during my doctoral studies, but throughout my entire life. Without their support in everyday life, I would never have even come close to preparing a doctoral dissertation.

Finally, I would like to thank my closest friends Jagoda Suskiewicz, Kamil Pusz and Michał Karkusiński, for their sincere interest in the subject of my work and the progress in preparing my doctoral dissertation and for believing in me, as well as for every moment spent together when I could rest from my research work and gather strength to continue it. Who would have thought years ago when we met as children/teenagers that one day I would prepare my own doctoral dissertation...

Abstract

Radiotherapy is one of the methods of treating cancer. Its effectiveness depends largely on the accuracy of the treatment plan developed and the precision of irradiation. Radiotherapy quality control is performed by dosimetric measurements. The only group of dosimeters capable of recording information on the dose distribution in 3D are gel chemical dosimeters. In recent years, various types of gel dosimeters have been proposed, which are constantly being developed. In this work two new modifications of the Fricke gel dosimeter are proposed: (1) the addition of sodium alginate as a compound binding iron ions and (2) the addition of sorbitol to the gelatin matrix to improve the temperature and mechanical properties of the matrix. In addition, new applications of gel dosimeters in radiotherapy are proposed.

The influence of the quality of water used to produce Fricke gel dosimeters on the stability of iron ions was studied. The obtained results showed a significant influence of the quality of the water on the autooxidation rate of the dosimeter. To obtain the highest stability of iron ions, it is necessary to use deionized water or at least twice-distilled water. By dripping solutions of 1.7-3.5% sodium alginate into Fricke solution containing 0-3.5% calcium chloride, macrocapsules were obtained. The shape and mechanical strength of the capsules depended on the viscosity of the alginate used and the concentrations of sodium alginate and calcium chloride solutions. The best properties were demonstrated by capsules obtained with 3.5% alginate and 3.5% CaCl_2 . By obtaining capsules by dripping sodium alginate solution into Fricke solution without calcium ions, the binding of iron ions to sodium alginate chains was proven. The obtained capsules are characterized by rapid diffusion of unbound metal ions and dye molecules into water. By introducing capsules into the gel matrix, a 1D dosimeter was obtained. Rapid diffusion of the active ingredients of the dosimeter from the capsules into the gel was observed, as well as a change in the capsule sizes after introduction into the matrix. The nature of the changes depended on the type of matrix material. The capsules in 25% Pluronic F-127 decreased their diameter by about 50%, while in the gelatin matrix they first decreased their diameter by about 5% and then increased it, but did not reach the initial size.

Preparation of iron alginate microgel requires further investigation. Addition of small concentrations of sodium alginate to the Fricke solution resulted in the precipitation of a white precipitate (alginic acid) due to the too low pH of the Fricke solution. Reducing the acid concentration by over 90% and removing the dye from the composition allowed obtaining microsized formations, however, further studies would be necessary to confirm the chemical composition of the obtained structures, because at the moment it cannot be unequivocally stated that it is iron alginate. Considering the mutually exclusive optimal pH of the Fricke solution and the sodium alginate solution, the need to remove the dye from the composition of the dosimeter and the potential introduction of impurities with alginate that accelerate the oxidation of Fe ions, it is recommended to search for other polymers capable of binding iron.

The effect of the addition of Fricke's solution and sorbitol on the mechanical and temperature properties of gelatin was investigated. The presence of acidic Fricke's solution lowers the gel-sol transition temperature and mechanical properties of gelatin by hydrolysis of hydrogen bonds. The presence of sorbitol partially protects the gelatin matrix from degradation, but this effect is insufficient. The gel containing Fricke's solution and sorbitol was used to prepare two-dimensional dosimeters for various applications in radiotherapy: (1) a dosimeter in a plastic container for performing a coincidence test of the radiation and mechanical isocenter of a medical accelerator, (2) and dosimeters of different

thicknesses for *in vivo* dosimetry (measurement of dose distribution on the patient's skin) acting simultaneously as a bolus. During the application studies, the possibility of using Fricke-XO-Gelatin with sorbitol for performing a coincidence test was demonstrated. Verification of the treatment plans using the thick and thin Fricke dosimeters showed the need for further optimization of the manufacturing method and the search for potential materials capable of replacing gelatin. Nevertheless, gel dosimeters may be promising tools for *in vivo* measurements.

The possibility of imaging three-dimensional Fricke gel dosimeters with an optical path of 6 cm using optical computed tomography was demonstrated. In order to avoid artifacts on scans, it was necessary to optimize the composition of the dosimeters and imaging conditions. Calibration of the dosimeters showed that the addition of sorbitol increased the sensitivity of the Fricke-XO-Gelatin dosimeter by 26%, and measurements of the diffusion coefficient showed a 50% decrease in the value of the Fricke-XO-Gelatin dosimeter coefficient after adding sorbitol. Verification of the treatment plan using the Fricke-XO-Pluronic F-127 showed the necessity of further optimization of the verification process. Using Fricke-XO-Gelatin with sorbitol, a successful verification of the treatment plan was carried out. The studies carried out showed a positive effect of sorbitol addition to the gelatin matrix on the properties of Fricke-XO-Gelatin. In addition, the possibility of using gel dosimeters in new applications in radiotherapy was shown. Hence, it can be considered that the aim of the work was achieved.

Streszczenie

Radioterapia jest jedną z metod leczenia nowotworów. Jej skuteczność zależy w dużej mierze od dokładności opracowanego planu leczenia i precyzji napromienienia. Kontrolę jakości radioterapii przeprowadza się poprzez pomiary dozymetryczne. Jedyną grupą dozymetrów zdolną do zapisu informacji o rozkładzie dawki w 3D są żelowe dozymetry chemiczne. W ostatnich latach zaproponowano różne rodzaje dozymetrów żelowych, które są stale rozwijane. W pracy zaproponowane zostały dwie nowe modyfikacje żelowego dozymetru Fricke: (1) dodatek alginianu sodu jako związku wiążącego jony żelaza oraz (2) dodatek sorbitolu do matrycy żelatynowej aby poprawić właściwości temperaturowe i mechaniczne matrycy. Ponadto zaproponowano nowe aplikacje dozymetrów żelowych w radioterapii.

Przebadano wpływ jakości wody użytej do produkcji dozymetrów żelowych Fricke na stabilność jonów żelaza. Uzyskane wyniki wykazały istotny wpływ jakości użytej wody. Aby uzyskać najwyższą stabilność jonów żelaza, konieczne jest stosowanie wody dejonizowanej lub co najmniej dwukrotnie destylowanej. Poprzez wkraplanie roztworów 1,7-3,5% alginianu sodu do roztworu Fricke zawierającego 0-3,5% chlorku wapnia uzyskano makrokapsułki. Kształt i wytrzymałość mechaniczna kapsułek zależały od lepkości użytego alginianu oraz stężeń roztworów alginianu sodu i chlorku wapnia. Najlepsze właściwości wykazały kapsułki uzyskane z 3,5% alginianu i 3,5% CaCl_2 . Poprzez otrzymywanie kapsułek poprzez wkraplanie roztworu alginianu sodu do roztworu Fricke bez jonów wapnia udowodniono wiązanie jonów żelaza do łańcuchów alginianu sodu. Uzyskane kapsułki charakteryzują się szybką dyfuzją niezwiązanych jonów metali i cząsteczek barwnika do wody. Wprowadzając kapsułki do matrycy żelowej uzyskano dozymetr 1D. Zaobserwowano szybką dyfuzję składników aktywnych dozymetru z kapsułek do żelu, a także zmianę rozmiarów kapsułek po wprowadzeniu do matrycy. Charakter zmian zależał od rodzaju materiału matrycy. Kapsułki w 25% Pluronic F-127 zmniejszyły swoją średnicę o około 50%, podczas gdy w matrycy żelatynowej najpierw zmniejszyły swoją średnicę o około 5%, a następnie ją zwiększyły, ale nie osiągnęły początkowego rozmiaru.

Zbadano wpływ dodatku roztworu Fricke'a i sorbitolu na właściwości mechaniczne i temperaturowe żelatyny. Obecność kwaśnego roztworu Fricke'a obniża temperaturę przejścia żel-zol i właściwości mechaniczne żelatyny poprzez hydrolizę wiązań wodorowych. Obecność sorbitolu częściowo chroni matrycę żelatynową przed degradacją, ale ten efekt jest niewystarczający. Żel zawierający roztwór Fricke'a i sorbitol wykorzystano do przygotowania dwuwymiarowych dozymetrów do różnych zastosowań w radioterapii: (1) dozymetr w plastikowym pojemniku do wykonywania testu zgodności izocentrum promieniowania i izocentrum mechanicznego akceleratora medycznego, (2) oraz dozymetry o różnych grubościach do dozymetrii *in vivo* (pomiar rozkładu dawki na skórze pacjenta) służące równocześnie jako bolus. Podczas badań aplikacyjnych wykazano możliwość wykorzystania Fricke-XO-Żelatyny z sorbitolem do wykonywania testu zgodności. Weryfikacja planów leczenia przy użyciu grubych i cienkich dozymetrów Fricke nie zakończyła się pełnym sukcesem i pokazała potrzebę dalszej optymalizacji metody produkcji oraz poszukiwania potencjalnych materiałów mogących zastąpić żelatynę. Niemniej jednak dozymetry żelowe mogą być obiecującymi narzędziami do pomiarów *in vivo*.

Wykazano możliwość obrazowania trójwymiarowych dozymetrów żelowych Fricke o ścieżce optycznej 6 cm przy użyciu optycznej tomografii komputerowej. Aby uniknąć artefaktów na skanach, konieczne było zoptymalizowanie składu dozymetrów i warunków obrazowania. Kalibracja dozymetrów

wykazała, że dodatek sorbitolu zwiększył czułość dozymetru Fricke-XO-Gelatin o 26%, a pomiary współczynnika dyfuzji wykazały 50% spadek wartości współczynnika dozymetru Fricke-XO-Gelatin po dodaniu sorbitolu. Weryfikacja planu leczenia przy użyciu dozymetru Fricke-XO-Pluronic F-127 wykazała konieczność dalszej optymalizacji procesu weryfikacji. Przy użyciu Fricke-XO-Gelatin z sorbitolem przeprowadzono pomyślną weryfikację planu leczenia. Przeprowadzone badania wykazały pozytywny wpływ dodatku sorbitolu do matrycy żelatynowej na właściwości Fricke-XO-Gelatin. Ponadto wykazano możliwość wykorzystania dozymetrów żelowych w nowych zastosowaniach w radioterapii. Stąd można uznać, że cel pracy został osiągnięty.

Table of contents

Abstract	4
Streszczenie	6
Table of contents	8
1. Introduction	11
2. Aim and scope of work	12
3. Literature survey	13
3.1. Fundamentals of radiotherapy	13
3.2. Types of radiotherapy	15
3.2.1. External Beam Radiation Therapy	15
3.2.2. Brachytherapy	16
3.3. Dosimetry of ionizing radiation.....	16
3.3.1. Ionizing chambers	17
3.3.2. Calorimeters	18
3.3.3. Electronic Portal Imaging Devices	18
3.3.4. Thermoluminescent dosimetry	19
3.3.5. Plastic scintillation dosimetry.....	19
3.3.6. Alanine dosimetry.....	20
3.3.7. Semiconductor dosimetry	20
3.3.8. Film dosimetry	20
3.3.9. Liquid chemical dosimetry	21
3.3.9.1. Absorption of ionizing radiation.....	22
3.3.9.2. Water radiolysis	23
3.3.9.3. Fricke solution.....	24
3.4. 3D gel dosimetry	27
3.4.1. Fricke gel dosimeters.....	27
3.4.1.1. Fricke-Gelatin dosimeters	29
3.4.1.2. Fricke-Agarose dosimeters.....	30
3.4.1.3. Fricke-Polyvinyl Alcohol (PVA) dosimeters	30
3.4.1.4. Fricke-Pluronic F-127 dosimeters	31
3.4.2. Other gel dosimeters.....	31
3.4.2.1. Polymer gel dosimeters	31
3.4.2.2. Radiochromic gel dosimeters	32
4. Materials and methods.....	33
4.1. Sodium alginate to reduce diffusion of Fe^{3+} ions	33

4.1.1. Water quality measurements. Impact of water quality on the stability of iron solutions.....	33
4.1.2. Streaming current measurements.....	33
4.1.3. Preparation of macrocapsules.....	33
4.1.4 Preparation of 1D dosimeter.....	34
4.1.5. Preparation of nano- microgel.....	34
4.1.6. Preparation of 3D dosimeter.....	35
4.1.7. UV-Vis measurements	35
4.1.8. Diffusion measurements	35
4.1.9 Dynamic light scattering measurements.....	35
4.1.10. Assessment of metal content in macrocapsules.....	35
4.1.11. Irradiation of macrocapsules	36
4.1.12. Measurements of irradiation effects and data processing.....	37
4.2. Fricke 2D Dosimeters for Quality Assurance.....	37
4.2.1. Gel preparation	37
4.2.2. Samples preparation	37
4.2.3. Thermal analysis.....	39
4.2.4. Mechanical analysis.....	39
4.2.5. Assessment of chemical stability of the Fricke-XO-Gelatin with sorbitol dosimeter	40
4.2.6. Irradiation	40
4.2.7. Readout and data processing	42
4.3. Application studies of the Fricke dosimeter using OCT.....	42
4.3.1. Samples preparation	42
4.3.2 Irradiation	42
4.3.3. Samples scanning and data processing.....	43
5. Results and discussion.....	45
5.1. Sodium alginate to reduce diffusion of Fe^{3+} ions	45
5.1.1. Stability of Fe^{2+} ions in water.....	45
5.1.2. Interactions between ingredients	54
5.1.3. Characteristics of macrocapsules	57
5.1.4. Diffusion of Fe, Ca and XO from macrocapsules	61
5.1.5. Characteristics of nano- and micro-gels.....	64
5.1.6. 1D capsule dosimeter	69
5.2. Characteristics of the Fricke-XO-Gelatin with sorbitol addition 2D dosimeter.....	73
5.2.1. Impact of sorbitol addition on the thermal properties of the dosimeter.....	73
5.2.3. Chemical stability of the dosimeter.....	77

5.2.4. Application of the two-dimensional Fricke dosimeter	79
5.2.4.1. Dosimeter response to ionizing radiation	79
5.2.4.2. Evaluation of Beam Size	86
5.2.4.3. Coincidence test of radiation and mechanical isocenters	87
5.2.4.4. Dosimeters calibration.....	89
5.2.4.5. Treatment planning verification: Fricke-XO-Gelatin (thin gel)	92
5.2.4.6. Treatment planning verification: Fricke-XO-Gelatin (thick gel).....	97
5.3. Application studies of the Fricke-XO-Gelatin with sorbitol and Fricke-XO-Pluronic F-127 3D dosimeters.....	103
5.3.1. Optimization of gel composition and measurement conditions. Calibration of the dosimeters.....	103
5.3.2. Determination of the diffusion coefficient of Fricke dosimeters.....	112
5.3.3. Treatment planning verification in 3D: Fricke-XO-Pluronic F-127.....	118
5.3.4. Treatment planning verification in 3D: Fricke-XO-Gelatin with sorbitol.....	127
6. Conclusions	134
Literature	137
Publications	151
Conferences	152

1. Introduction

Cancer, along with circulatory system diseases, is currently one of the most common causes of premature death. It is predicted that 1 in 5 people will develop cancer during their lifetime. One of the methods of treating cancer is radiotherapy. It is estimated that over 50% of cancer patients undergo it at some stage of treatment. Radiotherapy is an effective method of treating many cancers, however, due to the risk of excessive irradiation of healthy tissues, it requires precise planning of the therapeutic dose distribution and high-quality radiation sources. One of the stages of radiotherapy is the verification of the planned dose distribution, which is performed using dosimeters.

The only dosimetry method that allows recording a three-dimensional dose distribution is the 3D gel dosimetry developed 40 years ago. Gel dosimeters consist of a gel matrix (e.g. gelatin, agarose, poly(vinyl alcohol), Pluronic F-127) and a radiosensitive chemical system. As a result of irradiation, chemical reactions occur, producing products in a concentration proportional to the absorbed dose of ionizing radiation. The role of the gel matrix is to immobilize these products and thus fix the information about the three-dimensional dose distribution. Depending on the chemical system used, the dose distribution can be read using methods such as magnetic resonance imaging, computed tomography, optical computed tomography and ultrasound.

In recent years, the most developed dosimeters are radiochromic and polymeric. As part of my bachelor's thesis, I optimized and characterized the Fricke-XO dosimeter with a new proposed Pluronic F-127 gel matrix. I modified this dosimeter during my master's thesis by adding sodium chloride to improve the thermal stability of the matrix. In addition, I prepared a two-phase Fricke foam-gel dosimeter imitating soft tissue and lungs. Motivated by the desire to continue my research work and further develop 3D gel dosimetry for use in radiotherapy, I have taken up the subject of this work aimed at further modifications of the Fricke dosimeter and proposing new applications of gel dosimeters in radiotherapy.

2. Aim and scope of work

The aim of this work was to modify the Fricke gel dosimeter to improve its properties for use in radiotherapy (primarily by reducing the diffusion coefficient), and also to propose new applications of gel dosimeters in radiotherapy and to test the Fricke dosimeter in these applications. To achieve this aim, the following scope was performed:

1. Investigation of the influence of water quality on the stability of Fe ions.
2. Investigation of the stability of the active ingredients of the Fricke dosimeter as well as sodium alginate, calcium chloride, Pluronic F-127, gelatin and two organic iron salts (ferrous lactate and ferrous gluconate), and investigation of the reactions occurring between selected ingredients.
3. Optimization of the macrocapsules production process by dripping 1.7-3.5% sodium alginate into Fricke solution containing additionally 0-3.5% calcium chloride. The viscosity of sodium alginate and its concentration were optimized, as well as the concentration of calcium chloride and the storage time of the capsules in the solution needed to obtain the maximum calcium and iron content. The capsules were then characterized in terms of the diffusion rate of calcium, iron and dye from the capsules.
4. Introduction of capsules into a gel matrix to obtain a 1D dosimeter. Investigation of the effect of the matrix on the properties of the capsules. Irradiation of capsules in the matrix to verify their potential use as a 1D dosimeter.
5. Attempt to produce a microgel solution of sodium alginate and iron ions. Introduction of the microgel solution into a gel matrix to obtain a 3D dosimeter.
6. The gel-sol transition temperature of gelatin, gelatin with sorbitol, gelatin with Fricke solution, and gelatin with Fricke solution and sorbitol was investigated. Compressive strength and fatigue compressive strength were measured for the same materials.
7. Development of methods for manufacturing two-dimensional gel dosimeters for use as a bolus dosimeter, a thin dosimeter for measuring dose distribution on the skin, a dosimeter for performing quality assurance tests of a medical accelerator (test of coincidence of the radiation and mechanical isocenter of the accelerator), and then conducting application tests of the obtained dosimeters.
8. Optimization of the composition of three-dimensional dosimeters Fricke-XO-Gelatin, Fricke-XO-Gelatin with sorbitol, Fricke-XO-Pluronic F-127 to enable their imaging using optical computed tomography. Optimization of the imaging process. Calibration of dosimeters.
9. Determination of the Fe ions diffusion coefficient in the tested Fricke gel dosimeters. Investigation of the anisotropic diffusion phenomenon.
10. Verification of the treatment plan using Fricke-XO-Pluronic F-127 and Fricke-XO-Gelatin or Fricke-XO-Gelatin with sorbitol. The gelatin dosimeter variant with better parameters was selected for the experiment.

3. Literature survey

3.1. Fundamentals of radiotherapy

In the 21st century, cancer has become one of the leading causes of premature death due to non-communicable diseases (NCDs). It is estimated that approximately 30% of all deaths caused by NCDs are a result of cancer, which is the second most prevalent cause after circulatory diseases (40% of deaths caused by NCDs) [1]. According to data from the International Agency for Research on Cancer (IARC), the number of new cancer cases diagnosed in 2022 was approximately 20 million worldwide, while the number of deaths from this disease was approximately 9.7 million [2]. Considering the dynamic increase in the annual number of new cancer cases (in 2012 it was about 14.1 million [3]), it can be expected that up to 20% of people will develop cancer during their lifetime [2] and this percentage may increase in the forthcoming years. Consequently, the development of oncological treatment methods is crucial to enhance the length and quality of life of many millions of people.

The most important methods of cancer treatment are chemotherapy, surgery, radiotherapy and immunotherapy [4]. A brief overview of each method is provided in Table 1. Depending on the size, type and stage of the cancer, one type of therapy is used, or two or more types are combined [5].

Table 1. Characteristics of the most important methods of cancer treatment.

Cancer treatment method	Definition	Advantages	Disadvantages	References
Chemotherapy	Killing cancer cells by using drugs	<ul style="list-style-type: none"> - High rate of cancer cell killing - The only method capable of eradicating micrometastases - Potential ability to modulate anti-tumor immunity 	<ul style="list-style-type: none"> - A plethora of side effects caused by the toxicity of chemotherapy drugs to normal cells (e.g. nausea, diarrhea, fatigue, rash, hair loss, bone marrow damage, cognitive functioning impairment) - Long-term treatment can lead to damage or failure of multiple organs 	[6-9]
Surgery	Tumor removing by surgery	<ul style="list-style-type: none"> - Effective in treating most solid tumors - Possibility to remove a large tumor in a short time 	<ul style="list-style-type: none"> - High risk of recurrence - High risk of metastasis - Pain after surgery - Decreased quality of life due to permanent removal of an organ or its fragment (e.g. permanent stoma in some patients with rectal cancer) 	[6, 10-13]
Radiotherapy	Killing cancer cells by using ionizing radiation	<ul style="list-style-type: none"> - Only the tumor site is irradiated - Possibility of stimulating the body to develop an 	<ul style="list-style-type: none"> - Long and short term side effects due to radiation of healthy cells surrounding the tumor (type of side effects) 	[6, 13-15]

		immune response to the tumor	depends on the site of irradiation) - Increased risk of secondary cancers	
Immunotherapy	Activating the patient's immune system to kill cancer cells	- High accuracy, specificity and targeting of immunotherapy - Long time of effectiveness. Can prevent recurrences and metastases	- Limited types of curable cancers - May lead to autoimmune diseases - Risk of hyperprogressive disease hastening the patient's death	[6, 16]

It is estimated that at least 50% of cancer patients will undergo radiotherapy at some stage of treatment [17]. In some cases, radiotherapy can be used alone [18], but it is usually part of a combination therapy [19, 20]. The aim of radiation oncology is to damage deoxyribonucleic acid (DNA) molecules in cancer cells as a result of their exposure to ionizing radiation. DNA damage can occur after direct interaction with radiation or indirectly through reactions with radicals that are products of radiolysis of water present in cells [21]. Breaking the double helix of DNA leads to the death of cancer cells. However, this process is not immediate and can last up to several weeks after irradiation [21]. Cancer cell death induced by ionizing radiation can occur through various mechanisms, which are presented in Table 2.

Table 2. Types of cell death induced by ionizing radiation [21-23]

Apoptosis	A process of highly controlled, programmed cell death by self-destruction. Apoptosis is accompanied by cell shrinkage, blebbing of the cell membrane, and pyknosis (the process of chromatin condensation in the cell nucleus). As a result, apoptotic bodies are formed, which are engulfed by various subtypes of macrophages to avoid inflammation.
Necrosis	A process in which increased permeability of the cell membrane causes the cell to swell and damage the organelles. In addition, the level of adenosine triphosphate (ATP) in the cell is drastically reduced, which prevents it from continuing its physiological functions. Due to excessive swelling, the cell membrane is ruptured, followed by leakage of intracellular contents, which causes inflammation.
Mitotic catastrophe	Cell death process due to abnormal mitosis resulting from damage to a DNA fragment involved in cell cycle control. During mitotic catastrophe, abnormal segregation of chromosomes occurs and giant cells with one or more nuclei are formed. Ultimately, the giant cells die by delayed apoptosis or necrosis.
Autophagy	The process by which a cell digests its own macromolecules or organelles. Autophagy is designed to protect the cell by removing unnecessary or defective structures. The energy obtained as a result of autophagy can allow the cell to survive a period of starvation or repair damaged parts of the cell. However, autophagy lasting too long leads to cell death.
Senescence	A condition in which a cell has lost its ability to proliferate further as a result of DNA damage (e.g. due to exposure to ionizing radiation). For a period of time, the cell is able to carry out normal physiological processes, but eventually dies, mainly by apoptosis.

Although ionizing radiation is an effective tool in killing cancer cells, it also poses a threat to healthy tissues. To reduce the negative impact of radiation on normal cells, dose fractionation is used, i.e. dividing the total dose that the tumor must be irradiated with into regularly delivered (usually daily for five days a week for a specified number of weeks) smaller doses (usually 1.8-2 gray (Gy)) [24]. Dose

fractionation is used to give healthy cells time to repair damaged DNA. Although cancer cells can also perform repair processes at the same time, their DNA repair capabilities are usually lower [25] and with an appropriately selected therapeutic window (time between subsequent doses of radiation) they are not able to fully regenerate [22]. Additionally, during the breaks between fractions, cancer cells undergo reoxygenation, which increases their sensitivity to radiation [25]. Despite its advantages, fractionation does not fully spare healthy tissues, and most often side effects appear during treatment, depending on the site of the tumor [26]. Examples of side effects accompanying selected tumors are presented in Table 3.

Table 3. Potential side effects of radiotherapy for selected cancers [13, 17, 27, 28]

Type of cancer	Common curative dose	Possible side effects
High-Grade Glioma	60 Gy (1.8-2 Gy per fraction)	Fatigue, alopecia, headache, erythema, cognitive impairments, brain necrosis
Head and neck	56-70 Gy (1.8-2.2 Gy per fraction)	Xerostomia, dysphagia, mucositis, dental complications, voice changes, dysgeusia
Breast	45-50 Gy (1.8-2 Gy per fraction)	Fatigue, swelling and heaviness in the breast, radiation dermatitis, lymphedema
Thyroid	60-70 Gy (1.8-2 Gy per fraction)	Dermatitis, pharyngitis, tracheitis, dermatitis, cartilage necrosis, pulmonary fibrosis, esophageal stenosis, laryngeal edema
Ovary	22.5-30 Gy (1-1.5 Gy per fraction)	Bowel discomfort, vaginal irritation, radiation enterocolitis
Colorectal	40-74 Gy (1.8-2 Gy per fraction)	Rectal irritation, stool leakage, bladder irritation, diarrhea, blood in the stool
Prostate	70 Gy (2 Gy per fraction)	Radiation cystitis, erection problems, problems with urination,
Non-melanoma skin cancer	45 Gy (3 Gy per fraction)	Erythema, hypopigmentation, atrophy
Small cell lung cancer	66 Gy (2 Gy per fraction) or 45 Gy (1.5 Gy per fraction)	Cough, shortness of breath, radiation pneumonitis

3.2. Types of radiotherapy

Radiotherapy involves administering a therapeutic dose of ionizing radiation to the tumor area while simultaneously minimizing the dose to the surrounding healthy tissues. The most commonly used type of particles in radiotherapy are photons (high energy X-rays > 1 MeV). Additionally, such beams are used: electrons, protons, neutrons and heavy ions. Over the last decades, types of radiotherapy have been developed that allow for precise delivery of a radiation dose to the site of the tumor. Types of radiotherapy can be divided according to the location of the radiation source during treatment into External Beam Radiation Therapy (EBRT) and brachytherapy [17]. EBRT is a group of non-invasive methods using sources located outside the patient's body, while brachytherapy involves the positioning of a sealed isotope emitting low-energy gamma radiation into the tumor or its vicinity [29].

3.2.1. External Beam Radiation Therapy

External Beam Radiation Therapy treatment is a multi-step process that includes: diagnostic imaging, defining the areas to be irradiated, calculating the dose distribution in Treatment Planning Systems (TPS), verifying the plan and patient positioning, and irradiation. In EBRT, techniques such as radiation are used:

1. 3D conformal radiotherapy (3DCRT) – dose distribution adjusted using blocks, Multileaf Collimators (MLC) and mechanical or dynamic wedges.
2. Intensity Modulated Radiotherapy (IMRT) – field shape and dose intensity are modulated during exposition. This is possible by using MLC where leaves are moving independently [30,31].
3. Volumetric Modulated Arc Therapy (VMAT) - During irradiation with the VMAT technique, the accelerator constantly rotates around the patient [32,33]. The use of arc therapy allows for the delivery of highly conformal dose distributions while shortening the irradiation time and reducing the number of MUs compared to fixed gantry IMRT.
4. Stereotactic RadioTherapy (SRT) and Stereotactic RadioSurgery (SRS) – delivery of high doses to a small volume in a short time in single fraction or several, typical fractional doses are 10-20 Gy [34,35].
5. Flash radiotherapy - FLASH uses very high dose rates (2400-6000 Gy/min) compared to conventional radiotherapy (0.5-5 Gy/min), moreover, the entire therapeutic dose is administered in one fraction [36,37]. The basis of this method is the effect of increased radioresistance of healthy cells irradiated with high dose rates observed in the mid-20th century [38,39]. At the same time, it was noted that cancer cells show similar susceptibility to FLASH as to conventional radiotherapy [40]. The previously proposed explanations of the effect of radioresistance of healthy cells suggest that it results from the rapid depletion of oxygen in the cell, which leads to a state of transient hypoxia [41].

3.2.2. Brachytherapy

Brachytherapy is a radiation technique that involves placing a radiation source (in modern brachytherapy, iridium-192, cobalt-60, palladium-103 and iodine-125 are most often used) directly in the tumor or in its close vicinity [42]. In order to precisely place the source, it is necessary to perform precise imaging of the tumor. The specificity of brachytherapy is the rapid decrease of the dose with the distance from the tumor, which allows for the delivery of very high doses to the tumor while sparing healthy tissue. It is estimated that the probability of achieving local tumor control through brachytherapy is over 90%, while the probability of severe organ complications is below 5% [43]. A significant advantage of brachytherapy is the elimination of the problem of movement of the patient's organs during therapy, because due to the close proximity, the source moves together with the tumor [42]. The main disadvantages of brachytherapy include its invasiveness, sources are most often introduced during the procedure under local or general anesthesia. In addition, very precise source placement is necessary for the success of the therapy. Even a small inaccuracy can lead to insufficient irradiation of the tumor and increased toxicity to healthy organs. Currently, brachytherapy is mainly used in the treatment of reproductive system cancers (prostate, penile glands, cervix, vulvo-vaginal, endometrial), as well as head and neck, breast, skin, anus and bladder cancers.

3.3. Dosimetry of ionizing radiation

All of the described in section 3.2. methods of radiation therapy are highly precise in delivering the largest possible dose to the tumor while sparing the patient's healthy tissues. Personalized treatment plans and state-of-the-art medical accelerators are necessary to make this possible. Even the slightest inaccuracy can lead to therapy failure and increase the risk of life-threatening side effects, so it is essential to verify treatment plans and conduct routine quality assurance tests, which is the focus of ionizing radiation dosimetry [44-46]. Various dose measurement tools (dosimeters) have been developed over the years. This section briefly presents selected types of dosimeters, with particular emphasis on the Fricke chemical dosimeter.

3.3.1. Ionizing chambers

Ionization chambers are one of the most commonly used types of dosimeters in radiotherapy [47,48]. The most popular type of ionization chamber used in radiotherapy is the Farmer-type chamber (other types of ionization chambers used in radiotherapy include the well-type used in brachytherapy and the plane-parallel type), which consists of a gas-filled cavity with central electrode surrounded by a conductive wall that acts as an external electrode (Figure 1) [49]. During irradiation, the gas becomes ionized and ion-electron pairs are formed which are collected by the electrodes. This movement of charges to the electrodes generates an electric current, the measurement of which determines the delivered radiation dose [14]. An important parameter in dose measurements with an ionization chamber is the value of the voltage between the electrodes. The optimal value should allow for collecting all the generated ion-electron pairs [14]. When the voltage is too low, part of the ions will recombine before reaching the electrodes and the measurement result will be underestimated. The results of dose measurements with an ionization chamber should be corrected to take into account the temperature and atmospheric pressure at the time of measurement [50].

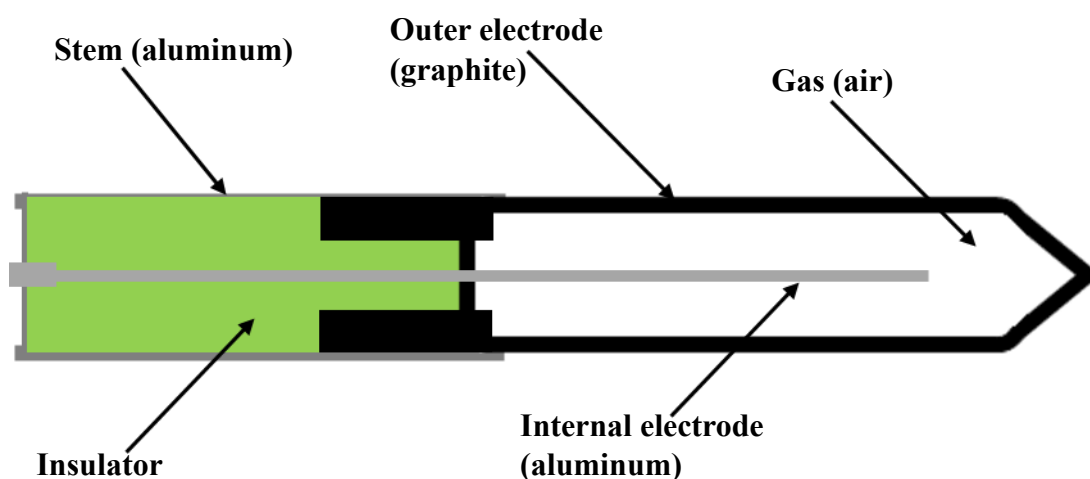


Figure 1. Schematic diagram of the Farmer type electrode. The cavity is usually filled with air, the central electrode is made of aluminum, and the outer electrode is made of graphite. The sensitive section of the chamber typically has a volume of 0.6 cm^3 [49]. The image is not shown to scale.

A single ionization chamber can act as a point radiation dosimeter [44]. To measure the dose distribution, multiple ionization chambers can be connected in an array. One example is the two-dimensional Seven29™ array presented in 2004 [51]. This consisted of 729 chambers arranged in a 27×27 matrix. A significant disadvantage of this approach is the relatively low spatial resolution (the distance between

neighboring chamber centers was 1 cm). However, in recent years, new models of chamber arrays have been presented that allow treatment plans to be verified with over 95% agreement [52].

3.3.2. Calorimeters

Dose measurement using calorimetric dosimeters involves measuring the increase in detector temperature caused by the absorption of radiation energy [53]. Due to their high tissue similarity, water calorimeters are ideal for dose measurement in radiotherapy. Nonetheless, complications associated with the use of water, such as convection and heat diffusion, made graphite calorimeters more commonly used [54]. An additional advantage of graphite is that its heat capacity is almost six times lower than that of water, resulting in much higher sensitivity of the graphite calorimeter [55]. Conventional calorimeters are very rarely used in clinical practice due to their large size, operational complexity and a requirement to maintain a strictly controlled environment [56,57]. Furthermore, calorimetric dosimeters are absolute dosimeters, meaning they do not require calibration; hence they are primarily used in primary standard laboratories to calibrate other types of dosimeters. However, as the measurement results using calorimeters are independent of the dose rate, these dosimeters are currently considered appropriate detectors for dose measurement in FLASH therapy [53,55]. For this reason, in recent years there has been an increasing interest in the development of small, easy-to-use and portable calorimeters [56-58].

3.3.3. Electronic Portal Imaging Devices

Electronic Portal Imaging Devices (EPID) are parts of the medical accelerators that were originally used to verify patient positioning during EBRT [59]. However, they have recently become increasingly popular in ionizing radiation dosimetry thanks to their high spatial resolution, almost linear dose response, good long-term stability and real-time readout. Modern EPIDs consist of an amorphous silicon (a-Si) layer deposited on a glass substrate to create an array of photodiodes [60]. Each photodiode is connected to its corresponding transistor, and together they form one pixel. This pixel array is covered with a phosphor screen, typically made of gadolinium oxysulfide doped with terbium ($\text{Gd}_2\text{O}_2\text{S:Tb}$), on which a 1 mm thick copper plate is placed [60]. The structure of a-Si EPIDs is shown in Figure 2. Photons of ionizing radiation incident on the metal plate are converted into electrons. These electrons are then converted in the scintillation layer into optical photons, which are absorbed by the photodiodes, generating charge in the process. The signal measured by the EPIDs is then used to reconstruct the dose distribution.

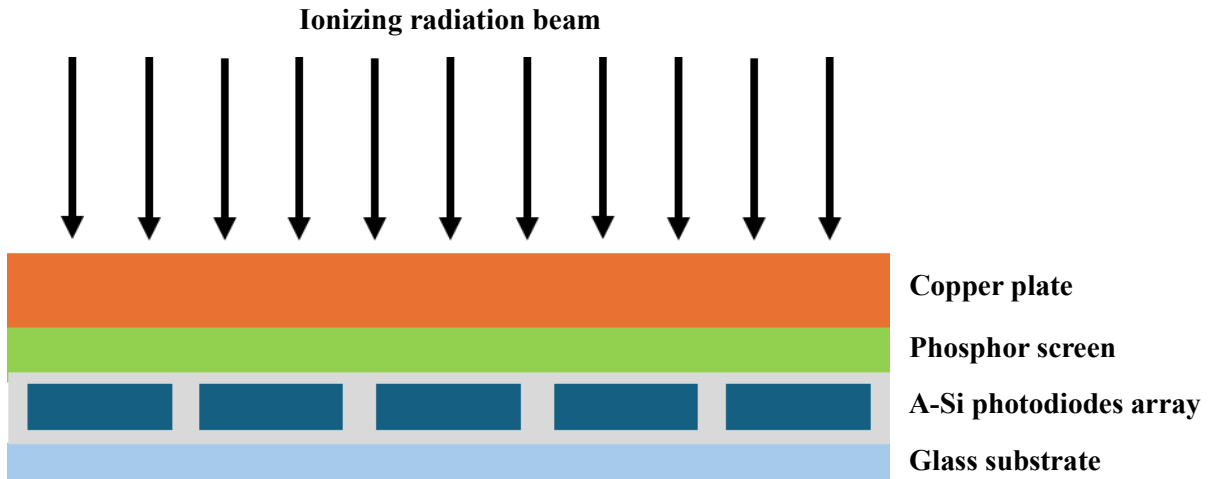


Figure 2. Schematic diagram of the a-Si EPID structure. The image is not shown to scale.

EPIDs are used to measure the dose distribution in 2D, however, it is possible to use them to calculate the dose distribution in 3D using the backward design [59]. A significant advantage of these dosimeters is that they can be used for *in vivo* dosimetry [59, 61]. The main disadvantage of EPIDs is their energy-dependent response resulting from their construction [62], which can lead to artefacts and measurement errors.

3.3.4. Thermoluminescent dosimetry

Thermoluminescent detectors (TLDs) are inorganic solids with a crystalline structure. They are most often made of lithium fluoride, lithium borate or calcium fluoride, which contain inorganic impurities such as copper, magnesium, phosphorus and titanium [63, 64]. When they absorb radiation energy, some electrons pass from the valence band to the conduction band. Electrons returning from the conduction band to the valence band can fall into an energy trap in the gap band created by the presence of impurities and achieve a metastable state [63]. Heating the TLD to an appropriately high temperature (depending on the material used) supplies the energy needed for electrons to leave the trap and return to the valence band, accompanied by the emission of a photon. By measuring the intensity of the emitted light, it is possible to calculate the delivered dose. TLDs are commonly used in clinical practice due to their good tissue equivalency, small size, high sensitivity, and ability to measure very small doses. The minimum dose that can be measured with the TLD-100 model (lithium fluoride containing magnesium and titanium impurities) is 10 μG [64]. TLDs enable point-based dose measurement. They can be placed in various organs of phantoms or glued to the patient's skin during therapy.

3.3.5. Plastic scintillation dosimetry

Plastic scintillators consist of a solid polymer (polystyrene (PS) or polyvinyltoluene (PVT)) doped with organic fluorescent dyes (aromatic compounds such as pyrene, 1,1,4,4-tetraphenylbutadiene (TPB) or 1,6-diphenyl-1,3,5-hexatriene (DPH)) [65,66]. A plastic scintillation dosimeter (PSD) is obtained by connecting a plastic scintillator to an optical fiber at the end of which a photodetector is located. The dose is measured by the scintillation process, i.e. the emission of visible or UV light as a result of the absorption of ionizing radiation. The emitted light is transmitted through an optical fiber to the photodetector, which converts it into an electrical signal. The most important advantage of PSD is its very short response time (1-10 ns), which allows for the measurement of the dose in real time [67]. High

temporal resolution makes PSDs also attractive dosimeters in FLASH radiotherapy, as they allow measurement of the dose delivered with each pulse of the accelerator.

3.3.6. Alanine dosimetry

Alanine is a naturally occurring amino acid [68]. Its irradiation produces stable radicals, the concentration of which can be measured using electron paramagnetic resonance (EPR) [69]. The intensity of the EPR signal is proportional to the number of radicals generated, which is proportional to the absorbed radiation dose. Alanine dosimeters are most often used in a form of a cylindrical pellet measuring 4.5 mm in diameter and 3.5 mm in height, although they are also available in film or gel form [69,70]. Dosimeters typically consist of alanine and a binder (e.g. paraffin, polyethylene (PE) or polyvinyl chloride (PVC)), although some researchers suggest using pure alanine placed in a glass tube to eliminate the background signal from the binder material during EPR measurements [69]. The advantages of alanine dosimeters include good tissue equivalence for photons and protons, high radical stability generated by irradiation (for over a year), sensitivity to low radiation doses (from 0.1 Gy), fast dose readings and low cost [70]. Due to their small size, alanine dosimeters are typically used as point radiation detectors that can be placed in phantoms or adhered to the patient's skin for *in vivo* dosimetry [71]. Recently, the use of alanine dosimeters in FLASH radiotherapy has been proposed [72].

3.3.7. Semiconductor dosimetry

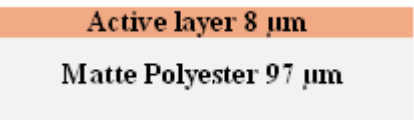
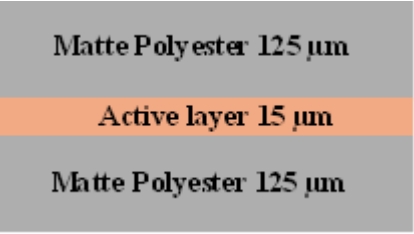
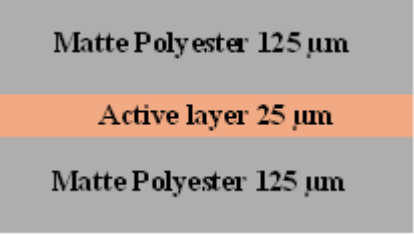
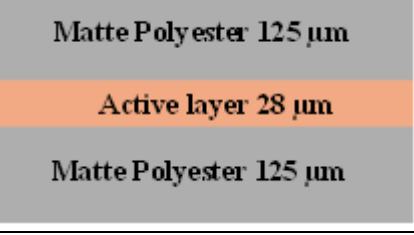
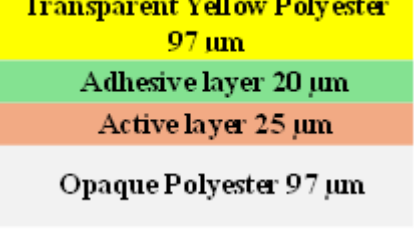
Semiconductor dosimeters are a type of detector in which electron-hole pairs are formed due to irradiation [73]. When these pairs diffuse to the electrodes, a current proportional to the absorbed radiation dose flows. The most commonly used types of semiconductor detector include diodes, metal–oxide–semiconductor field-effect transistors (MOSFETs) and diamonds. Key advantages include a linear dose response, stable sensitivity and a relatively small sensitive volume, as well as a real-time dose response [73]. Semiconductors can be used in both phantom and *in vivo* dosimetry. They can be used for point dose reading and dose distribution in one, two or three dimensions e.g. a single diode acts as a point dosimeter, but it can be connected in 1D, 2D and quasi-3D arrays. An example of a quasi-3D detector is the commercially available ArchCheck dosimeter (SunNuclear, USA) consisting of 1386 diodes arranged in a spiral shape inside a doughnut-shaped cylindrical poly(methyl methacrylate) (PMMA) phantom (the distance between the diodes is 1 cm) [73].

3.3.8. Film dosimetry

Film dosimeters can be divided into radiographic and radiochromic films. Radiographic films typically comprise a 0.2 mm-thick transparent polyester base covered on both sides with a radiosensitive emulsion [74]. The emulsion contains silver halide crystals suspended in gelatin. Irradiation causes ionization of the silver halide crystals, creating a latent image. After irradiation, the film requires further processing, including development, fixing, washing and drying. During development, the film is immersed in a developer solution that reduces the silver ions formed during irradiation into metallic silver. The film is then washed with a fixing agent to remove the remaining silver halide crystals, rinsed to remove all compounds except metallic silver and finally dried with heated air [74]. The resulting film is blackened proportionally to the absorbed dose. Reading the measured dose distribution can be performed using point densitometers that measure optical density (OD), or by processing the digitized image (scanned with a laser scanner) in software [75].

Radiochromic films have favorable characteristics over radiographic films. Both types of films have advantages such as high resolution in 2D measurements, ruggedness, and permanent recording, however radiochromic films are also almost tissue-equivalent, do not exhibit sensitivity to visible light, and most importantly, do not require a complex process of post-irradiation film processing [76]. The most commonly used in clinical practice are Gafchromic™ films [77]. Commercially available models differ in structure (characteristics of selected models are presented in Table 4), but all of them have an active layer consisting of monomers that polymerize after absorbing ionizing radiation. As a result of polymerization, the color of the active layer changes proportionally to the radiation dose [78]. The dose distribution reading is most often performed by analyzing the digitalized image in software (scanned with a laser scanner) [79].

Table 4. Properties of commercially available Gafchromic™ films [76]. The film structure images are not shown to scale.

Film model	Dose range [Gy]	Film structure
HD-V2	10-100	
MD-V3	1-100	
EBT-XD	0.04-40	
EBT3	0.01-30	
XR-QA2	0.001-0.2	

3.3.9. Liquid chemical dosimetry

Chemical dosimeters are a group of ionizing radiation detectors in which chemical reactions occur after irradiation. Dose measurement using them is performed by measuring the increase in the concentration of products or the decrease in the concentration of substrates of these reactions. Over the years, many chemical dosimeters have been developed, such as the Fricke dosimeter, leucodye-based dosimeters, the cerium dosimeter, the ferroin dosimeter, and the benzene dosimeter [80]. Since liquid chemical dosimeters are not currently used in clinical practice [81], only the Fricke solution, which is one of the most popular chemical dosimeters and the subject of this dissertation, will be characterized in this section.

3.3.9.1. Absorption of ionizing radiation

The interaction of ionizing radiation with matter varies depending on the type of radiation. In the case of a stream of charged particles, their energy is lost mainly as a result of collisions with electrons in atoms [80]. Depending on the amount of transferred energy, the atom may be excited or, if the energy is high enough, ionized. If the particle is an electron, it is also possible to lose energy through interactions with atomic nuclei. When an electron comes close to an atomic nucleus, its velocity vector changes and a quantum of electromagnetic radiation, the so-called braking radiation (bremsstrahlung), is emitted [80,82].

The absorption of high-energy electromagnetic radiation by matter can occur according to three mechanisms, depending on the energy of the photons: the photoelectric effect, the Compton effect and the pair production effect [80,82]. The photoelectric effect is a mechanism of transferring energy to a medium via photons of the lowest energy. Photons collide with orbital electrons and transfer all their energy to them. The electrons are set in motion, and their kinetic energy corresponds to the difference in the energy of the incident photon and the binding energy of the electron in the atom. The Compton effect is a phenomenon of scattering radiation quanta on free electrons and orbital electrons when the energy of the incident photons is much higher than the binding energy of the electron in the atom. As a result of Compton scattering, a recoil electron is created, to which part of the energy of the incident photon has been transferred, and a secondary photon with lower energy than the primary photon (Figure 3). When a photon with energy higher than twice the rest energy of the electron (1.02 MeV) enters the strong electric field of the nucleus, it can decay with the formation of a negatron-positron pair due to the pair production effect. The energy of the photon is taken over by the created pair. The negatron loses energy through collisions with orbital electrons, while the positron after partial slowing down recombines with the electron, which is accompanied by the emission of two annihilation quanta with opposite directions and energies equal to 0.511 MeV.

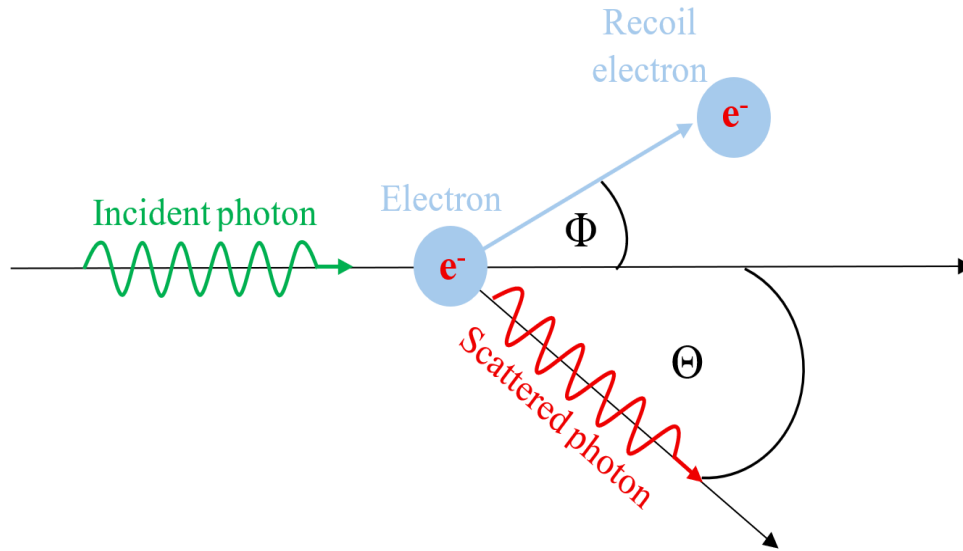


Figure 3. Compton scattering scheme.

3.3.9.2. Water radiolysis

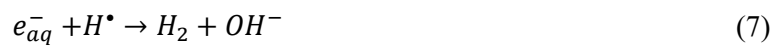
When the medium absorbing the energy of ionizing radiation is water, its radiolysis occurs. Water radiolysis is a process consisting of three successive stages: physical, physicochemical and chemical [80,82,83]. The physical stage lasts about 1 fs from the moment of water irradiation. During this time, part of water molecules is ionized and some are excited (equations (1) and 2)).

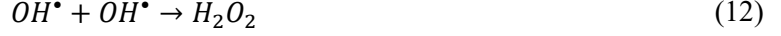


In the time from 10^{-15} s to 10^{-12} s after irradiation, the physicochemical stage of water radiolysis takes place. At this stage, reactions of ions with water molecules, decomposition of excited water molecules and solvation of electrons take place (equations (3)-(5) respectively).

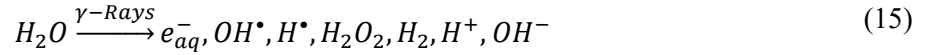


In the chemical stage lasting from 10^{-12} s to 10^{-6} s, diffusion of reaction products (3)-(5) and reactions of these products with each other (equations (6)-(14)) as well as reactions with dissolved substances (e.g. components of chemical dosimeters) take place.





The radiolysis of water can be summarized by the equation (15). The radiolysis products participate in the oxidation of ferrous ions in the Fricke dosimeter, which is described in the next section.



3.3.9.3. Fricke solution

The ferrous-ferric dosimeter (later called the Fricke dosimeter) was proposed in 1927 by Hugo Fricke and Sterne Morse [84]. It was an acidified solution of ferrous ions (Fe^{2+}), consisting of ferrous sulphate (recommended concentration 1 mM) and 0.4 mM sulphuric acid. As a result of irradiation, the ferrous ions were oxidized to ferric (Fe^{3+}). Initially, the increase in the product concentration was measured using electrometric titration [85], later spectrophotometric methods were used, measuring the value of the absorption maximum at a wavelength of 304 nm [86,87]. The mechanism of reactions occurring in the Fricke dosimeter after irradiation was proposed in 1949 [88] and can be described by equations (16)-(21)



As one can notice, single H radical formed in reaction (16) leads to the oxidation of three Fe^{2+} ions. The reaction of H^{\bullet} with oxygen (equation (17)) leads to the formation of the HO_2^{\bullet} radical, which in reaction (18) oxidizes the first ferrous ion and also forms HO_2^{-} ion. Further, HO_2^{-} reacting with H^{+} (equation 18) forms hydrogen peroxide (H_2O_2), which in reaction (21) oxidizes the second ferrous ion and forms the OH^{\bullet} radical. The resulting radical oxidizes the third ferrous ion in reaction (20). One molecule of hydrogen peroxide oxidizes two Fe^{2+} ions. The first in direct reaction (21), and the second indirectly by reaction of the OH^{\bullet} radical formed in (21) with the ferrous ion (equation (20)). The OH^{\bullet} radical oxidizes one Fe^{2+} ion in reaction (20). The above observations allow the calculation of the theoretical chemical yield of Fe^{3+} ions formation using equation (22). The chemical yields of H^{\bullet} and OH^{\bullet} radicals and H_2O_2 molecule formation in a solution containing 0.4 mM of sulphuric acid irradiated with gamma rays from a Co-60 source are 3.7, 2.9 and 0.8 Part./100 eV, respectively [89].

$$G(Fe^{3+})_{Air} = 3G(H^\bullet) + 2G(H_2O_2) + G(OH^\bullet) \quad (22)$$

The theoretical value of the chemical yield of the oxidation reaction of Fe^{2+} ions in a solution containing 0.4 mM H_2SO_4 was calculated as 15.5 ions/100 eV for ^{60}Co γ -rays [89]. Theoretically, the precise knowledge of the reactions occurring in the dosimeter and the resulting knowledge of the chemical yield values allows the Fricke dosimeter to be treated as an absolute detector because the dose absorbed by the solution can be calculated using equation (23) [90].

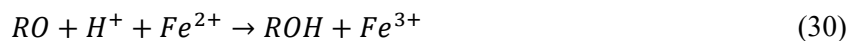
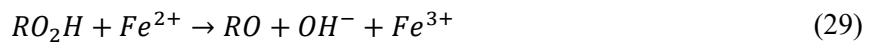
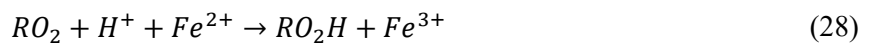
$$\Delta[Fe^{3+}] = \frac{D \cdot G(Fe^{3+}) \cdot 10\rho}{N_A \cdot e} \quad (23)$$

where $\Delta[Fe^{3+}]$ is the increase in Fe^{3+} ion concentration, D is the dose, $G(Fe^{3+})$ is the chemical efficiency of ferric ions formation, ρ is the density, N_A is Avogadro's number, and e is the number of joules per electron volt. It should be noted, however, that the value of $G(Fe^{3+})$ depends on various factors related to both the composition of the dosimeter and the irradiation conditions. The value of $G(Fe^{3+})$ strongly depends on the oxygen content in the solution [89]. In a situation where a deoxygenated solution is used or oxygen is consumed during irradiation (for a standard Fricke dosimeter irradiated in the presence of air, oxygen consumption occurs after the delivery of a dose of about 400 Gy [89], which is a rather unusual value in radiotherapy), the reaction mechanism is changed. The reactions described by equations (17)-(19) do not occur (reaction (20) still occurs because H_2O_2 is a product of water radiolysis, which is also formed in reactions other than (19), such as the reaction of two OH^\bullet radicals (equation (12)). However, reaction (24) becomes more important, as it was too slow in solution with oxygen and the vast majority of H^\bullet radicals participated in the three orders of magnitude faster reaction (17). As a result of these changes, the chemical efficiency of Fe^{3+} ion formation is calculated from formula (25). It is 8.2 ions/100 eV for ^{60}Co γ -rays [89].



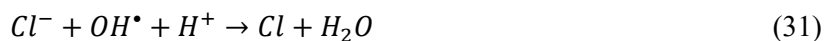
$$G(Fe^{3+})_{Deair} = G(H^\bullet) + 2G(H_2O_2) + G(OH^\bullet) \quad (25)$$

Organic impurities (marked with the general formula RH where H is the hydrogen atom and R is the remaining part of the organic molecule) have a significant influence on the chemical yield of Fe^{3+} ions formation [91]. In the presence of oxygen, the reactions described by equations (25)-(29) occur.



From the reactions (26)-(30) it results that one RH molecule leads to oxidation of three Fe^{2+} ions which results in a significant increase of the $G(Fe^{3+})$ value. In order to mitigate the influence of organic impurities, the addition of 1 mM $NaCl$ [92] was proposed. The presence of chloride ions results in reactions (31) and (32). In (31) chloride ions react with OH^\bullet radicals. This reaction is about 100 times faster than the reaction of OH^\bullet radicals with the vast majority of organic impurities [80]. As a result of

(31), reaction (26) almost does not occur and consequently the chain of reactions (27)-(30) does not occur either. One can notice that as a result of reaction (31) reaction (20) does not occur which should lower the $G(\text{Fe}^{3+})$ value. However, this value remains constant due to reaction (32). Currently, NaCl is added to the Fricke dosimeters very rarely. This is due to the higher purity of modern reagents in comparison to the reagents used in the 20th century [93]. Chloride ions can also catalyze the oxidation reaction of Fe^{2+} ions with oxygen, which may limit the storage time of dosimeters [80].



When a solution with organic contaminants is deoxygenated, no oxidation of ferrous ions is observed. Reactions (17)-(19) and (27)-(30) do not occur, and most of the H and OH radicals react with organic molecules to form organic radicals that can reduce Fe^{3+} ions.

The advantage of the Fricke solution is its insensitivity to deviations in the concentration of components that may arise during their weighing, which allows for good reproducibility of this dosimeter [80]. The concentration of ferrous ions should be in the range of 0.1-10 mM. However, it should be noted that an increase in the concentration of ferrous ions leads to an increase in the rate of autoxidation of the dosimeter (oxidation reaction of the non-irradiated Fe^{2+} solution by oxygen) and leads to a decrease in the storage time of the solution. When the Fe^{2+} concentration is lower than 0.1 mM, the reactions become slow, while above 10 mM a decrease in $G(\text{Fe}^{3+})$ is observed. NaCl used in a concentration of 1 mM can affect the value of $G(\text{Fe}^{3+})$ only when the salt concentration is increased to 10 mM [94]. Sulphuric acid in the Fricke liquid dosimeter should be used in concentrations of 0.05-0.5 M. Below the lower limit the $G(\text{Fe}^{3+})$ value decreases, while above the upper limit it increases.

No effect of solution temperature on the chemical efficiency of Fe^{3+} ion formation was observed, or the temperature effect was negligible [80]. The $G(\text{Fe}^{3+})$ value is also independent of the dose rate up to a threshold value of 10^6 Gy/s [91]. Above this dose rate, the $G(\text{Fe}^{3+})$ value decreases due to the increased rate of competitive interrational reactions [80]. The $G(\text{Fe}^{3+})$ value in the Fricke solution strongly depends on the type and energy of radiation, which is a significant disadvantage of the dosimeter and led to its discontinuation [95] after decades of serving as a dosimetry standard in all laboratories where X-rays and gamma rays of relatively high intensity were used [96]. Nevertheless, some research groups are still developing the Fricke solution for applications such as blood irradiation or irradiation of small animals [97,98].

In the case of using the standard Fricke solution in radiotherapy, a significant disadvantage of this detector is the minimum dose that must be irradiated to observe a measurable change. Depending on the source, the threshold dose is 20 Gy [81] or 40 Gy [91]. Both values are much higher than the fractional dose used in conventional radiotherapy (Table 3 in section 3.1.). The first approach consisted in increasing the sensitivity of analytical methods. This allowed to reduce the threshold dose to 0.5 Gy but required much more time and more qualified personnel than in the case of spectrophotometric measurements [91]. An alternative was to use the phenomenon of increased chemical efficiency of Fe^{3+} ion formation in the presence of organic pollutants. The first tests were carried out by adding 0.1 M formic acid (HCOOH) and simultaneously eliminating NaCl [91]. This allowed to increase the $G(\text{Fe}^{3+})$ value by about 15 times compared to the standard solution. This modification, however, has not found

wider application due to the dependence of the reactions rate on temperature. Another approach was the addition of 1.3 mM benzoic acid (in the absence of NaCl) [91]. It allowed for the reduction of the threshold dose to 1 Gy. Additionally, it increased the solution's resistance to autoxidation as a result of the formation of complex compounds by benzoic acid molecules and ferrous ions. The modification of the Fricke solution with benzoic acid was the subject of many studies in the 20th century (the leader was B.L. Gupta [98-102]), and even modernly it arouses the interest of researchers still developing the Fricke liquid dosimeter [81].

3.4. 3D gel dosimetry

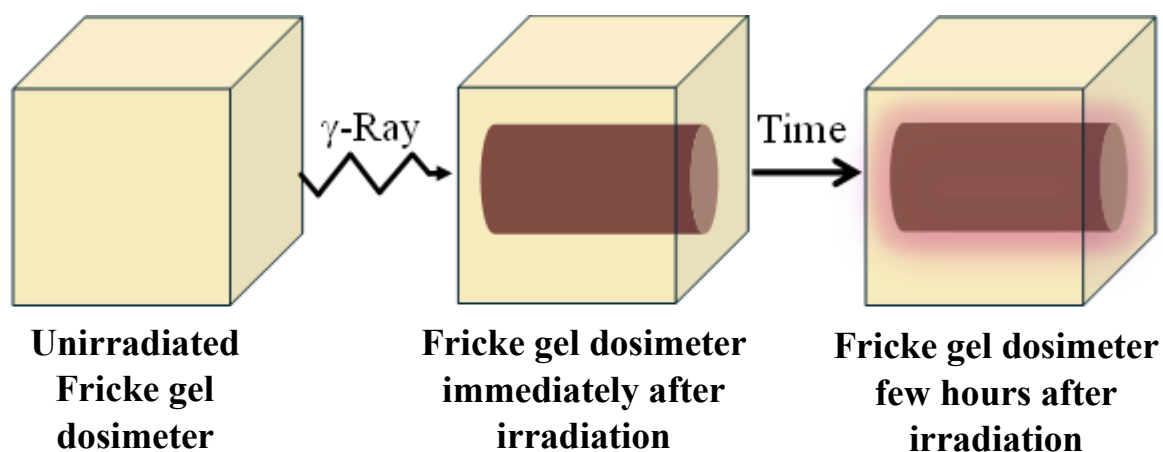
The types of dosimeters presented in section 3.3. share a common disadvantage, which is the inability to record the dose distribution in 3D. In order to obtain a three-dimensional dose distribution using 1D and 2D dosimeters, it is necessary to use transformations, which is associated with a loss of spatial resolution and uncertainties related to the approximations used. This is particularly problematic in the case of IMRT or SRT irradiation, where steep dose gradients occur. The only type of detectors that allow for recording the dose distribution in 3D are gel dosimeters [103]. These detectors consist mainly of water, which makes them radiologically equivalent to soft tissue. In addition, gel materials can be modified to imitate other types of tissues. Lung-mimicking dosimeters were obtained by adding Styrofoam beads to the gel [104] or by foaming the gel [105,106]. Bones can be imitated by gels with the addition of calcium hydrogen phosphate dihydrate [107] or hydroxyapatite [108,109]. Recently, the idea of a multiphase dosimeter consisting of gels imitating different tissues has been proposed [110]. A group of deformable gel dosimeters has also been presented [111-114]. Such detectors can be elastically deformed during irradiation, imitating the natural movement of irradiated tissues.

3.4.1. Fricke gel dosimeters

The first three-dimensional gel dosimeter consisted of a Fricke solution and a gelatin matrix was proposed in 1984 [115,116]. Magnetic Resonance Imaging (MRI) was used to read the dose distribution. The presence of a gelling agent causes the properties of the gel and liquid Fricke dosimeters to differ significantly. The $G(\text{Fe}^{3+})$ value of the dosimeter with a 1.5% agarose matrix was about 100 ions/100 eV [17], which was due to the fact that the long organic chains of the gelling agents acted as organic impurities and led to the chain oxidation reaction of Fe^{2+} ions according to reactions (11)-(15) (section 3.3.9). The effect of the NaCl addition, successfully used in Fricke solutions to control the influence of organic impurities on the $G(\text{Fe}^{3+})$ value, in the gel turned out to be negligible due to the too high concentration of the gelling agents [90]. The addition of benzoic acid also had no effect on the properties of Fricke gels [118]. However, increasing sensitivity was not necessary because the presence of the gel matrix enabled the measurement of doses used in radiotherapy. The standard Fricke solution contained 400 mM sulphuric acid. Due to the degradation of the gel matrix, the H_2SO_4 concentration was significantly reduced to values not exceeding 50 mM. This allowed to maintain the uniformity of the gel while not negatively affecting the sensitivity of the gel dosimeters [95]. For the Fricke gel dosimeters, no effect of radiation quality was observed in the energy range of 6-18 MeV, and the dosimeter response was not dependent on the dose rate in the range of 1-24.2 Gy/min [95].

The biggest disadvantage of Fricke gel dosimeters is the diffusion of ferric ions in the gel matrix [119]. In a short time, this leads to the deterioration of scanned gel images and introduces significant uncertainty in the read dose distribution. To reduce the influence of diffusion, it would be necessary to

perform dose distribution measurements shortly after irradiation, which in practice is not always possible due to limited access to MRI, which is also used in patient diagnostics, and often also the need to transport the dosimeter because MRI may be located in a different place than the accelerator. To reduce the diffusion coefficient, two strategies were investigated. The first one assumed changing the morphology of the gel matrix by using different gelling agents, as well as cross-linking additives to limit the mobility of iron ions by creating a maze-like gel structure. This strategy will be presented in detail in sections 3.4.1.1.-3.4.1.4. An alternative approach was to introduce chelating compounds binding ferric ions into larger and less mobile complexes. The first proposed chelating agent was xylenol orange (XO) [120]. Xylenol orange is an organic dye present in the form of a di- or tetrasodium salt. Depending on the concentrations of Fe^{3+} ions and XO molecules, four complexes can be formed, differing in the stoichiometry of the dye and iron [121]. The ratio of XO to Fe^{3+} ions can be 3:1, 2:1, 1:1 or 1:2. The binding of ferric ions is accompanied by a color change from orange to purple. The addition of XO reduced the diffusion coefficient from 1.46 to $0.81 \text{ mm}^2\text{h}^{-1}$ for 4% gelatin and from 1.33 to $0.97 \text{ mm}^2\text{h}^{-1}$ for 1% agarose, nevertheless diffusion still remained a significant problem [122,123]. Furthermore, the sensitivity of measurements using MRI was reduced [95]. However, the most important effect of the presence of XO in the Fricke dosimeter was the possibility of reading the dose distribution using more easily accessible optical methods, such as optical computed tomography (OCT). [124]. Nine other ferric ion chelating dyes were tested [125]. However, besides XO, only methylthymol blue (MTB) exhibited suitable properties for use in Fricke gel dosimeters. Figure 4 shows the macroscopic (A) and microscopic (B) changes occurring after irradiation in a Fricke radiochromic dosimeter containing XO.



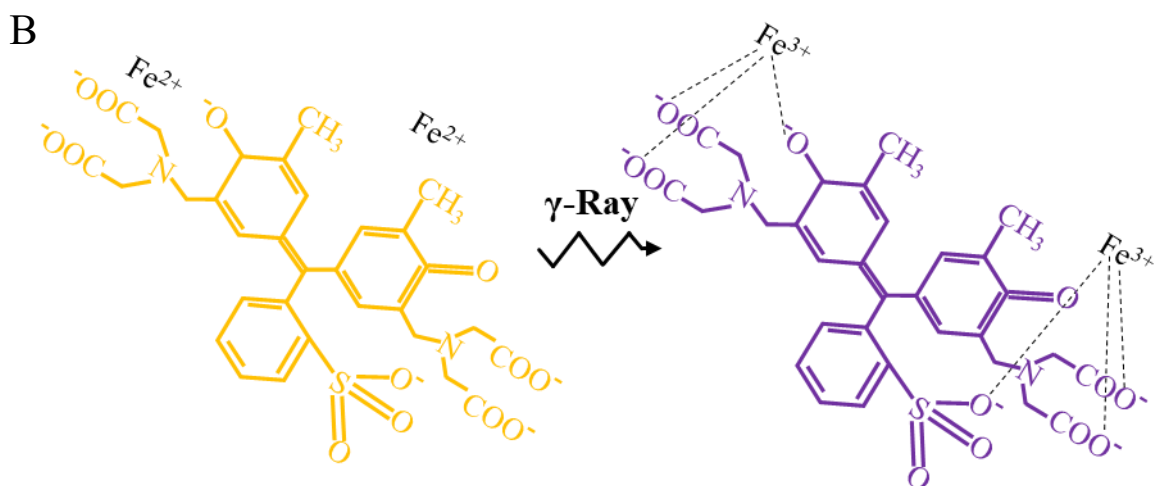


Figure 4. A: Macroscopic scheme of changes occurring in the Fricke radiochromic dosimeter (with XO) after irradiation. **B:** Microscopic scheme of changes occurring in the Fricke radiochromic dosimeter after irradiation. The XO molecule does not bind Fe^{2+} ions present in the unirradiated dosimeter. When ferrous ions are oxidized to ferric ions after irradiation, they are bound by XO, which is accompanied by a color change of the gel from orange to purple, proportional to the absorbed dose. Due to ferric ions diffusion, the recorded dose distribution deteriorates significantly within a few hours of irradiation.

3.4.1.1. Fricke-Gelatin dosimeters

Gelatin was the first gelling agent used in gel dosimetry and remains the most popular gel matrix to this day. It is a natural material of animal origin. Its advantages include high transparency in the visible light range, which allows for reading the dose using optical methods. Gelatin dosimeters are also relatively easy to prepare. Powdered gelatin is dissolved in water at a temperature of about 50°C , and then, after cooling to $35\text{--}40^\circ\text{C}$, Fricke's solution is added and cooled further until a gel is obtained. The entire process is not laborious and can be completed in about an hour. The most significant disadvantage of gelatin is the low gel-sol transition temperature. Depending on the concentration, the melting of the gelatin used in dosimeters (high-strength gelatin) occurs at temperatures of $28\text{--}34^\circ\text{C}$, but temperatures exceeding 23°C can affect the uniformity of the gel [126]. This requires precise control of the temperature at which the dosimeter is irradiated, transported and imaged. Another disadvantage is the ageing-related yellowing of the gel. However, this is a more significant problem in other types of gel dosimeters. The autoxidation processes of ferrous ions significantly shorten the shelf life of the dosimeter, hence the ageing processes of gelatin are not a factor limiting its use in Fricke dosimeters.

Various modifications have been proposed for the Fricke-Gelatin dosimeter to improve its properties, primarily to reduce the diffusion coefficient. The most important modification was the XO additive discussed in section 3.4.1. The introduction of formaldehyde to the Fricke-XO gel reduced the diffusion coefficient to $0.44\text{ mm}^2\text{h}^{-1}$ [127]. Additionally, formaldehyde, as a cross-linking agent for gelatin, increases its gel-sol transition temperature [128]. However, the toxicity of formaldehyde prevented this additive from being widely used [129]. Even lower diffusion coefficients were obtained by adding 40% sucrose ($0.145\text{ mm}^2\text{h}^{-1}$) or 40% glycerol ($0.175\text{ mm}^2\text{h}^{-1}$) to gelatin [130]. The disadvantage of the sucrose additive was its optical activity, which could lead to artifacts formation during imaging. Complete cessation of iron ion diffusion was achieved by introducing 1% nanoclay into 3% gelatin [131]. Immobilization of ions occurred by adsorption in the nanoclay interlayer. Since XO-Fe complexes did

not adsorb, it was necessary to eliminate xylenol orange from the composition. Hence, reading of the dose distribution was possible only using MRI. The applied modification reduced the sensitivity of the dosimeter forty times compared to the Fricke gelatin dosimeter with the addition of XO and only allowed recording of high doses (the lowest applied dose was 200 Gy). The use of MTB as a chelating agent instead of XO increased the sensitivity of the dosimeter by about 10% [132], but the effect of this change on other parameters of the dosimeter has not been studied. Adding a complexing agent for Fe^{2+} ions (1,10-phenanthroline) and glyoxal resulted in slowing down the autoxidation of ferrous ions, but at the cost of about 40% decrease in sensitivity [133]. The diffusion coefficient of the gel modified in this way was about $0.78 \text{ mm}^2\text{h}^{-1}$ (the authors of the study did not provide the exact value of the diffusion coefficient, but only a graph from which the value of the coefficient could be read).

3.4.1.2. Fricke-Agarose dosimeters

During the first two decades of the development of gel dosimetry, agarose was the most commonly used gel matrix, next to gelatin. Agarose is a natural polysaccharide usually obtained from seaweed. Agarose dosimeters were characterized by higher sensitivity than gelatin detectors, but on the other hand they showed a higher ferric ion diffusion coefficient [90,95]. In addition, the preparation of the dosimeter was a much more complex process than in the case of gelatin dosimeters. Agarose was dissolved at a temperature of about 90°C , which was associated with the loss of oxygen leading to a loss of sensitivity [119]. Therefore, it was necessary to purge the gel with oxygen in the final phase of preparation. Fricke's solution was added to the dissolved agarose at a temperature of 70°C . Such a high temperature could accelerate the processes of autoxidation of ferrous ions and degradation of the matrix in the presence of sulphuric acid. To reduce the diffusion coefficient of Fe^{3+} ions, agarose was modified by adding XO (section 3.4.1). To further reduce the diffusion of ferric ions, sucrose was added to the agarose gel with XO, but this had a marginal effect on the value of the diffusion coefficient, which decreased from 0.97 to $0.95 \text{ mm}^2\text{h}^{-1}$ [123]. An alternative approach was to introduce a polyethylene honeycomb structure into the phantom containing the agarose gel [134]. The results of the reading of the dose distribution using MRI after 2 and 24 h after irradiation were identical. This approach was associated with a certain loss of spatial resolution and also allowed for the reading of the dose only using MRI. With the introduction of the idea of optical imaging of gels and the development of Fricke radiochromic dosimeters, another disadvantage of agarose was revealed. It scatters visible light sufficiently to be considered a translucent material, unsuitable for imaging by optical methods [135]. Due to all its disadvantages, agarose has ultimately fallen into disuse.

3.4.1.3. Fricke-Polyvinyl Alcohol (PVA) dosimeters

PVA is a synthetic polymer obtained by hydrolysis of polyvinyl acetate (PVAc). The first dosimeters with a PVA matrix were presented in 2000 [136]. Two gel matrices of the same composition (20% PVA) were prepared. The first was obtained by cooling the PVA and Fricke solution to 5°C (hydrogel) and the second to -20°C (cryogel). The cryogel was opaque and the dose distribution could only be read using MRI. The hydrogel showed high transparency and almost five times lower autoxidation rate of ferrous ions compared to the dosimeter with 4% gelatin matrix. Moreover, the sensitivity of the gel was $0.046 \text{ a.u.}^{-1}\text{Gy}^{-1}$, while the diffusion coefficient of Fe^{3+} ions in the hydrogel was only $0.140 \text{ mm}^2\text{h}^{-1}$. An almost twofold increase in the sensitivity of the dosimeter ($0.073 \text{ a.u.}^{-1}\text{Gy}^{-1}$) was obtained by cross-linking the gel matrix with glutaraldehyde (GTA) and simultaneously reducing the PVA concentration to 10 [137] and 9.1% [138]. Despite a twofold reduction in the PVA concentration, the diffusion coefficient in both

compositions was $0.170 \text{ mm}^2\text{h}^{-1}$. Reducing the PVA concentration to 5% and replacing XO with MTB resulted in a decrease in the diffusion coefficient to $0.150 \text{ mm}^2\text{h}^{-1}$, with no change in sensitivity [139]. Further modification by adding 3 M dimethyl sulfoxide (DMSO) reduced the diffusion coefficient value to $0.074 \text{ mm}^2\text{h}^{-1}$ at the cost of a decrease in sensitivity ($0.049 \text{ a.u.}^{-1}\text{Gy}^{-1}$) [140]. Recently, it was suggested to add 0.8% gellan gum (GG) instead of DMSO [141]. The obtained dosimeter showed the highest sensitivity of all tested modifications ($0.086 \text{ a.u.}^{-1}\text{Gy}^{-1}$) and at the same time the lowest diffusion coefficient ($0.070 \text{ mm}^2\text{h}^{-1}$).

3.4.1.4. Fricke-Pluronic F-127 dosimeters

Recently, a new gel matrix has been proposed with Pluronic F-127 [142]. It is a synthetic block copolymer consisting of polyethylene oxide (PEO) and polypropylene oxide (PPO) (general formula $[\text{PEO}]_{x1}[\text{PPO}]_y[\text{PEO}]_{x2}$) [143]. It is a non-toxic compound, approved by the Food and Drug Administration (FDA, Silver Spring, MD, USA) [144,145]. It is characterized by transparency higher than gelatin [146], and a wide temperature range ($20\text{--}80^\circ\text{C}$), in which it remains a gel [143]. It is possible to lower the lower temperature of the sol-gel transition by adding sodium chloride (to 16°C when 0.2 M NaCl is added), which also results in an increase in the sensitivity of the dosimeter ($0.057 \text{ a.u.}^{-1}\text{Gy}^{-1}$ and $0.086 \text{ a.u.}^{-1}\text{Gy}^{-1}$ for the gel without NaCl and with salt, respectively) [147]. Measurements of the diffusion coefficient of Fe^{3+} ions showed that the diffusion rate is dependent on gravity [148]. The determined diffusion coefficients were $0.41 \text{ mm}^2\text{h}^{-1}$ and $0.17 \text{ mm}^2\text{h}^{-1}$ for diffusion in the direction consistent with gravity and in the direction opposite to it, respectively.

3.4.2. Other gel dosimeters

The diffusion of Fe^{3+} ions and the autoxidation of the dosimeter during storage are the two biggest disadvantages of Fricke gels. So far, the proposed modifications of this gel have brought only partial success, hence the research groups have been looking for other radiosensitive compositions, which will be briefly characterized in this section.

3.4.2.1. Polymer gel dosimeters

Polymer gel dosimeters are a group of detectors containing monomers dispersed in a gel matrix. As a result of irradiation, polymerization occurs to a degree dependent on the absorbed dose. The first proposed polymer dosimeter contained acrylamide (Aam) and *N,N'*-methylenebisacrylamide (Bis) monomers in agarose saturated with nitrogen oxide [149]. The dosimeter was named acronym BANANA after its composition. A year later, Aam and Bis were added to nitrogen-saturated gelatin [150]. The new dosimeter, named the acronym BANG, was patented [151] and became commercially available. Imaging the dose distribution was initially performed using MRI, but in later years it was proposed to use more readily available techniques such as x-ray CT [152] and ultrasound imaging [153].

The most significant disadvantage of the first polymer dosimeters was the need to prepare them in anaerobic conditions. Atomic oxygen reacted with free radicals formed after irradiation in the structure of monomers, which led to inhibition of the polymerization reaction. This problem was solved with the demonstration of the MAGIC dosimeter, containing methacrylic acid, ascorbic acid, copper and a gelatin matrix [154]. In this dosimeter, oxygen was bound in organometallic complexes and did not affect polymerization. The creation of the MAGIC dosimeter initiated a new group of normoxic polymer

dosimeters, which were developed in the following years, among others, by adding new oxygen scavengers such as tetrakis(hydroxymethyl)phosphonium chloride (THPC) [155]. A noteworthy contribution to the development of polymer gel dosimetry is made by the Polish DosLab team, of which the author of this work is a member [156,157]

3.4.2.2. Radiochromic gel dosimeters

Radiochromic gel dosimeters change color after absorbing a dose of ionizing radiation similarly to Fricke dosimeters containing XO or MTB. However, it is customary to distinguish Fricke and radiochromic dosimeters as two separate groups of gel dosimeters. Radiochromic dosimeters include micellar gels containing leucodyes such as leucomalachite green [158] and leucocrystal violet [159]. Leucodyes are compounds that are sparingly soluble in water. In micellar gels, their particles are enclosed within the hydrophobic core of the micelle, which limits the diffusion of the dye in the matrix. Another group of radiochromic dosimeters are gels with tetrazolium salts (such as 2, 3, 5-triphenyltetrazolium chloride (TTC) [146], nitro blue tetrazolium chloride (NBT) [160]), which after irradiation convert to colored and water-insoluble formazan. They are characterized by zero diffusion, but their disadvantage is relatively low sensitivity. In PVA-iodide gel dosimeters, the color change occurs as a result of the formation of complexes between PVA molecules and triiodide ions formed after irradiation of the dosimeter [161]. The advantages of the PVA-iodide dosimeter include a very low diffusion coefficient ($0.002 \text{ mm}^2\text{h}^{-1}$) and the possibility of reversing radiation-induced reactions by heating the gel at 45°C for 24 h [162], which allows for multiple measurements using a single dosimeter.

4. Materials and methods

4.1. Sodium alginate to reduce diffusion of Fe^{3+} ions

4.1.1. Water quality measurements. Impact of water quality on the stability of iron solutions

Impact of four different types of water (including tap water, distilled, redistilled and deionized) on the stability of Fricke dosimeter components was examined. Each water parameters such as hardness, pH and conductivity were determined. Conductivity was measured with a CC-505 conductivity meter (ELMETRON, Poland) and pH was measured with a SevenExcellence S400 pH meter (Mettler Toledo, Poland). Water hardness was determined by titration of water samples with an ethylenediaminetetraacetic acid (EDTA) solution at a concentration of 0.011 mol/dm^3 (the titre was set to a standard calcium chloride (CaCl_2) solution at a concentration of 0.015 mol/dm^3) with addition of a mixture of eriochrome black and sodium chloride (NaCl). To determine the stability of ferrous ions solutions in particular type of water the solutions of different concentrations from 0.1 mM to 10 mM of iron salt were prepared. Samples were stored in the refrigerator and in the room temperature. Changes occurring in the samples during storage time were assessed organoleptically and through spectrophotometric measurements (4.1.7.). The characteristics of each type of water used are shown in Table 5.

Table 5. Characteristics of each type of water used in the Fe^{2+} ion stability study

Type of water	Water hardness [$^\circ\text{dH}$]	pH [-]	Conductivity [$\mu\text{S/cm}$]
Tap water	12.17	7.46	378.9
Distilled	0.35	6.95	11.15
Re-distilled	-	5.77	1.23
Deionised	-	5.63	1.16

4.1.2. Streaming current measurements

Streaming current measurements of solutions of Fricke dosimeter components (sulphuric acid (VI) (H_2SO_4), ferrous ammonium sulfate (VI) (FAS), xylene orange (XO)), calcium chloride and sodium alginate as well as potential measurements for reactions between these compounds were performed using a PCD-03 particle charge detector (Mütek, Germany). Streaming current of solutions of compounds was measured for 10 minutes, taking readings every 30 seconds. Streaming current measurements for the reaction were performed by gradually adding 50 μl of solutions of Fricke dosimeter components and calcium chloride to 15 ml of 0.25% sodium alginate solution. Subsequent volumes of solutions were added after obtaining a stable value of the measured potential which was read every 10 seconds.

4.1.3. Preparation of macrocapsules

Macrocapsules were prepared from three sodium alginates with different viscosities: $2.800 \text{ mm}^2/\text{s}$ at 25°C (0.1%) (low viscosity, Sigma, USA), $6.271 \text{ mm}^2/\text{s}$ at 25°C (0.1%) (medium viscosity, Sigma, USA) and $5.366 \text{ mm}^2/\text{s}$ at 25°C (0.1%) (medium viscosity, Heppe, Germany). Sodium alginates were dissolved in redistilled water at 45°C to obtain solutions (1.7%-3.5%), which were filled into 10 ml syringes

(Braun, Germany). The syringe was suspended above a beaker containing 50 ml of Fricke's solution (50 mM H_2SO_4 pure per analysis (p. p. a.) (Chempur, Poland), 1 mM FAS p. p. a. (Chempur, Poland) and 0.165 mM XO (Sigma-Aldrich, Germany) in redistilled water) and CaCl_2 (0%-3.5%) so that the outlet (outside diameter: ~ 3.9 mm, inside diameter: ~ 2.3 mm) was 25 cm above the solution surface. Then, approximately 4 mL of sodium alginate solution was added dropwise to the Fricke's solution while gently stirring (150 rpm) with a magnetic stirrer (IKA, Germany) (Figure 5). After completion of the addition process, the stirring speed was increased to 350 rpm. The capsules were kept in a continuously stirred solution for 15-360 min to increase the iron content inside them. During the tests, the concentration and type of alginate used, the concentration of calcium chloride and the storage time of the capsules in the solution were optimized.

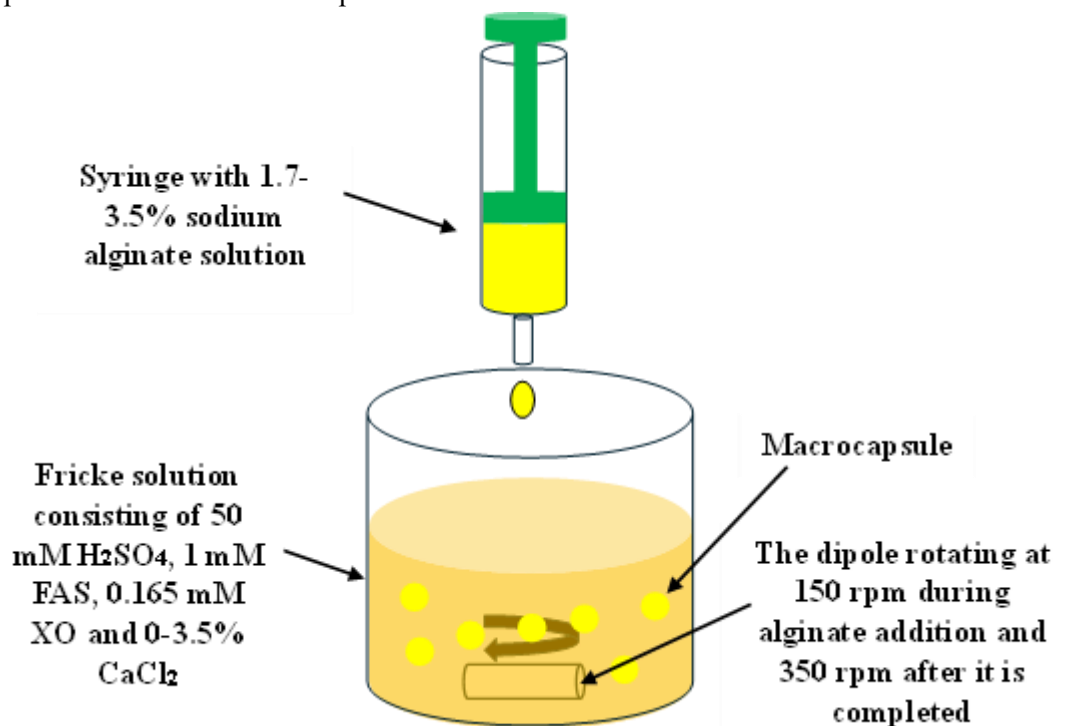


Figure 5. Scheme of obtaining macrocapsules by dripping sodium alginate solutions into a solution of Fricke dosimeter components and CaCl_2 . Capsules are formed by the reaction of calcium ions with sodium alginate. The resulting calcium alginate is insoluble in water and precipitates from the solution in the form of a gel. The reaction is fast enough to maintain the spherical shape of the falling drop.

4.1.4 Preparation of 1D dosimeter

The 1D dosimeter consisted of a macrocapsule obtained according to section 4.1.3 and a gel matrix (25% Pluronic F-127 (Sigma, USA) or 3.5% gelatin (Sigma, USA)). The gel was introduced into PMMA cuvettes to a height of 2 cm. After the matrix gelled, the macrocapsule was placed in the center of the gel surface and then the cuvette was completely filled with the gel solution.

4.1.5. Preparation of nano- microgel

Low viscosity alginate (Sigma, USA) and a medium viscosity alginate (Heppe, Germany) were used to prepare the nano- and micro-gels. First, a sodium alginate solution was prepared in 80% of the final volume of redistilled water. In the remaining 20% of the water volume, FAS (Chempur, Poland) was dissolved, and then sulphuric acid (VI) was added. The solution prepared in this way was added in small

portions (approx. 200 μL) to sodium alginate with vigorous stirring (approximately 800 rpm) (C-MAG HS 7-IKA, Germany) to ensure good dispersion of iron ions and to prevent the formation of alginate and Fe^{2+} aggregates. The sulphuric acid and FAS solution was added using an automatic pipette, placing its tip in the alginate solution, close to the dipole. The final concentrations of the components were as follows: 0.015-0.65% sodium alginate, 0-2 mM FAS, 0-50 mM sulphuric acid (VI). The pH values of the microgels solutions were measured using pH-meter HI 221 (Hanna Instruments, Poland). To characterize the obtained microgels with microscopic observations and DLS measurements, XO dye was not added to the solution.

4.1.6. Preparation of 3D dosimeter

Xylenol orange was added to the microgel obtained according to 4.1.5. The concentration of XO in the microgel solution was 0.165 mM. Gel matrix (Pluronic F-127) was prepared by dissolving in the microgel solution. Pluronic F-127 gel was obtained by introducing alternating layers of the microgel solution and Pluronic F-127 in powder form into a beaker and then storing in a refrigerator ($\sim 4^\circ\text{C}$) until complete dissolution.

4.1.7. UV-Vis measurements

UV-Vis measurements were performed using a V-530 spectrophotometer (Jasco, Japan). Absorption and transmittance measurements of samples in PMMA cuvettes were carried out in the wavelength range of 190-700 nm with a resolution of 1 nm. Air was used as a reference in the measurements.

4.1.8. Diffusion measurements

The rate of diffusion of iron and calcium ions from macrocapsules into water was assessed using the inductively coupled plasma atomic emission spectroscopy (ICP-OES) technique (section 4.1.10.). Samples were prepared by placing five capsules into PMMA cuvettes, followed by pouring 3.5 mL of redistilled water. The cuvettes were closed with a polyethylene (PE) cap. The capsules were stored in water for 15 min-72 h, then removed from the cuvette and blotted on a paper towel for about 30 s and placed into a glass vial.

Measurements of the diffusion rate of the dye from the capsules to water were carried out by placing 15 capsules in a glass beaker with a volume of 25 mL and pouring them with 10 mL of re-distilled water. The capsules were stored for a specified period (20–180 min). Then 3.5 mL of water was taken from the beaker and added into PMMA cuvettes. Spectrophotometric measurements section (4.1.7.) were used to determine the concentration of the dye in the water.

4.1.9 Dynamic light scattering measurements

The mean hydrodynamic diameter distribution of structures formed by mixing sodium alginate solutions with Fricke dosimeter components was assessed using dynamic light scattering (DLS, Particle Size Analyser, NICOMP, USA).

4.1.10. Assessment of metal content in macrocapsules

Samples prepared according to section 4.1.8. were weighed into glass tubes on an analytical balance with an accuracy of five decimal places. Approximately 0.2 grams of sample was weighted, and 4 ml of concentrated nitric acid (65% HNO₃, Baker Analyzed) were added. The tubes covered with polytetrafluoroethylene (PTFE, Teflon) caps were placed in the UltraWAVE microwave assisted digestion system (Milestone, Italy). In this system inert gas (nitrogen) under pressure (40 bar) is pumped into the reactor before the decomposition process begins. The decomposition in microwave system consisted of three stages. Stage I: temperature inside the reactor: 20 °C, maximum power: 1500 W, maximum pressure inside: 120 bar, duration: 15 min. Stage II: gradual increase of the temperature inside the reactor until reaching the temperature of 220 °C at the end of the second stage, maximum power: 1500 W, maximum pressure inside the reactor: 150 bar, duration: 10 min. Stage III: maintaining the temperature at 220 °C, maximum power: 1500 W, maximum pressure inside the reactor: 150 bar, duration: 8 min. After the completion of decomposition process, the samples were quantitatively transferred into 50 ml volumetric flasks. A 2 ml of 10 mg/kg internal standard of indium solution (ICP class, Merck, Germany) was added before the final dilution of the samples with deionized water.

Prior to the quantitative analysis using the ICP-OES technique (iCAP 7400, Thermo Scientific, USA), calibration curves were prepared for the 1000 mg/kg Merck IV multi-element ICP standard (Multi-element ICP standard, Merck, Germany). The calibration curve was prepared based on the stock standards from which serial dilutions were prepared. The multi-element ICP standard concentrations range was 0.02-2 mg/kg. The Fe levels were monitored using four emission lines for Fe. The Fe concentration values were finally given against the following emission line: Fe II (ion line) 259.940 nm (Axial), In 325.609 nm (Axial). The correctness of the obtained results was verified, by analyzing the certified river water material WatR Supply Metals 697 (Eraqc) and a satisfactory agreement was obtained between the results for Fe and the certified values. Parameters of the ICP-OES iCAP 7400 spectrometer (Thermo Scientific, USA) were as follows: number of replicates: 3, auxiliary gas 0.5 L/min, plasma gas 12 L/min, carrier gas 0.5 L/min, torch: quartz, nebulizer: concentric, quartz, RF generator power: 1150 W, internal standard: Ind, torch setting mode: Axial (Fe, In), spectral range: 166–847 nm, resolution: 7 pm at 200 nm, detector: semiconductor CID, optics: simultaneous analyzer with Echelle optics (52.91 grooves/mm).

4.1.11. Irradiation of macrocapsules

The capsules were made of medium viscosity Heppe and low viscosity Sigma alginates in reaction of 3.5% alginate with Fricke solution (FAS: 1 mM, XO: 0.165 mM, H₂SO₄: 50 mM) containing 3.5% CaCl₂ by dropwise addition of sodium alginate solution into the Fricke solution with Ca²⁺. They were irradiated with X-rays of a TrueBeam medical accelerator (Varian, USA). For this purpose, the capsules were placed in holes with a diameter of 5 mm in a template made of poly(methyl methacrylate) with a thickness of 5 mm. This template was located between plates SP34 phantom made of RW3 (IBA, Germany); the thickness of the plates on top and bottom was 4.5 and 5 cm, respectively (Figure 6). The radiation conditions were as follows: 6 MV (with flattening filter, WFF), monitor unit rate of 600 MU/min, field of irradiation: 20 cm × 20 cm, source-to-surface distance SSD=95 cm, dose 2, 3, 5, 7, 10, and 20 Gy. In turn, UV-Vis cuvettes (1 cm optical path) with alginate capsules with Fricke solution in Pluronic F-127 or gelatine matrix were irradiated in a W-1-DD1-2 water phantom (GeVero Co., Lodz, Poland) with a TrueBeam accelerator. The following settings were applied: energy of 6 MV WFF, monitor unit rate of 600 MU/min, field size of 20×20 cm², SSD=95 cm, depth=5 cm, dose=20 Gy.

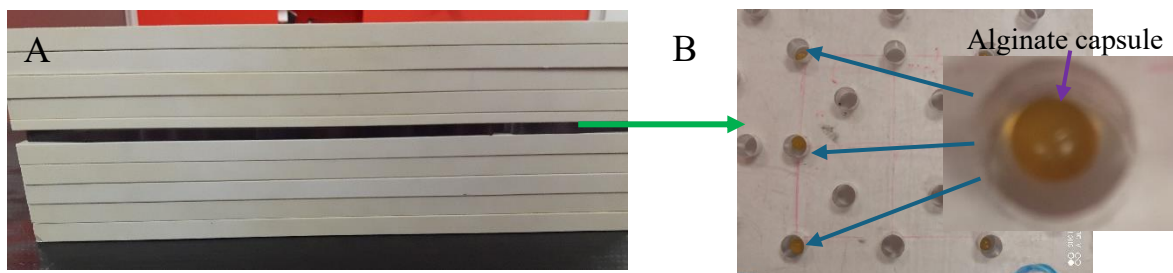


Figure 6. Irradiation of alginate capsules. Phantom SP34 (RW3 plates) (A) and a poly(methyl methacrylate) template with holes and capsules inside the holes (B).

4.1.12. Measurements of irradiation effects and data processing

The effect of ionizing radiation on the capsules was assessed based on their color change. For this purpose, photographs of the capsules were taken using a digital microscope (Delta Optical Smart 5MP PRO digital microscope, Poland) connected to a personal computer. During the pictures taking, the microscope was located in a $60 \times 60 \times 60$ LED shadowless tent (Pro Stuff®, Poland) to ensure repeatable lighting conditions. Pictures of the capsules were taken immediately after irradiation. The analysis of the obtained photographs was performed in the ImageJ software (National Institutes of Health, USA).

4.2. Fricke 2D Dosimeters for Quality Assurance

4.2.1. Gel preparation

The Fricke-XO-Pluronic F-127 dosimeter was prepared using 25% w/w Pluronic F-127 (Sigma, USA), 50 mM H_2SO_4 p. p. a. (Chempur, Poland), 1 mM FAS p. p. a. (Chempur, Poland), and 0.165 mM XO (Sigma-Aldrich, Germany). Pluronic F-127 was dissolved in 80% of the final volume of water by adding alternating layers of Pluronic and water to the beaker. The beaker was covered with Parafilm® and placed in a refrigerator ($\sim 4^\circ\text{C}$) until the Pluronic was completely dissolved. The dosimeter components were dissolved in the remaining 20% of the final volume of water. The prepared Fricke solution was added to the Pluronic F-127 solution while stirring gently.

To prepare the Fricke-XO-Gelatin dosimeter with sorbitol, gelatin (type A, 300 Bloom, Sigma, USA) was dissolved in water in 55°C . After complete dissolution, it was cooled down to 33°C and then, Fricke solution consisting of sulphuric acid (Chempur, Poland), ferrous ammonium sulphate (FAS, Chempur, Poland) and xylene orange disodium salt (XO, Sigma, USA), was added. All ingredients of Fricke solution were dissolved in 5% of final water mass. The sorbitol solution prepared in 35% of final water mass was added by syringe. The syringe outlet was placed near dipole present in a beaker with gelatin to improve the mixing of all compounds. The final concentrations of all ingredients were as follows: 5.99% gelatin, 23% sorbitol, 50 mM sulphuric acid, 0.5 mM FAS and 0.165 mM XO. Additionally, in the studies of thermal and mechanical properties, gels with the following compositions were used: 8% gelatin, 6% gelatin with 23% sorbitol and 7.96% gelatin with Fricke solution (the concentrations of the components in the Fricke dosimeter were 50 mM sulphuric acid, 0.5 mM FAS and 0.165 mM XO). Double distilled water was used to prepare all samples. All reagents were weighed on a laboratory scale with an accuracy of ± 0.1 mg.

4.2.2. Samples preparation

Samples of the Fricke-XO-Pluronic F-127 and Fricke-XO-Gelatin with sorbitol dosimeters for determining the radiation isocenter of the TrueBeam medical accelerator (Varian, USA) were prepared by pouring dosimeter solutions obtained according to section 4.2.1. into a cuboidal container made of PMMA (Figure 7A). The dimensions of the container were 12 cm × 12 cm × 0.3 cm. During the pouring of the solutions, the container was placed on a leveled stainless steel plate. After filling the container, it was covered with a sheet of rigid foil, and then two stainless steel plates were placed on the sample to remove excess solution. After 15 minutes, the steel plates were removed and the container with the Fricke-XO-Gelatin with sorbitol dosimeter was placed in a refrigerator (~4°C) for 24 hours. The Fricke-XO-Pluronic F-127 dosimeter was irradiated within an hour after preparation.

Bolus samples were prepared by pouring the Fricke-XO-Gelatin with sorbitol dosimeter solution into a PMMA frame placed on a sheet of rigid foil resting on a leveled stainless steel plate (Figure 7B). The internal dimensions of the frame were 10 cm×10 cm×0.5 cm. After filling, the frame was covered with a sheet of rigid foil and two stainless steel plates were placed on top of the sample to remove excess solution. After 15 min, the steel plates were removed and the frame covered with rigid foils on top and bottom was placed in a refrigerator (~4°C) for 72 h. Such sample was used for experiment of verification of a treatment planning system calculated irradiation plan

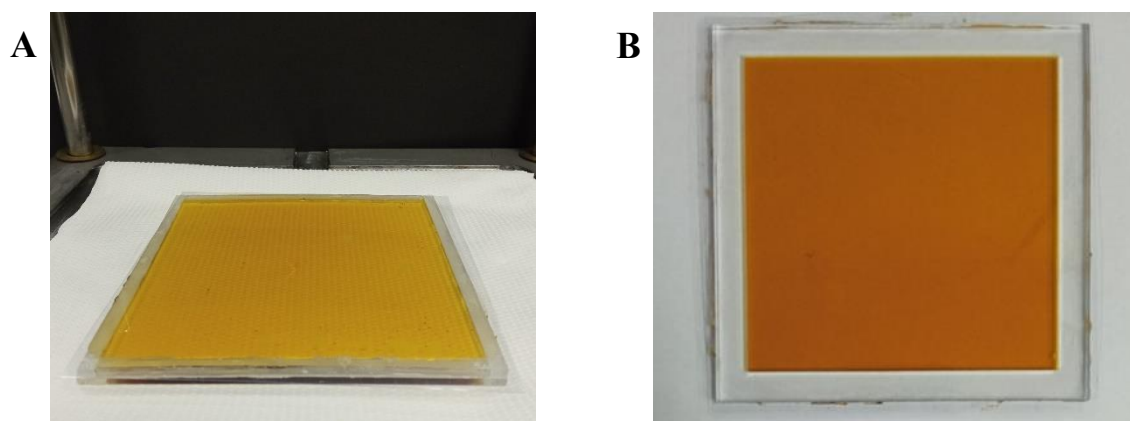


Figure 7. Fricke-XO-Gelatin with sorbitol dosimeter **A:** in a cuboidal container placed on a leveled steel plate. **B:** in a frame covered on both sides with sheets of rigid foil.

A thin dosimeter with a gel layer thickness of 1 mm was prepared by pouring the dosimeter solution onto a sheet of rigid foil placed on a leveled steel plate (Figure 8A). The poured solution was covered with another sheet of foil and pressed with steel plates to remove excess solution and obtain a gel of the desired thickness. The distance between the plates was controlled by placing bronze discs between them (Figure 8B). After 15 minutes, the plates pressing the sample were removed and then the gel remaining between the two sheets of rigid foil was wrapped in aluminum foil and placed in a refrigerator for 24 hours. After this time, a dosimeter sample of dimensions 10 cm × 10 cm × 0.1 cm was cut out with a sharp knife (Figure 8C). The sides of the sample were wrapped with Parafilm® to protect the gel from drying out. Afterwards the sample was kept in a refrigerator until irradiation (the total time from preparation to irradiation was 72 h). Such sample was used for experiment of verification of a treatment planning system calculated irradiation plan.

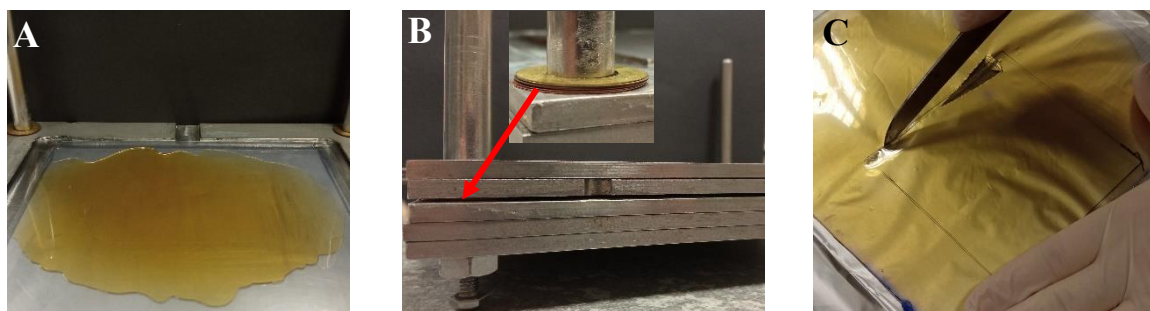


Figure 8. **A:** Fricke-XO-Gelatin with sorbitol dosimeter solution poured onto a sheet of rigid foil lying on a leveled steel plate. **B:** Dosimeter solution between two sheets of rigid foil placed on a leveled steel plate and pressed with two other plates to remove excess solution and obtain a gel layer thickness of 1 mm. The distance between the plates was controlled by metal discs placed in the corners of the plate (their location is indicated by the red arrow). **C:** Cutting a $10 \times 10 \text{ cm}^2$ thin dosimeter sample using a knife.

Samples for compression strength measurements were made of 8% gelatin, 6% gelatin with 23% sorbitol, 7.96% gelatin with Fricke solution and 5.99% gelatin with Fricke solution and 23% sorbitol (the amount of gelatin in the samples was the same, the difference in gelatin concentration between the gels is due to the addition of sorbitol and the ingredients of the Fricke solution). The solutions of the tested gels were poured into an aluminum cylindrical mold with a height and internal diameter of 2.5 cm, covered from the bottom with Parafilm[®]. After filling, the top of the mold was covered with Parafilm[®], and the entire cylinder was placed in a refrigerator for 24 h (at approximately 4 °C). For an hour before mechanical tests, the gels were thermostated at the temperature of the room in which the measurements were performed (approximately 23 °C). The samples were removed from the molds immediately before measurement.

4.2.3. Thermal analysis

An analysis of the effect of sorbitol addition on the thermal stability of the dosimeter was performed using differential scanning calorimetry (DSC, Q200, TA Instruments, USA). The instrument was calibrated for both temperature and enthalpy using indium (melting point and heat of fusion are 156.6 °C and 28.57 J g⁻¹, respectively). The measurements were performed on samples of 8% gelatin, 6% gelatin with 23% sorbitol, 7.96% gelatin with Fricke solution, and 5.99% gelatin with Fricke solution and 23% sorbitol. As the stability of the Fricke solution and sorbitol sample was also evaluated over time, the sample in the Petri dish was tightly covered with several layers of Parafilm[®] to prevent it from drying out. The set procedure comprised the first heating starting typically from the temperature of 5 °C to 45 °C, then cooling down to 5 °C and the second heating to 45 °C. The temperature rate in heating was 2 °C/min, as the results did not differ when the heating was performed, in initial experiments, with a rate of 1 °C/min.

4.2.4. Mechanical analysis

The effect of sorbitol addition on the mechanical properties of gelatin and gelatin-Fricke gels was evaluated using a Hounsfield H10KS testing machine (Tinius Olsen, Great Britain) through compressive strength and fatigue compressive strength tests on cylindrical gel samples (section 2.2). For compressive strength measurements, samples were placed at the center of an aluminum table and compressed with a

40 mm diameter aluminum pin at a constant rate of 10 mm/min until failure (Figure 9A), with force recorded using a 100 N transducer. Load-displacement data were converted into stress-strain characteristics using the equations $\sigma=F/S$ (where σ is stress [N/m²], F is the applied load [N], and S is the initial cross-sectional area of the sample [m²]) and $\epsilon=l/l_0$ (where ϵ is strain [-], l is sample deformation [mm], and l_0 is the initial sample length [mm]). From these curves, deformation at break, compressive force at failure, and Young's modulus (E) - determined as the slope of the linear stress-strain region, were extracted. Fatigue compression tests were conducted by cyclically deforming the samples 100 times at a frequency of 20 cycles per minute, using a 200 N load cell (QLMH-25, Bengbu Qili Sensing System Engineering Co. Ltd., China) (Figure 9B). The applied compression strain levels were 20, 40, and 60%, with corresponding compression rates of 200, 400, and 600 mm/min, respectively.

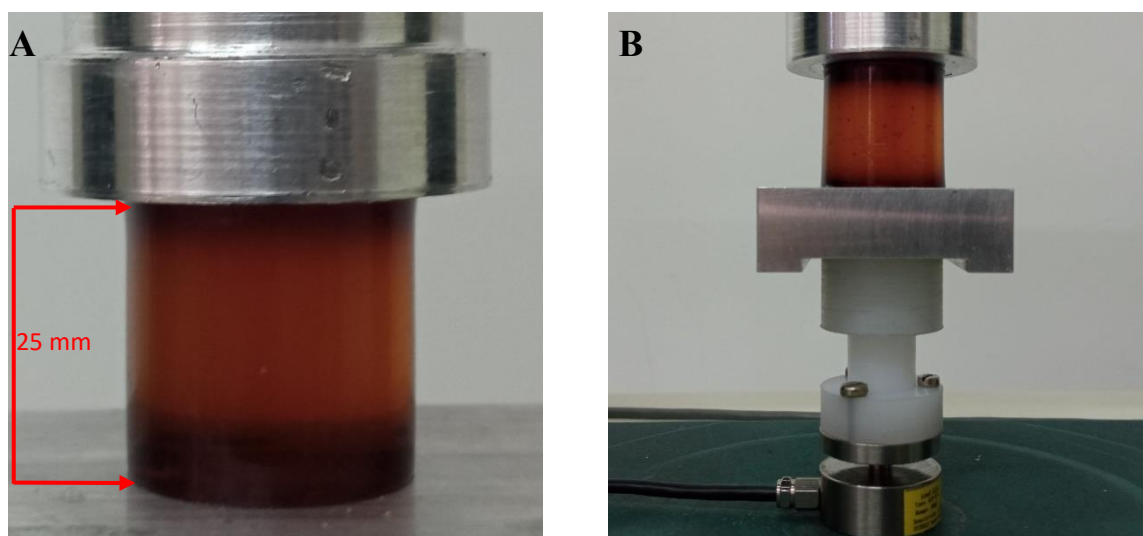


Figure 9. Cylindrical sample of Fricke-XO-Gelatin with sorbitol with a height of 25 mm and a base diameter of 25 mm placed on an aluminum table and compressed at a speed of 10 mm/min with an aluminum pin with a diameter of 50 mm (A) and on an aluminum table located on the force meter in the cyclic compression system (B).

4.2.5. Assessment of chemical stability of the Fricke-XO-Gelatin with sorbitol dosimeter

The Fricke-XO-Gelatin with sorbitol dosimeter solution was poured into PMMA cuvettes with an optical path length of 1 cm and covered with a PE plug. The cuvettes were stored in different conditions: on a table (temperature of about 25°C, access to light), in a cabinet (temperature of about 25°C, no access to light) and in a refrigerator (temperature of about 4°C, no access to light). The color changes of the samples over time were measured spectrophotometrically (4.1.7.).

4.2.6. Irradiation

All 2D dosimeter samples were irradiated using a TrueBeam medical accelerator (Varian, USA). To determine the optimal irradiation parameters, two Fricke-XO-Pluronic F-127 and one Fricke-XO-Gelatin with sorbitol dosimeters in cuboidal container (section 4.2.2.) were irradiated with different gaps of the high-definition multileaf collimator (HD MLC) of the accelerator and different monitor units. On the first Fricke-XO-Pluronic F-127 dosimeter, eight stripe-shaped areas (dimensions of each stripe was 0.5 cm × 4 cm) were irradiated with the following MU: 500, 1000, 1500, 2000, 2500, 5000, 7500, and

10,000 MU, while the gap of the HD MLC was 5 mm. Six striped areas of another sample were irradiated with 2500 MU using the following gaps of the HD MLC: 0, 1, 2, 5, 10, and 20 mm. Eight striped areas of the Fricke-XO-Gelatin with sorbitol dosimeter were irradiated with the following MU: 250, 500, 750, 1000, 1500, 2000, 2500, 4000 and the HD MLC gap was 5 mm. Each sample was placed on five slabs (each 1 cm thick) of the SP34 RW3 phantom during irradiation. Two slabs of thicknesses of 1 cm and 0.5 cm, respectively, were placed on top of the dosimeters. The irradiation parameters were as follows: X-rays, with a 10 MV FFF (flattening filter free) beam, monitor unit rate 2400 MU/min, jaw size X: 4 cm, Y: 3 cm, gantry and collimator set to 0°. The accelerator isocenter was set on the surface of the samples, with a SSD=100 cm.

To perform the coincidence test of radiation and mechanical isocenters, two samples of the Fricke-XO-Pluronic F-127 dosimeter and one sample of the Fricke-XO-Gelatin with sorbitol dosimeter were irradiated with a 2D shot pattern. Samples with the Pluronic matrix were irradiated with 2500 MU and 750 MU, respectively, while the dosimeter with the gelatin matrix was irradiated with 1500 MU. During irradiation, the dosimeters were positioned between SP34 RW3 slabs arranged in the same way as during the irradiation conditions optimization experiment. The dosimeters were set at the accelerator isocenter using a LAP laser system (LAP GmbH Laser Applikationen, Germany). The irradiation parameters were as follows: X-rays, 10 MV FFF, monitor unit rate of 2400 MU/min, 5 mm gap of the HD MLC, jaw size X: 2 cm and Y: 20 cm, SSD 100 cm, collimator angle set at 0°, 90°, 150°, 240°, and gantry set to 0°.

Bolus and thin dosimeter calibration was performed by irradiating two samples of each type. The following doses were applied: 2.5, 5, 7.5, 10, 12.5, 15, 17.5, and 20 Gy. The dosimeters were placed on fifteen slabs of the SP34 RW3 phantom, each 1 cm thick, and then six slabs of the phantom with a total thickness of 4.7 cm and 4.9 cm, respectively, were placed on them. During irradiation, the gels remained in a PMMA frame covered with a rigid foil. The following irradiation settings were applied: X-rays, 10 MV FFF, monitor unit rate of 2400 MU/min, jaws size of X: 3 cm, Y: 3 cm, gantry and collimator set to 0°. The accelerator isocenter was set on the center of the dosimeter, SSD 95 cm, and the surface of the dosimeter was perpendicular to the central axis of the radiation beam. The required number of MUs was achieved after the dosimetric measurements were performed with the aid of an ionising chamber (CC04) with an electrometer (Dose-1), both IBA.

Verification of the treatment plans generated in the Eclipse Treatment Planning System treatment planning system (TPS) (v. 16.1, Varian Medical Systems, USA, Acuros External Beam v. 16.1.0, dose grid: 1×1×1 mm³) was performed using bolus and thin Fricke-XO-Gelatin with sorbitol dosimeters. Additionally, one bolus dosimeter was irradiated with doses of 2.5, 5, 7.5, and 10 Gy to check the reproducibility of the gel dosimeter. The irradiation conditions were identical as for calibration. The second bolus sample remaining in the PMMA frame was placed on the surface of the SP34 RW3 phantom with a thickness of 20 cm and irradiated with 750 MU per beam according to the treatment plan. The irradiation conditions were as follows: X-rays, 10 MV FFF, monitor unit rate 2400 MU/min, field size X: 5 cm Y: 5 cm, gantry and collimator angle 0°. The SSD set on the phantom surface was equal to 100 cm. Thin dosimeter sample was placed on the surface of the 20 cm thick SP34 RW3 phantom and covered with a 15 cm × 15 cm × 1 cm Bolx with skin bolus (CQ Medical™, USA). On the sample one 5 cm × 5 cm field was irradiated with 2000 MU per beam, and three 2 cm × 2 cm fields were irradiated with 400, 800 and 1200 MU per beam. The remaining irradiation conditions were the same as for the bolus dosimeter. Measured dose distributions with Fricke-XO-Gelatin with sorbitol were compared with dose distributions calculated using TPS and additionally using myQA iON (v. 2.1.0 IBA,

Germany, SciMoCa, dose grid: 1 mm × 1 mm × 1 mm; MC simulations). Scans of the experimental system (phantom with gel dosimeter) used to perform the calculations were made using Somatom Sensation Open CT scanner (Siemens AG Medical Solutions, Germany).

4.2.7. Readout and data processing

Irradiated dosimeters were scanned using an HP Scanjet G3010 flatbed scanner (Hewlett-Packard, USA) operating at the following settings: resolution of 150 dpi, brightness = 0, contrast = 0. To observe changes occurring in the irradiated samples, dosimeter scanning was repeated within 24 h of irradiation. Samples were stored in approximately 20 °C. During scanning, the container with dosimeter was covered with three sheets of white paper with a grammage of 120 g/m² (POL Effect, International Paper, Poland). The polyGeVero-CT software package [163,164] (GeVero Co., Poland) was used to perform the calculations related to the coincidence test of radiation and mechanical isocenters. The comparison of the measured dose distribution with the calculations performed using TPS and the results of the Monte Carlo simulation was performed with the aid of the polyGeVero software package [165] (GeVero Co., Poland). The comparison was performed by calculating the local gamma index distribution (3% dose difference (DD) and 3 mm distance-to-agreement (DTA) criteria), comparing the dose profiles and the isodoses.

4.3. Application studies of the Fricke dosimeter using OCT

4.3.1. Samples preparation

The Fricke-XO-Gelatin was prepared by dissolving porcine gelatin (Type A, 300 Bloom, Sigma, USA) in 80% of the final volume of double-distilled water at 55°C. The solution was then cooled to 35°C and a solution of the Fricke dosimeter components (H₂SO₄, FAS, XO) dissolved in 20% of the final volume of double-distilled water was added. The Fricke-XO-Pluronic F-127 and Fricke-XO-Gelatin with sorbitol were prepared as described in section 4.2.1. The concentrations of the components in the prepared solutions were: 4-8% gelatin, 25% w/w Pluronic F-127, 50 mM H₂SO₄, 0.5 mM FAS, 0.04-0.165 mM XO and 23% sorbitol. The solutions were poured into 400 ml vials (Modus Medical Devices, Canada) made of polyethylene terephthalate (PETE).

4.3.2 Irradiation

All samples were irradiated using TomoTherapy[®] TomoHD[™] (Accuray, USA) (Figure 10A) medical accelerator. Calibration of the dosimeters was performed in the dose range of 1-4.15 Gy. The dose distribution is presented in Figure 10B. To determine the diffusion coefficient of Fe³⁺ ions, an area of 1 cm height and diameter equal to the sample diameter was irradiated uniformly with a dose of 3 Gy at the half height of the dosimeter. During irradiation, the samples were put in a template made of polyurethane (PUR) (Figure 10C) and placed at the accelerator isocenter. After irradiation, samples were stored and imaged at approximately 22 °C.

The treatment plan was verified using the Fricke-XO-Pluronic F-127 and Fricke-XO-Gelatin with sorbitol dosimeters. Two samples of each dosimeter were prepared for verification. One of them was used for calibration performed analogously to the one described above. The second sample was

irradiated according to the treatment plan generated for brain metastasis irradiation. The maximum planned dose was 4.15 Gy. The dosimeter was placed in a water-filled 3D printed skull phantom made of a bone-imitating material based on calcium compounds [166] (Figure 10D). All samples were irradiated with 6 MV X-rays, monitor units rate of 400 MU/min.

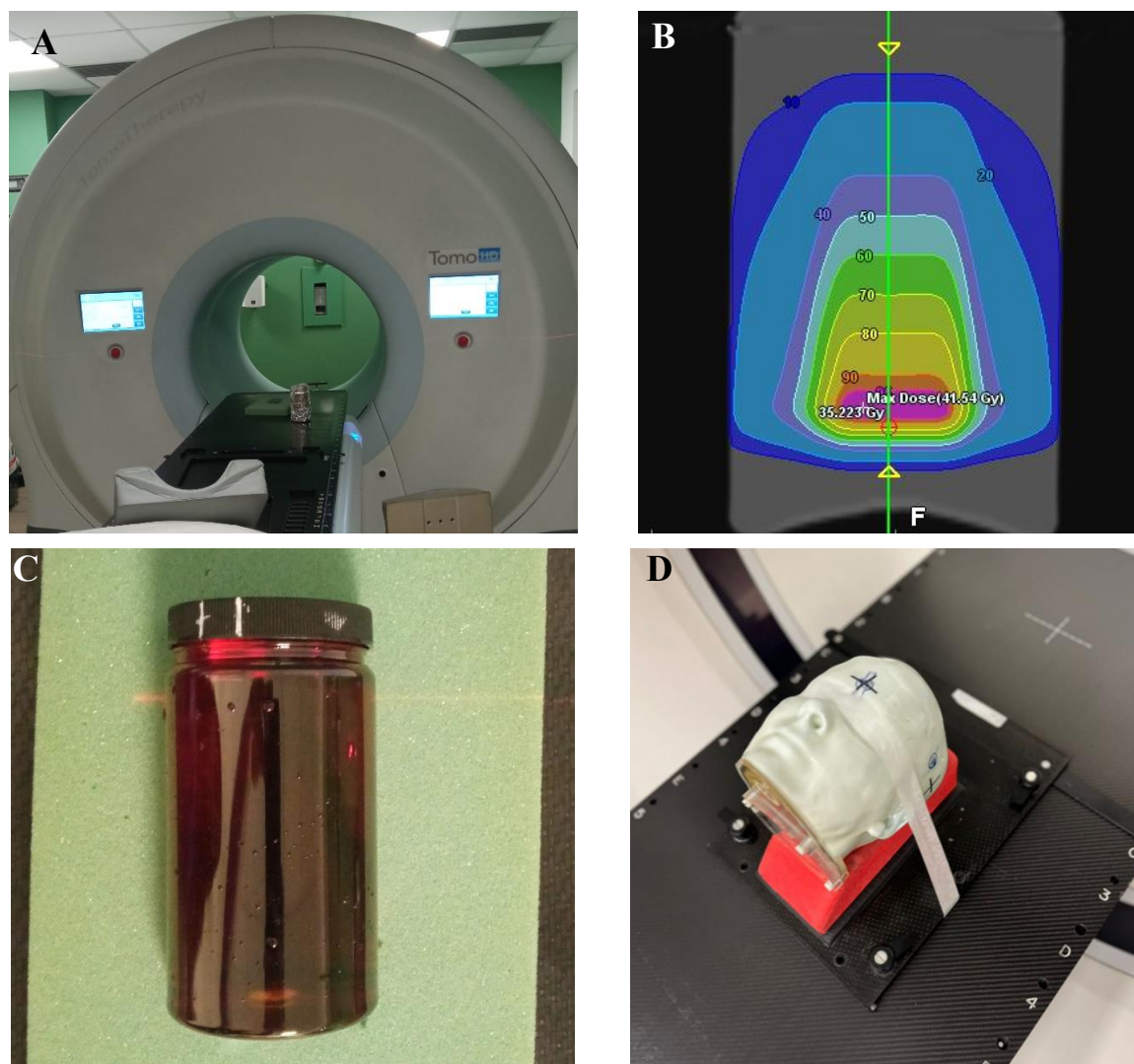


Figure 10. A: TomoTherapy® TomoHD™ medical accelerator (Accuray, USA) B: Calibration sample irradiation pattern generated in TPS. Doses shown in the image are 10× higher than those actually applied during irradiation C: Fricke-XO-Pluronic F-127 dosimeter in a 400 ml PETE vial placed in a PUR temple D: Phantom simulating a human head made of a material simulating bone density additionally covered with a layer of resin due to the high fragility of the material used to print the phantom. The gel dosimeter is located inside the phantom filled with water.

4.3.3. Samples scanning and data processing

The dosimeters were scanned using a Vista 15 optical computed tomography (Modus Medical Devices, Canada) capable of scanning with two wavelengths of light (589 nm - orange light and 633 nm - red light) (Figure 11). During the measurement, the samples were placed in a tank with refractive index matching liquid (water and poly(propylene glycol) mixture). The obtained results were processed in the polyGeVero software package (GeVero Co. Poland) (section 4.2.7.) The comparison of the measured

dose distributions with the TPS calculations was performed by calculating the gamma index distribution, comparing the dose profiles and the isodose distribution.



Figure 11. Fricke-XO-Pluronic F-127 dosimeter irradiated according to the calibration plan ([Figure 10B](#)) placed in OCT with orange light (589 nm) turned on. Sample seen from the CCD (Charged-Coupled Device) matrix side of the tomograph.

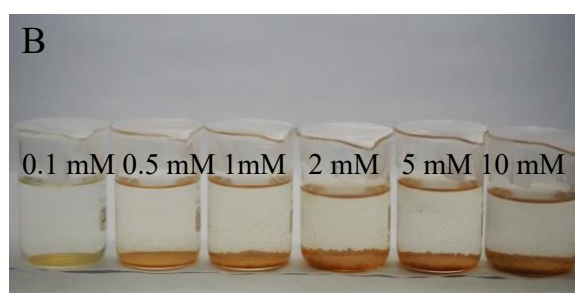
5. Results and discussion

5.1. Sodium alginate to reduce diffusion of Fe^{3+} ions

In this part of the work, a modification of the Fricke dosimeter with the addition of sodium alginate, a macromolecular compound capable of binding metal ions (mainly divalent, although binding trivalent is also possible), is presented. The main purpose of this modification is the immobilization of iron ions and reduction of the dosimeter diffusion coefficient. An attempt was made to obtain a dosimeter in the form of macrocapsules, which can be used as point detectors of ionizing radiation, and in the form of a solution of nano-, micro-gels dispersed in a gel matrix. In addition, the effect of water quality on the stability of the active components of the Fricke dosimeter was studied. The results presented in this section were described in the manuscript submitted on June 10, 2025, which is currently at the review stage [167].

5.1.1. Stability of Fe^{2+} ions in water

The influence of water purity on the stability of iron ions was examined for 0.1–10 mM FAS solutions prepared in tap water, distilled water, redistilled water, and deionized water stored at room temperature or in a refrigerator (Figures 11–18). The use of tap water results in immediate precipitation of sediment from the solution, regardless of the FAS concentration and storage conditions. For distilled water, precipitation occurs within 24 hours of preparation. The amount of precipitate is smaller than for tap water, but precipitation occurs regardless of sample concentration. Samples stored in the refrigerator contained less sediment 24 hours after preparation compared to samples stored in the cabinet at room temperature. The use of redistilled and deionized water gave very similar results. In both cases, no precipitation was observed for the least concentrated sample throughout the entire experiment period. For a concentration of 0.5 mM, the precipitation occurs after about 48 hours in very small amounts, and the situation is similar for samples with a concentration of 1 mM. In both cases, the method of storage has no apparent significance, but analyzing the absorption spectra (Figures 19–22) it can be concluded that changes occur slightly slower for samples stored in the refrigerator. It should be noted that the characteristics of deionized and redistilled water are very similar (as is the stability of iron when using these solvents). The difference in ferrous ions stability between solutions with distilled and redistilled water is clearly visible in this experiment, so it should propagate onto the stability of Fricke dosimeters. For this reason, all solutions and dosimetric systems examined further in this work were prepared with redistilled water.



C

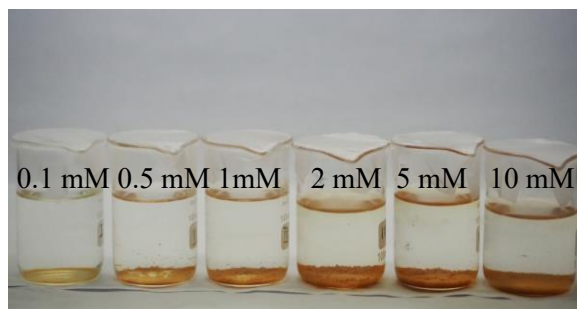
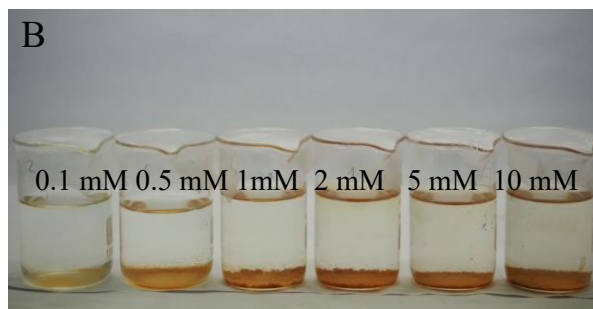


Figure 11. Photographs of 0.1–10 mM FAS solutions after preparation (0 h) (A) and storage for 24 h (B) and 48 h (C) in a refrigerator ($\sim 4^{\circ}\text{C}$) for the solutions prepared in tap water.



C

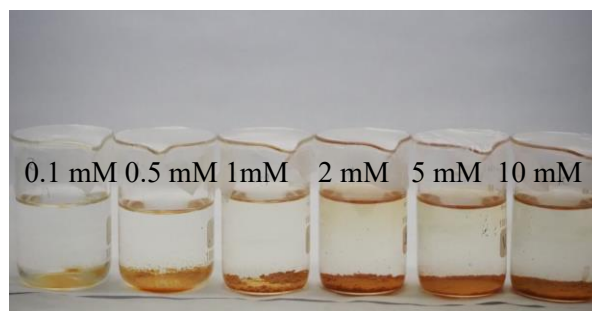
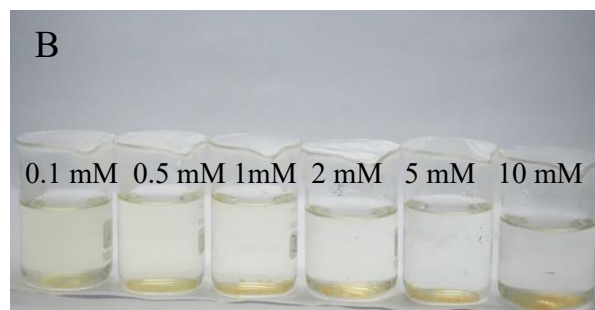
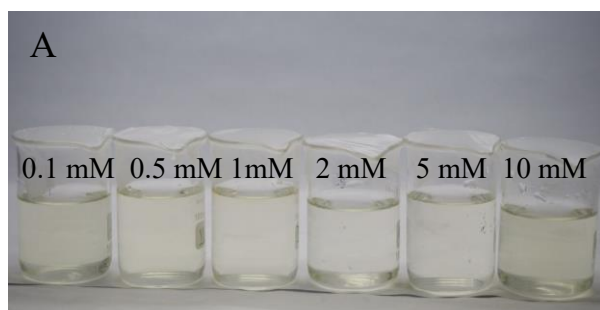


Figure 12. Photographs of 0.1–10 mM FAS solutions after preparation (0 h) (A) and storage for 24 h (B) and 48 h (C) at room temperature ($\sim 21\text{--}23^{\circ}\text{C}$) for the solutions prepared in tap water.



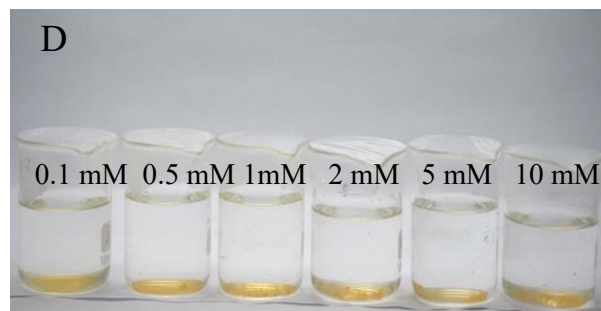
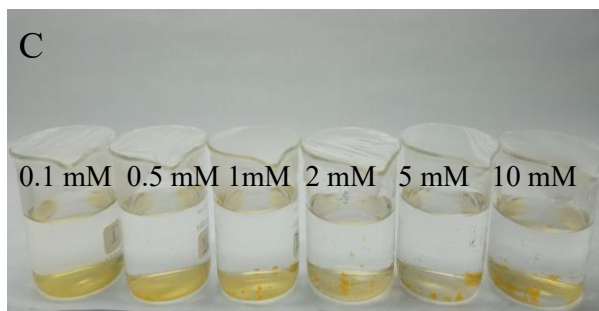


Figure 13. Photographs of 0.1–10 mM FAS solutions after preparation (0 h) (A) and storage for 24 h (B), 72 h (C), 168 h (D) in a refrigerator ($\sim 4^{\circ}\text{C}$) for the solutions prepared in distilled water.

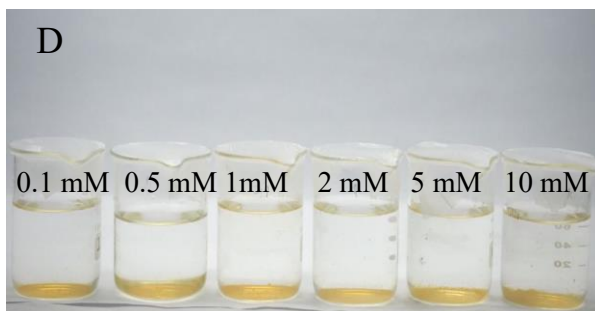
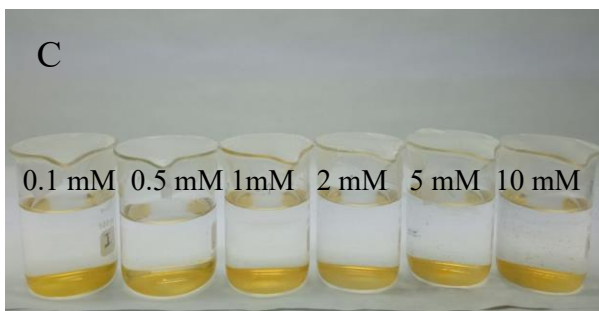
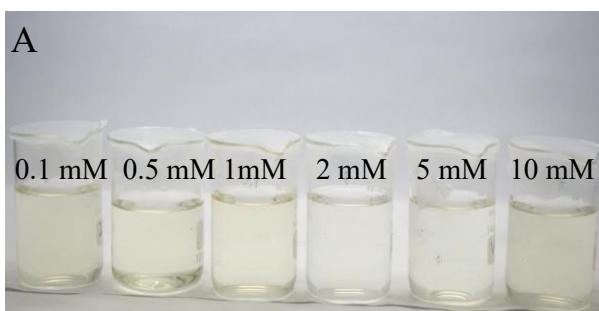
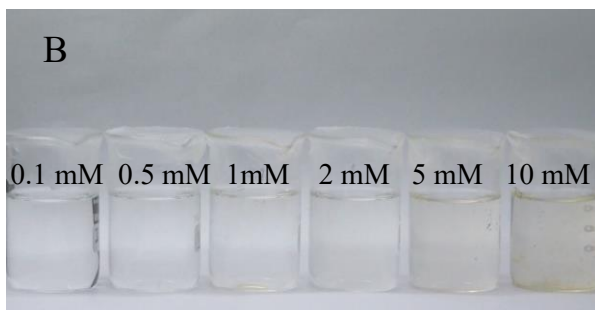
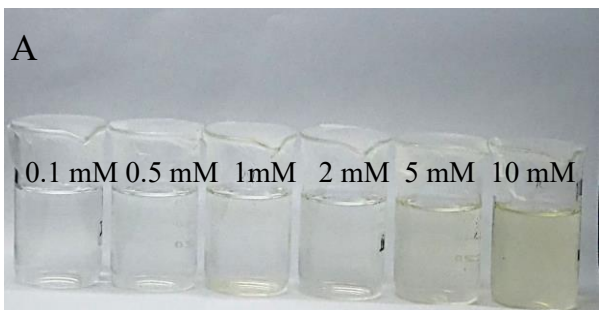
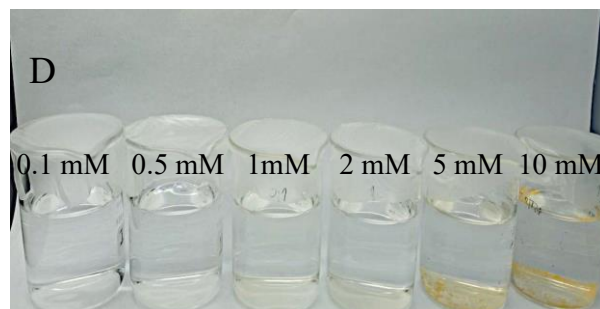
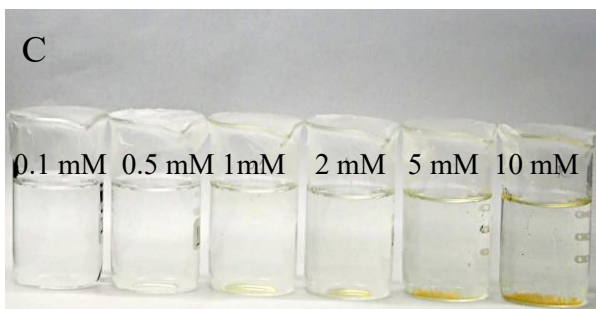


Figure 14. Photographs of 0.1–10 mM FAS solutions after preparation (0 h) (A) and storage for 24 h (B), 72 h (C) and 168 h (D) at room temperature ($\sim 21\text{--}23^{\circ}\text{C}$) for the solutions prepared in distilled water.





E

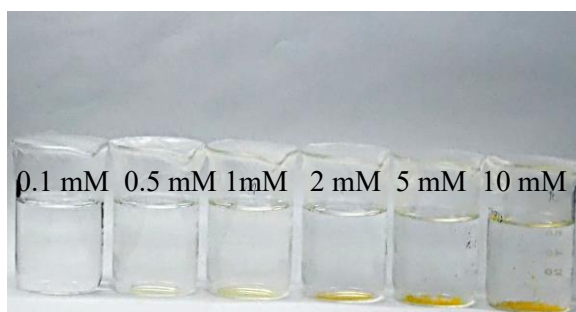
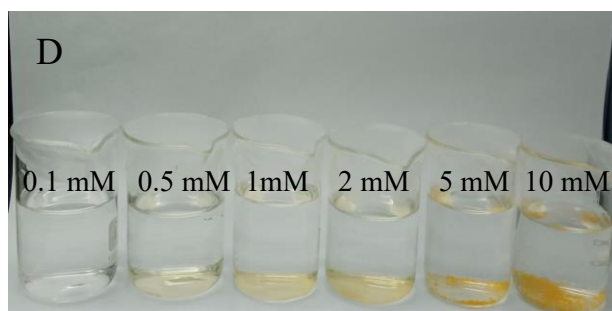
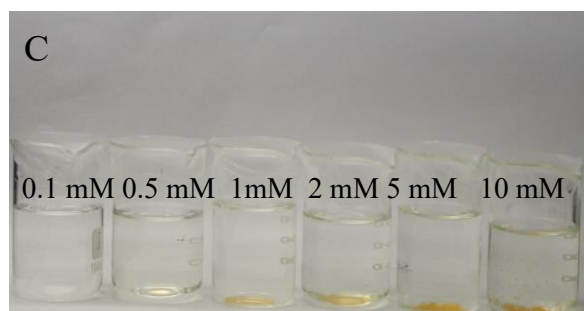
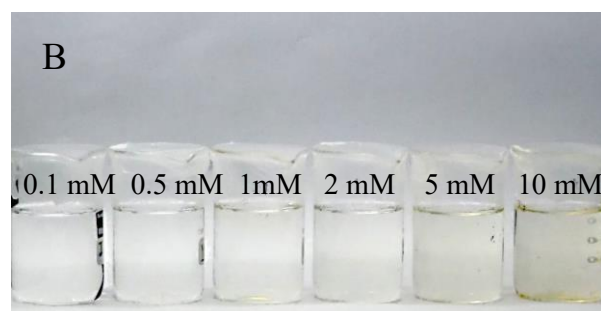
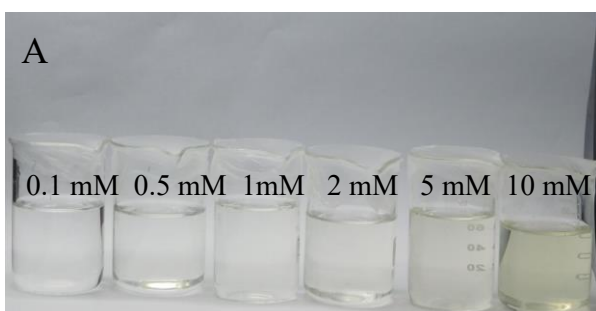


Figure 15. Photographs of 0.1–10 mM FAS solutions after preparation (0 h) (A) and storage for 24 h (B), 48 h (C), 72 h (D), 168 h (E) in a refrigerator ($\sim 4^\circ\text{C}$) for the solutions prepared in redistilled water.



E

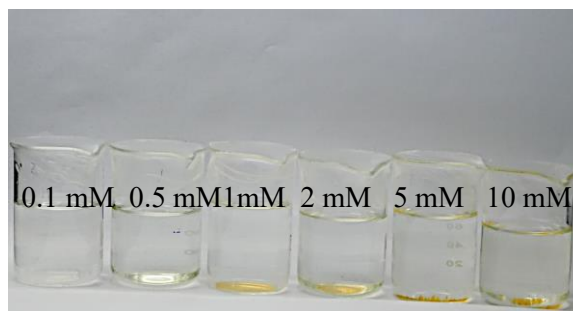
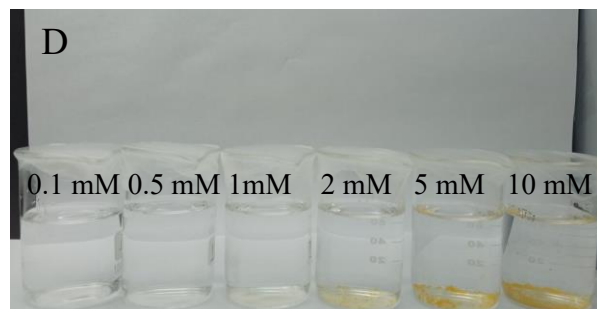
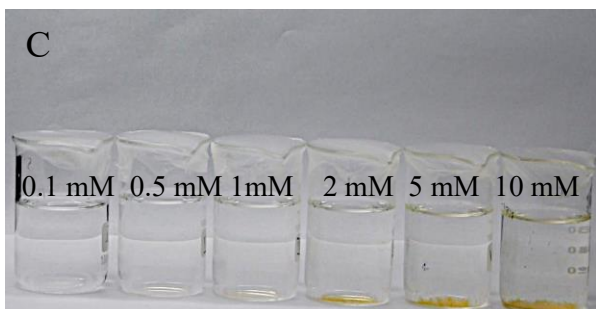
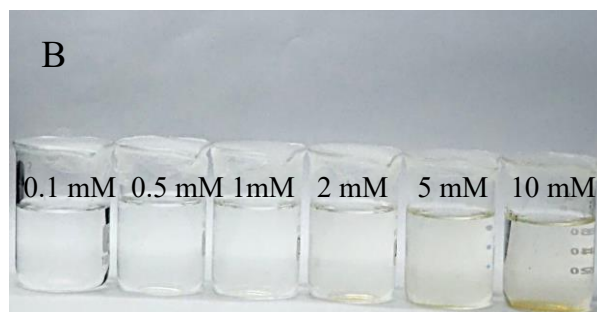
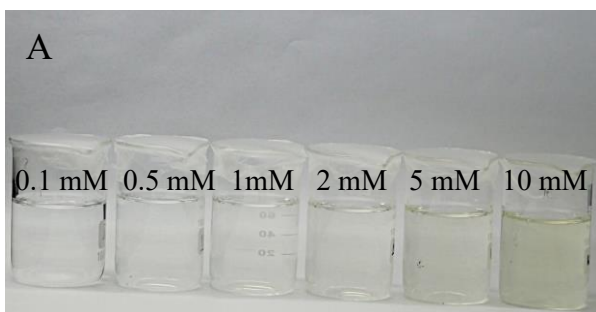


Figure 16. Photographs of 0.1–10 mM FAS solutions after preparation (0 h) (A) and storage for 24 h (B), 48 h (C) 72 h (C) and 168 h (D) at room temperature ($\sim 21\text{--}23^\circ\text{C}$) for the solutions prepared in redistilled water.



E

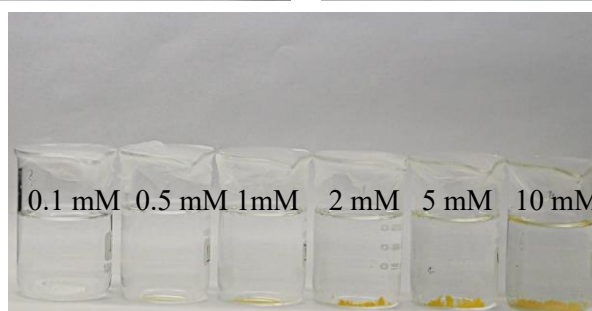
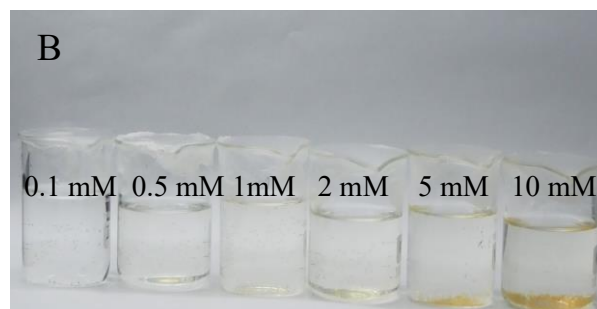
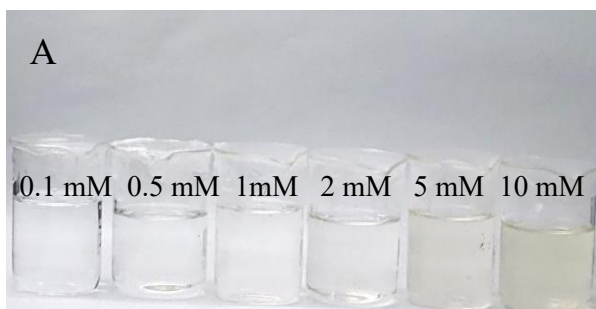


Figure 17. Photographs of 0.1–10 mM FAS solutions after preparation (0 h) (A) and storage for 24 h (B), 48 h (C), 72 h (D), 168 h (E) in a refrigerator ($\sim 4^\circ\text{C}$) for the solutions prepared in deionized water.



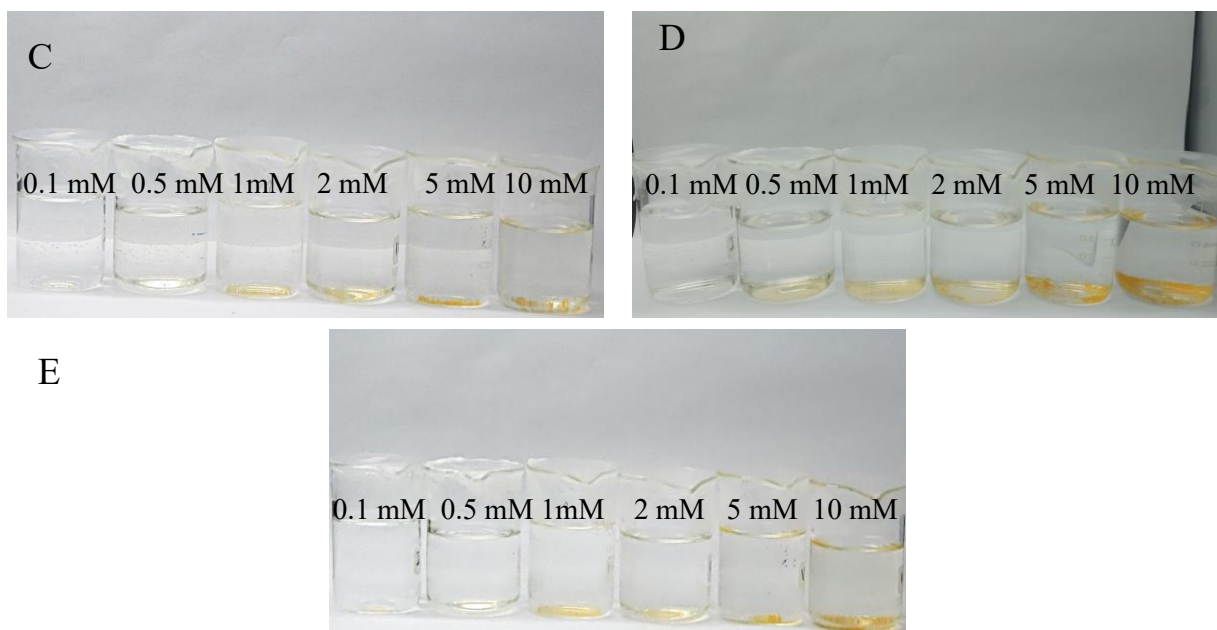
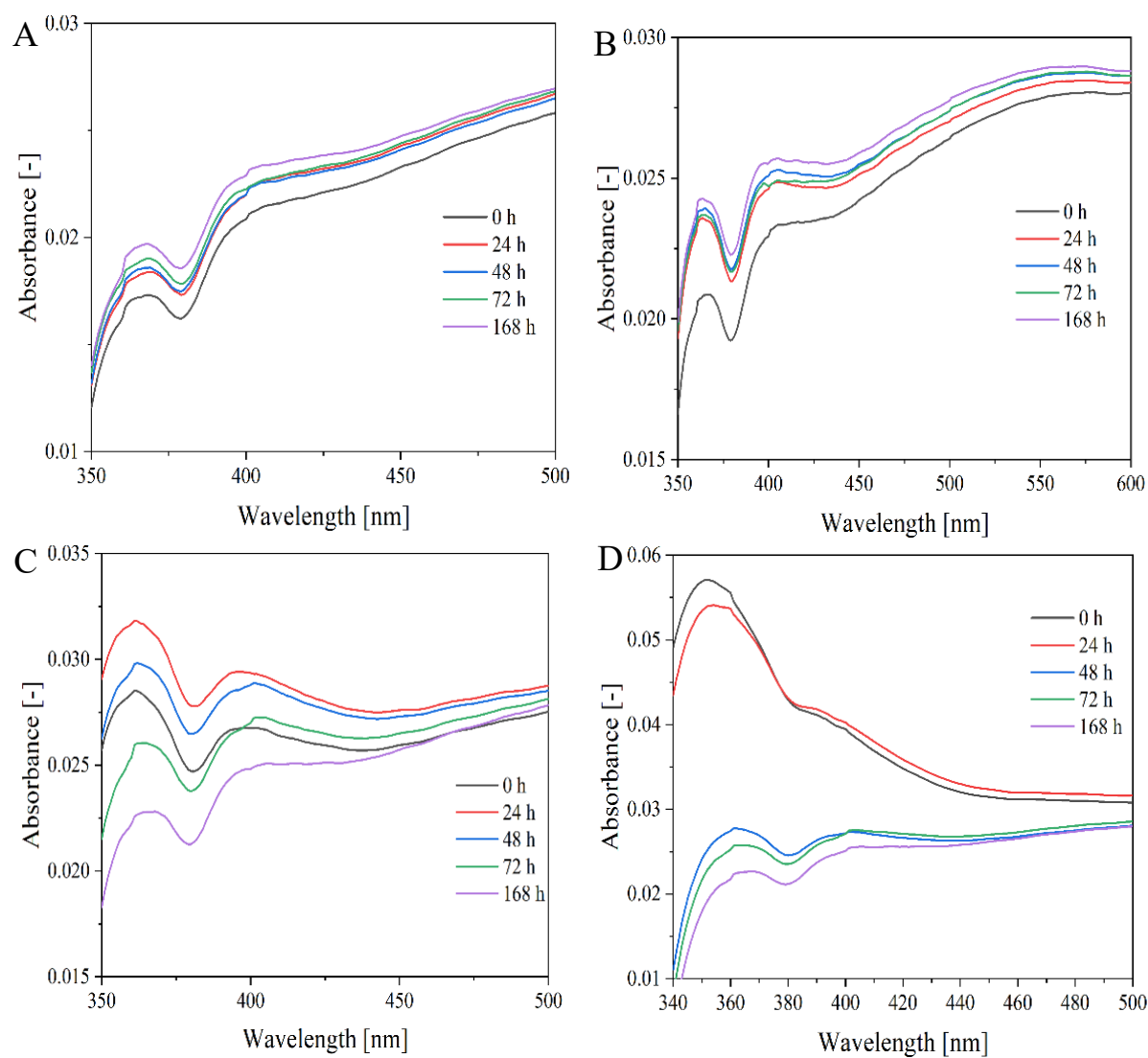


Figure 18. Photographs of 0.1–10 mM FAS solutions after preparation (0 h) (A) and storage for 24 h (B), 48 (C), 72 h (D) and 168 h (E) at room temperature ($\sim 21\text{--}23^\circ\text{C}$) for the solutions prepared in deionized water.



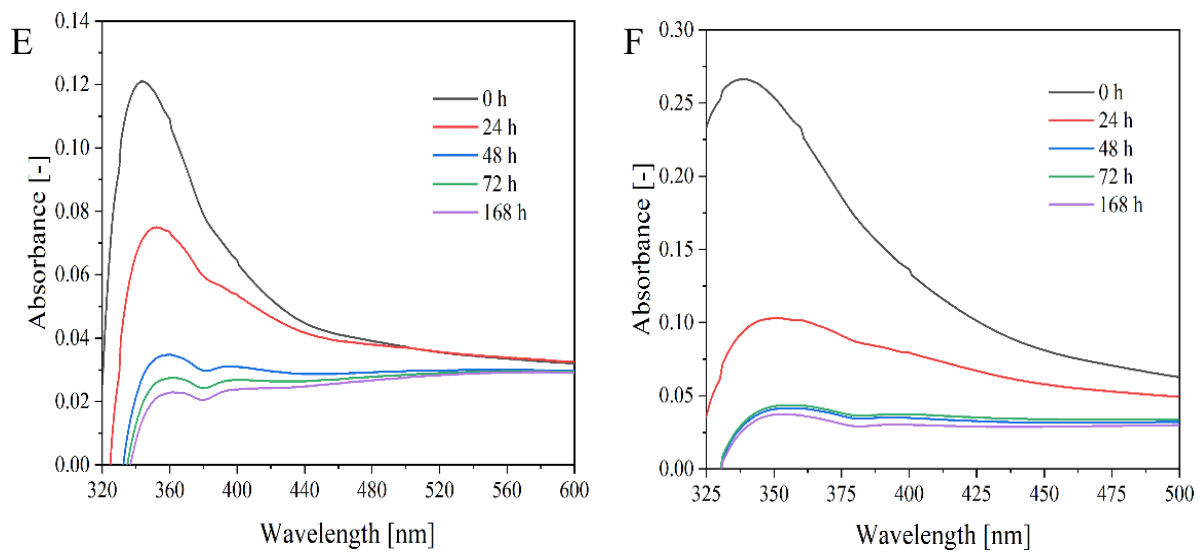
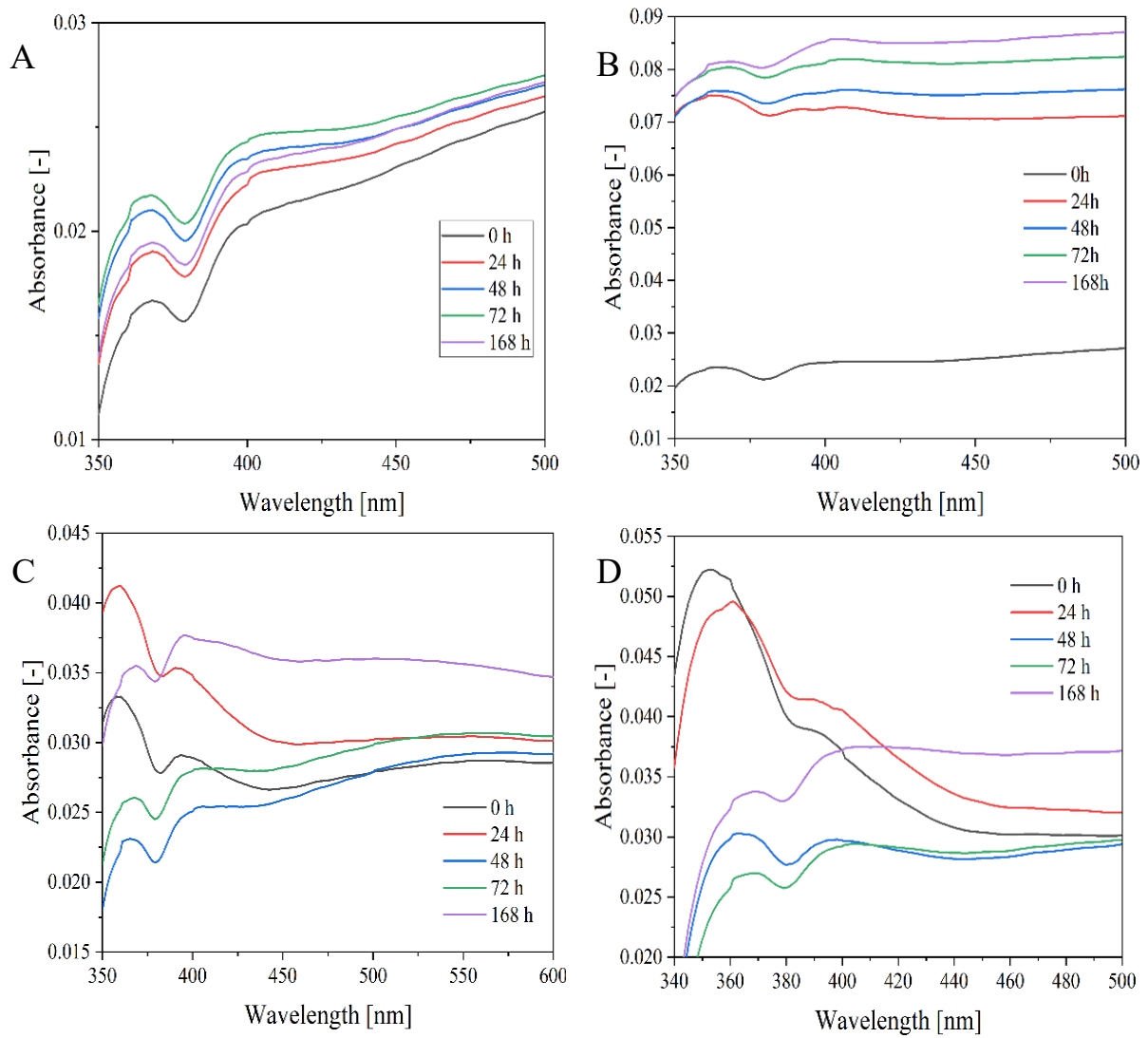


Figure 19. Absorption spectra of FAS solutions in deionized water and stored in the refrigerator ($\sim -4\text{ }^{\circ}\text{C}$): 0.1 mM (A), 0.5 mM (B), 1 mM (C), 2 mM (D), 5 mM (E) and 10 mM (F).



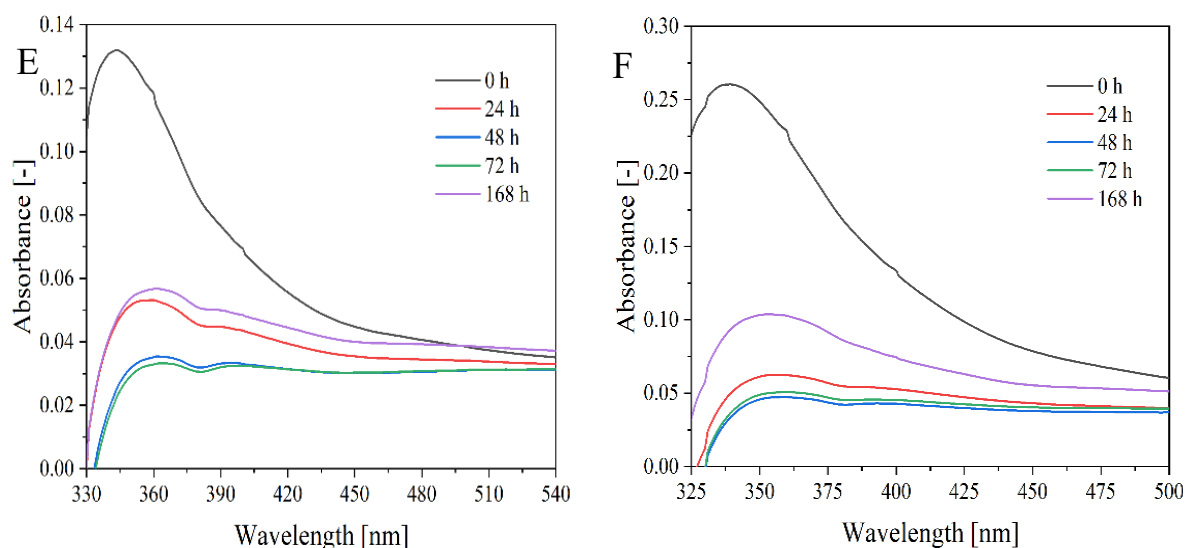
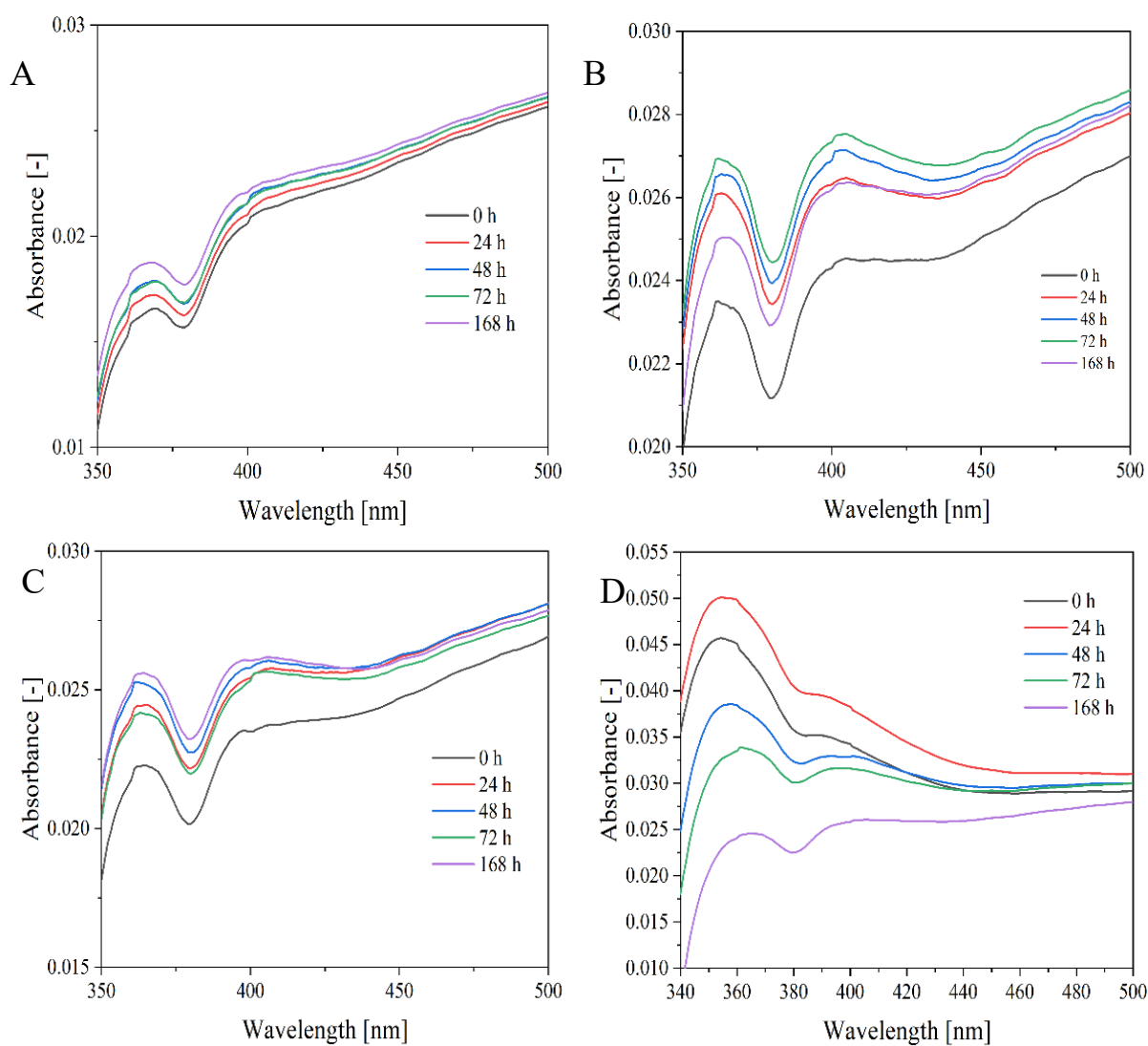


Figure 20. Absorption spectra of FAS solutions in deionized water and stored in a cabinet ($\sim 21\text{--}23^\circ\text{C}$): 0.1 mM (A), 0.5 mM (B), 1 mM (C), 2 mM (D), 5 mM (E) and 10 mM (F).



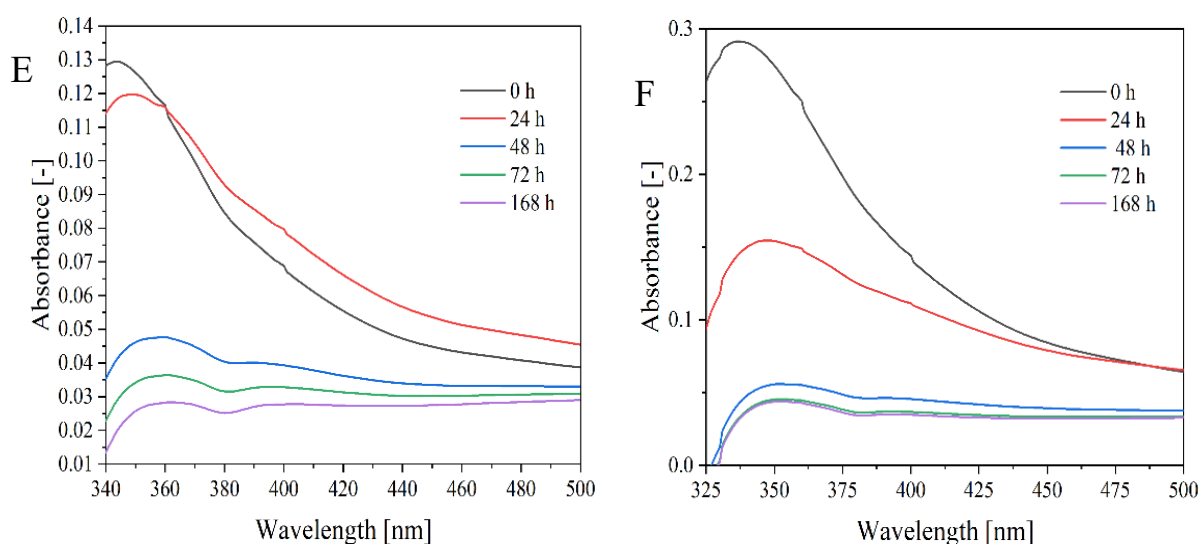
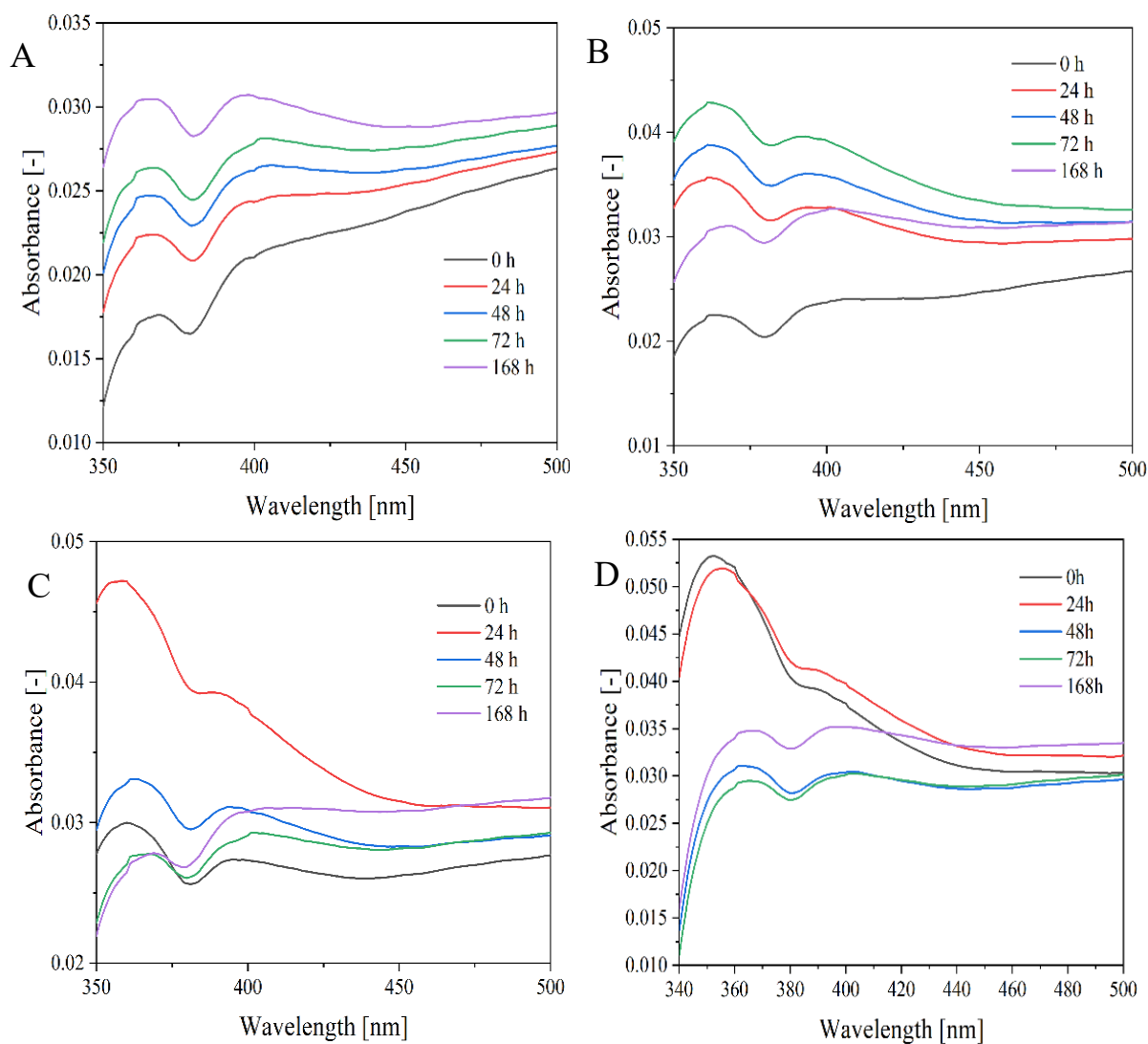


Figure 21. Absorption spectra of FAS solutions in redistilled water and stored in the refrigerator ($\sim -4^{\circ}\text{C}$): 0.1 mM (A), 0.5 mM (B), 1 mM (C), 2 mM (D), 5 mM (E) and 10 mM (F).



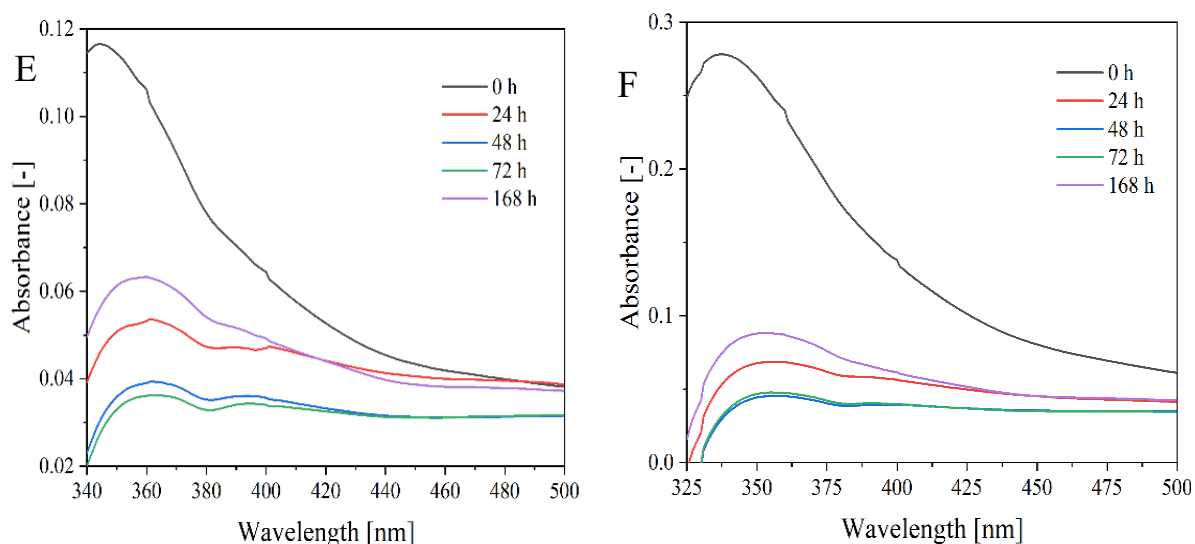
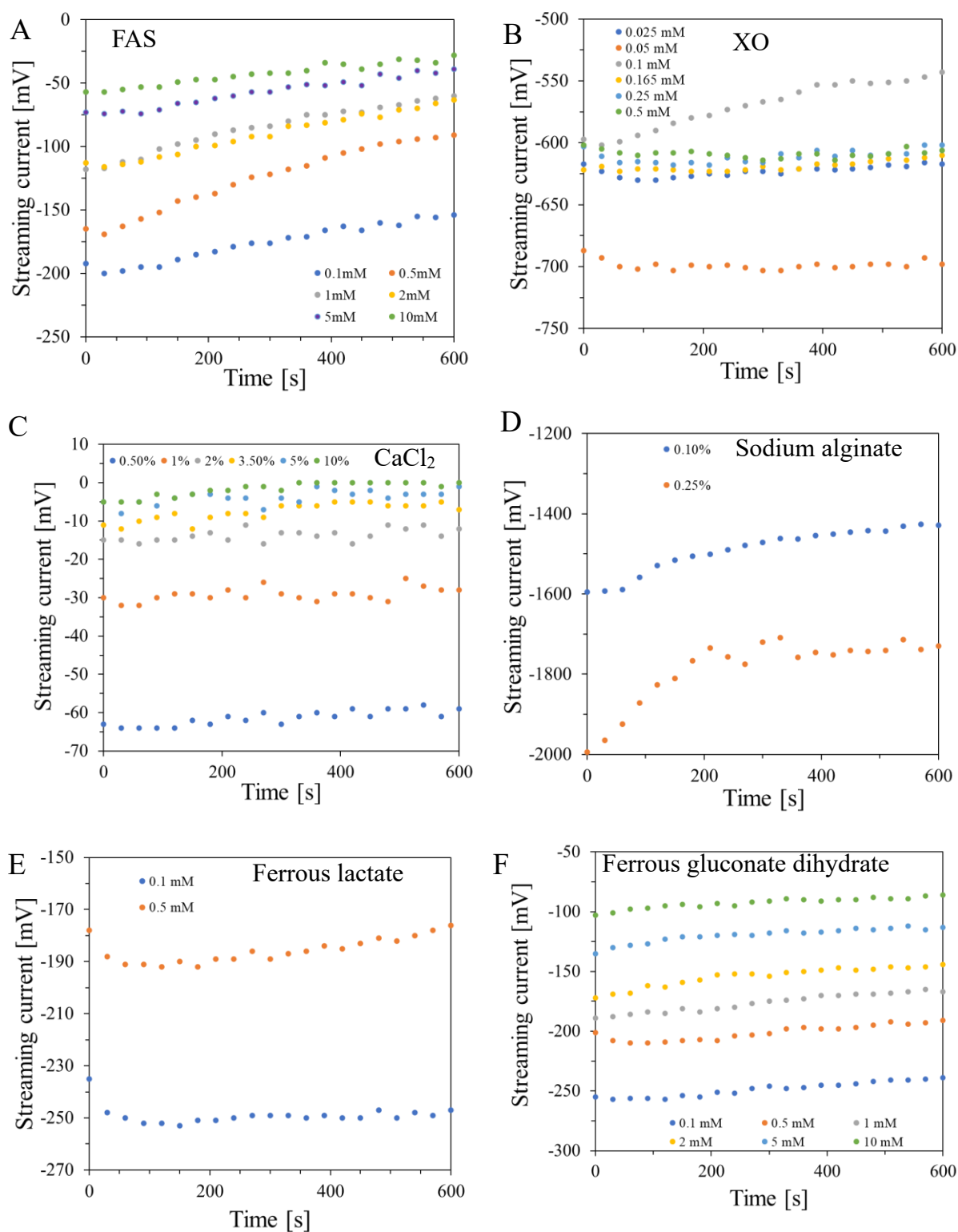


Figure 22. Absorption spectra of FAS solutions in redistilled water and stored in a cabinet (~21–23° C): 0.1 mM (A), 0.5 mM (B), 1 mM (C), 2 mM (D), 5 mM (E) and 10 mM (F).

5.1.2. Interactions between ingredients

Preparation of nano-, micro-gel structures required investigation of the stability of the component substrates in solutions, their chemical character and possible interactions between them. Therefore, streaming current measurements were performed for FAS, XO, CaCl_2 , sodium alginate, ferrous lactate, ferrous gluconate dihydrate, sulphuric acid, gelatin, Pluronic F-127, and for the reactions between components of sodium alginate and FAS, sodium alginate and CaCl_2 , sodium alginate and ferrous lactate, sodium alginate and ferrous gluconate dihydrate, and FAS and XO. The solutions were prepared in double distilled water (streaming current: -490 mV). The results are presented in Figure 23. The value of streaming current for the compounds is related to their concentration (Figure 23 A–I). It increases with an increase in concentration for FAS, CaCl_2 , ferrous lactate, ferrous gluconate dihydrate, gelatin and Pluronic F-127. It is a reverse tendency for sodium alginate; it decreases if the concentration of sodium alginate increases. For XO, the streaming current changes with concentrations in a more complex manner. First, it decreases for the two lowest concentrations, which is followed by a significant increase for 0.1 mM concentration and then a drop in values for the remaining concentration, which oscillate around similar values of streaming current. The streaming current for sulphuric acid was changing very fast and in a chaotic manner, most probably due to the high conductivity of the acid solution. The streaming current for gelatin takes the positive values over the entire concentration range (Figure 23 G). This may have some consequences on the interactions between alginate micro-gels containing Fe ions and gelatin matrix of a dosimeter composed of the micro-gels and gelatin matrix. The streaming current for Pluronic F-127, which is non-ionic co-polymer, increases with its concentration (Figure 23 H). The reason for this may be Pluronic F-127 molecules adsorption at the interface (gold electrodes-solution) and shielding against water molecules of a highly negative streaming current.



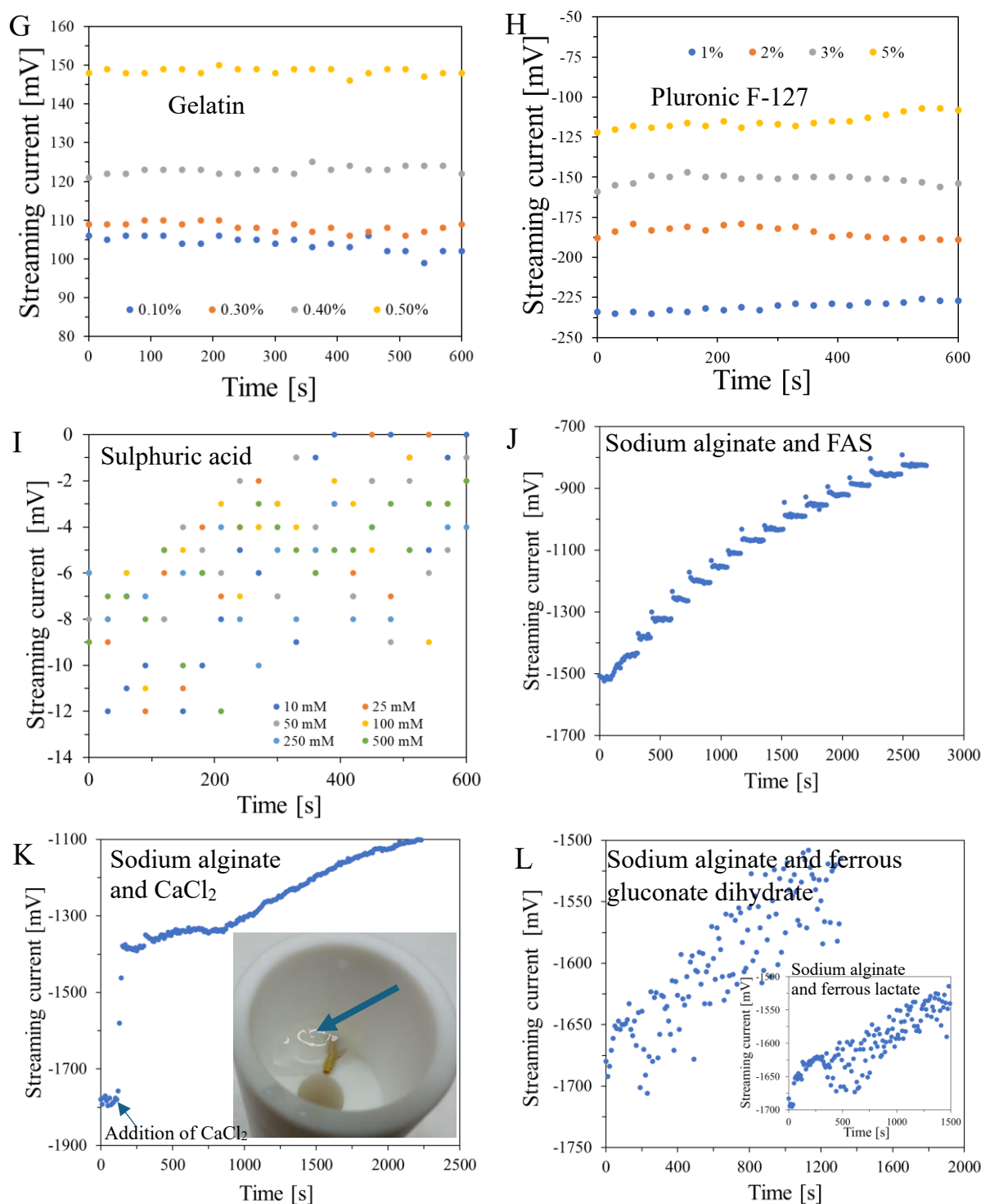


Figure 23. Streaming current of FAS (A), XO (B), CaCl₂ (C), sodium alginate (D), ferrous lactate (E), ferrous gluconate dihydrate (F), gelatin 300 Bloom, type A (G), Pluronic F-127 (H) and sulphuric acid (I) solutions. In J–L, the graphs corresponding to the reaction of the following substrates are presented: sodium alginate and FAS (J), sodium alginate and CaCl₂ (K), sodium alginate and ferrous gluconate dihydrate (L), and sodium alginate and ferrous lactate – inset in (L). For each reaction, 15 mL of 0.25% sodium alginate was titrated periodically in 50 mL portions of: 1 mM FAS (J), 3.5% CaCl₂ (K), 1 mM ferrous gluconate dihydrate (L), and 1 mM ferrous lactate – inset in (L). Inset in (K) is a photograph of a measuring cup with calcium alginate hydrogel formed (indicated with the blue arrow).

Each solution of the compounds characterizes with specific stability over time of measurement, as shown in [Figure 23](#). The most stable is CaCl_2 and ferrous gluconate dihydrate over entire range of concentration examined, XO for all concentrations apart from 0.1 mM. For FAS and sodium alginate an increase in streaming current was observed for all concentrations; the same applies to XO for 0.1 mM. For ferrous lactate the streaming current initially decreases, then stabilizes and at longer measurement time it can increase for some concentrations. It should be noted that the streaming current is negative for all compounds; however, particularly for low concentrations of compounds, the negative streaming current of double distilled water can contribute to the streaming current values of the solutions. Hence, the analysis of the streaming current values is not enough to conclude about the possible reactions between these negatively charged compounds. Therefore, it was important to investigate the reactions of Ca^{2+} and, most importantly, Fe^{2+} with sodium alginate to verify the assumption on the possibility of binding these ions with sodium alginate. Firm binding of Fe^{3+} with sodium alginate can be used for reducing the diffusion of iron ions in a 3D dosimeter matrix. The results are shown in [Figure 23 J–L](#). From these results it is evident that both Ca^{2+} and Fe^{2+} react with sodium alginate and in consequence the streaming current values increase; become less negative. The reaction between the components can also burden measurement, which is related to either precipitation of the product, formation of e.g., microgels and even macrogels. This is visible by large fluctuation of the values and even gel formation in the measurement cell ([Figure 23 K, L](#)). The results in this section showed the interaction between sodium alginate, ferrous and calcium ions, which were further used for the manufacturing of nano-, microgels/capsules.

5.1.3. Characteristics of macrocapsules

The capsules were made by dropping the sodium alginate solution of different concentrations (1.7, 2, 2.3, 2.7, 3 and 3.5%) into the Fricke solution containing 0, 1, 1.5, 2.5 and 3.5% CaCl_2 . Photos of capsules obtained using alginate at concentrations of 1.7% and 3.5% and calcium chloride at concentrations of 0–3.5% are presented in photographs in [Figures 24, 25, and 26](#), for Sigma low, Sigma medium and Heppe medium viscosity, respectively. A criterion for organoleptic evaluation of the capsules was chosen, that the proper capsules should have a repetitive, spherical shape and sufficient mechanical strength so that they do not fall apart when gripped with the fingers.

A summary of the selected conditions for producing the best alginate capsules meeting the criterion is presented in [Table 6](#). In short, for low viscosity Sigma alginate, acceptable capsules (most spherical and with adequate mechanical strength) or very good capsules (all spherical and with adequate mechanical strength) are formed for 1.7–3.5% alginate solution in reaction with Fricke solution and 1.5–3.5% CaCl_2 . However, for medium viscosity Sigma alginate, the only acceptable capsules are formed with 1.7% sodium alginate in reaction with Fricke solution and 1.5% CaCl_2 . For other reaction conditions, well-shaped capsules could not be obtained. Lower alginate concentrations produce disks of varying thickness, while higher concentrations produce a teardrop shape. This is due to the high viscosity of alginate. At high concentrations, the droplets escaping from the syringe are unable to form a spherical shape on their way from the syringe outlet to the liquid surface. In the case of Heppe alginate, acceptable or very good capsules can be formed using 1.7–3.5% alginate solution, Fricke solution and 1–3.5% CaCl_2 . Heppe alginate capsules appear more transparent than those prepared from Sigma alginates (no filtration of the alginate solutions was used). The mechanical properties of the capsules, assessed organoleptically, appear to be comparable to those of low-viscosity Sigma alginate capsules. Based on

the above observations, low-viscosity Sigma alginate and medium-viscosity Heppe alginate are the most promising for forming capsules for dosimetric purposes.

It should be noted that it is possible to obtain capsules without Ca^{2+} in the forming solution for all alginate concentrations and alginate types (viscosities) (Figure 24 A, E, Figure 25 A, D and Figure 26 A, E). The capsules are of irregular shape; however, the fact they are formed confirms that Fe^{2+} ions bind sodium alginate chains which leads to physical hydrogels.

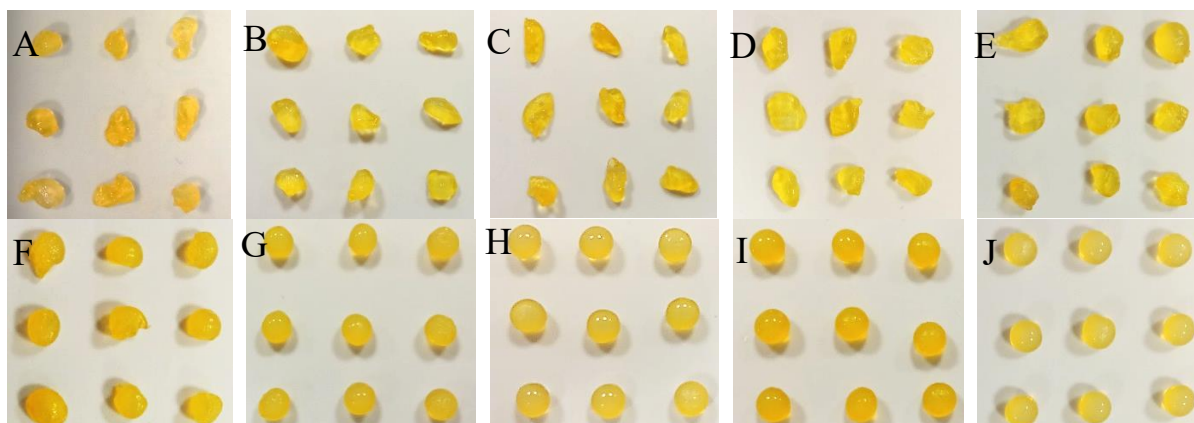


Figure 24. Alginate capsules obtained by dropping the sodium alginate polymer solution of a low viscosity (Sigma) to the Fricke solution containing CaCl_2 of 0% (A, F), 1% (B, G), 1.5% (C, H), 2.5% (D, I), and 3.5% (E, J). The concentration of the sodium alginate solution was as follows: 1.7% (A–E), 3.5% (F–J).

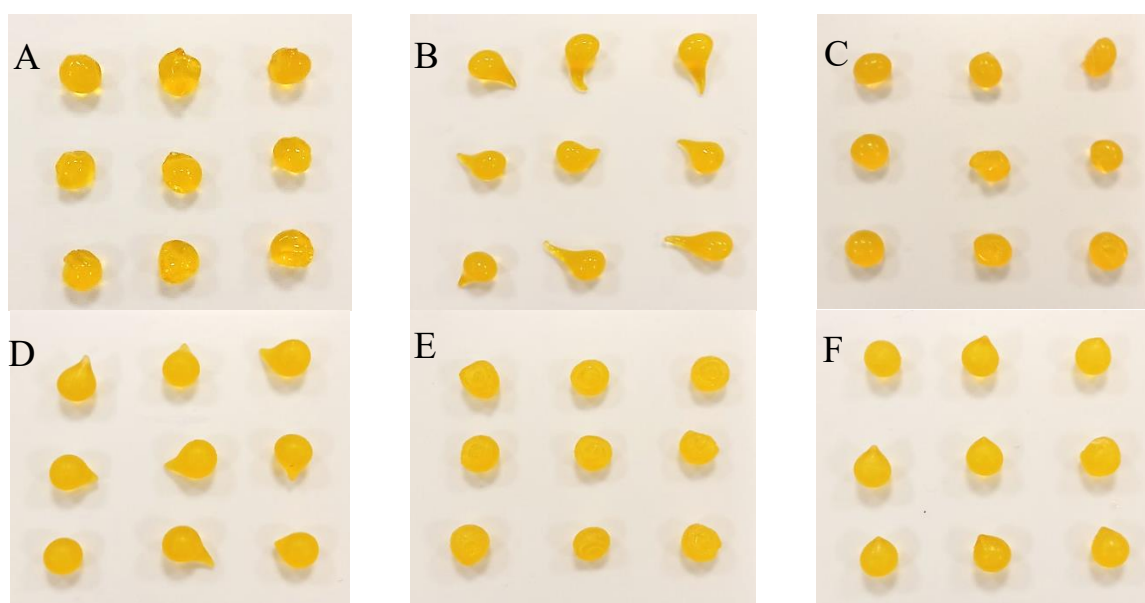


Figure 25. Alginate capsules obtained by dropping the sodium alginate polymer solution of a medium viscosity (Sigma) to the Fricke solution containing CaCl_2 of 0% (A, D), 1% (B, E), 1.5% (C, F). The concentration of the sodium alginate solution was as follows: 1.7% (A–C), 3.5% (D–F).

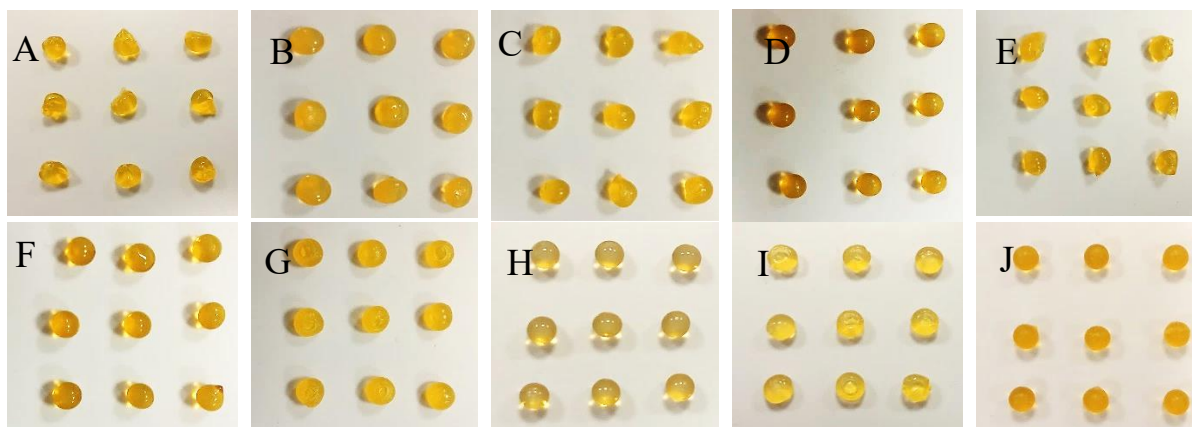


Figure 26. Alginate capsules obtained by dropping the sodium alginate polymer solution (medium viscosity, Heppe) to the Fricke solution containing CaCl_2 of 0% (A, F), 1% (B, G), 1.5% (C, H), 2.5% (D, I), and 3.5% (E, J). The concentration of the sodium alginate solution was as follows: 1.7% (A–E), 3.5% (F–J).

Table 6. Characterisation of alginate capsules made from sodium alginate reaction with Fricke and CaCl_2 solutions.

No.	Alginate type	Alginate concentration [%]	CaCl_2 concentration [%]	Comment
1	Low viscosity, Sigma	2.7	2.5	Acceptable
2			3.5	
3		3.0	2.5	Very good
4			3.5	
5		3.5	1.5	Acceptable
6			2.5	Very good
7			3.5	
8	Medium viscosity, Sigma	2.7	1.5	Acceptable
9	Medium viscosity, Heppe	2.7	1.5	Very good
10			2.5	
11		3.0	1	Acceptable
12			1.5	Very good
13			2.5	
14			3.5	
15		3.5	1.5	
16			2.5	
17			3.5	

The stability of alginate capsules produced by the dropwise addition of sodium alginate solution to Fricke's solution containing Ca^{2+} ions was tested on capsules stored in Fricke's solution at either 4 °C in a refrigerator or 21–23 °C in a cabinet, both without access to daylight. The results are shown in [Figure 26](#). It was found that the optimal storage condition for the capsules was low temperature (refrigerator), which preserves the color for several weeks. However, when alginate capsules are removed from the forming solution (Fricke's solution with or without calcium ions) and stored at approximately 25 °C with access to laboratory light, their color becomes unstable and changes over time, as shown in [Figure 27](#). The color of Heppe and Sigma alginate capsules changes from light yellow to brown. This color change is analogous to that observed when the capsules are irradiated with ionizing radiation ([Figure 28](#)). When irradiated, the color of the capsules changes after they have absorbed the dose, and does not change during storage in air, unlike non-irradiated capsules. Capsules made of Heppe alginate appear to be slightly more sensitive to irradiation, turning a darker shade of brown.

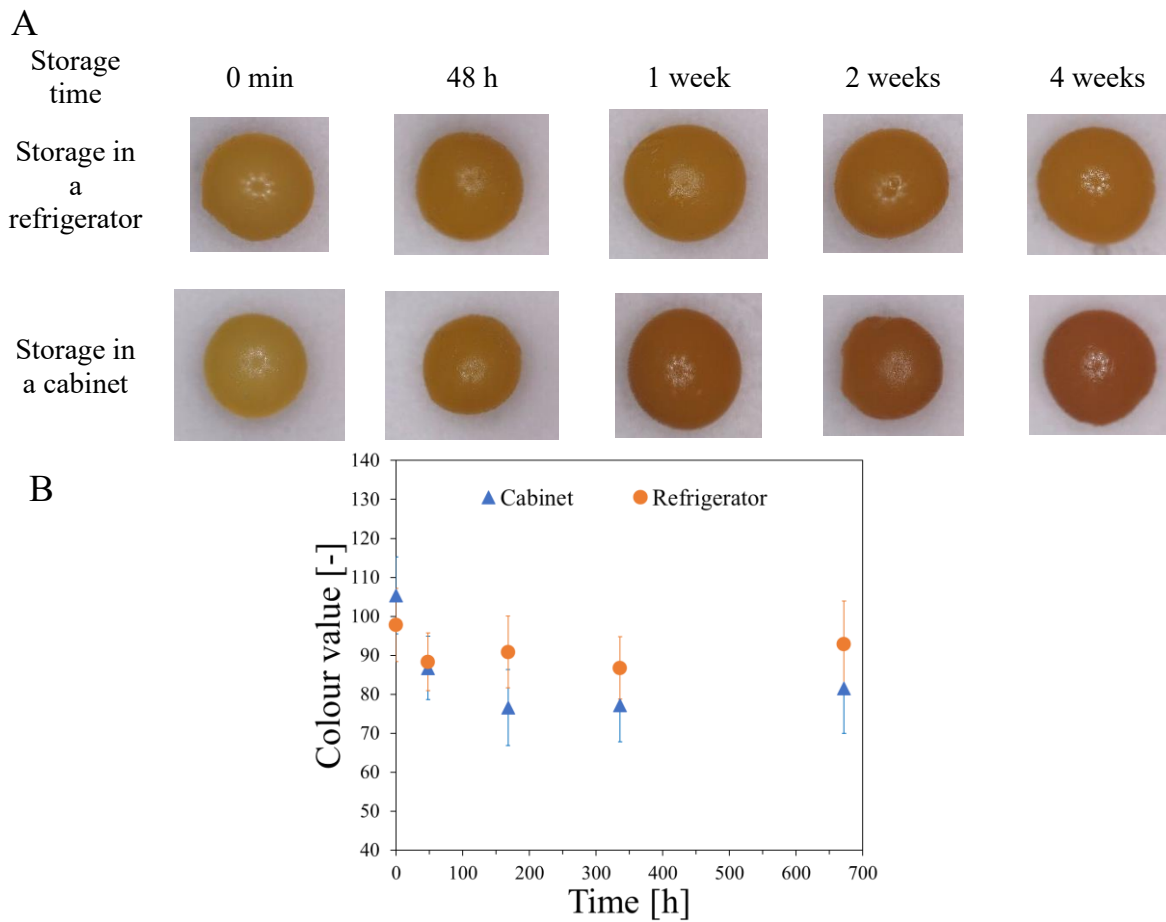
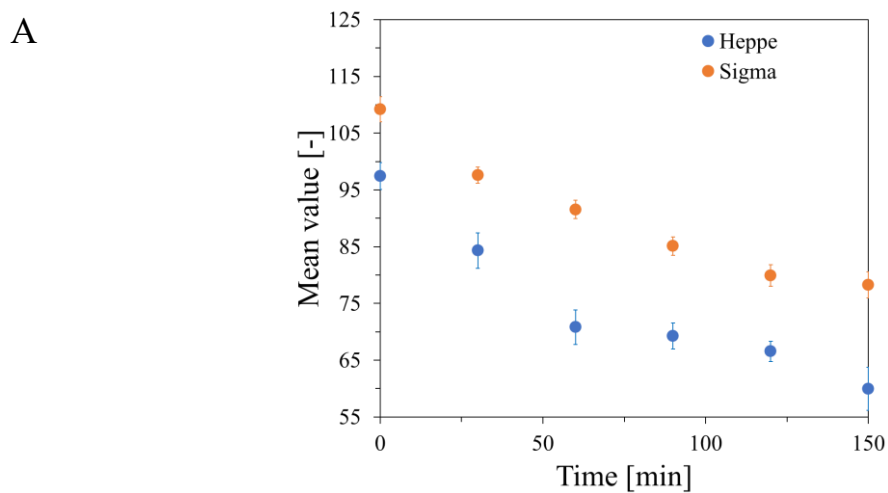


Figure 26. Stability of the capsules made in reaction of 3.5% alginate (low viscosity Sigma) with Fricke solution (FAS: 1 mM, XO: 0.165 mM, H₂SO₄: 50 mM) containing 3.5% CaCl₂ by dropwise addition of sodium alginate solution into the Fricke solution with Ca²⁺ (A). The capsules stored in the Fricke solution either in a refrigerator at about 4 °C or in a cabinet at about 21–23 °C (without access to daylight). Top of the figure contains photographs of the capsules during storage (A). The graph (B) corresponds to the color values of the capsules read with ImageJ software over time of storage (mean values of circular ROIs covering the entire capsules).



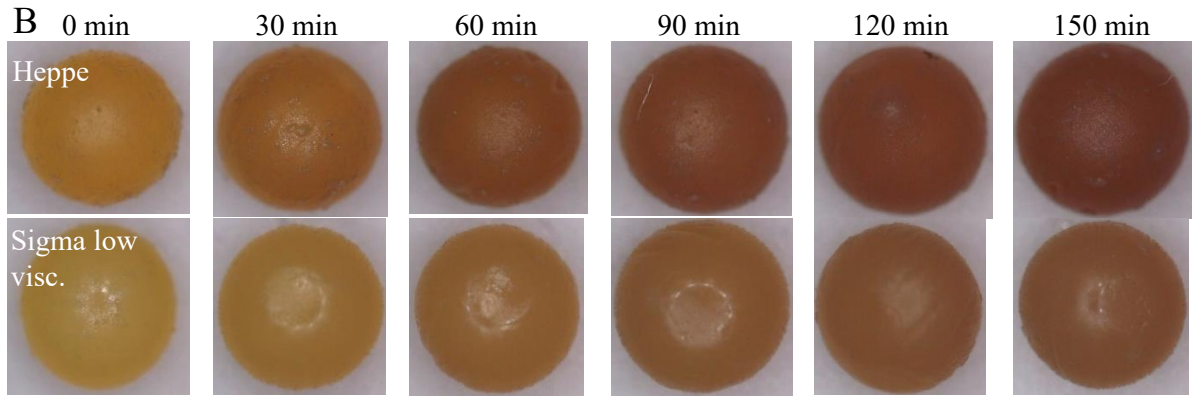


Figure 27. A: Stability of alginate capsules containing Fricke solution. A mean value of color for the photographs taken with a microscope (Delta Optical Smart 5MP PRO digital microscope) versus storage time at about 25 °C with access to laboratory light, removed from Fricke solution, for the capsules formed with Heppe medium viscosity and Sigma low viscosity alginates. Beneath the graph are the photographs (B) of the capsules taken at 0–150 min after formation (first row: capsules made of Heppe and second row: capsules made of Sigma alginate). The capsules were made in reaction of 3.5% alginate with Fricke solution (FAS: 1 mM, XO: 0.165 mM, H₂SO₄: 50 mM) containing 3.5% CaCl₂ by dropwise addition of sodium alginate solution into the Fricke solution with Ca²⁺.

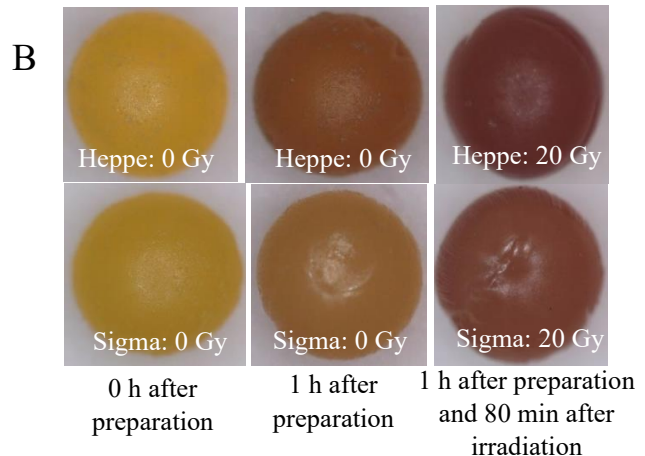
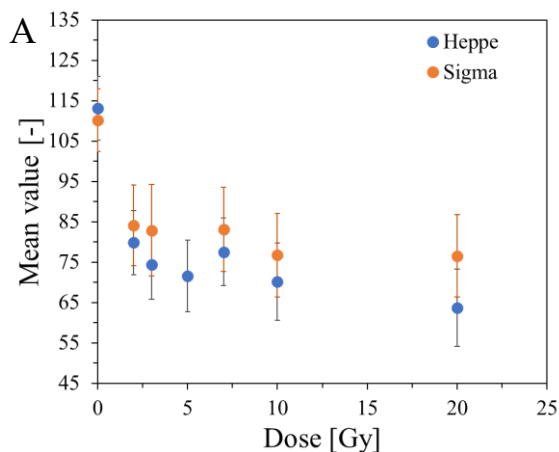


Figure 28. Response of alginate capsules containing Fricke solution to irradiation with X-rays of a TrueBeam medical accelerator (Varian, USA): mean value of color for the photographs taken with a microscope (Delta Optical Smart 5MP PRO digital microscope) versus absorbed dose (A) and example photographs of non-irradiated and irradiated capsules (B). The capsules were made of Heppe and a low viscosity Sigma alginate in reaction of 3.5% alginate with Fricke solution (FAS: 1 mM, XO: 0.165 mM, H₂SO₄: 50 mM) containing 3.5% CaCl₂ by dropwise addition of sodium alginate solution into the Fricke solution with Ca²⁺. The capsules were immersed (0 Gy) and removed from the Fricke solution (20 Gy) and not immersed in the solution after irradiation. The photographs of capsules are magnified: $\times 38$. The values in A are averages for 3-6 capsules and were calculated from about 50000 pixels.

5.1.4. Diffusion of Fe, Ca and XO from macrocapsules

As demonstrated in previous sections, alginate capsules can be formed by reaction of sodium alginate solution with Fe ions, either with or without the presence of Ca ions. Such capsules are formed by adding the sodium alginate solution to an aqueous solution of these ions and keeping it beneath the surface of the solution for an arbitrary chosen amount of time. The capsules form when the ions bind to the alginate's carboxylate groups, leading to intermolecular crosslinking. However, it was supposed that, in

addition to this reaction, the capsules may contain non-bonded ions through the simple absorption of the Fricke solution, with or without calcium ions. To investigate this, the content of Fe and Ca ions in the capsules was analysed using ICP-OES in the following cases:

- (1) the reaction time between the sodium alginate solution and the Fricke solution containing 3.5% CaCl_2 (Figure 29);
- (2) the capsules prepared by reacting sodium alginate with the Fricke solution containing 3.5% CaCl_2 and a different concentration of FAS. The diffusion of Fe and Ca ions from the capsules was studied (Figure 30 A–E).
- (3) The same as (2), but with other compounds containing Fe ions tested instead of FAS: ferrous lactate and ferrous gluconate dihydrate (Figure 30 F–H).

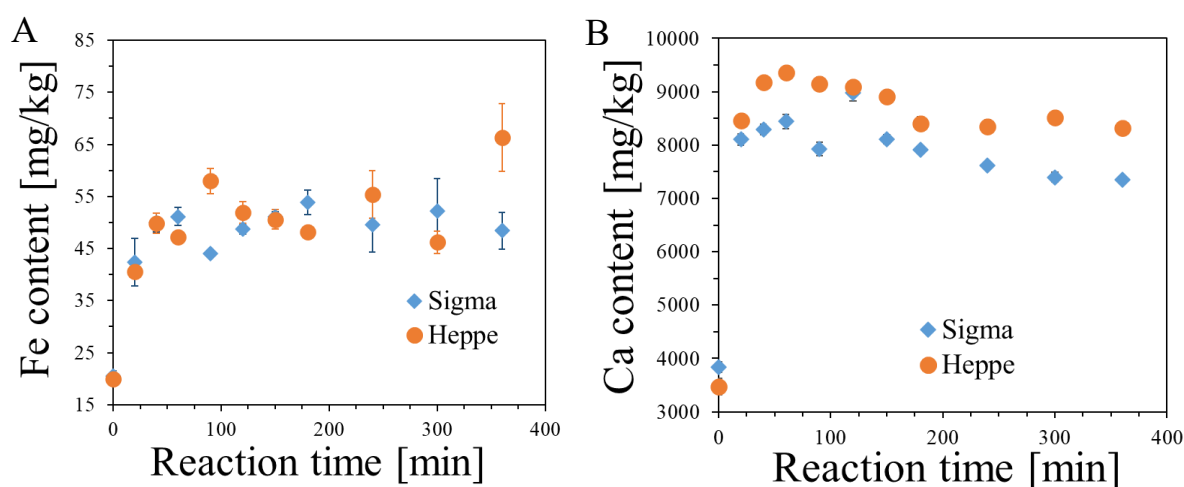
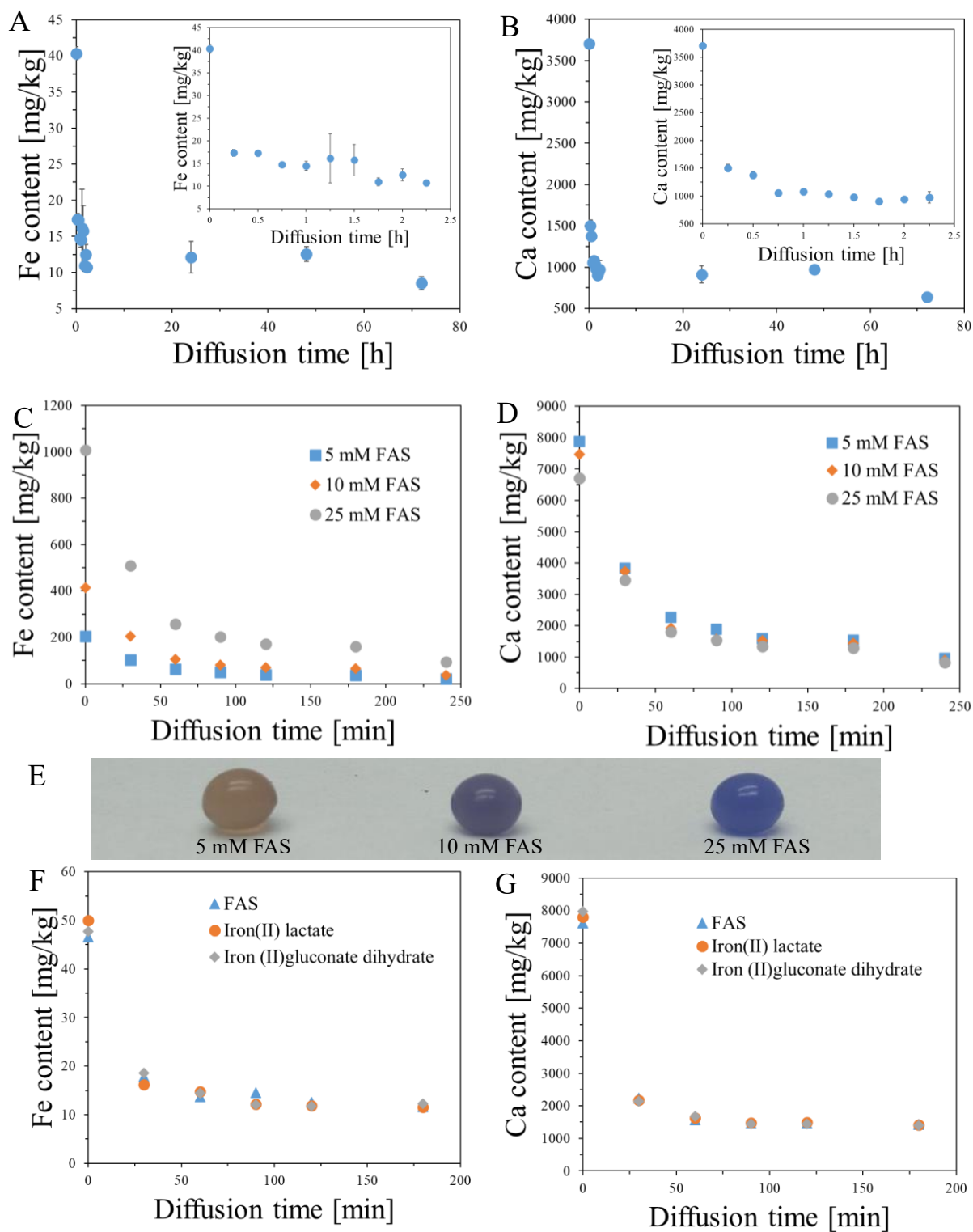


Figure 29. Content of Fe (A) and Ca (B) per 1 kg of capsules (average weight of one capsule: 0.034 g) in relation to reaction time between sodium alginate solution (Sigma and Heppe) and Fricke solution (FAS: 1 mM, H_2SO_4 : 50 mM, XO: 0.165 mM) containing 3.5% CaCl_2 . Measurements performed with the aid of ICP-OES. The reaction was carried out at a temperature of about 23 °C. Throughout the experiment, the contents of the beaker were stirred with a magnetic stirrer at a speed of about 450 rpm.

The Fe and Ca content of alginate capsules increases with reaction time (Figure 29). For Fe, the content stabilises at around 100 minutes, while for Ca, the content reaches a maximum value at around 50 minutes and then decreases; after around 300 minutes, the content appears to stabilise. When comparing the two types of alginates, it was found that they bind Fe ions similarly, but Heppe has a higher affinity for binding Ca ions than Sigma alginate. The diffusion experiments (Figure 30) revealed that neither Ca nor Fe is retained in the capsules when they are immersed in water. Most of the ions transfer to the water. For example, only around 15% of Fe and Ca ions remain in the alginate capsules (Figure 30 A, B). The concentration of FAS in the Fricke solution does not affect the Fe content of the capsules during diffusion studies; however, the higher the concentration, the more Fe is retained in the capsules (Figures 30 C, D). Conversely, the higher the concentration of FAS in the Fricke solution, the more the capsules turn to blue color (Figure 30E). This prevents them from being used as 1D dosimeters. Additionally, the type of compound containing Fe ions has no impact on their retention in capsules immersed in water (Figure 30 F, G). The type of compound containing Fe^{2+} ions affects the initial color of the alginate capsules. This is similar for FAS and ferrous lactate, but much darker yellow for ferrous gluconate dihydrate (Figure 30 H). Apart from examining Fe and Ca diffusion from alginate capsules, XO diffusion was also assessed (Figure 31). These results clearly show that XO is not permanently retained in large quantities

in the capsules and that about 95% is released into the water. In summary, although alginate capsules can be formed by crosslinking alginate chains with both Fe and Ca ions by adding the alginate solution dropwise to the Fricke solution containing XO and Ca ions, most components important from a dosimetric point of view are released when the capsules are immersed in water.



H



Figure 30 Examination of diffusion of Fe (A, C, F) and Ca (B, D, G) from alginate capsules (average weight of one capsule: 0.034 g) made by reaction of sodium alginate solution (Sigma) (3.5%) with Fricke solution (FAS: 1 mM, H₂SO₄: 50 mM, XO: 0.165 mM; reaction time= 40 min) containing 3.5 CaCl₂ (A, B), different concentrations of FAS (C, D), and different compounds containing Fe (F, G) (concentration of each compound: 1 mM). In E and H, the photographs of capsules made of different concentrations of FAS and different compounds containing Fe, respectively, are shown. The capsules were immersed in 3.5 mL of re-distilled water. Measurements performed with the aid of ICP-OES. For A and B, the water with the capsules was changed after 48 hours of diffusion, for C and D, the water was changed after 180 minutes, and for F and G, after 120 minutes.

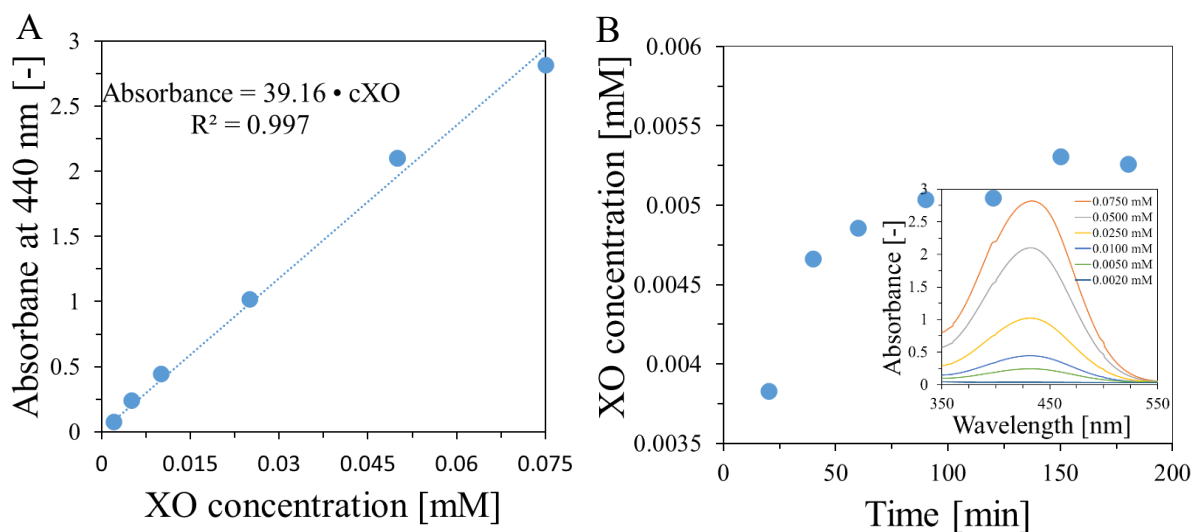
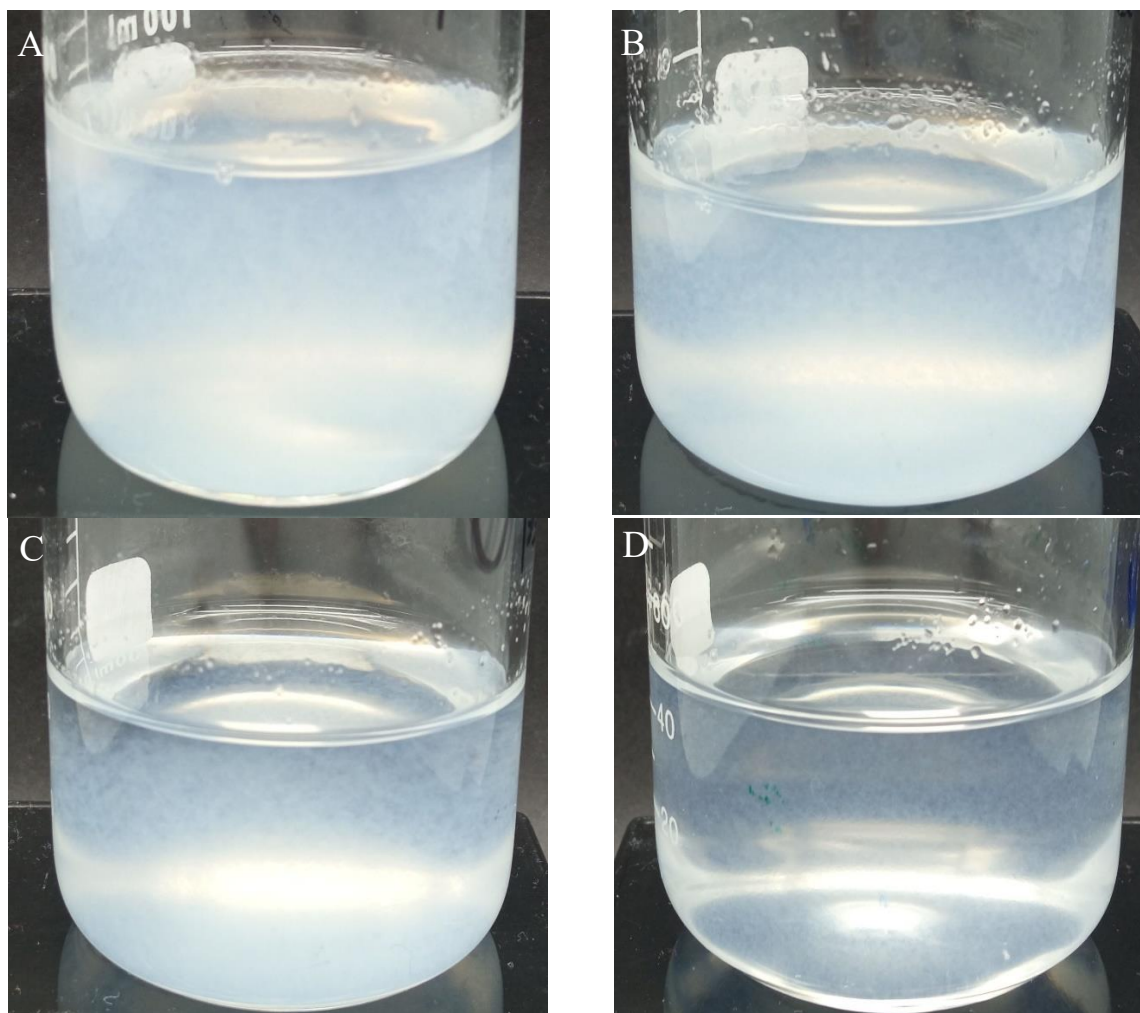


Figure 31. Diffusion of XO from alginate capsules prepared by reaction of sodium alginate (3.5%) with Fricke solution (FAS: 1 mM, H₂SO₄: 50 mM, XO: 0.165 mM) (B). The capsules were immersed in redistilled water. A is for the calibration curve that was obtained after registering the absorbance spectra (inset in B).

5.1.5. Characteristics of nano- and micro-gels

The first composition tested for obtaining nano-, micro-gels by reaction of sodium alginate with Fricke solution components consisting of 0.015-0.65% Sigma low viscosity sodium alginate, 1 mM FAS and 50 mM H₂SO₄. Additionally, a sample containing 0.5% sodium alginate and 50 mM H₂SO₄ without FAS was prepared. The pH value of the tested solutions ranged from approximately 1.4 (for the lowest alginate concentrations) to approximately 1.8 (for the highest alginate concentrations). The obtained gels are presented in Figure 32 and the transmittance spectra for the nano-, micro-gel solution are presented in Figure 33 A. The graph shows (Figure 33 A) that as the concentration of alginate decreases; the transmittance value of the samples increases. For the lowest concentration of 0.015%, the transmittance is similar to the transmittance of re-distilled water. In the photographs in Figure 32, suspended white structures are visible in the solutions, the number of which decreases with decreasing alginate concentration. The same structures are also visible in the solution without FAS (Figure 32 H), which indicates that the precipitated compound is not iron alginate, but most likely alginic acid. In an environment with a pH value below about 3.6 [168,169], the carboxyl groups of alginate protonate, and then hydrogen bonds are formed between the hydrogens of the carboxyl groups, which leads to the formation and precipitation of a physical gel. To avoid the formation of alginic acid, the pH of the

solutions should be increased by reducing the concentration of sulphuric acid. It should be noted, however, that the addition of acid not only increases the efficiency of the radiation oxidation of ferrous ions [170] but also inhibits the oxidation of ferrous ions by oxygen present in the solution [171]. When 0.1 mM XO was added to a solution of 0.5% alginate and 1 mM FAS, without sulphuric acid, the initial orange colour of the solution changed to purple (indicating oxidation of the iron present in the solution) within about 3 min (Figure 33 E). However, as can be seen in Figures 15 and 16, the oxidized iron compounds did not precipitate from the FAS solution in redistilled water (pH= 5.77) until 24 h after preparation. According to the literature, the presence of Fe^{3+} complexing anions in the solution significantly increases the oxidation rate of Fe^{2+} ions [172]. Xylenol orange added to Fricke solutions is a complexing agent for ferric ions, hence the decision was made not to add the dye to the dosimeters containing nano-, micro-gels. It should be noted that removing the dye makes it impossible to read the dose distribution using optical methods (current 3D optical computed tomography scanners), although it should still be possible to read using nuclear magnetic resonance (1D) and magnetic resonance imaging (3D).



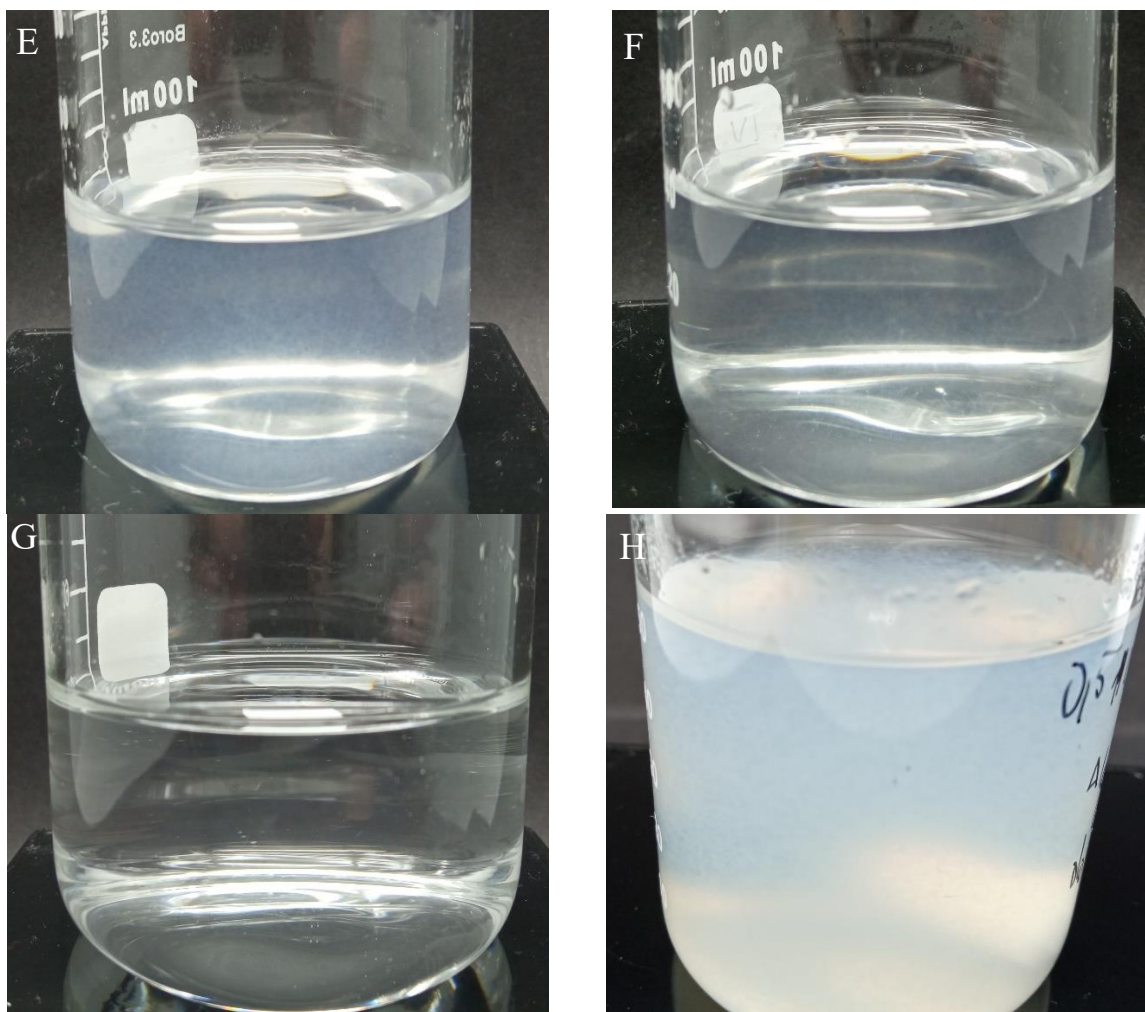


Figure 32. Nano- and micro-gels as prepared through the reaction of sodium alginate with the Fricke solution (FAS and sulphuric acid added to sodium alginate solution), for sodium alginate concentrations: 0.65% (A), 0.5% (B), 0.25% (C), 0.15% (D), 0.1% (E), 0.05% (F), 0.015% (G), and 0.5% without FAS added (H).

For the next attempt to obtain nano-, micro-gels, 0.1-0.6% sodium alginate Heppe, 1 mM FAS and 1-3 mM sulphuric acid were used. The concentrations were selected so that the pH of the solutions was in the range of 3.9-4.2 to significantly reduce the degree of protonation of the carboxyl groups of alginate while increasing the rate of autoxidation of Fe^{2+} ions as little as possible. After preparing the solutions, their transmittance was measured (Figure 34 A), and in addition, within 360 hours of preparation, measurements of the hydrodynamic diameters of the micro-gels were carried out using DLS (Figure 34 B). Cuvettes with FAS and alginate solutions are presented in Figure 34 C-E. The transmittance of all solutions increased significantly compared to samples containing 50 mM sulphuric acid (Figure 33 A), and no precipitated compounds were observed with the naked eye in fresh solutions (Figure 34 C). The influence of alginate concentration and storage time on the diameters of structures present in solutions cannot be determined based on DLS measurements. The obtained results are arranged in a chaotic manner, which may be due to the presence of air bubbles formed while vigorous mixing the solution during addition of FAS and sulphuric acid to alginate. The microscopic photograph of the sample containing 0.5% alginate shows many structures suspended in the solution (Figure 34F). The yellow color of the visible structures suggests the presence of iron bound to alginate, but further studies (e.g. analysis using a transmission electron microscope (TEM)) would be necessary to confirm this.

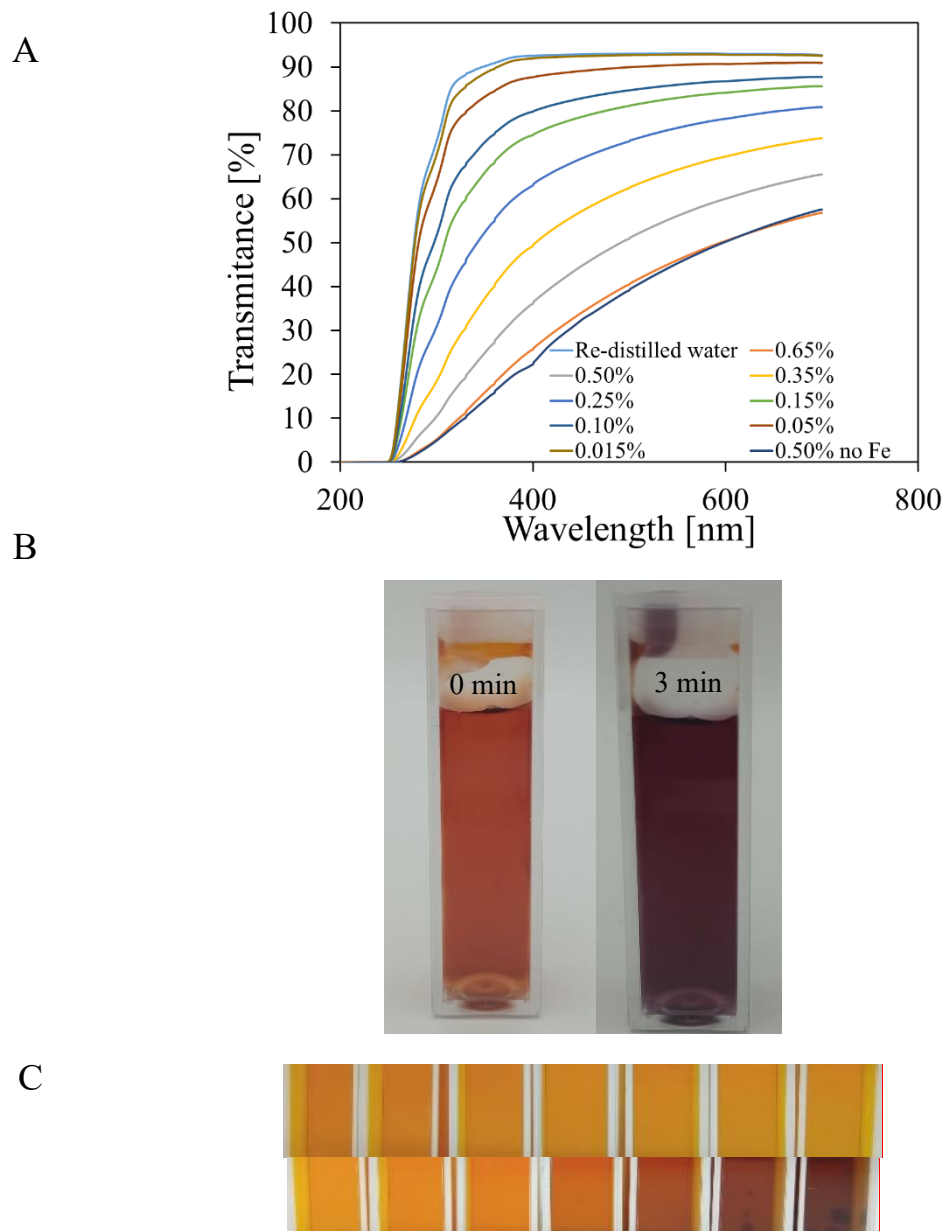


Figure 33. In **A** the transmittance spectra for the micro-gel solution made of 0.65–0.015% alginate solutions and re-distilled water are shown. In **B** photographs of a solution of 0.5% sodium alginate and 1 mM FAS, without sulphuric acid, taken immediately and 3 minutes after the addition of 0.1 mM XO are presented. In **C**, the photographs are presented for micro-gels in Pluronic F-127 matrix before (first line) and after irradiation (second line) for the doses of 0, 1, 2, 5, 10, 15, and 20 Gy.

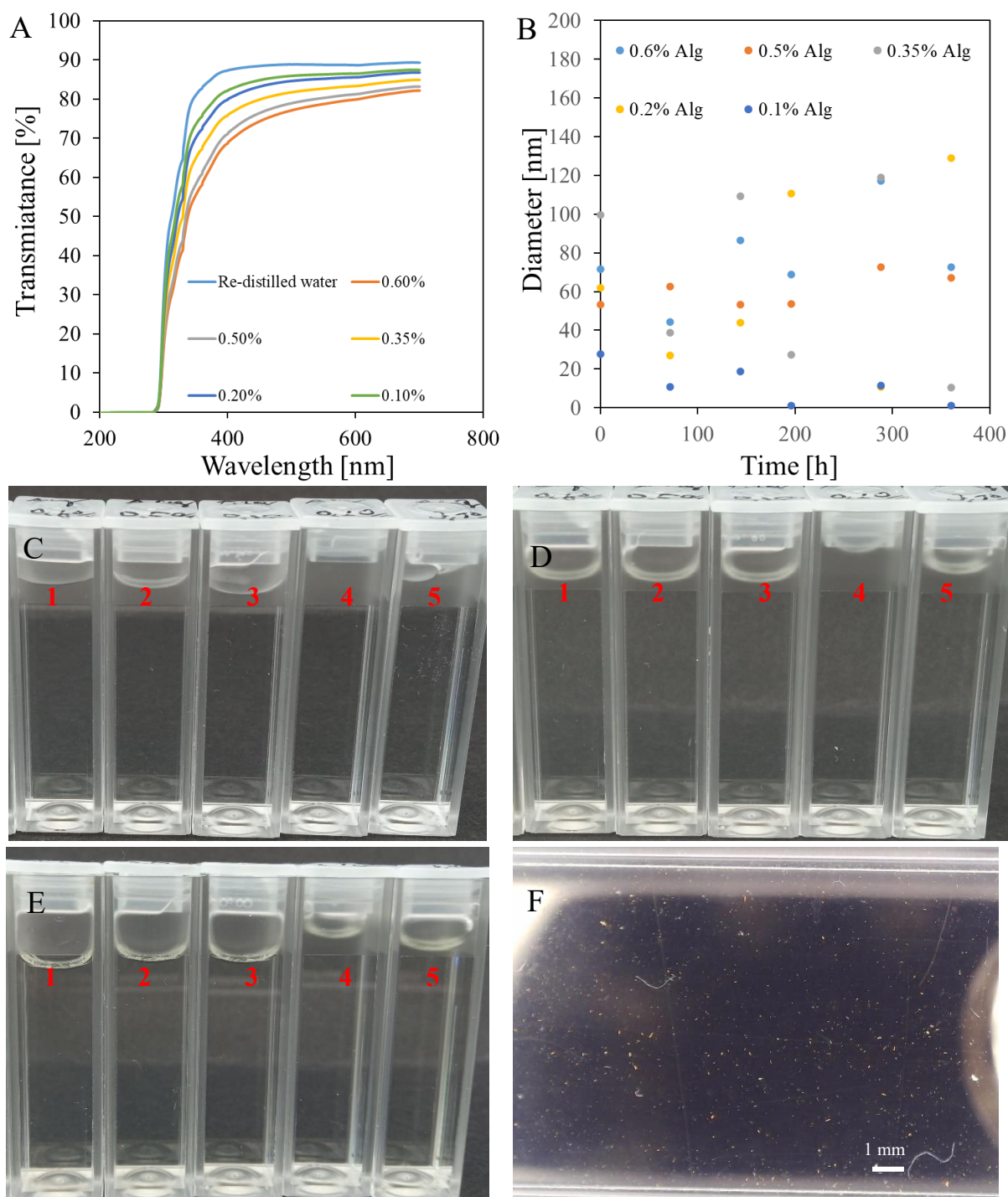


Figure 34. **A:** transmittance spectra of solutions of 0.1-0.6% sodium alginate Heppe, 1 mM FAS and 1-3 mM H_2SO_4 (pH of solutions in the range of 3.9-4.2). **B:** Hydrodynamic diameters of microstructures present in the tested solutions over time. **C, D and E:** photos of cuvettes with tested solutions taken immediately after preparation (**C**) and 7 (**D**) and 14 (**E**) days after preparation, respectively. The numbers 1 to 5 indicate the following concentrations of sodium alginate in solution: 0.6% (1), 0.5% (2), 0.35% (3), 0.2% (4), 0.1% (5). **F:** microscopic photo of 0.5% sodium alginate solution taken 17 days after preparation of the solution.

The effect of radiation on the formation of nano-, micro-gels was studied by irradiating solutions of 0.5% sodium alginate (both medium viscosity Heppe and low viscosity Sigma were tested) and 2 mM FAS. Two variants of solutions were prepared, differing in the content of sulphuric acid. In one variant,

2 mM H₂SO₄ was added (pH of solutions about 3.9), in the other no acid was added (pH about 5.7). About 1 hour passed from the preparation of solutions to irradiation, and the assessment of the formed structures was carried out by taking microscopic photographs one hour after irradiation. The obtained images were almost identical as photo in [Figure 34 F](#). All samples contained suspended structures. This may indicate rapid oxidation of Fe²⁺ ions and the formation of ferric alginate structures. It should be noted that sodium alginate contains up to about 40% of ash, which is an inorganic salt found in algae from which the polymer [173] was produced. Among the salts there may be copper compounds [174], which even in trace amounts is a catalyst for the oxidation of Fe²⁺ ions [172], as well as other metals that can bind with alginate, which can lead to the formation of microstructures. Further studies are necessary to better understand all the processes occurring in the tested solutions. However, taking into account the multitude of complications related to the use of alginate in the Fricke dosimeter, such as the mutually exclusive optimal pH conditions for sodium alginate and the Fricke solution, the effect of ash contained in alginates on the rate of autooxidation of Fe²⁺ ions and the need to remove the dye from the dosimeter composition, it is suggested to investigate other polymers capable of binding ferric ions. A modification of the capsules by incorporation of other Fe ions binding polymers in their structure would be an option as well.

The effect of the presence of a microgel on the response of the Fricke dosimeter to ionizing radiation was checked by irradiating (0-20 Gy) a composition containing 0.015% sodium alginate, 1 mM FAS, 50 mM sulphuric acid and 0.165 mM XO. The photographs of irradiated samples ([Figure 33 C](#)) show that the irradiation is accompanied by a dose-dependent colour change. A characteristic feature of some samples is the appearance of macrostructures (aggregates) with a clearly darker colour than the rest of the sample. The number of structures is the greatest for the highest doses. No such observations were seen immediately after irradiation. Possibly, the gels turned into a sol during transport, which facilitated aggregation. Due to the formation of alginic acid and the presence of competing XO, only a small part of the Fe³⁺ ions is predicted to be bound to the alginate.

5.1.6. 1D capsule dosimeter

The use of alginate capsules containing a Fricke dosimeter solution was tested in a radiotherapy environment ([Figure 35 A, B](#)), in which a linear accelerator was used to emit X-rays for irradiation. The experiment aimed to evaluate the system's ability to make point measurements of radiation dose. Fricke-alginate capsules were embedded in Pluronic F-127 or gelatin gel matrices. The experimental results demonstrate the Fricke-alginate capsules' response to X-ray irradiation in the gel matrices, manifested by a change in color. Due to Fe²⁺ diffusion from the capsules, the surrounding area also changed color during irradiation ([Figure 35 C](#)). Cuvettes containing the capsules in the gel matrices were photographed, and the profiles passing through the capsules and their surroundings were analyzed ([Figure 35 E, F](#)). The results clearly show a decrease in the green channel value (RGB color model) after 20 Gy absorption, similar for both matrices. This system, consisting of cuvettes containing capsules with a Fricke dosimeter embedded in a gel matrix, shows promise for dosimetry applications. The experiment also revealed that the release of the Fricke solution from the capsules worsens their dose response and color change. Too low content of the Fricke solution in the capsules eliminates their use as dosimetry systems. In conclusion, the alginate capsules in the current design should be considered reservoirs for the Fricke solution; however, they require further chemical modifications to prevent leakage of Fricke components. Additionally, the effect of the matrix on the shape of the capsules was observed and is discussed below.

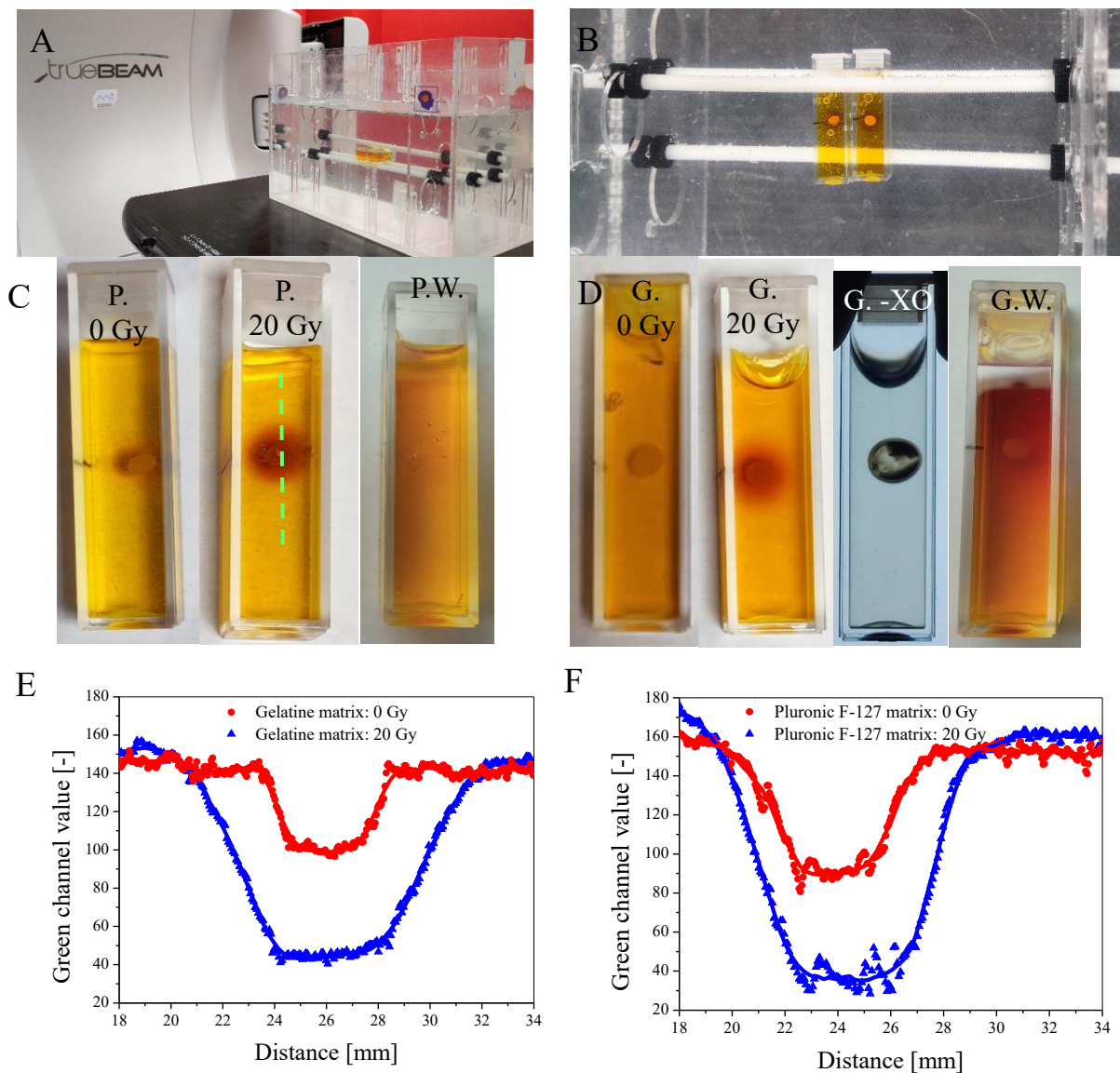
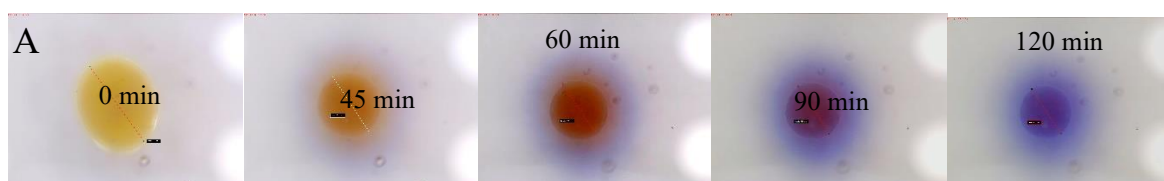


Figure 35. Response to irradiation of alginate capsules with Fricke solution in Pluronic F-127 or gelatine matrix. **A:** Irradiation set up. Samples in cuvettes of 4.7 cm height and 1 cm optical path are immersed in water (water phantom, W-1-DD1-2, GeVero Co.); the water phantom is on a bench of the TrueBeam accelerator (Varian). **B:** Top view of the samples in the water phantom. **C** and **D:** Samples before and after irradiation (20 Gy) for the dosimeters with Pluronic F-127 (**C**) and gelatine (**D**) matrix; in **D** a cuvette with gelatine matrix and capsule containing Fricke dosimeter without XO dye is also shown (G.-XO) for comparison. P. and G. denote Pluronic F-127 and gelatin, respectively; P.W. and G.W. denote Pluronic F-127 and gelatin matrices, respectively, with capsules that were washed (for 2 days) before immersion in the matrices and after irradiation (20 Gy). **E** and **F:** Profiles along the samples as indicated by green dashed line in **C**. The values are for the green channel of RGB color space.

Figures 36 and 37 illustrate the performance of alginate capsules containing Fricke dosimetric solution embedded in a Pluronic F-127 or gelatin matrix for up to 120 minutes. The capsules were prepared by dropping a sodium alginate solution into a Fricke solution containing 0–3.5% CaCl_2 . For the alginate capsules in Pluronic F-127 (Figure 36 A), three phenomena can be observed: (1) the capsules shrink over time, (2) the Fricke dosimeter components are released, and (3) the released components and the shrunk capsules change color due to the conversion of Fe^{2+} into Fe^{3+} which occurs faster outside the capsules as there was no acid added to the matrix. The shrinking process occurs dynamically just after

the capsules immersion in the Pluronic F-127 matrix and appears to stabilize after 120 minutes. Capsules without CaCl_2 are the least vulnerable to shrinking, while those with 2.5% CaCl_2 are the most vulnerable. The behavior of the alginate capsules differs greatly when embedded in a gelatin matrix (Figure 36 B, C). All capsules containing CaCl_2 shrink to a much lesser extent within the first 40 minutes than capsules embedded in Pluronic F-127. They then stabilize up to about 60 minutes and swell and stabilize between 110 and 120 minutes. Exceptional behavior was observed for the capsule without CaCl_2 (Figure 36 C): it significantly swelled throughout the entire measurement time. This behavior is most likely associated with the type of polymer forming the matrices (non-ionic Pluronic F-127 and cationic gelatin), the interactions between the capsule components and the matrices, and the ionic strength of the matrices and capsules. The latter was taken into consideration. In this respect, the capsules were introduced into a Pluronic F-127 or gelatine gel matrix to which 0 to 0.5 mM NaCl was added. Increasing the ionic strength of the Pluronic matrix had no effect on the capsule shrinkage process, regardless of the concentration of added sodium chloride (Figure 37 C). The capsules immersed in the gelatine matrix with the addition of NaCl shrank for the first 40 minutes after introduction into the gel (Figure 37 D). After this time, they reached their minimum diameter, and after another 20 minutes they began to increase their diameter. This is a different behaviour than the capsules embedded in gelatine without salt, which also shrank for the first 40 minutes, but after reaching the minimum diameter, it did not change further. The observations made indicate that increasing the ionic strength of the matrix did not overcome the phenomenon of changes in the capsule diameter during storage in the gel. An alternative attempt to stop the shrinkage of the capsules was to create a shell around them. For this purpose, the capsules were immersed in a 0.1% solution of poly-L-lysine for 0 to 10 minutes. Then the capsules were introduced into a gel matrix. Regardless of the time of immersion in poly-L-lysine, covering the capsules did not stop their shrinkage in the gel matrix (Figure 37 A, B). In this respect and considering the diffusion of Fricke components for the capsules discussed above, other ionic polymers should be tested in the future to improve the performance of the capsules. For instance, introduction of poly(vinyl alcohol) and poly(dimethylsiloxane) may be one such possibility, as presented elsewhere [175]. In this work, Zhang et. al developed capsules (pellets) made of PVA with Fricke's solution, which were additionally coated with poly(dimethylsiloxane) (Sylgard 184). The obtained capsules with an average diameter of 2.57 mm were characterized by good mechanical strength. Moreover, after placing in a gel matrix (PVA), no changes in the size of pellets or diffusion of dosimeter components outside the capsules were observed. In turn, however, a significant disadvantage of the proposed solution is the complex process of obtaining capsules, which consists of dripping the PVA solution from Fricke into liquid nitrogen (-196°C), repeating the process of freezing (-20°C) and thawing (25°C) of the pellets three times, and then covering them with Sylgard by immersing them in degassed poly(dimethylsiloxane) heated to 50°C in a semi-cured state. In the future, it should be attempted to coat alginate macrocapsules with Sylgard. If this modification stops capsule shrinkage while preventing the diffusion of dye and Fe ions, alginate macrocapsules with the active ingredients of the Fricke dosimeter will be easy to obtain, promising 1D dosimeters with good tissue equivalence.



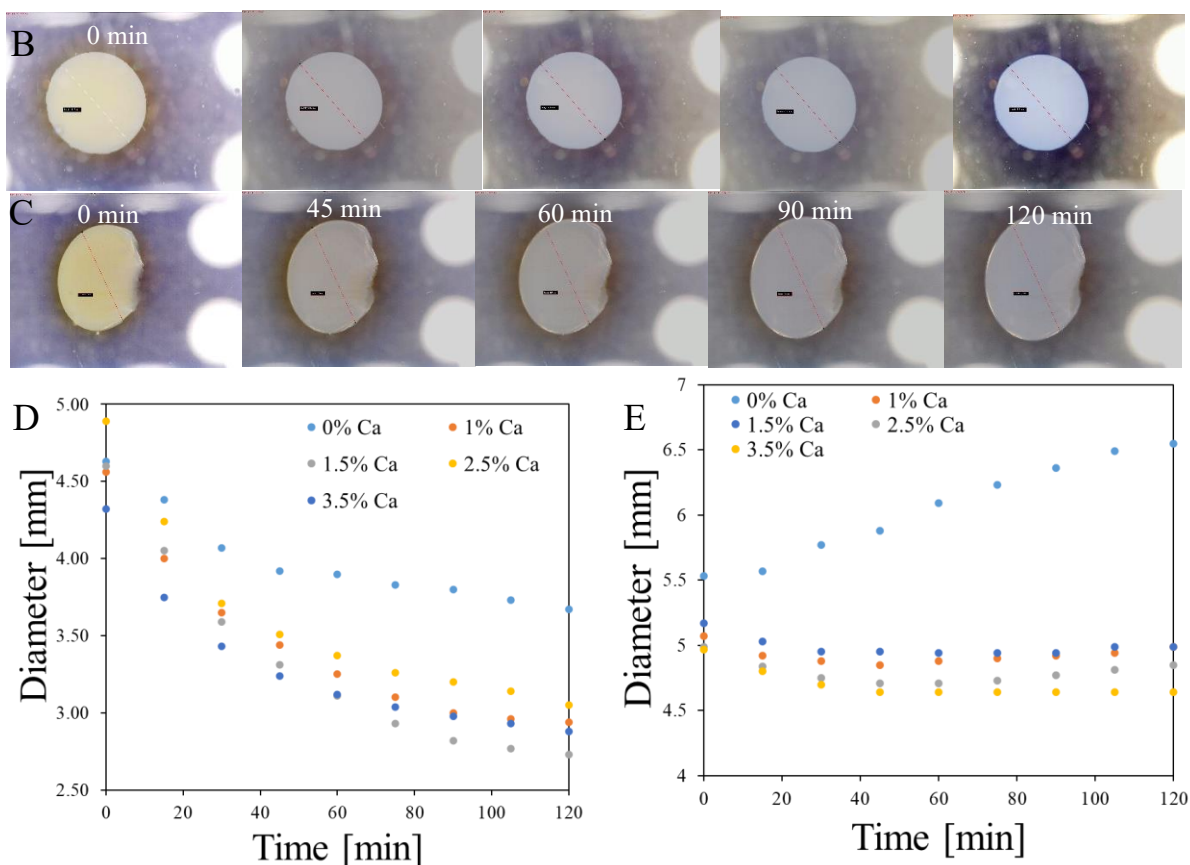
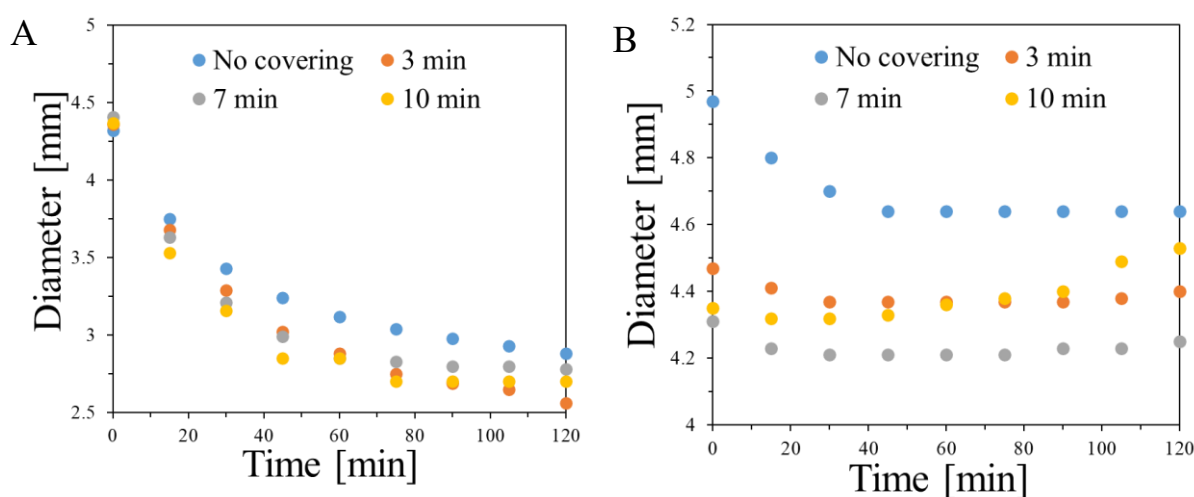


Figure 36 Performance of alginate capsules containing Fricke dosimeter embedded in Pluronic F-127 and gelatin matrices. **A:** Pluronic F-127 matrix, $c \text{ CaCl}_2 = 1.5\%$; **B:** Gelatin matrix, $c \text{ CaCl}_2 = 1.5\%$; **C:** Gelatin matrix, $c \text{ CaCl}_2 = 0\%$; **D,E:** Change of size of alginate capsule in Pluronic F-127 (**D**) and gelatine (**E**) matrix over time of storage at room temperature ($\sim 23^\circ \text{C}$). Capsules formed in reaction of 3.5% sodium alginate with Fricke solution: 1 mM FAS, 50 mM H₂SO₄, 0.165 mM XO containing 0–3.5% CaCl₂. Black bars in **A**, **B** and **C** denote the distance of 0.75 mm. Dashed lines indicate the positions where the diameter was measured.



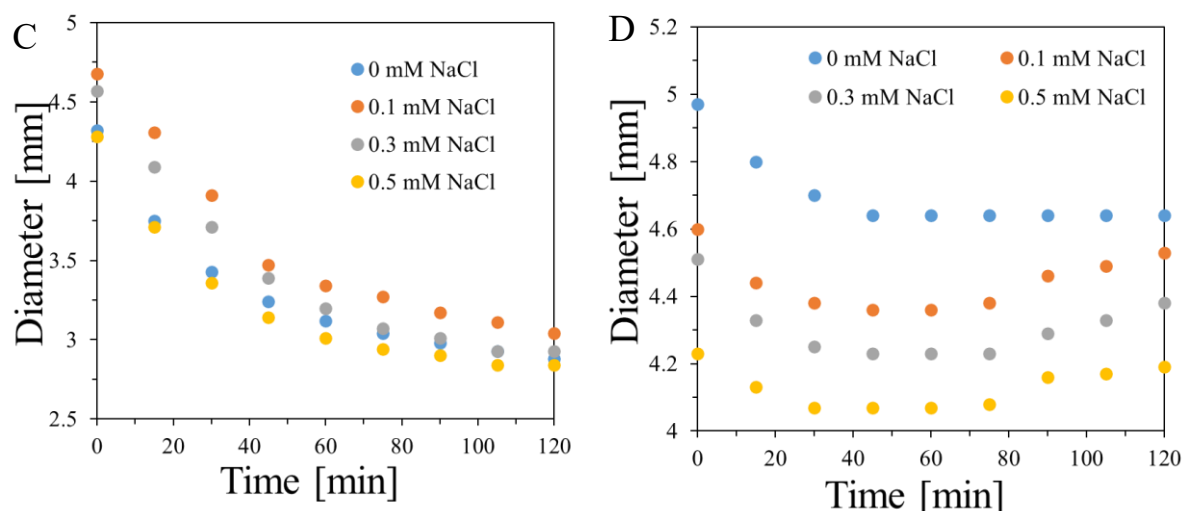


Figure 37 Performance of alginate capsules containing Fricke dosimeter embedded in Pluronic F-127 and gelatine matrices. **A** and **B** correspond to the capsules treated with poly-L-lysine and immersed in the Pluronic F-127 and gelatine matrices, respectively. **C** and **D** are for the capsules immersed in Pluronic F-127 (**C**) and gelatine matrices (**D**) at different ionic strength – concentrations of NaCl. Capsules formed in reaction of 3.5% sodium alginate with Fricke solution: 1 mM FAS, 50 mM H₂SO₄, 0.165 mM XO containing 3.5% CaCl₂

5.2. Characteristics of the Fricke-XO-Gelatin with sorbitol addition 2D dosimeter

This part of the work presents a modification of the Fricke-XO-Gelatin dosimeter by the addition of sorbitol, an organic compound belonging to the group of sugar alcohols. Sorbitol is often added to gelatin products as a plasticizer. The purpose of the applied modification of the dosimeter is to improve the mechanical properties of the gelatin matrix and, consequently, to obtain a two-dimensional flexible dosimeter. In this part of the work, the influence of sorbitol on the thermal and mechanical properties of the dosimeter was investigated. The DSC technique was used for thermal analysis, which consisted in determining the phase transition temperature of the system, while the mechanical tests examined the material's compressive strength and fatigue strength. In addition, the chemical stability of the dosimeter was determined organoleptically and spectrophotometrically, depending on the storage method. The following three applications of the modified gel were proposed:

1. a dosimeter in a plastic container to perform a coincidence test of the radiation and mechanical isocenter of the medical accelerator
2. a thick dosimeter acting simultaneously as a bolus. The bolus is a material placed on a patient surface to increase the dose during irradiation of the skin or tissues located at a shallow depth. Dosimeter that is also a bolus can be used in *in vivo* measurements
3. a thin dosimeter to determine the dose distribution on the patient's skin. During skin irradiation, a thin dosimeter could be placed between the patient and the bolus. Due to its small thickness, the dose distribution measured with this dosimeter would be almost identical to the dose distribution on the skin.

Part of the results described in this section have been published [176]. The remaining results are described in a manuscript submitted on June 3, 2025, which is currently at the review stage [177].

5.2.1. Impact of sorbitol addition on the thermal properties of the dosimeter

Thermograms for the Fricke-XO-Gelatin dosimeter with sorbitol that were obtained using DSC are shown in Figure 38 A. The formation of solid gels from gelatin solutions upon cooling is due to the formation of hydrogen bonds between the chains' molecules [178]. The gel of 8% gelatin melts at approximately 34.8 °C (the peak transition temperature). Following the incorporation of Fricke's solution into a gelatin matrix, a decrease in the phase transition temperature of approximately 3°C is observed upon heating. Despite the negligible alteration in the gelatin concentration (~0.49%), the decline in the phase transition temperature can be attributed to the low pH (approximately 1.4) of the Fricke solution, which contains sulphuric acid. In an environment with a high acidity level, gelatin undergoes a process known as partial hydrolysis. This chemical reaction results in a reduction in the strength of the gel and, consequently, a decrease in the sol-gel transition temperature [178,179]. The incorporation of sorbitol has been shown to result in an increase in the phase transition temperature of both plain gelatin and gelatin with Fricke solution, with an approximate increase of 0.7 °C and 1.5 °C, respectively. The presence of a high concentration of sorbitol in gelatin has been shown to increase its melting point by stabilizing its structure [179]. In the system with Fricke solution, the presence of sorbitol has been shown to exert a protective effect on gelatin structure by forming additional sorbitol-gelatin and sorbitol-sorbitol bonds. These substances may undergo hydrolysis prior to the rupture of gelatin-gelatin hydrogen bonds [178]. However, when the pH is sufficiently low, the protective effect of sorbitol may be inadequate. This can result in the destruction of hydrogen bonds between gelatin polypeptide chains and, ultimately, the hydrolysis of these macromolecules. The phase transition temperature of the dosimeter with sorbitol decreased by approximately 1.2 °C over a period of 12 days (Figure 38 B). After this time, the sol-gel transition temperature stabilizes at approximately 32.1 °C, which is about 0.3 °C higher than the melting temperature of the dosimeter without sorbitol after just four hours following preparation (Figure 38 A). This finding suggests that the incorporation of sorbitol leads to a modest enhancement in the thermal properties of the Fricke-XO-Gelatin dosimeter.

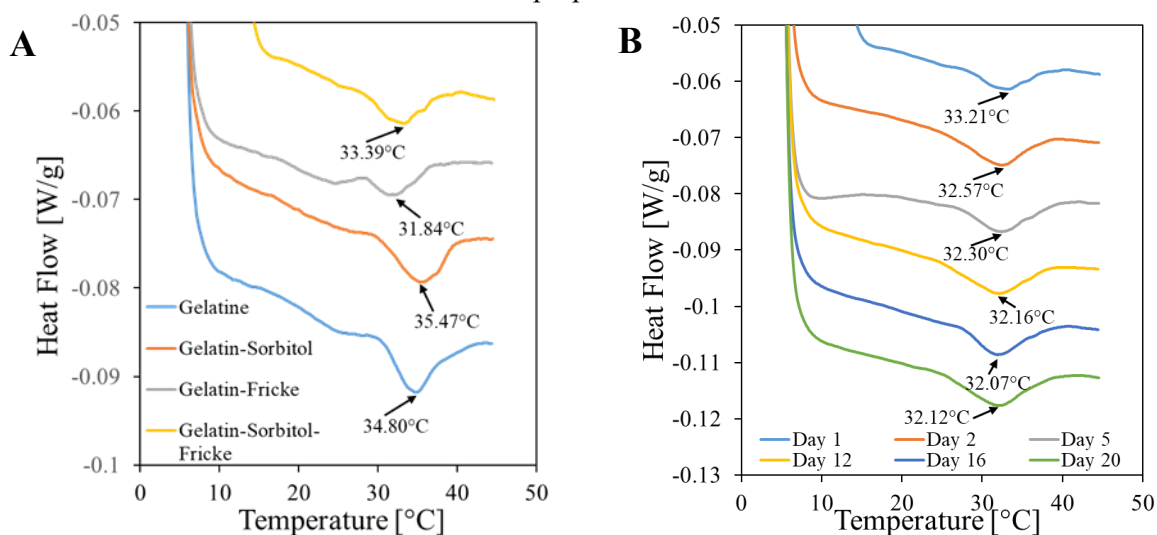
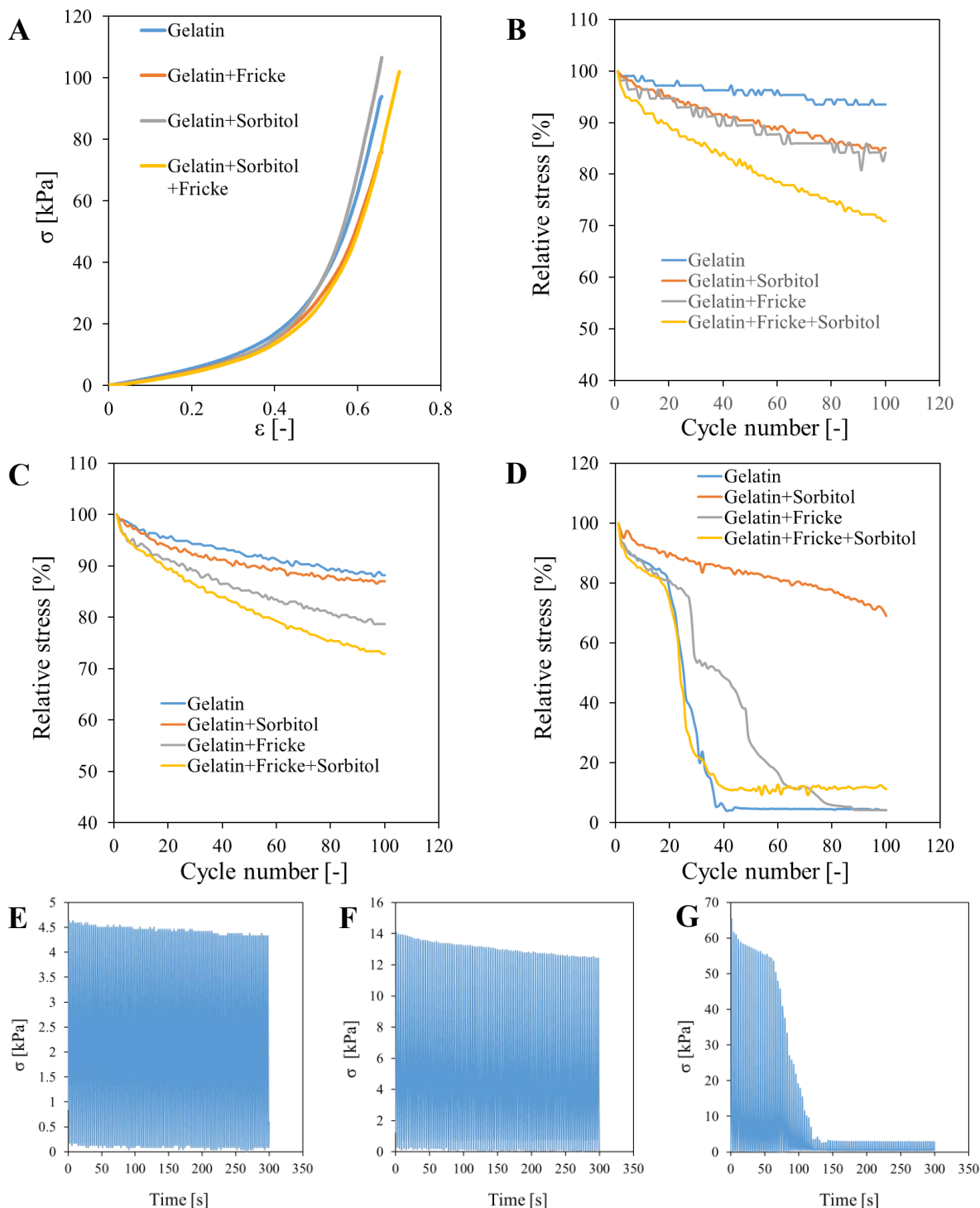


Figure. 38 A: Thermograms obtained for the first heating of 8% gelatin samples, 7.96% gelatin with Fricke, 6% gelatin with Fricke and 23% sorbitol, 5.99% gelatin with 23% sorbitol. The concentrations of the Fricke solution components in the samples were 50 mM H₂SO₄, 0.5 mM FAS, 0.165 mM XO. Measurements were performed 4 h after preparation. **B:** Thermograms for the first heating of gelatin with sorbitol and Fricke samples obtained at the following times from sample preparation: 1, 2, 5, 12, 16, and 20 days.

5.2.2. Impact of sorbitol addition on the mechanical properties of the dosimeter

The representative stress-strain characteristics of the tested materials are presented in [Figure 39 A](#). The dependence of relative stress (σ_{rel} [%])—defined as the percentage ratio of the stress at maximum deformation after n compression cycles (n being a natural number from 1 to 100) to the stress at maximum deformation after the first cycle—is demonstrated in [Figure 39 B–D](#) for various strains (20–60%). Furthermore, the temporal dependence of stress is illustrated in [Figure 39 E–G](#). The mean values of Young's modulus, deformation at break, and compressive strength of the tested gels are outlined in [Table 7](#). As demonstrated in [Figure 39 A](#), the stress-strain characteristics of the gelatin-based gels manifest a nonlinear mechanical response, with stress increasing gradually at low strain and sharply rising beyond a strain of 0.4. Both sorbitol and Fricke's solution significantly influence the mechanical properties of gelatin, albeit in divergent manners. Sorbitol has been demonstrated to enhance the gel's compressive strength while concurrently reducing Young's modulus and increasing deformation at break, particularly under high-strain conditions. This phenomenon is attributed to sorbitol's role in plasticizing the material, which disrupts hydrogen bonding between gelatin macroparticles, thereby increasing polymer chain mobility and, consequently, reducing material stiffness [180,181]. Conversely, the incorporation of Fricke's solution has been observed to diminish the gel's compressive strength, an effect that is most evident in samples devoid of sorbitol. Furthermore, Fricke's solution has been shown to reduce Young's modulus and slightly augment deformation at break. At elevated strain levels, all specimens exhibited strain hardening, a phenomenon characterized by a rapid increase in stress prior to failure. These findings highlight the interplay between sorbitol and Fricke's solution in modulating the mechanical behavior of gelatin-based gels, balancing strength, flexibility, and stiffness. During the course of fatigue tests, the incorporation of sorbitol resulted in a noticeable increase in the stress drop at maximum deformation when the samples were compressed by 20%. This finding indicates that sorbitol enhances the material's plasticity, enabling it to accommodate cyclic deformation with enhanced structural adaptability. At a compression level of 40%, the stress drop observed between the gelatin and gelatin-sorbitol samples became comparable, indicating that at moderate deformation levels, both materials exhibited similar mechanical responses. However, under 60% compression, a significant difference was observed: pure gelatin fractured after only 18 cycles, while the gelatin-sorbitol sample remained intact throughout the entire test duration. This finding suggests that sorbitol enhances the material's resistance to cyclic loading, likely due to its plasticizing effect, which facilitates the mobility of gelatin chains. The enhanced chain mobility enables the gel to undergo reorganization under cyclic compression, thereby postponing the occurrence of structural failure. In contrast, the rigid hydrogen-bonded network present in pure gelatin exhibits a lack of flexibility, resulting in progressive bond breakage and eventual material failure under sustained high-strain conditions. The presence of Fricke's solution led to a substantial reduction in stress at maximum strain across all tested compression levels in both gelatin and gelatin-sorbitol samples. The effect was particularly pronounced at 60% strain, where both gels containing Fricke's solution exhibited rapid failure. Gelatin broke after 22 cycles, while gelatin-sorbitol broke after 17 cycles. The initial failure of the gelatin-sorbitol specimen in this case indicates that, under typical conditions, sorbitol offers mechanical reinforcement but is inadequate to protect the gel structure in a highly acidic environment. This behavior is consistent with prior observations on the impact of Fricke's solution on gelatin's mechanical properties. At low pH, the solution hydrolyzes hydrogen bonds between polypeptide chains, thereby weakening the overall gel structure. While sorbitol has been demonstrated to stabilize intermolecular interactions to a certain degree, its protective effect is inadequate to counteract the degradation induced by acid hydrolysis. In light of these findings, it is crucial to consider strategies that mitigate the detrimental effects of acidity on the mechanical properties of gelatin-based gels. One potential approach involves the utilization of alternative radiation-sensitive components, such as tetrazolium salts [160], which may offer comparable

dosimetric properties without compromising gel stability. Furthermore, given that bolus materials should ideally exhibit a Young's modulus comparable to human soft tissue (ranging from 10^4 to 10^9 Pa) [182], the Fricke-XO-Gelatin with sorbitol formulation falls within this range but is positioned near the lower limit. This finding indicates that, while the material exhibits residual elasticity, further optimization may be necessary to enhance its mechanical robustness. Furthermore, the gel's low pH could pose challenges for direct application on human skin, potentially leading to irritation or discomfort. To address these concerns, it is necessary to explore packaging solutions or additional structural modifications that improve both the mechanical durability and biocompatibility of the bolus material.



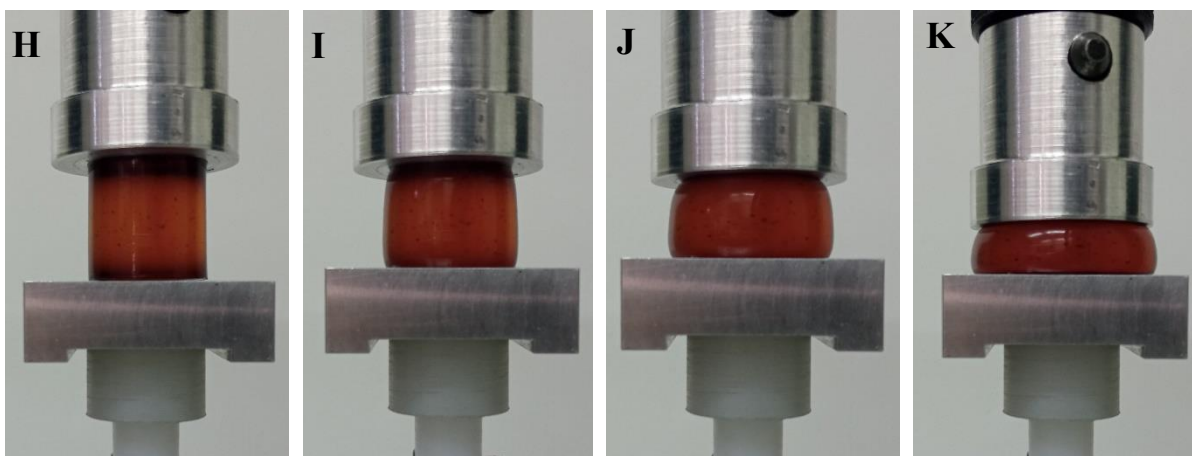


Figure 39. A: Example compression stress-strain (stress: \square [Pa], strain: \square [-]) characteristics of 8% gelatin, 6% gelatin with 23% sorbitol, 7.96% gelatin with Fricke and 5.99% gelatin with 23% sorbitol and Fricke. The concentrations of the Fricke solution components in the samples were 50 mM H_2SO_4 , 0.5 mM FAS, 0.165 mM XO. Measurements were performed 24 h after preparation. The dependence of relative stress as a function of compression cycle number is shown in B (20% strain), C (40% strain) and D (60% strain). Example stress as a function of time for gelatin is shown in E (20% strain), F (40% strain) and G (60% strain). H, I, J and K present the shape of Fricke-XO-Gelatin with sorbitol deformed by 0, 20, 40 and 60%, respectively.

Table 7. The mean values of Young's modulus ($E=s/e$, where s denotes stress and e denotes strain), deformation at break and compressive strength of the tested Fricke-XO-Gelatin with sorbitol gels. The samples tested were 8% gelatin, 6% gelatin with 23% sorbitol, 7.96% gelatin with Fricke and 5.99% gelatin with Fricke and 23% sorbitol. The concentrations of the Fricke solution components in the samples were 50 mM H_2SO_4 , 0.5 mM FAS, 0.165 mM XO. Measurements were performed 24 h after preparation.

Sample	Compression test		
	Young Modulus [kPa]	Deformation at break [-]	Compressive strength [kPa]
Gelatin	24.9±0.97	0.64±0.014	87.9±4.6
Gelatin+Sorbitol	19.5±0.59	0.67±0.011	108.1±3.8
Gelatin+Fricke	21.1±0.47	0.66±0.003	70.5±4.7
Gelatin+Sorbitol+Fricke	20.5±2.81	0.71±0.017	107.1±15.1

5.2.3. Chemical stability of the dosimeter

The chemical stability of Fricke-XO-gelatin with sorbitol was evaluated based on samples stored under different conditions (see Section 4.2.5). Photographs were taken (Figure 40) and measurements were made using a UV-Vis spectrophotometer (Figure 41). The dosimeter stored on the laboratory table (marked as 1 in Figure 40) darkened significantly to brown after only 24 hours of storage (Figure 40 B). After another 24 hours, the sample had lightened to orange (Figure 40 C) and continued to lighten over time, changing color to yellow (Figure 40 D). These changes result from the sample absorbing too high a dose of UV radiation [183]. The dosimeter stored in the cabinet (marked 2) retained its initial color for 48 hours after preparation (Figures 40 A–C). After 144 hours of storage, the gel darkened to a dark orange color (Figure 40 D). The sample continued to darken over time. After 216 hours, the dosimeter turned brown (Figure 40 E). After four weeks, it turned purple (Figure 40 G), indicating the complete oxidation of the ferrous ions present in the dosimeter. The refrigerated sample (marked 3) did not visibly change color within two weeks after preparation (Figures 40 A–F). After one month, the gel darkened to an orange color that persisted until the end of the six-week observation period (Figure 40 H).

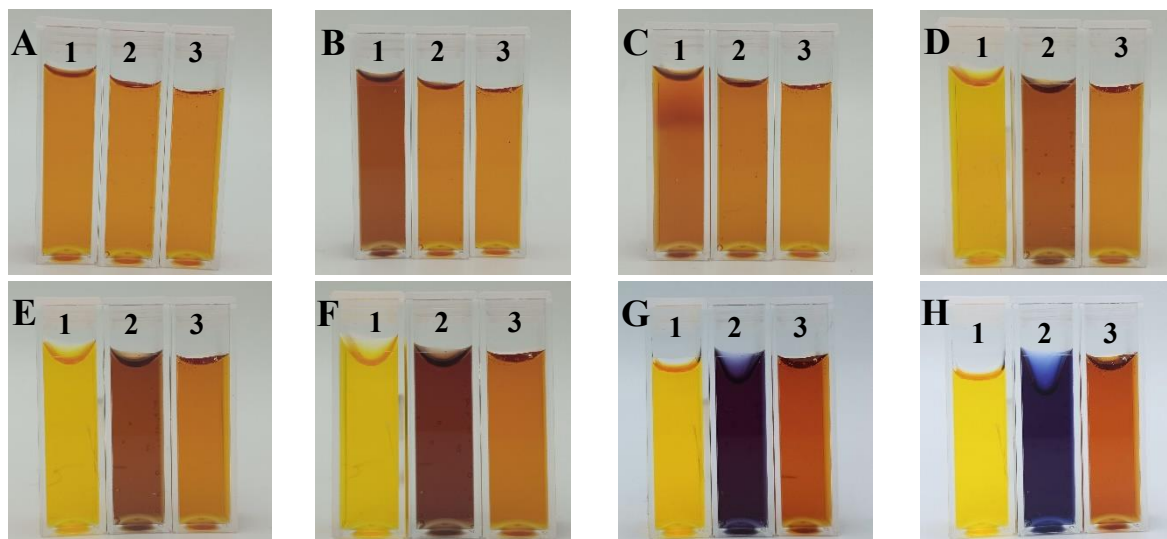


Figure 40. Photographs of Fricke-XO-Gelatin with sorbitol samples stored under different conditions. The numbers on the top of the cuvettes indicate storage conditions (1: table, room temperature (approximately 25 °C), light access; 2: cabinet, room temperature, no light access; 3: refrigerator, temperature approximately 4 °C, no light access). Photographs were taken at the following times from preparation: 0 h (A), 24 h (B), 48 h (C), 144 h (D), 216 h (E), 2 weeks (F), 4 weeks (G), and 6 weeks (H).

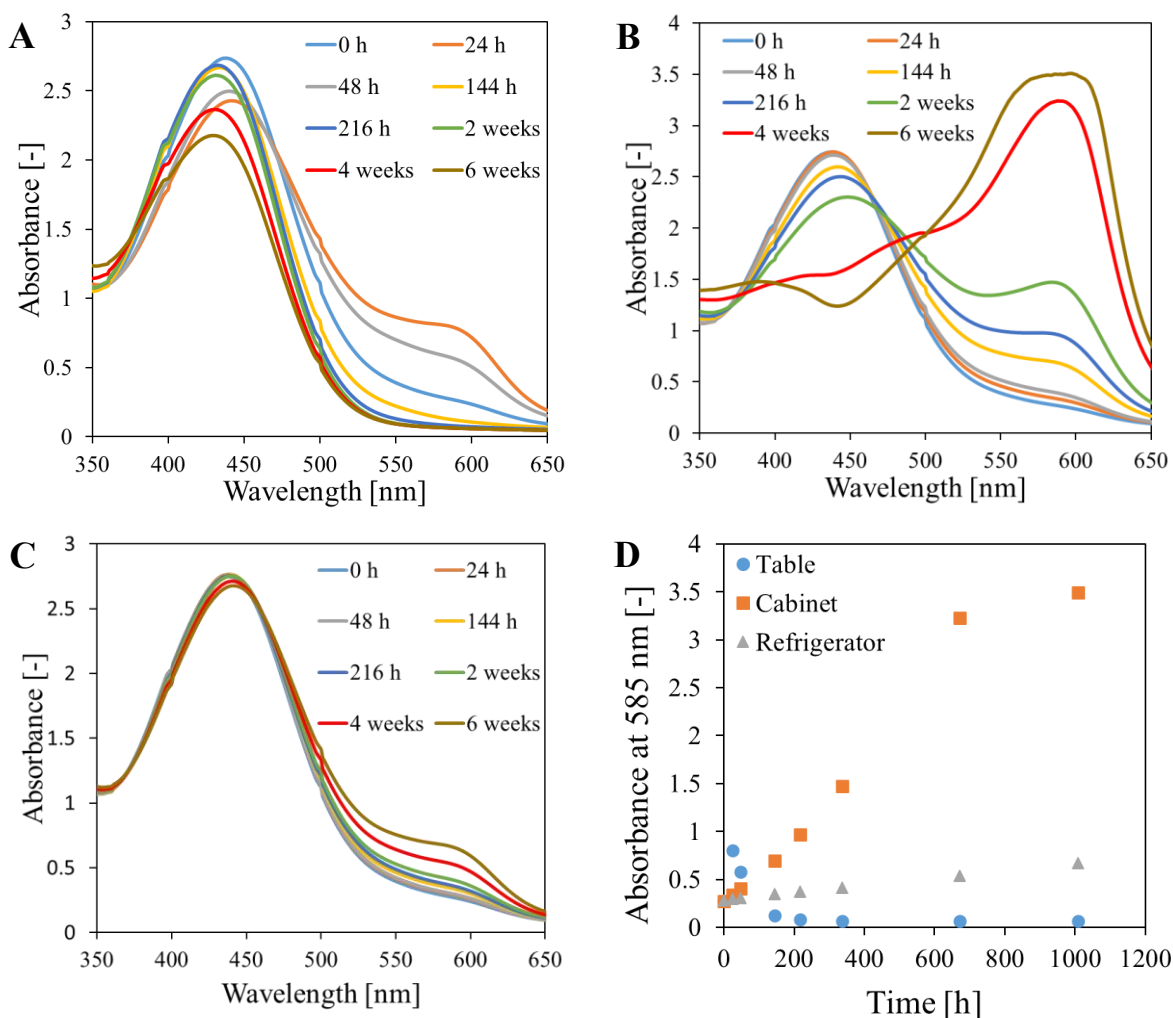


Figure 41. Absorption spectra of the Fricke-XO-Gelatin with sorbitol dosimeter stored under the following conditions: table, room temperature (approximately 25 °C), access to light (**A**); cabinet, room temperature, no access to light (**B**); refrigerator, temperature approximately 4 °C, no access to light (**C**). The change in the absorbance value at 585 nm during storage of the dosimeter is shown in **D**.

Spectrophotometric measurements (Figure 41) revealed that the absorption spectra of the samples consist of two bands in the wavelength range of approximately 350-525 nm and 525-650 nm. The spectra change during storage of the samples. For the sample stored on the table (Figure 41 A), these changes correspond to the observations made based on the photographs (Figure 40, sample 1). The spectra show a distinct darkening of the sample as an increase in the absorption maximum at 585 nm and a simultaneous decrease in the absorption maximum at 440 nm. During storage, absorption maximum decreases at 585 nm, and the absorption maximum shifts hypsochromically to 430 nm. This is visible in the photographs as a change in the gel's color from orange to yellow. The spectra (Figure 41 B, sample 2) show the gradual darkening and color change from orange to purple observed for the dosimeter stored in the cabinet as an increase in the absorption maximum at 585 nm and a simultaneous decrease in the maximum at 440 nm. No color changes were observed in the pictures of the sample stored in the refrigerator (Figure 40, sample 3) within two weeks of preparation. However, within 14 days of storage, a slight increase in the absorption maximum at 585 nm is visible in the spectra (Figure 41 C). The absorption maximum at 440 nm barely changed during this time. The increase in the absorption maximum after four and six weeks is less significant compared to the changes in the samples stored on the table and in the cabinet (Figure 41 D). The experiment indicated that Fricke-XO-Gelatin dosimeters with sorbitol should be stored in the refrigerator. Even under optimal storage conditions, changes related to the oxidation of ferrous ions occur in the gel, but these are negligible enough to successfully use the dosimeter (stored in the refrigerator for several weeks) in applications, for example, for dose distribution measurements or for performing a coincidence test of radiation and mechanical isocenter of a medical accelerator. For this purpose, before performing measurements, the dosimeter should be calibrated using a gel with the same storage history as the one used for the measurements.

5.2.4. Application of the two-dimensional Fricke dosimeter

5.2.4.1. Dosimeter response to ionizing radiation

A potential application of the two-dimensional Fricke-XO-Gelatin with sorbitol dosimeter is to perform a coincidence test of the radiation isocenter (the central point of the smallest sphere through which all central axes of the photon beam pass for any angular settings of the arm, collimator, and table of the medical accelerator [184]) and the mechanical isocenter (defined as the intersection of the rotation axes of the collimator, couch, and gantry [185]) of the medical accelerator. Determining the radiation isocenter involves calculating its radius and distance from the mechanical isocenter. The measurement system for performing the test consisted of the Fricke-XO-Gelatin with sorbitol gel dosimeter in a cuboidal PMMA container (section 4.2.2.), an HP Scanjet G3010 flat-bed type scanner (section 4.2.7.), and the polyGeVero-CT software package (4.2.7.). The studies were also conducted using the Fricke-XO-Pluronic F-127 dosimeter and the results obtained using both tested dosimeters were compared.

Before the coincidence test, the irradiation parameters were optimized in terms of the irradiated field width and MUs values. The MUs values were optimized by irradiating eight areas of each of the tested dosimeters with different Monitor Units while the gap of the HD MLC was set to 5 mm (section 4.2.6).

The samples were then scanned within 24 h after irradiation. The scans obtained are presented in [Figures 42 and 43](#). The irradiated areas of both dosimeters changed color from initially yellow to dark blue and purple for each MU value. Over time, the irradiated stripes became wider and blurrier due to the diffusion of Fe^{3+} ions. A purple color appeared on the edges of both dosimeters within two hours of irradiation, resulting from autooxidation of ferrous ions. Local autooxidation may result from the design of the container. The vessel walls are glued to the bottom with silicone glue. As a result of contact between the gel and the glue, accelerated oxidation of Fe^{2+} ions may occur. The resulting change of color in the Fricke-XO-Gelatin with sorbitol dosimeter is small and does not change over time, which does not affect the measurement. However, in the Fricke-XO-Pluronic F-127 sample, the area where the autooxidation occurs increases over time, which indicates lower chemical stability of this dosimeter composition compared to the gelatin gel. Due to the diffusion occurring in both samples, and in the case of the Fricke-XO-Pluronic F-127, also rapid autooxidation of the ferrous ions, the scanning of the dosimeters should take place as soon as possible after irradiation.

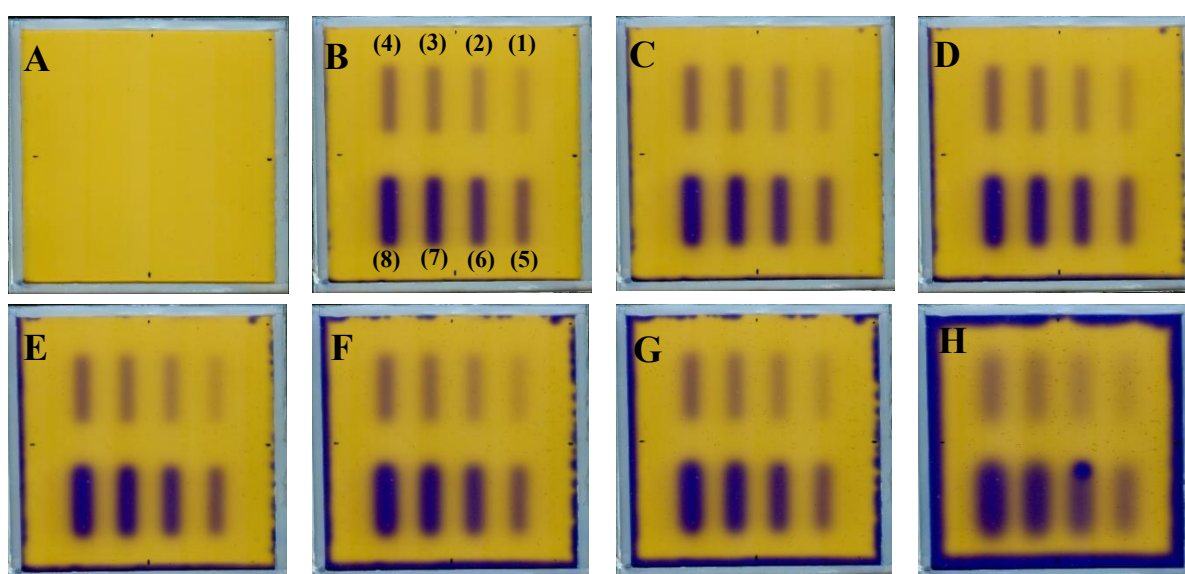
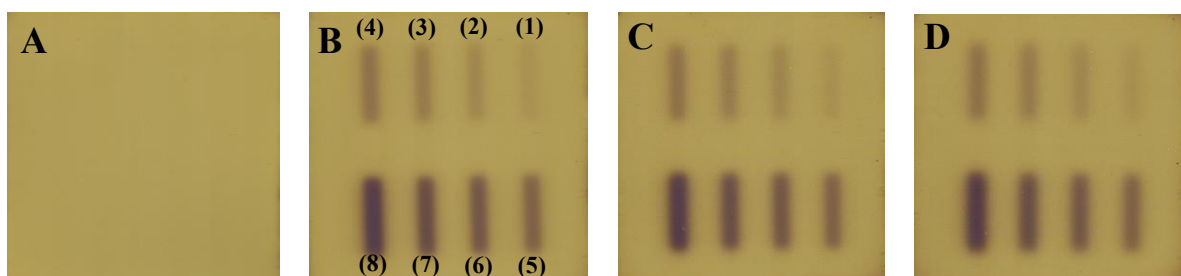


Figure 42. Response of the Fricke-Pluronic F-127 dosimeter to irradiation with the TrueBeam medical accelerator. (A) Sample just after preparation, **B-H**: the same sample after irradiation (time from preparation to irradiation equals 48 min) and scanned with an HP Scanjet G3010. The time after irradiation to scanning was 44 min (**B**), 109 min (**C**), 169 min (**D**), 209 min (**E**), 359 min (**F**), 419 min (**G**), and 1199 min (**H**). Irradiation pattern: $0.5 \times 4 \text{ cm}^2$ stripes. The stripes irradiated with 500 (1), 1000 (2), 1500 (3), 2000 (4), 2500 (5), 5000 (6), 7500 (7), and 10,000 (8) MUs, as shown in (**B**).



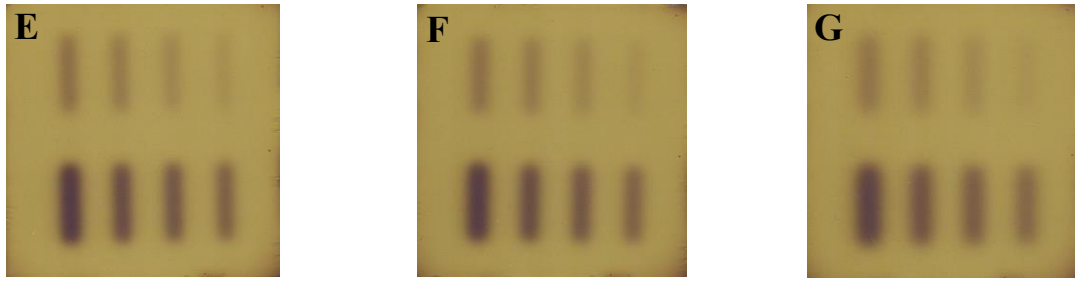
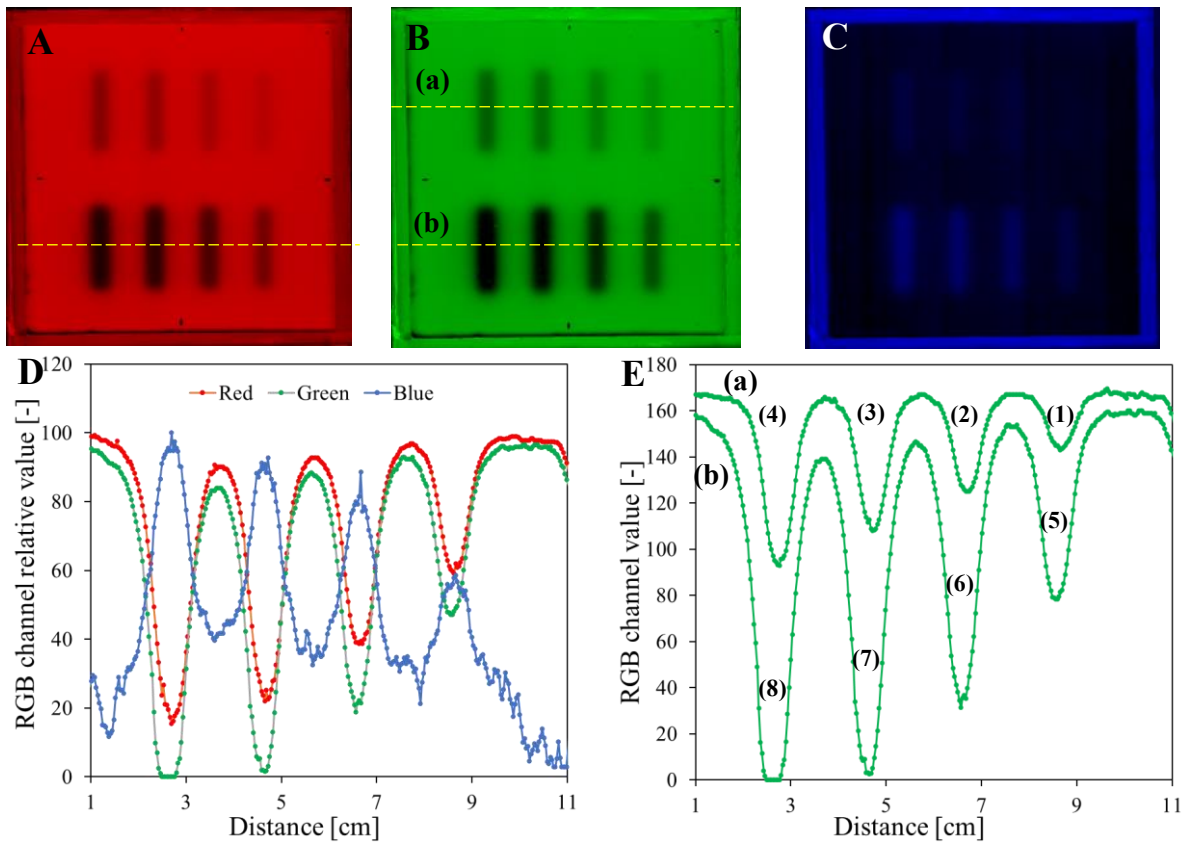


Figure 43. The scans of the Fricke-XO-Gelatin with sorbitol sample before (A) and after (B-G) irradiation with 250 (1), 500 (2), 750 (3), 1000 (4), 1500 (5), 2000 (6), 2500 (7), and 4000 (8) MU (as shown in B). Sample scanning was performed at the following times after irradiation: 113 min (B), 234 min (C), 345 min (D), 423 min (E), 568 min (F), and 1437 min (G).

The images of the scanned samples were split into the red, green, and blue channels (RGB) of the RGB color model (Figures 44 A–C and 45 A–C), and the profiles (Figures 44 D, E and 45 D, E) across the irradiated areas were determined for each RGB channel to find which one contributed the most to the sample color after irradiation. For both dosimeters the largest change was found for the green channel, which, as a consequence, was used in further data analysis. The relations of the green channel value versus monitor units for both dosimeters are presented in Figures 44 F and 45 F. The linear ranges of these relations are shown in Figures 44 G and 45 G. The Fricke-XO-Gelatin with sorbitol dosimeter indicates a higher sensitivity (absolute value of the slope parameter in the equation of the linear function), however the Fricke-XO-Pluronic F-127 dosimeter is characterized by a wider range of linear response to ionizing radiation.



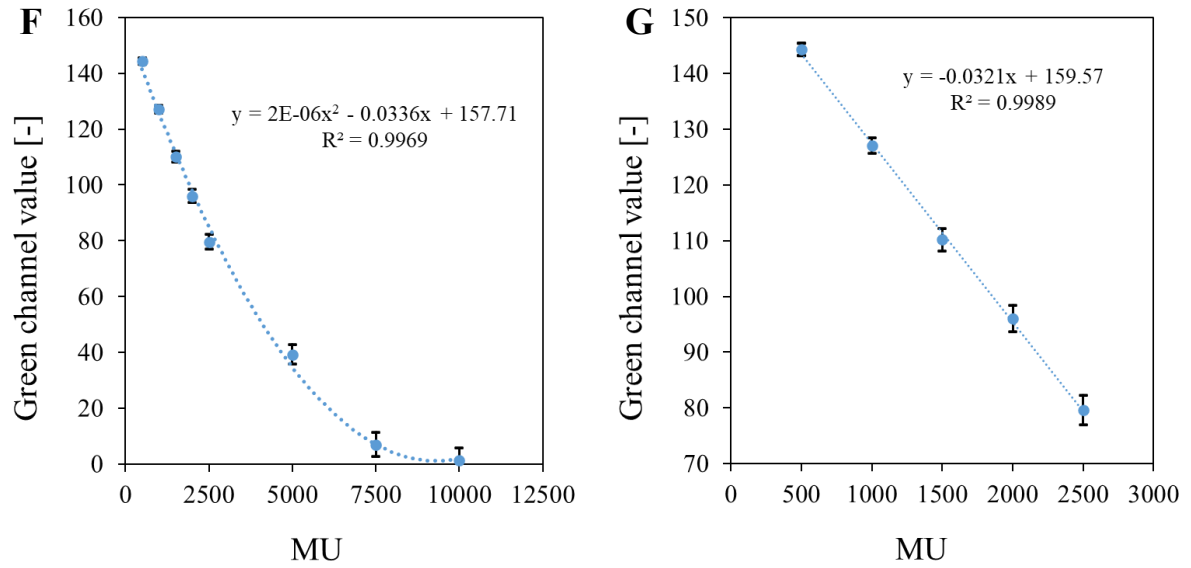
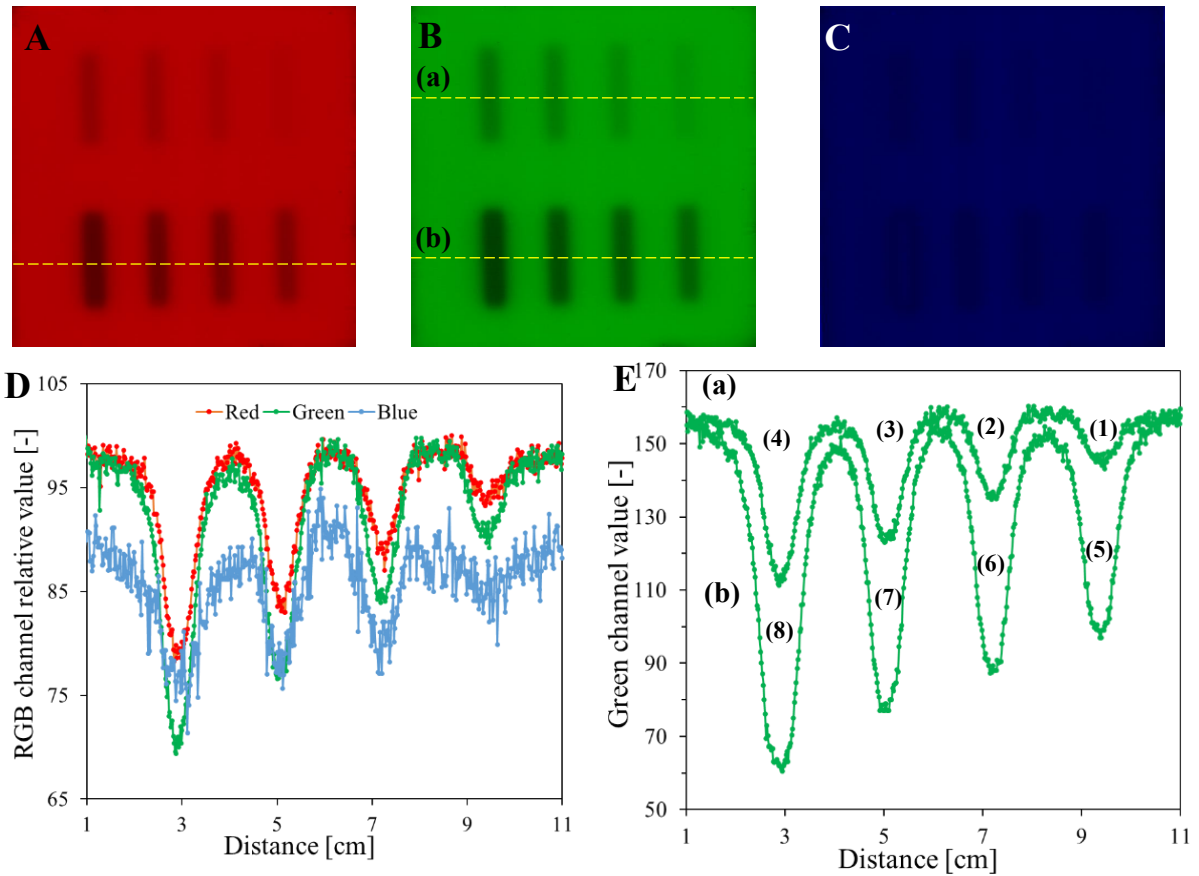


Figure 44. Irradiation response analysis of the Fricke-XO-Pluronic F-127. **A-C:** Images correspond to the image in [Figure 42B](#) resolved into red (**A**), green (**B**), and blue (**C**) channels of RGB color model. **(D)** Profiles for red, green, and blue channels that were taken across the irradiated stripes (bottom part, as indicated in **A** by the yellow dashed line). **(E)** Profiles across the irradiated regions for the green channel, as indicated by the yellow dashed lines in **(B)**, for top (a) and bottom (b) stripes. (1)–(8) represent treatment with 500, 1000, 1500, 2000, 2500, 5000, 7500, and 10,000 MUs, respectively. **F:** The relation of the green channel value versus monitor units. **G:** The same relationship as in **F** but in the range of the linear response of the dosimeter.



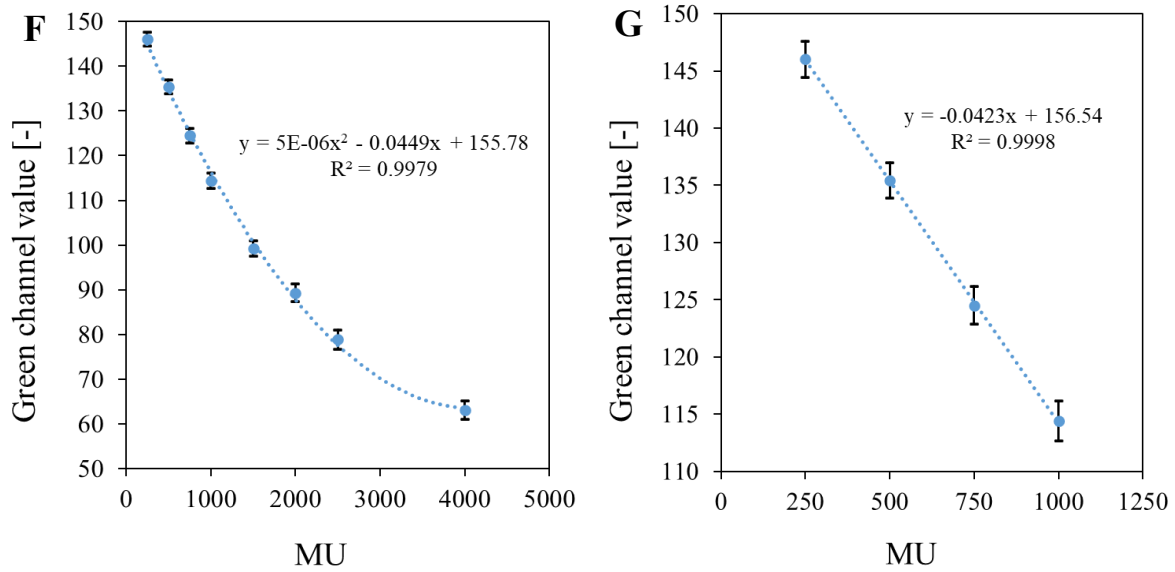
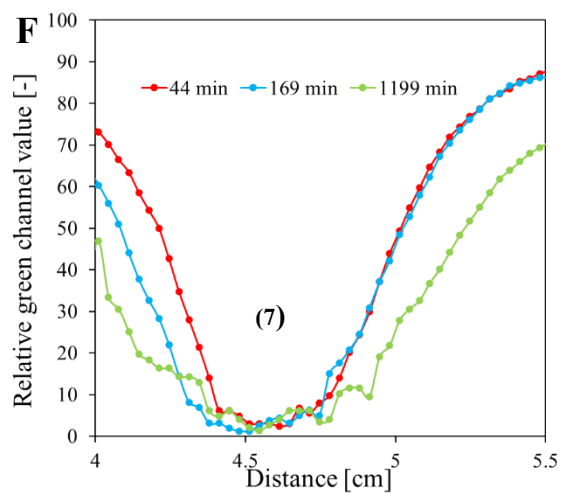
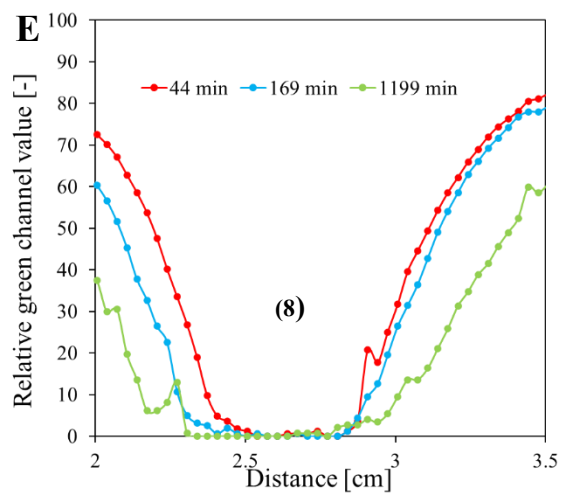
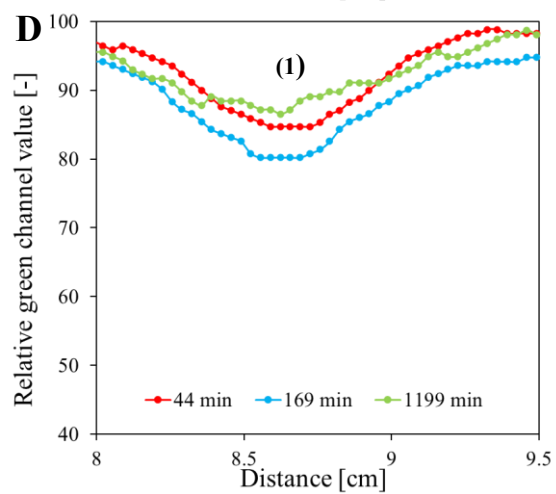
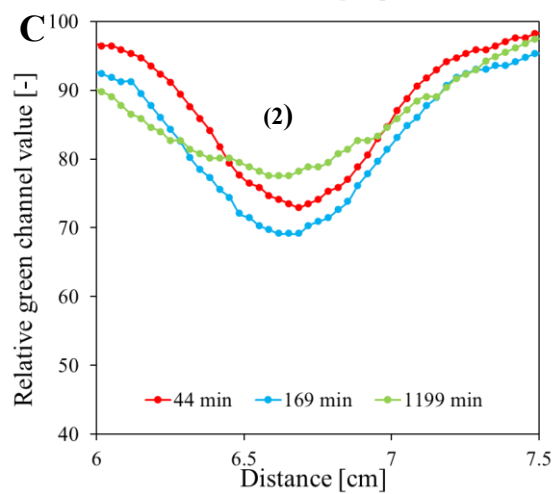
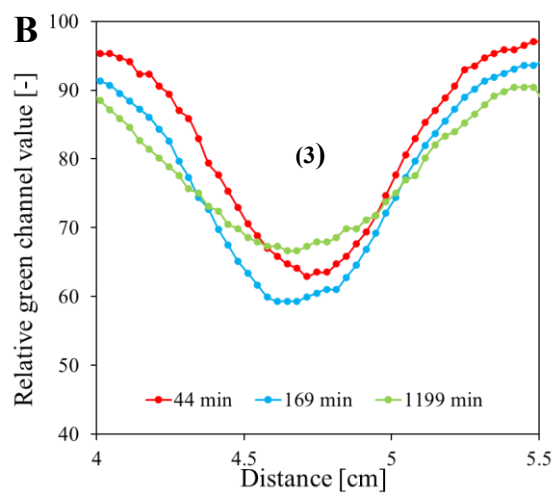
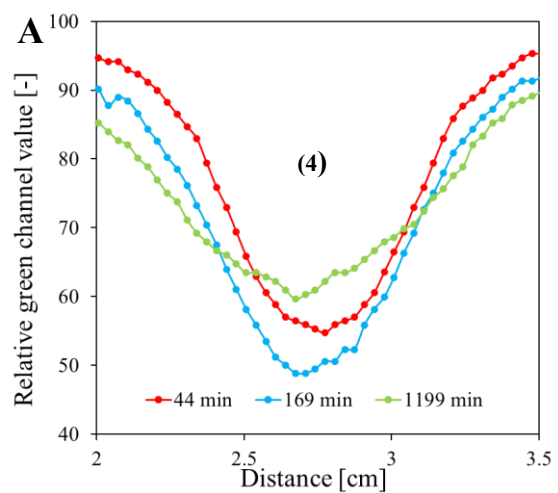


Figure 45. Irradiation response analysis of the Fricke-XO-Gelatin with sorbitol. **A-C:** images obtained by decomposing a scan of the dosimeter sample taken 113 min ([Figure 43 B](#)) after irradiation into red (**A**), green (**B**) and blue (**C**) channels of the RGB color model. **D:** red, green and blue color profiles determined across the bottom of the irradiated sample (indicated by the yellow dashed line in **A**). **E:** green channel value profiles determined across the top and bottom of the sample (indicated by the yellow dashed lines in **B**). Profiles marked with a number in **E** correspond to the stripes marked with the same numbers in [Figure 43 B](#). **F:** The relation of the green channel value versus monitor units. **G:** The same relationship as in **F** but in the range of the linear response of the dosimeter.

[Figures 46](#) and [47](#) present profiles across the irradiated areas 44, 169, and 1199 minutes after irradiation of the Fricke-XO-Pluronic F-127 and 113, 234, and 1437 minutes after irradiation of the Fricke-XO-Gelatin with sorbitol. During the time between 44 and 169 min after irradiation, the green channel value for all the irradiated areas of the Pluronic dosimeter increased. This change is related to the increase in the color intensity of the irradiated strips, indicating that the oxidation of ferrous ions in the Fricke-XO-Pluronic F-127 dosimeter occurs up to 3 h after irradiation. Furthermore, during this time interval, there was a significant broadening of the profiles as a result of diffusion of Fe^{3+} ions. For the gelatin dosimeter, the green channel value for the irradiated areas remained unchanged between 113 and 234 minutes. The width of the profiles also did not change significantly during this time, which indicates a lower diffusion coefficient of ferrous ions in gelatin with sorbitol than in Pluronic. The profiles along the irradiated areas of both dosimeters were significantly widened in less than 24 hours after irradiation, and the green channel values decreased. Both phenomena are related to the diffusion of Fe^{3+} ions, which is the limiting factor when using both dosimeters. The problem can be overcome by performing the scan within 3 hours after irradiation.

For both dosimeters, all irradiated areas changed color sufficiently to perform the coincidence test. Hence, each tested MU value can be used in the measurement. However, to shorten the test time, it is optimal to irradiate the Fricke-XO-Pluronic F-127 dosimeter with a beam of 500-2500 MU, and the Fricke-XO-Gelatin with sorbitol dosimeter with a beam of 250-2000 MU.



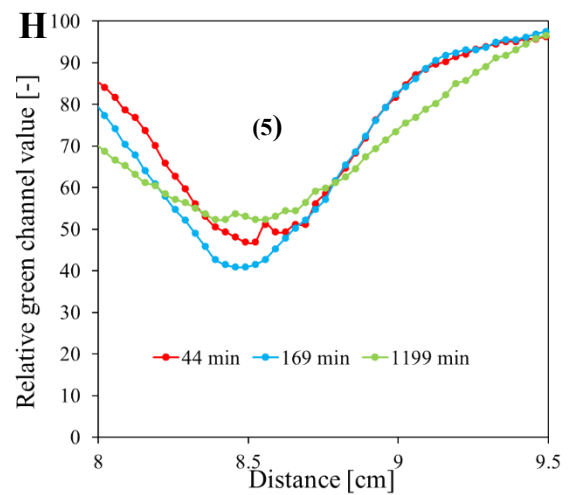
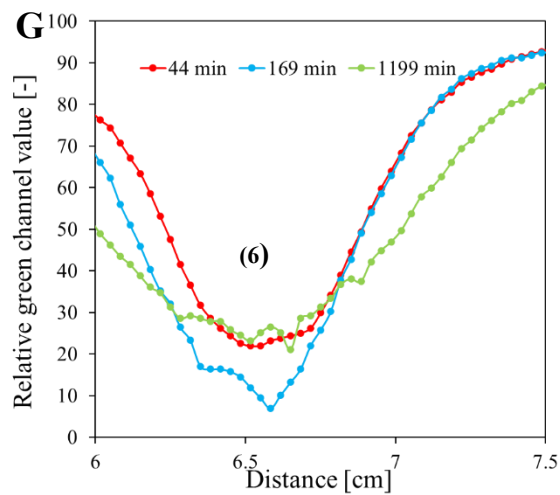
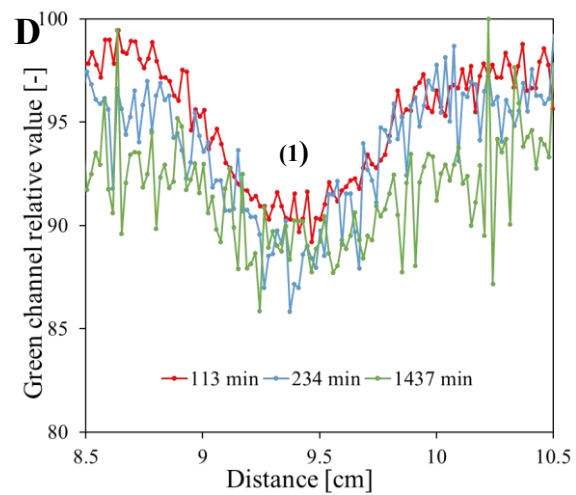
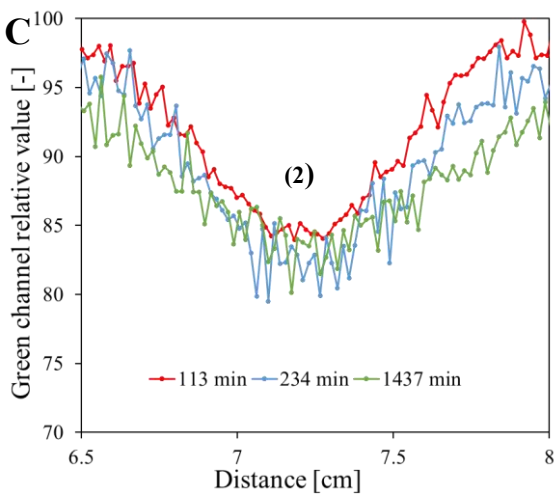
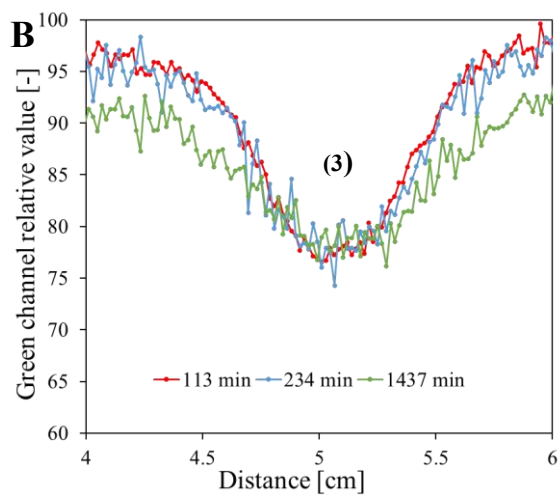
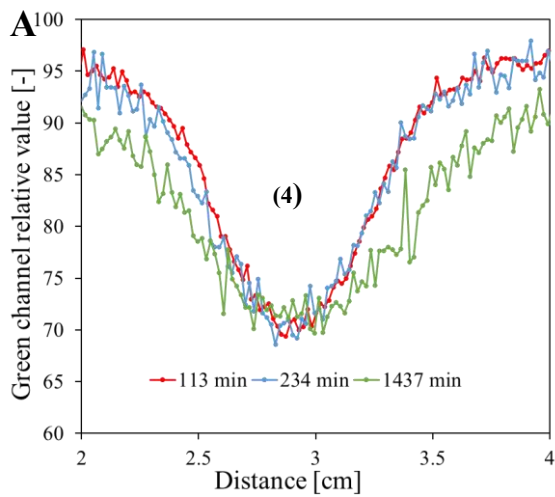


Figure 46. Profiles determined across the color stripes obtained after irradiation of the Fricke-XO-Pluronic F-127 sample with the following MU values: 500 (1), 1000 (2), 1500 (3), 2000 (4), 2500 (5), 5000 (6), 7500 (7), and 10000 (8). Numbers 1-8 correspond to irradiated areas in [Figure 42 B](#)



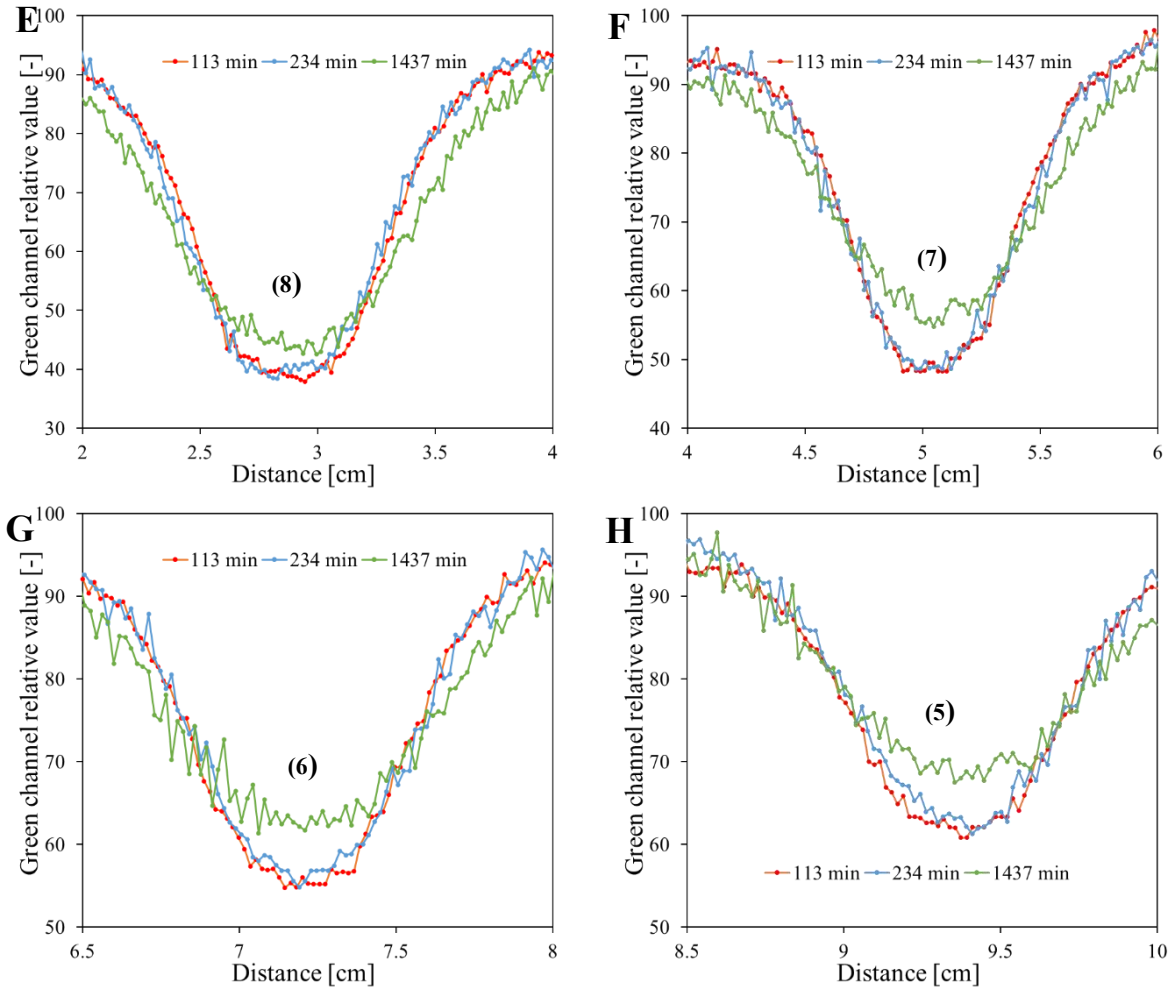


Figure 47. Profiles determined across the color stripes obtained after irradiation of the Fricke-XO-Gelatin with sorbitol with the following MU values: 250 (1), 500 (2), 750 (3), 1000 (4), 1500 (5), 2000 (6), 2500 (7), and 4000 (8). Numbers 1-8 correspond to irradiated areas in [Figure 43 B](#).

5.2.4.2. Evaluation of Beam Size

The optimization of beam size was achieved through the utilization of a Fricke-XO-Pluronic F-127 dosimeter. [Figure 48](#) presents an image of the scanned sample irradiated with different field sizes (MUs for every beam was 2500), the green channel image, and the profiles of the irradiated areas recorded 52 and 246 minutes after irradiation. For each field size, the change in the relative green channel value is clearly visible in the profiles. However, in the case of irradiation with 10 and 20 mm gaps of the HD MLC, a significant increase in the color intensity of the irradiated areas was observed between 52 and 246 minutes after irradiation. Furthermore, these regions exhibit a substantial size in comparison to the dimensions of the dosimeter. For the remaining field sizes, the profiles of the irradiated areas demonstrate stability over the duration of the measurements. However, due to the relatively high intensity of the color, the HD MLC gaps of 2 and 5 mm would be the most appropriate for determining the radiation isocenter.

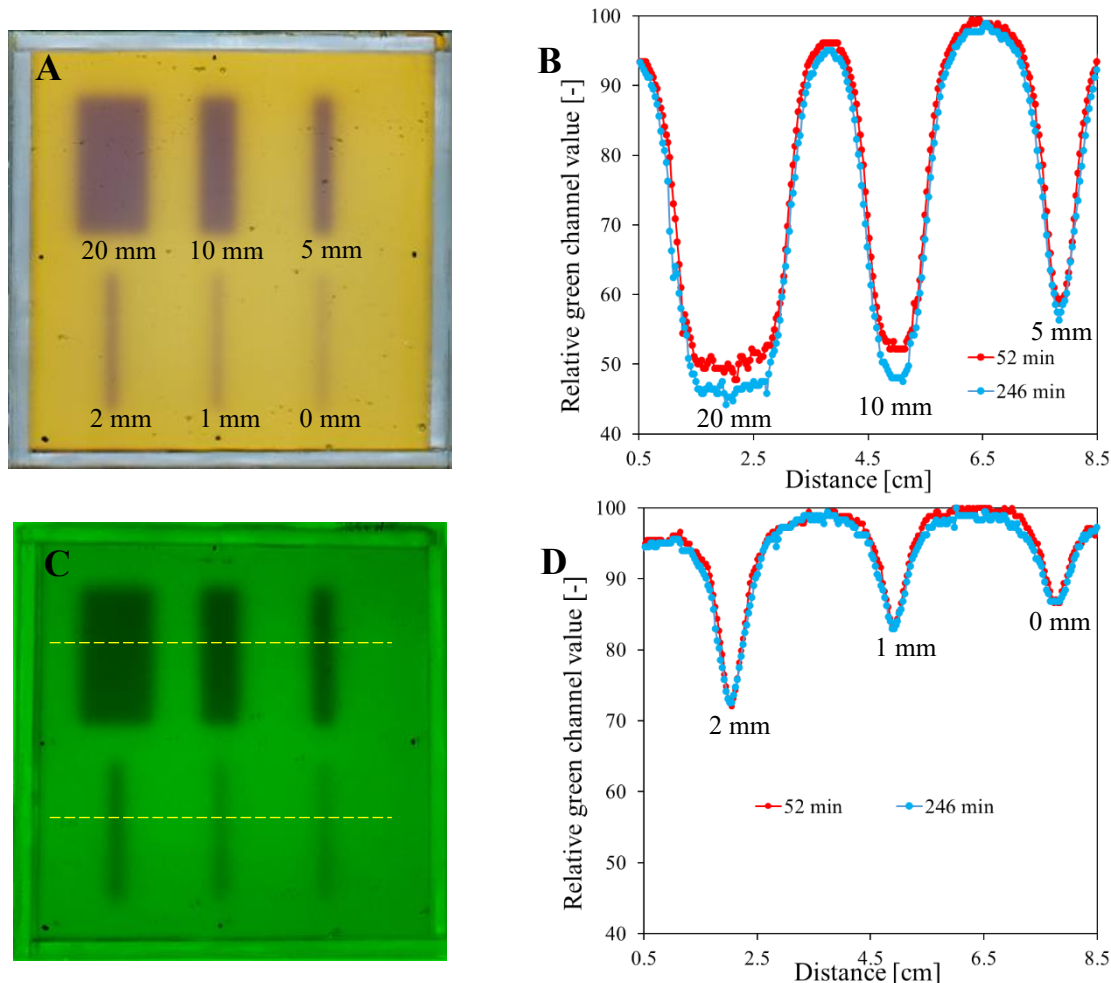


Figure 48. Response to irradiation of the Fricke-XO-Pluronic F-127 dosimeter with the TrueBeam medical accelerator with 2500 MU per beam and various field sizes: 0, 1, 2, 5, 10, and 20 mm. (A) Image after scanning with an HP Scanjet scanner taken 52 min after irradiation. (B) Image of the green channel of the RGB color space; the yellow dashed lines indicate positions of the profiles across the irradiated regions presented in (C, D)

5.2.4.3. Coincidence test of radiation and mechanical isocenters

The coincidence test was performed for two Fricke-XO-Pluronic F-127 dosimeters and one Fricke-XO-Gelatin with sorbitol. The test consisted of the following steps: (1) 2D star shot irradiation of the dosimeters with 750 MU and 2500 MU per beam for Pluronic gels and 1500 MU per beam for gelatin gels, (2) scanning of the samples using the HP Scanjet G3010 scanner, (3) calculations related to the test based on the 2D images of the irradiated dosimeter sample using the dedicated tools of the polyGeVero-CT software package. The sample scans were decomposed into the red, green, and blue channels of the RGB color model. The green channel images (Figure 49 A, C, E) were used for analysis. The results of the calculations (isocenter radius and offset - distance between the radiation and mechanical isocenters) are presented in Figure 49 B, D, F. The calculated isocenter radius and offset were 0.15 mm and 0.29 mm for the Fricke-XO-Gelatin with sorbitol dosimeter and 0.17 mm and 0.57 mm and 0.19 mm and 0.46 mm for the Fricke-XO-Pluronic F-127 dosimeters irradiated with 750 MUs and 2500 MUs per beam, respectively. All calculated values are within the tolerance limits for the star shot measurement: ± 1 mm [186]

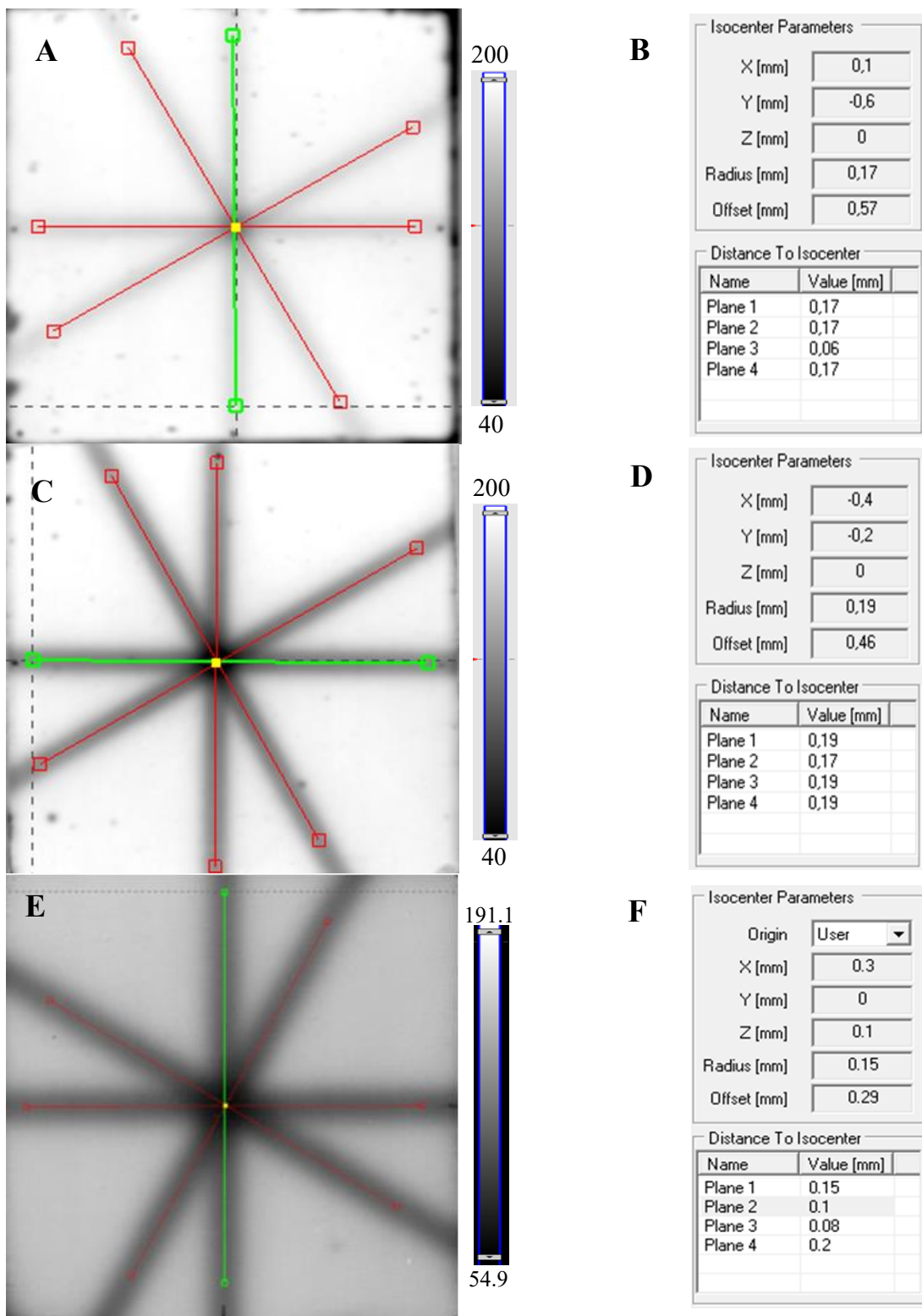


Figure 49. Application of Fricke-XO-Gelatin with sorbitol to the coincidence test of radiation and mechanical isocenter for the TrueBeam medical accelerator. Green channel images obtained by splitting the samples scans into RGB color model channels viewed in the polyGeVero-CT software package are presented in **A** (Fricke-XO-Pluronic F-127 irradiated with 750 MUs per beam), **C** (Fricke-XO-Pluronic F-127 irradiated with 2500 MUs per beam) and **E** (Fricke-XO-Gelatin with sorbitol irradiated with 1500 MUs per beam). Red and green lines are specific tools for determining the isocenter, while the yellow dot indicates the location of the radiation isocenter. Calculation results of the coincidence test are presented in **B** (Pluronic gel irradiated with 750 MUs per beam), **D**

(Pluronic gel irradiated with 2500 MUs per beam) and **F** (Gelatin gel irradiated with 1500 MUs per beam).

The diffusion of Fe^{3+} ions was observed for both tested dosimeters. In consequence, the colored stripes of the star shot irradiated dosimeter diffuse and the star image becomes blurred, analogous to the blurring of the colored stripes presented in [Figures 42 and 43](#). This effect may determine image processing towards computations related to the coincidence test. The impact of this effect was assessed using a Fricke-XO-Pluronic F-127 dosimeter. The results are presented in [Figure 50](#) for the scans performed 70 min after the first scan for a dosimeter irradiated with 750 MUs/beam and 94 and 194 min after the first scan for a dosimeter irradiated with 2500 MUs/beam. Despite the blurring of the images, data processing was successfully executed using the polyGeVero-CT software package. The results obtained are similar to each other and to those obtained from the initial scan. Otherwise, they remained within the tolerance limits. The obtained results clearly show that the Fricke-XO-Gelatin with sorbitol and Fricke-XO-Pluronic F-127 dosimeters in a cuboidal container are appropriate tools for determining the radiation isocenter of the True-Beam accelerator. High-accuracy measurements should be possible for even lower monitor units per beam settings than 750 MUs, thereby positioning this dosimeter as a competitive alternative to Gafchromic films, which require an irradiation of 600 MUs per beam [187]. Comparing both tested dosimeters, the Fricke-XO-Gelatin with sorbitol gel shows better properties for use in the coincidence test of the radiation and mechanical isocenter of a medical accelerator than the Fricke-XO-Pluronic F-127. The dosimeter with gelatin is characterized by slower diffusion of Fe^{3+} ions, higher chemical stability and higher sensitivity to ionizing radiation.

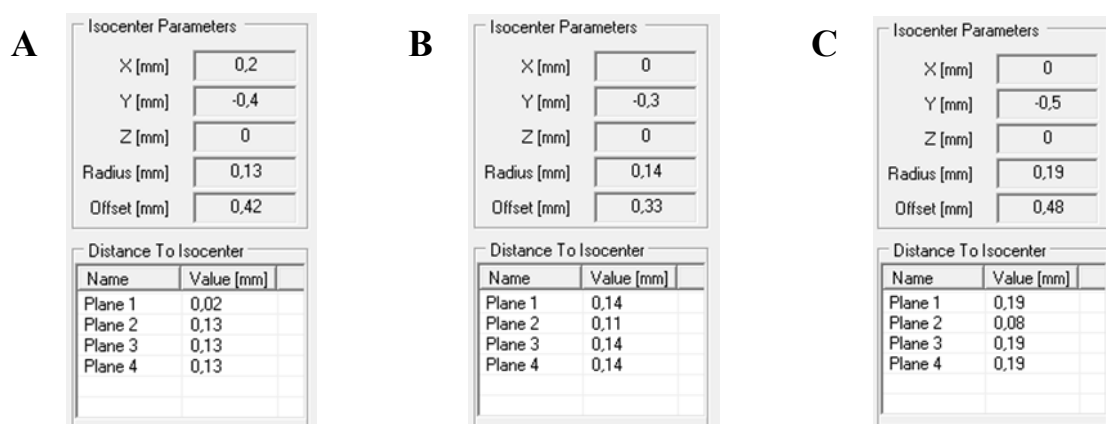
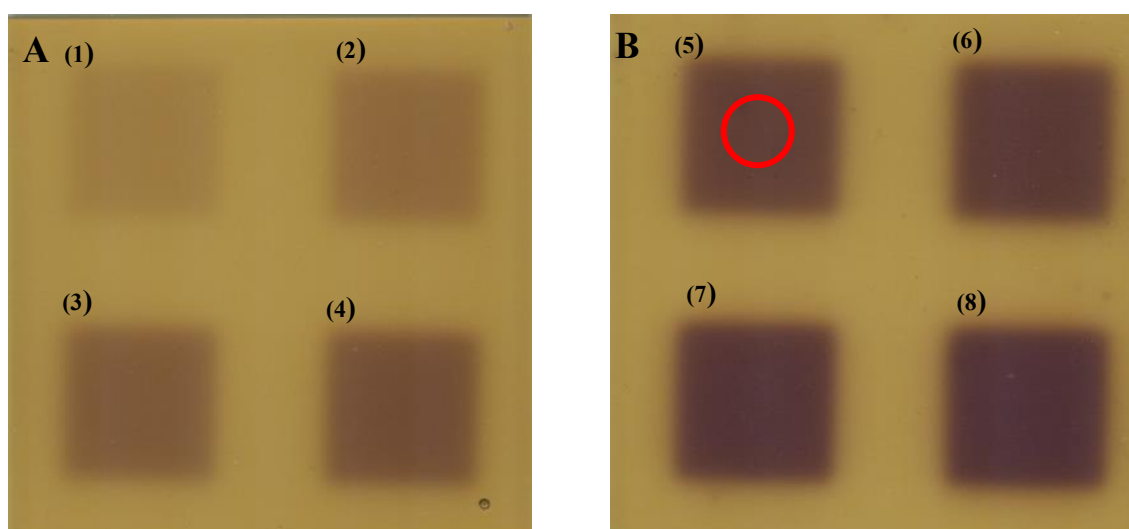


Figure 50. Response of the Fricke-XO-Pluronic F-127 dosimeter to irradiation with the TrueBeam medical accelerator according to the star shot pattern: the coincidence test of the mechanical and radiation isocenters. The number of monitor units per beam was 750 (**A**) and 2500 (**B**, **C**). The dosimeter was scanned a period of time after irradiation: 70 min after the first scanning (**A**) and 94 (**B**) and 194 min (**C**) after the first scanning (the data for the first scan are presented in [Figure 49](#)). After scanning, the green channel images of RGB were processed in polyGeVero-CT.

5.2.4.4. Dosimeters calibration

The scans of the bolus and thin dosimeter samples irradiated with doses ranging from 2.5 to 20 Gy are presented in [Figure 51 A-D](#). The unirradiated bolus is dark yellow, while the unirradiated thin dosimeter is light yellow. This difference in color intensity results from the different thickness of the gel layer, which is 5 mm for the bolus and 1 mm for the thin dosimeter. Both dosimeters turn purple after irradiation, with the color becoming more intense with increasing radiation dose. Color inhomogeneities in the form of vertical stripes of different brightness are slightly visible in the scans. This occurs probably due to the insufficient quality of the scanner used and impact of the structure of foils covering the gels. [Figure 51 E-H](#) shows the value of the green channel as a function of dose for the scanned samples. The

values presented in the graphs are the mean green channel values in the central part of the irradiated area, which is limited by a 1.5 cm diameter circle (indicated by the red circle in [Figure 51 B](#)). Calibration of the bolus dosimeter was performed in the range of 2.5-20 Gy (Series I in [Figure 51 E, F](#)) and repeated in the range of 2.5-10 Gy (Series II in [Figure 51 E, F](#)). These calibrations for both series were performed on Fricke-XO-Gelatin with sorbitol using fresh and aged stock solutions. The objective of this investigation was to determine the impact of storage on the dosimeter dose response. The obtained calibration curves differ from each other. The green channel values for the same doses are lower in Series II than in Series I, and the standard deviation of the values in Series II is higher. These differences are likely due to the partial self-oxidation of the ferrous ions. Both calibration samples were prepared with the same stock Fricke solution; however, the solution was two weeks older at the time of the repeated calibration. Additionally, the second calibration sample was irradiated three days after preparation, whereas the first calibration sample was used two days after preparation. The thin dosimeter is characterized by higher standard deviation values for the green channel, which may result from the inhomogeneous thickness of the gel layer due to the use of an imperfect preparation method. Before pressing with a steel plate, the dosimeter solution was poured and covered with a sheet of foil. It was not possible to control the thickness of the gel during the covering process, which could have led to excessive pressure on the solution in some places. Additionally, cutting out the sample with a knife may have affected the gel thickness, particularly at the sample boundaries. The results indicate the need to improve the method used to prepare the thin dosimeter. In summary, the following characteristics are important for further applications of such samples: (1) both Fricke-XO-Gelatin with sorbitol, bolus and thin gel, respond dynamically to irradiation up to 20 Gy; above this dose the dosimeters become saturated, (2) the linear dose response is up to about 12.5 Gy, (3) the threshold dose was not estimated because the samples were not irradiated below 2.5 Gy, (4) the calibration equations are given in [Figures 51 E-H](#), with the slope parameters of the linear regression indicating the dose sensitivities of the samples, (5) the calibration relations are dependent on the freshness of the Fricke stock solution and self-oxidation of Fe^{2+} ions. Consequently, caution should be exercised when designing the application study. For example, if the dosimeter is used for 3D dose verification in radiotherapy dosimetry, both the calibration dosimeter and verification gel samples should be used from the same stock solution with the same storage history.



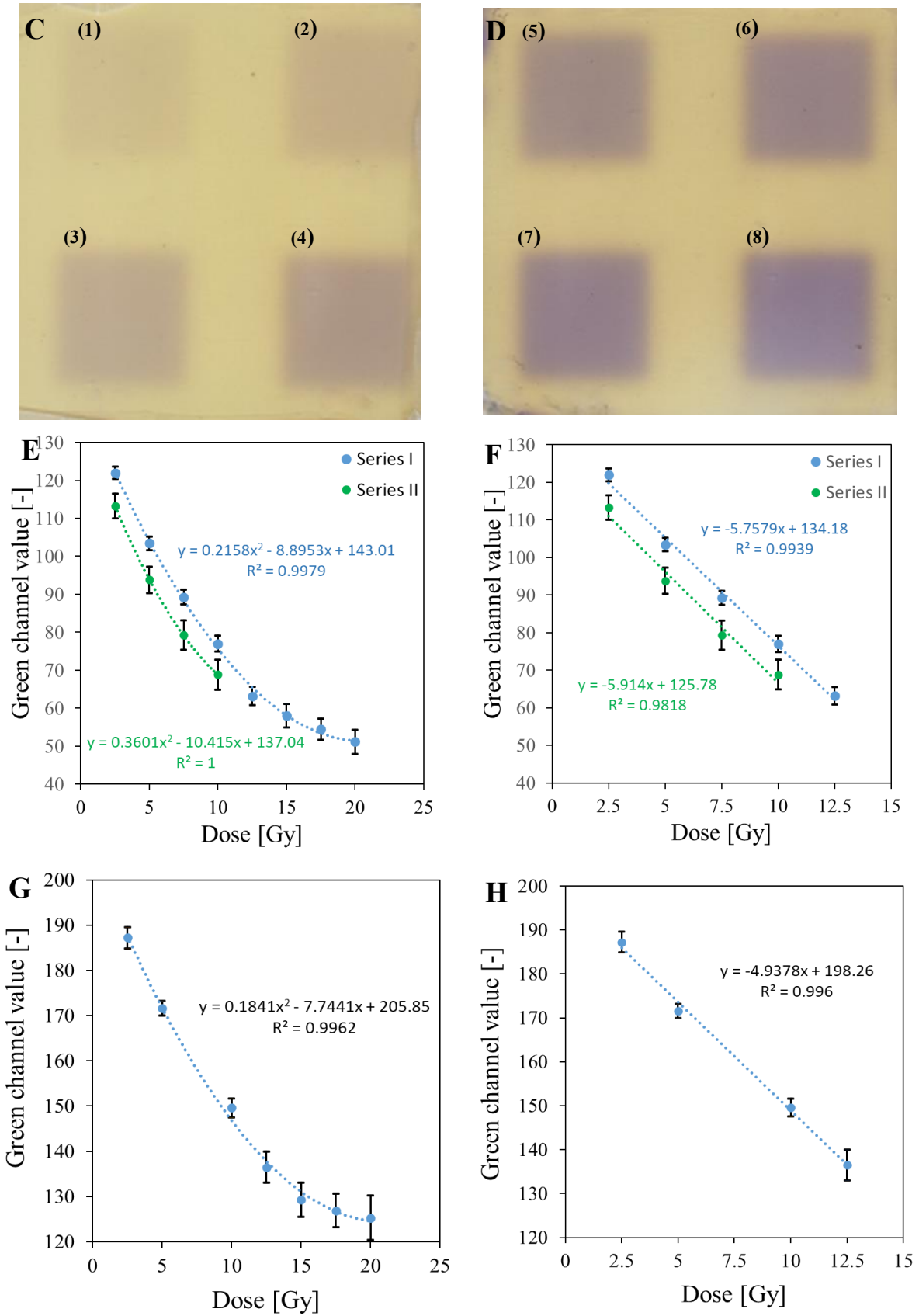


Figure 51. Dose response of Fricke-XO-Gelatin with sorbitol in form of a bolus and thin gel samples. **A** and **B**: Scans of the bolus samples irradiated with the following doses: 2.5 (1), 5 (2), 7.5 (3), 10 (4), 12.5 (5), 15 (6), 17.5 (7), and 20 Gy (8). The red circle in B limits the area used to determine the green channel mean value. **C** and **D**: Scans of the thin dosimeters. Numbers 1-8 denotes to the same doses

as in **A** and **B**. Green channel value versus dose relationship for bolus and thin dosimeter is presented in **E** and **G**, respectively. **F** and **H** refers to the same relation, however, for a narrower range of doses and using linear regression. **F** refers to bolus and **H** to the thin dosimeter

5.2.4.5. Treatment planning verification: Fricke-XO-Gelatin (thin gel)

A treatment plan generated using a TPS was verified using a thick (Figure 52 A) and a thin dosimeter. Additionally, Monte Carlo simulations were performed using myQA iON, and the results were compared to the measured dose distribution by the dosimeters and the TPS-calculated data. This section presents the results for the thin dosimeter, and the next section presents the results for the thick bolus dosimeter. During irradiation, the samples rested on a 20 cm SP34 RW3 phantom. The thin dosimeter was covered with a 10 mm thick BolX with a skin bolus (Figure 52 B). The approach to using the thin dosimeter and thick bolus in this experiment was that the dosimeter should be used with the boluses commonly used in radiotherapy. It should be covered with one to study the dose distribution on the skin surface. Meanwhile, the thick bolus serves as both a bolus and a 2D dosimeter.

Figure 53 shows the comparison of the dose distribution measured using a thin dosimeter (scan of the sample presented in Figure 52 C) with the dose distribution calculated in the Eclipse Treatment Planning System and the myQA iON software. Figures 54 and 55 show the comparisons of the dosimeter with the TPS and the TPS with the myQA iON/MC simulations, respectively. At a glance, one can see that the measured dose distribution in the area with the highest dose is non-uniform, unlike the calculated distributions. The measured mean dose in the central area is 16.63 ± 1.20 Gy, whereas the mean doses for the TPS and myQA iON/MC simulations are 17.27 ± 0.50 Gy and 17.27 ± 0.60 Gy, respectively. These values amount to percentage dose differences with respect to the measured dose of 3.85%. The mean dose values measured and calculated for the remaining irradiated areas are presented in Table 8 (The table summarizes the results presented in sections 5.2.4.5. and 5.2.4.6 and is therefore placed at the end of section 5.2.4.6.) The gamma index comparison of the measured and calculated dose distributions is as follows: Twenty-five percent of the pixels are above 1 for the dosimeter versus the myQA iON/MC simulations; 27% of the pixels are above 1 for the dosimeter versus the TPS; and 0% of the pixels are above 1 for the TPS versus the myQA iON/MC simulations. For the agreement between the measured and calculated dose distributions to be considered acceptable, the number of pixels with a gamma index below 1 must be within 0–5% [188]. This means that the dose distribution calculations in the TPS were verified by the myQA iON/MC simulations; however, the verification using the thin dosimeter was unsuccessful in some way. Judging by the results in Figures 53 D and 54 D, the inner left part of the larger square has a satisfactory gamma index, whereas the region on the right has more pixels above 1. These results strongly indicate nonuniformity of the manufactured dosimeter due to the preliminary manufacturing technology adopted, but they do not disqualify the system as a whole. As presented in Figure 53 C, the isodoses superimposed outline square shapes of the irradiated regions and are mostly close to each other for both datasets. In some parts, however, they deviate from each other due to the poorer quality of the images obtained for the dosimeter. The dose profiles along the X, Y, and Z axes for the calculated results in the TPS and MyQA iON/MC simulations are very similar. The only clear difference appears along the Z-axis in the range of -45 to -35 mm, where the dose value calculated in TPS is higher. When comparing the profiles obtained for the measured dose distribution with those for the calculated dose distribution, greater similarity is visible for the Z-axis profiles. Along the X axis, a clear dose difference appears in the range of 0 to 25 mm. Verifying the treatment plan revealed significant discrepancies between the measured and calculated dose distributions. The source of these

differences may be the insufficient quality of the scanner used. [Figure 53 A](#) of the measured dose distribution shows vertical stripes in the area irradiated with the highest dose (a phenomenon described in Section 5.2.5.1). These stripes are also visible in the X-axis profile, which is wavy within the range of the highest dose. Additionally, the results may have been influenced by the non-uniform thickness of the gel layer and possible imperfections in the rigid foil sheets. For the thin dosimeter to be used for verifying the dose distribution on the skin and the treatment plan, improvements to the manufacturing and scanning methods are necessary. Nevertheless, it is clear that such a dosimeter shows great promise for TPS verification purposes in radiotherapy applications.

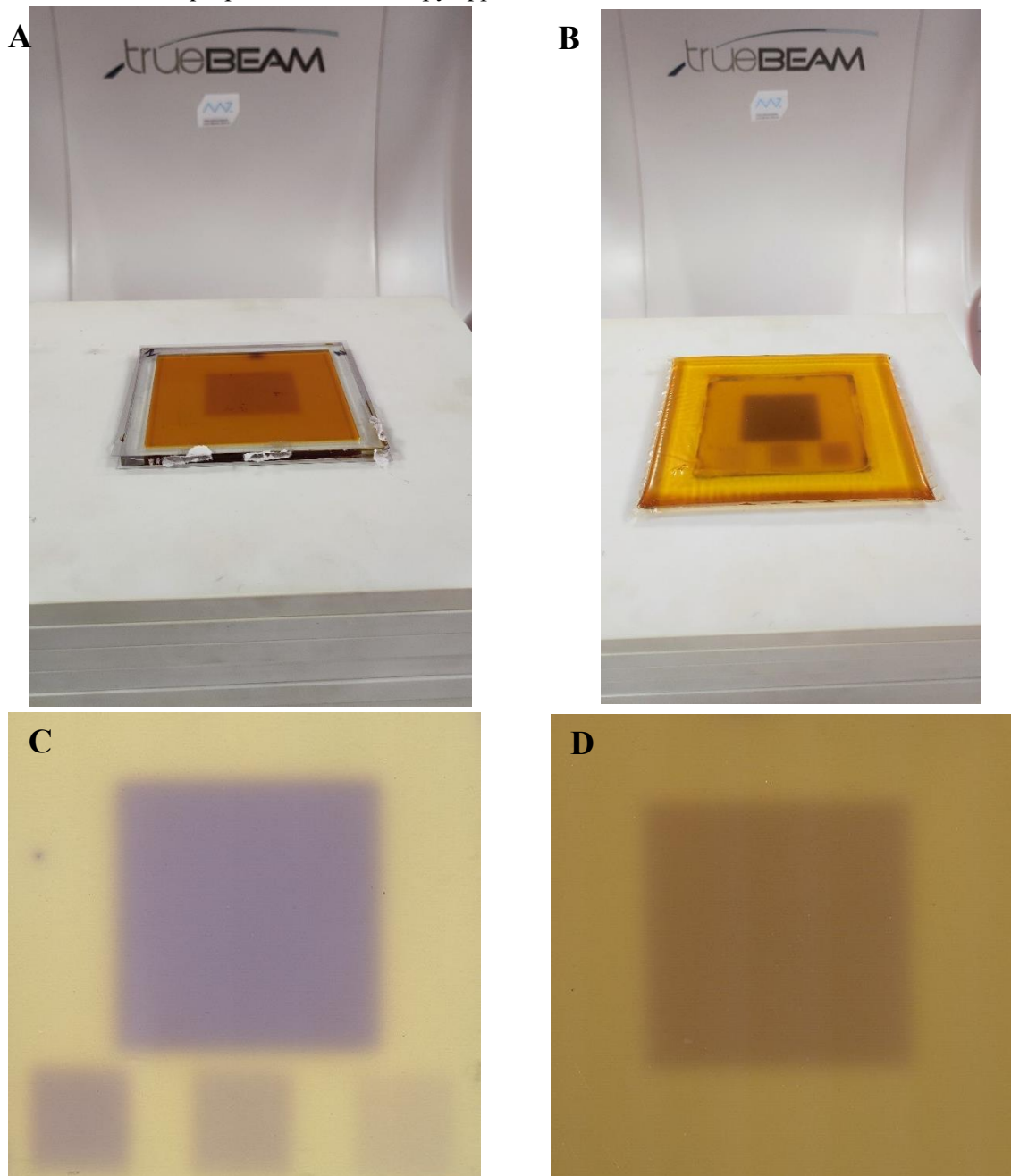
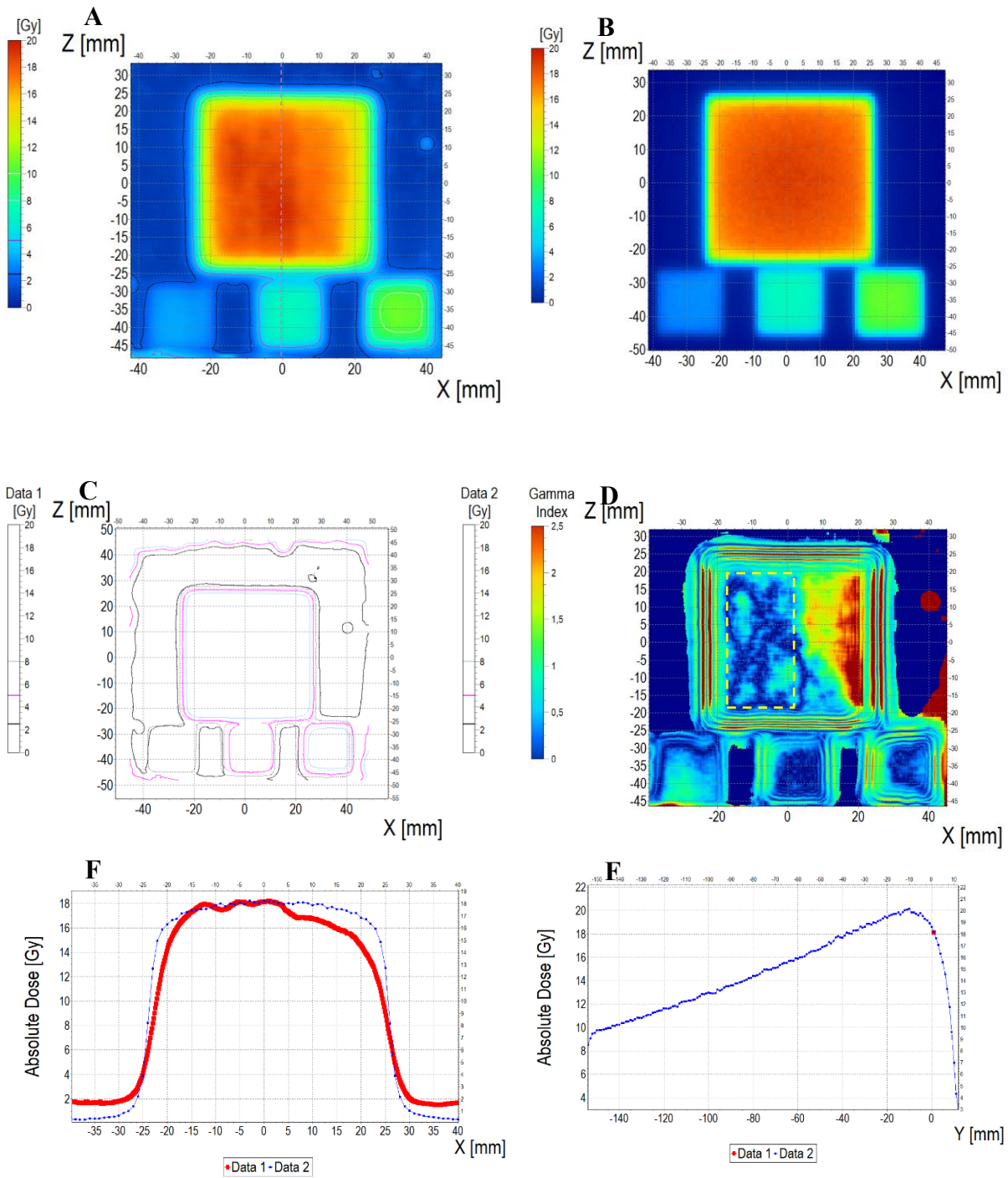


Figure 52. Fricke-XO-Gelatin with sorbitol samples after irradiation with a TrueBeam accelerator (Varian, USA). **A:** Thick dosimeter located on the slabs of the SP34 RW3 phantom. **B:** Thin dosimeter placed on SP34 RW3 phantom. The sample was covered with a 10 mm thick BolX with skin bolus. Scans of thin Fricke-XO-Gelatin with sorbitol dosimeter (**C**) and bolus (**D**) samples irradiated according to the treatment plan. Scans were obtained 80 min (bolus) and 94 min (thin dosimeter) after irradiation.

Fricke-XO-Gelatin (thin gel) vs. myQA



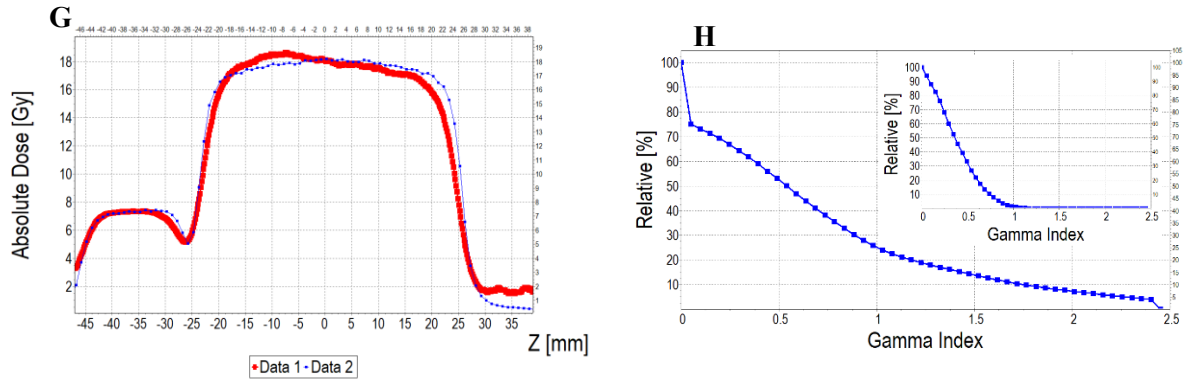
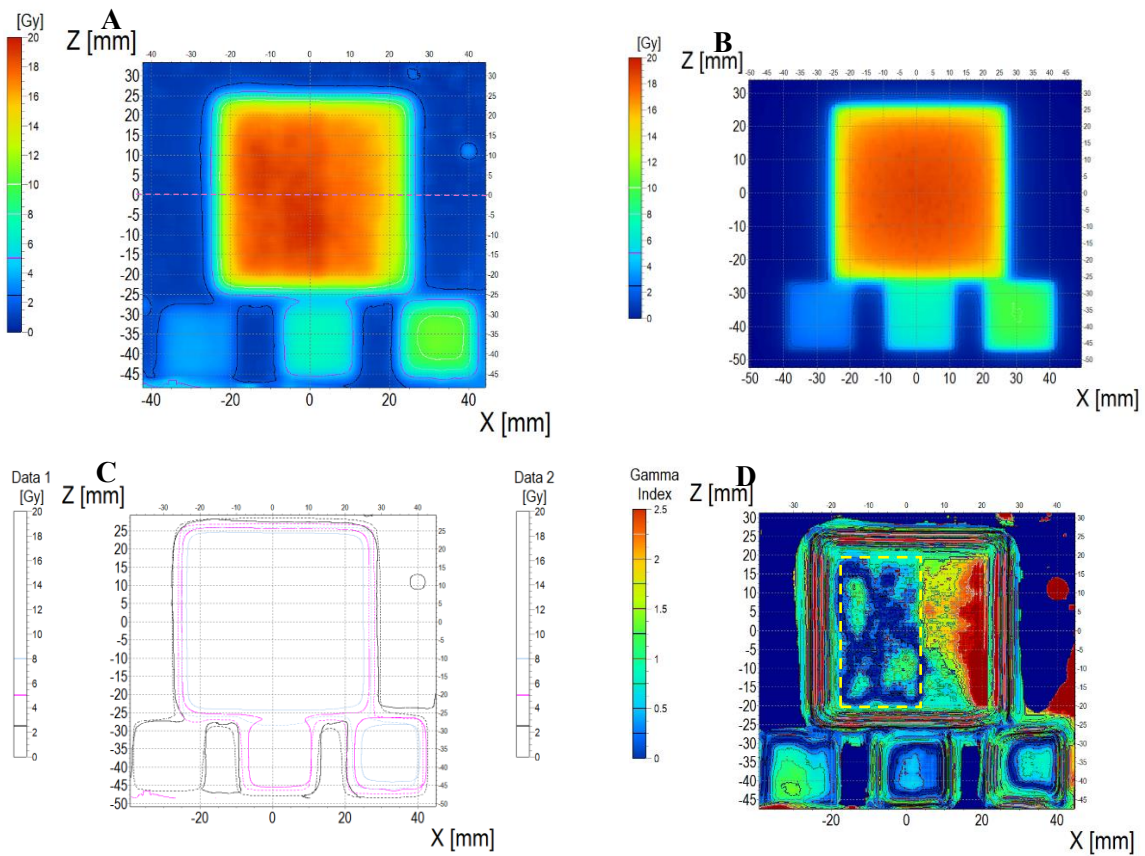


Figure 53. Comparison of dose distribution measured with Fricke-XO-Gelatin 2D dosimeter (thin gel) and calculated with myQA iON/MC simulations. **A** and **B**: ZX planes of dose distributions for Fricke-XO-Gelatin and myQA iON/MC simulations, respectively, **C**: superimposition of isodoses, **D**: gamma index (DD=3%, DTA=3mm), **E**, **F** and **G**: profiles along **Z**, **Y** and **Z** axes (position of profiles is presented in **A** by the lilac dashed lines), and **H**: gamma index histogram. Inset in **H**: a gamma index histogram for a ROI indicated in **D** with the yellow dashed line; 1.2% pixels above gamma index=1.

Fricke-XO-Gelatin (thin gel) vs. TPS



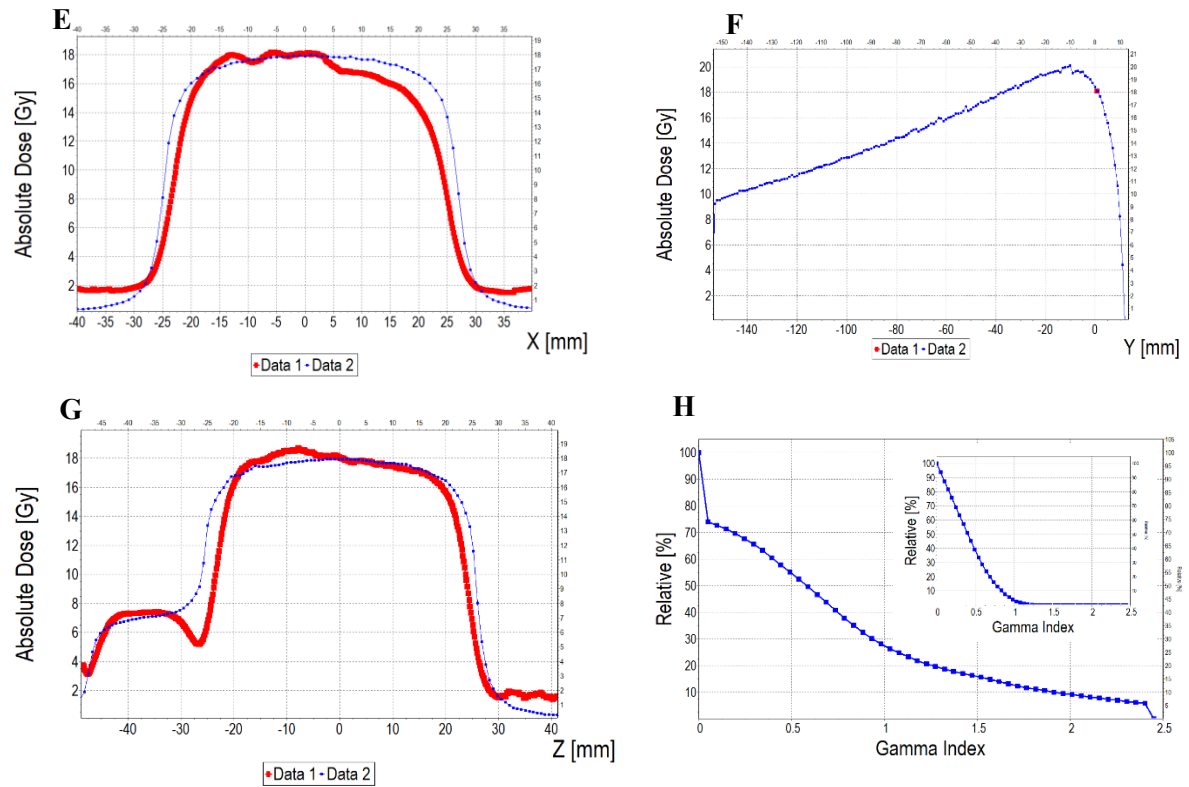
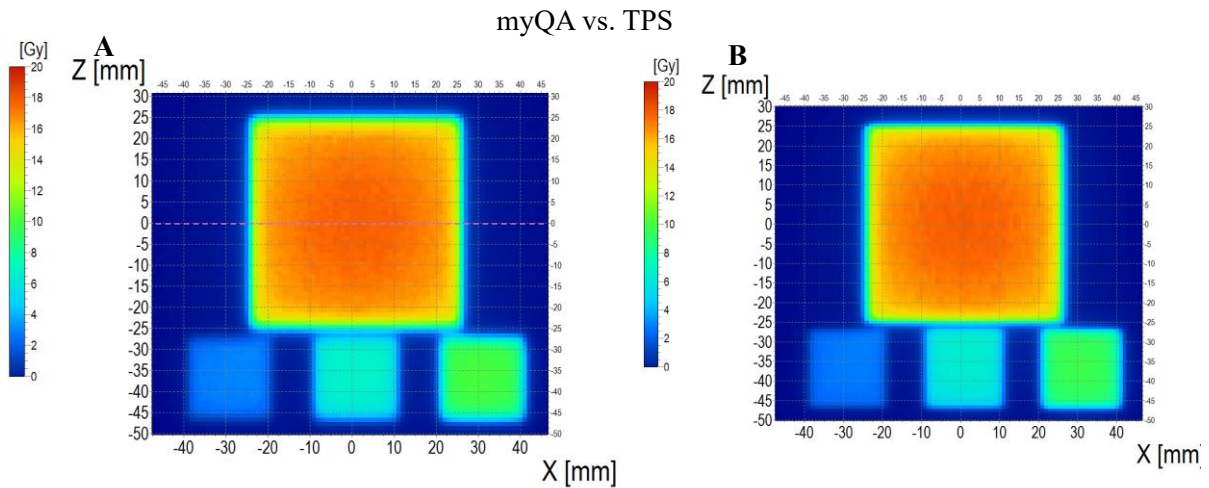


Figure 54. Comparison of dose distribution measured with Fricke-XO-Gelatin 2D dosimeter (thin gel) (Data 1) and calculated with TPS (Data 2). **A** and **B**: ZX planes of dose distributions for Fricke-XO-Gelatin and TPS, respectively, **C**: superimposition of isodoses, **D**: gamma index (DD=3%, DTA=3mm), **E**, **F** and **G**: profiles along Z, Y and Z axes (position of profiles is presented in **A** by the lilac dashed lines), and **H**: gamma index histogram. Inset in **H**: a gamma index histogram for a ROI indicated in **D** with the yellow dashed line; 3.3% pixels above gamma index=1.



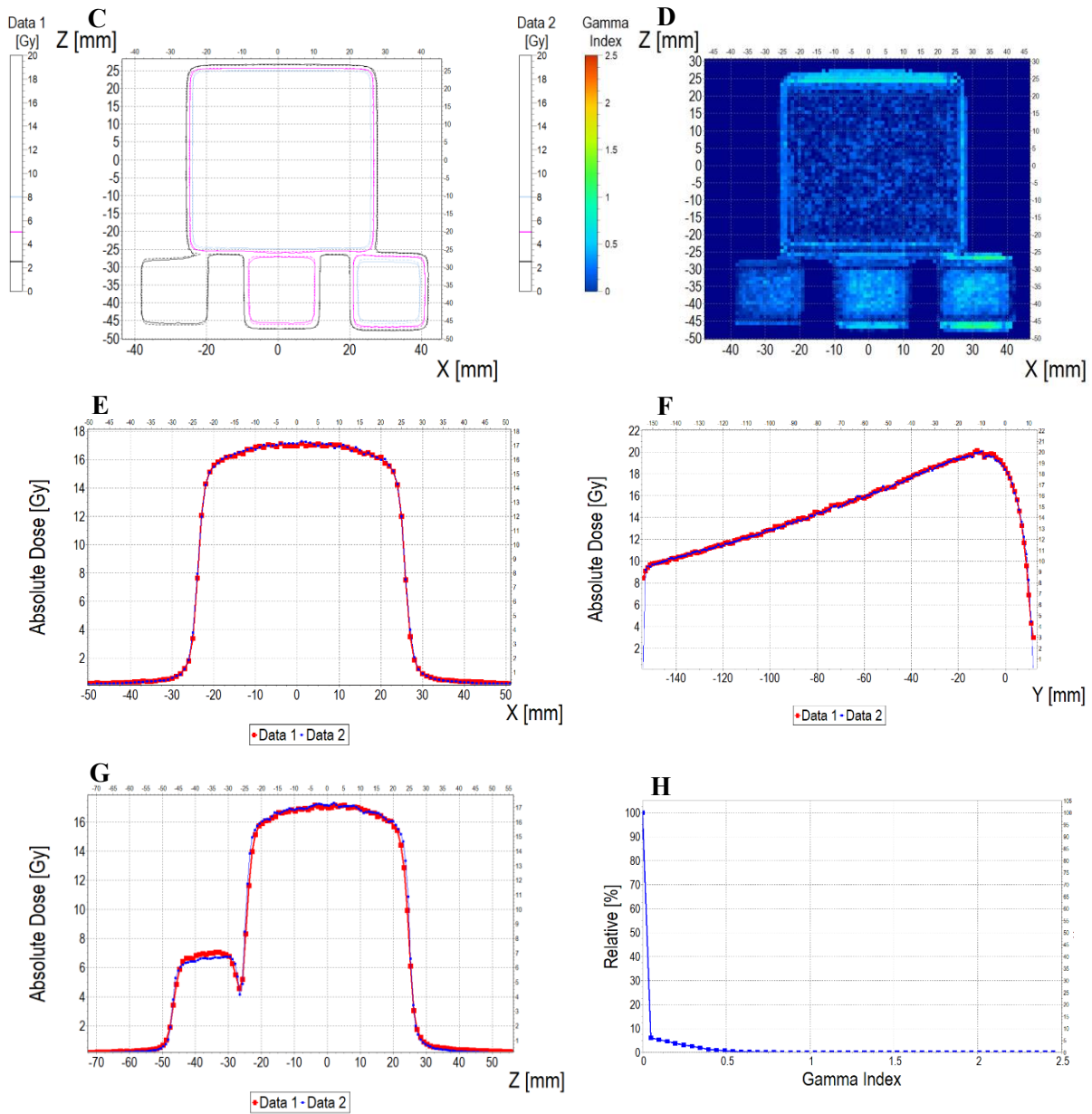


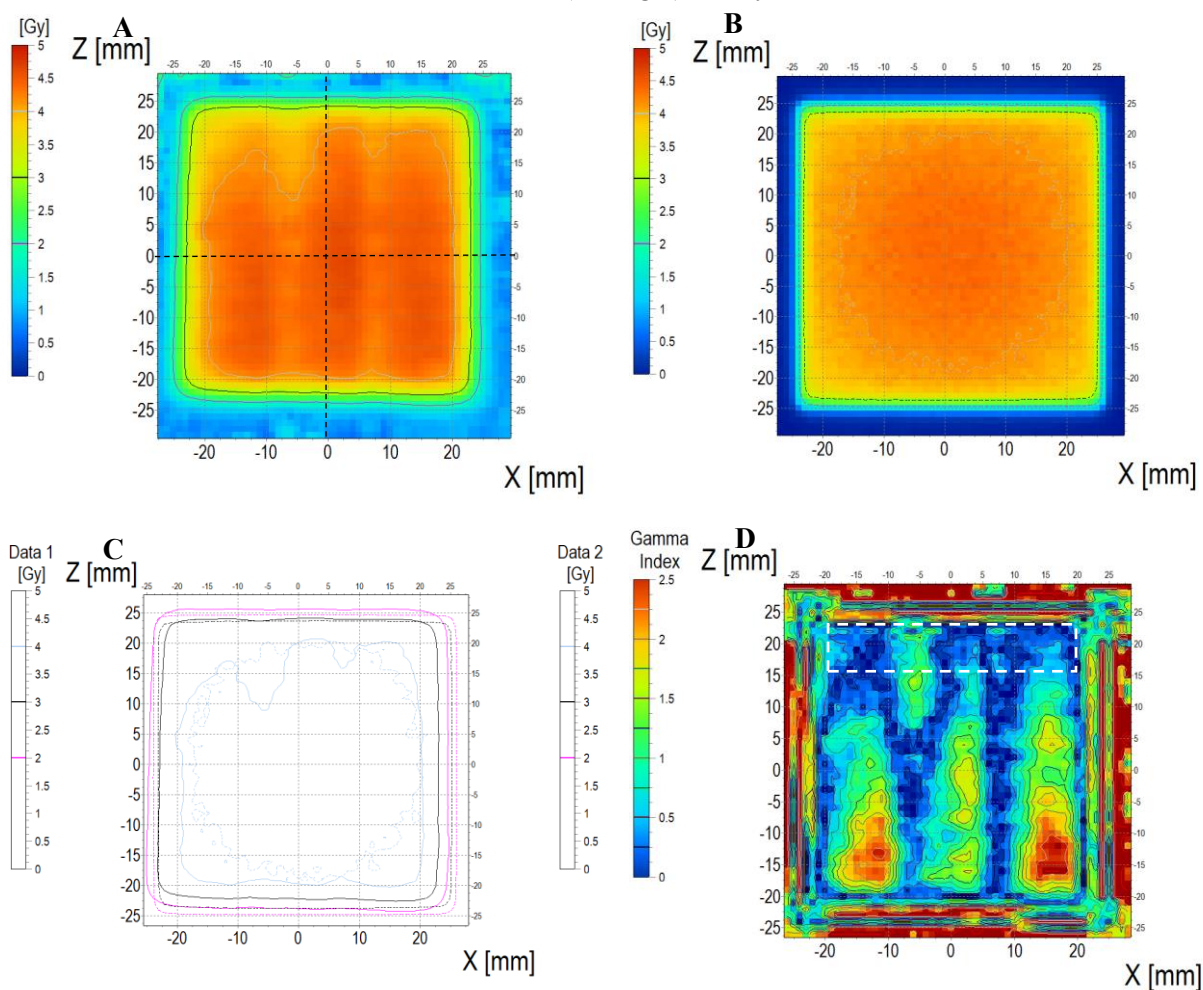
Figure 55. Comparison of dose distribution calculated with myQA iON/MC simulations and TPS. **A** and **B**: ZX planes of dose distributions for myQA iON/MC simulations and TPS, respectively, **C**: superimposition of isodoses, **D**: gamma index (DD=3%, DTA=3mm), **E**, **F** and **G**: profiles along Z, Y and Z axes (position of profiles is presented in **A** by the lilac dashed lines), **H**: gamma index histogram.

5.2.4.6. Treatment planning verification: Fricke-XO-Gelatin (thick gel)

Figure 56 (dosimeter vs. myQA iON/MC simulations), Figure 57 (dosimeter vs. TPS), and Figure 58 (TPS vs. myQA iON/MC simulations) show the comparison of the dose distribution measured using a thick dosimeter (scan of the sample presented in Figure 52 D) with the dose distribution calculated in the TPS and simulated with the aid of myQA iON software/MC simulations. As with the thin dosimeter verification, the measured dose distribution is non-uniform, taking the shape of three wide bands of higher dose separated by narrow bands of lower dose. The measured mean dose in the irradiated area was 4.16 ± 0.20 Gy. The doses calculated using the TPS and the myQA iON/MC simulations were 4.36 ± 0.10 Gy and 4.06 ± 0.10 Gy, respectively. The percentage difference between the measured and

calculated TPS doses is -4.81%, which falls within the required accuracy range of $\pm 3\text{-}5\%$ [189]. The mean dose calculated by myQA iON/MC simulations differed from the dose calculated by TPS by 7.39%, which is not accurate enough. The gamma index value exceeds 1 for 50% of the pixels when comparing the measured and calculated doses for the TPS, and for 65% of the pixels when comparing the measured and calculated doses in the myQA iON/MC simulations. In contrast, 0% of pixels had a gamma index value greater than 1 for TPS vs. myQA iON/MC simulations. Similar to the thin dosimeter, verifying the treatment plan using the thick dosimeter posed challenges in some respects. Although the mean measured and calculated dose values are similar, their distribution differs significantly. These differences are caused by the stripes visible in the scans. The stripes are also visible in the profiles plotted along the X-axis (across the stripes). The obtained profiles are wavy and differ in shape from those obtained in the TPS and myQA iON/MC simulations. However, the profiles along the Z-axis (along the stripes) for the measured and calculated dose distributions are similar in shape. The presence of bands may be caused by poor scanning quality, scanner quality, suboptimal quality of the foils covering the dosimeter on both sides, or other issues not recognized in this study. However, the most likely cause is the currently adopted manufacturing method of the dosimeters and scanning issues. Further research is needed to optimize dosimeter performance and scanning, despite these preliminary results proving the potential of the developed dosimetry system.

Fricke-XO-Gelatin (thick gel) vs. myQA



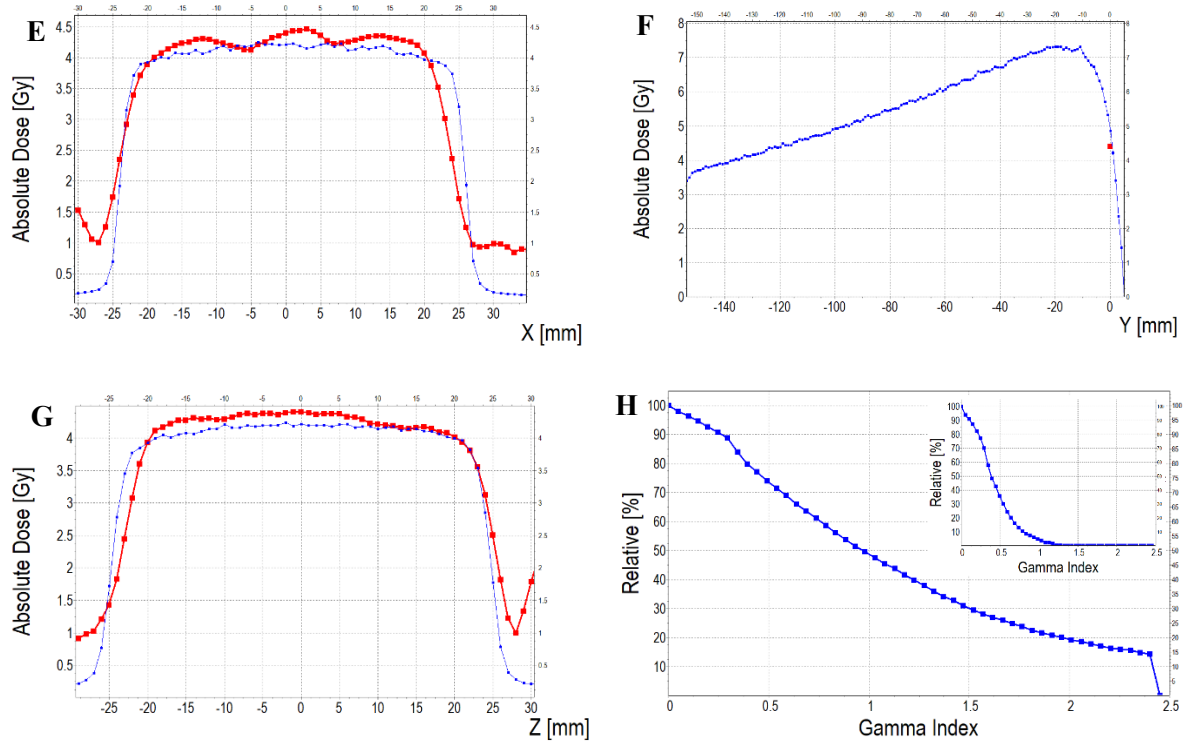
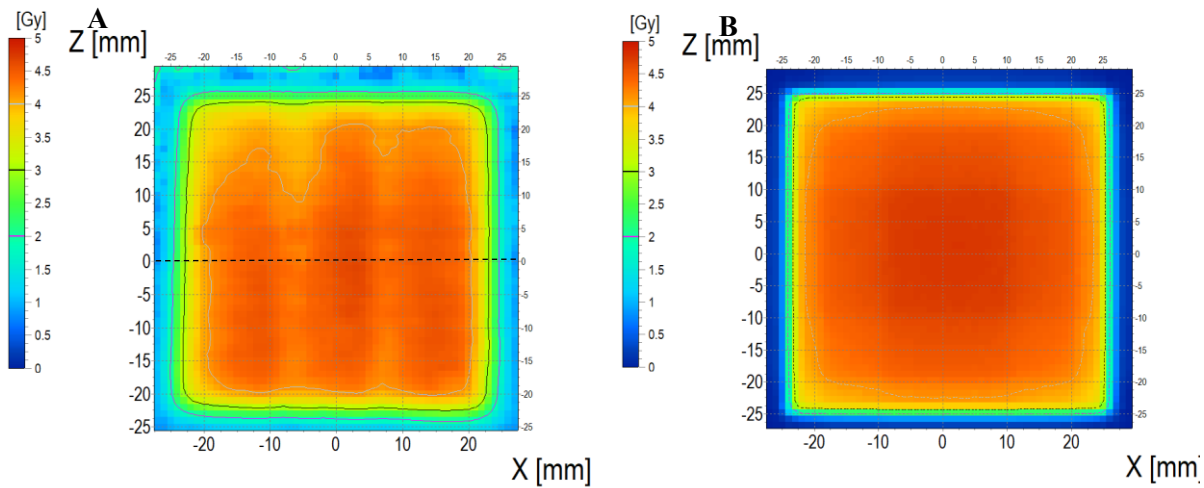


Figure 56. Comparison of dose distribution measured with Fricke-XO-Gelatin 2D dosimeter (thick gel) and calculated with myQA iON/MC simulations. **A** and **B**: ZX planes of dose distributions for Fricke-XO-Gelatin and myQA iON/MC simulations, respectively, **C**: superimposition of isodoses, **D**: gamma index (DD=3%, DTA=3mm), **E**, **F** and **G**: profiles along Z, Y and Z axes (position of profiles is presented in **A** by the black dashed lines), and **H**: gamma index histogram. Inset in **H**: a gamma index histogram for a ROI indicated in **D** with the white dashed line; 4.4% pixels above gamma index=1.

Fricke-XO-Gelatin (thick gel) vs. TPS



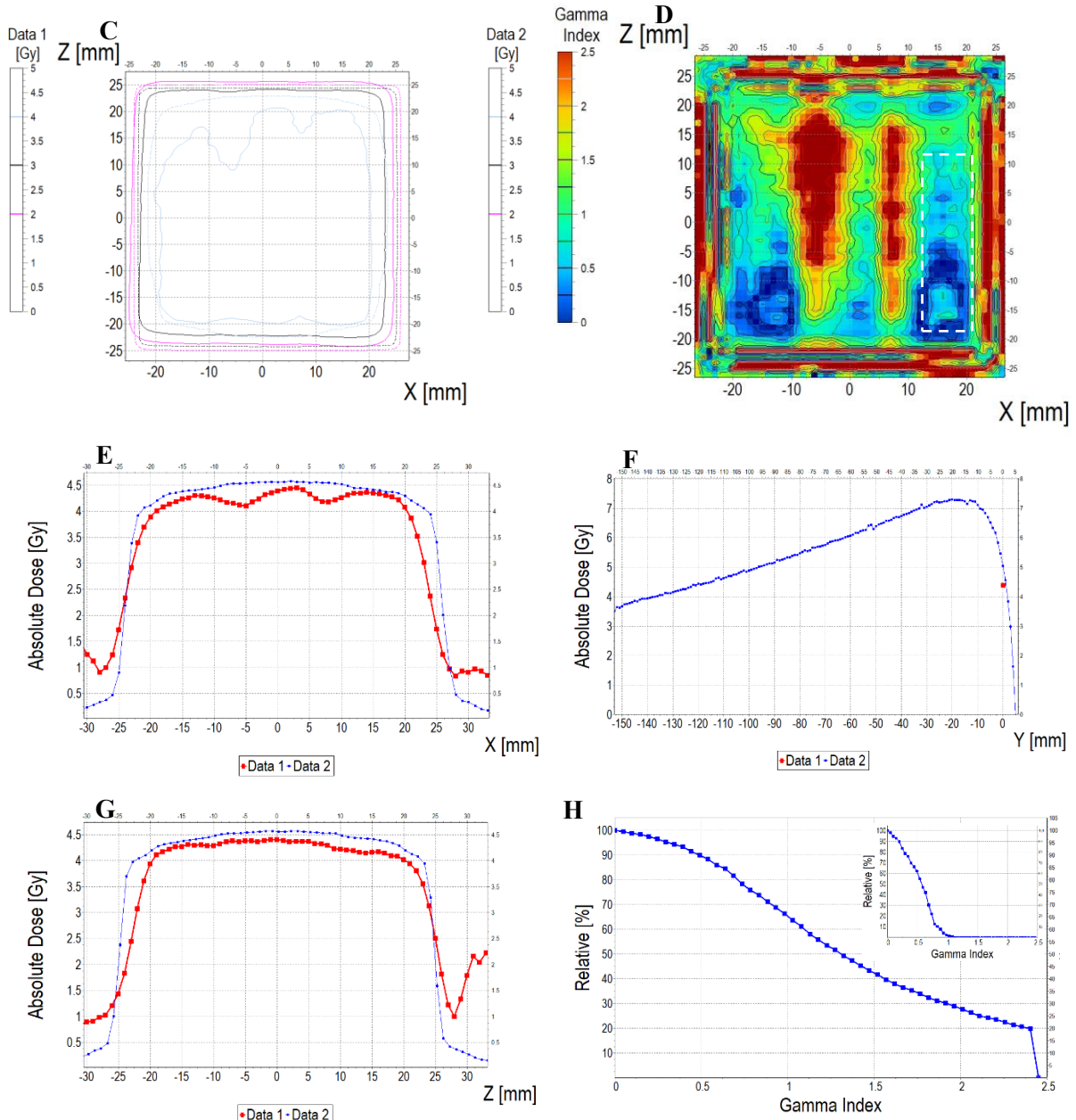


Figure 57. Comparison of dose distribution measured with Fricke-XO-Gelatin 2D dosimeter (thick gel) and calculated with TPS. **A** and **B**: ZX planes of dose distributions for Fricke-XO-Gelatin and TPS, respectively, **C**: superimposition of isodoses, **D**: gamma index (DD=3%, DTA=3mm), **E**, **F** and **G**: profiles along Z, Y and Z axes (position of profiles is presented in **A** by the black dashed lines), and **H**: gamma index histogram. Inset in **H**: a gamma index histogram for a ROI indicated in **D** with the white dashed line; 1.8% pixels above gamma index=1.

myQA vs. TPS

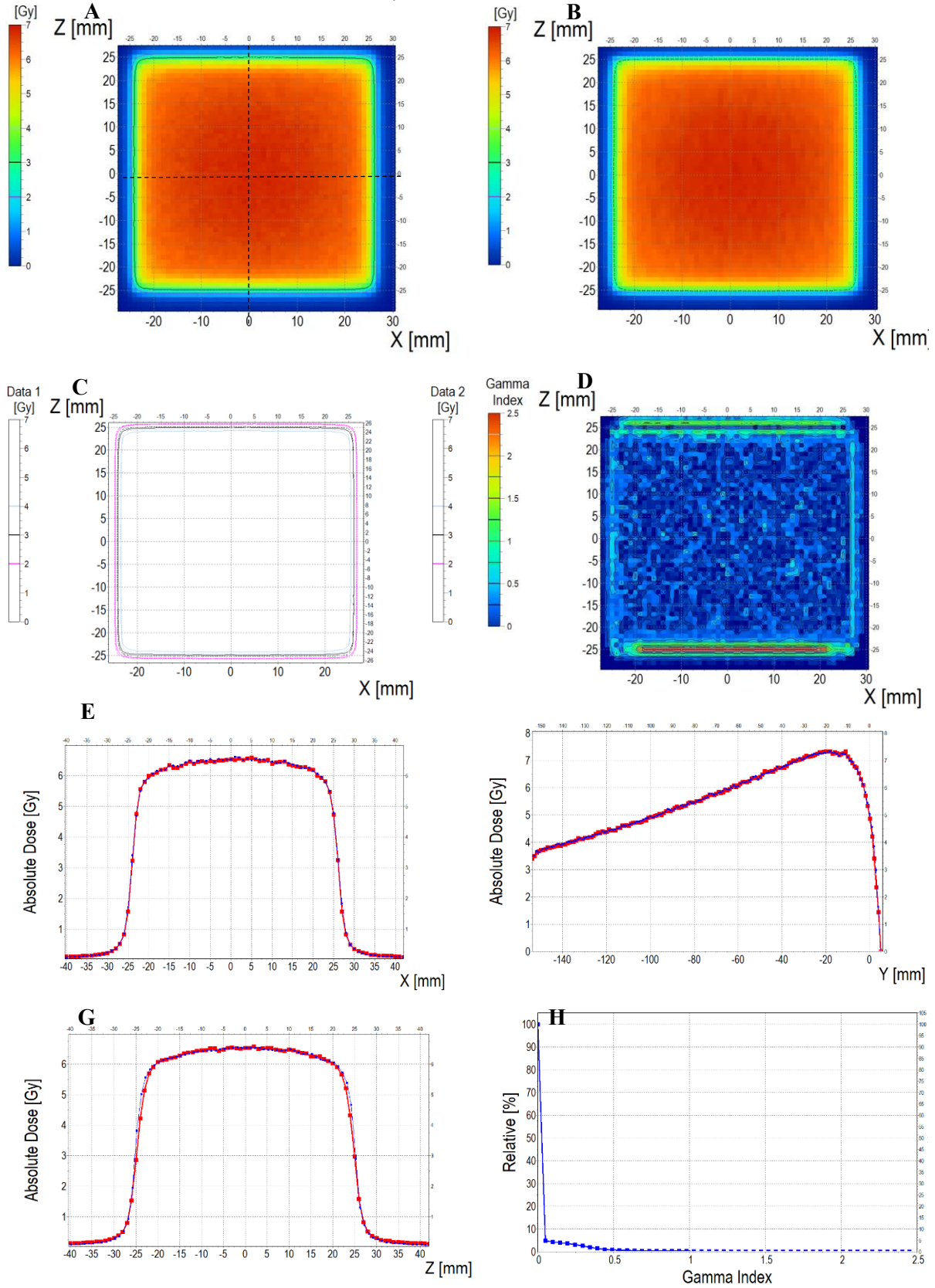


Figure 58. Comparison of dose distribution calculated with myQA iON/MC simulations and TPS. **A** and **B**: ZX planes of dose distributions for myQA iON/MC simulations and TPS, respectively, **C**: superimposition of isodoses, **D**: gamma index (DD=3%, DTA=3mm), **E**, **F** and **G**: profiles along Z, Y and Z axes (position of profiles is presented in **A** by the black dashed lines), **H**: gamma index histogram.

Table 8. Comparison of doses for Fricke-XO-Gelatin with sorbitol thin and thick gel dosimeters with myQA iON/MC simulations (abbreviated to myQA in this table) and TPS for a ROI of 40×40 mm² and 15×14 mm² (smaller regions are shown in [Figure 53](#), [Figure 54](#) and [Figure 55](#)), located in the middle of the irradiated square regions (image in plane resolution: 1×1 mm²).

No.	Parameter	For thin Fricke-XO-Gelatin gel (four square regions irradiated)						For thick Fricke-XO-Gelatin gel (one square region irradiated)					
		Fricke-XO-Gelatin vs. myQA		Fricke-XO-Gelatin vs. TPS		myQA vs. TPS		Fricke-XO-Gelatin vs. myQA		Fricke-XO-Gelatin vs. TPS		myQA vs. TPS	
		Fricke-XO- Gelatin (1)	myQA (2)	Fricke-XO- Gelatin (1)	TPS (2)	myQA (1)	TPS (2)	Fricke-XO- Gelatin (1)	myQA (2)	Fricke-XO- Gelatin (1)	TPS (2)	myQA (1)	TPS (2)
1	Minimum dose [Gy]	12.06	15.23	12.06	15.42	15.23	15.42	3.54	3.67	3.54	3.86	3.67	3.86
		2.95	2.54	2.95	2.63	2.54	2.63						
		4.50	4.82	4.50	5.07	4.82	5.07						
		7.04	6.94	7.04	7.36	6.94	7.36						
2	Maximum dose [Gy]	18.60	18.27	18.60	18.14	18.27	18.14	4.48	4.27	4.48	4.57	4.27	4.57
		4.25	3.83	4.25	3.61	3.83	3.61						
		7.42	7.45	7.42	7.10	7.45	7.10						
		10.76	10.81	10.76	10.25	10.81	10.25						
3	Mean dose [Gy]	16.63	17.27	16.63	17.27	17.27	17.27	4.16	4.06	4.16	4.36	4.06	4.36
		3.92	3.55	3.92	3.41	3.55	3.41						
		6.77	6.95	6.77	6.73	6.95	6.73						
		9.69	9.99	9.69	9.74	9.99	9.74						
4	STD dose [Gy]	1.2	0.6	1.2	0.5	0.6	0.5	0.2	0.1	0.2	0.1	0.1	0.1
		0.3	0.2	0.3	0.2	0.2	0.2						
		0.6	0.5	0.6	0.4	0.5	0.4						
		0.9	0.8	0.9	0.6	0.8	0.6						
5	Mean dose difference [%]= 100- (2)×100/(1)	-3.85		-3.85		0.00		2.40		-4.81		-7.39	
		9.44		13.01		3.94							
		2.66		0.59		3.17							
		3.10		0.52		2.50							

5.3. Application studies of the Fricke-XO-Gelatin with sorbitol and Fricke-XO-Pluronic F-127 3D dosimeters

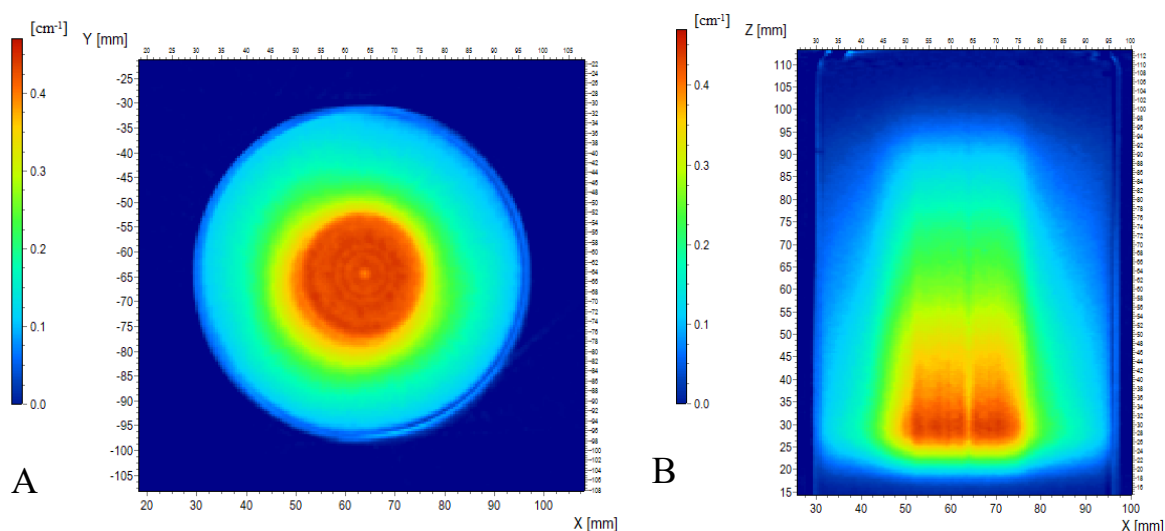
The research presented in this part of the work was performed during a three-month internship (15.09.2024-14.12.2024) carried out in the Laboratory of Physics of the Medical School of the National Kapodistrian University of Athens. The research was of an applied nature. Fricke-XO-Gelatin, Fricke-XO-Gelatin with sorbitol and Fricke-XO-Pluronic F-127 dosimeters were imaged using OCT. The compositions of the dosimeters and imaging conditions were optimized. The diffusion coefficients of the dosimeters were determined. In addition, the treatment plan was verified using Fricke-XO-Pluronic F-127 and Fricke-XO-Gelatin with sorbitol. Two manuscripts are being prepared in cooperation with scientists from Athens.

5.3.1. Optimization of gel composition and measurement conditions. Calibration of the dosimeters

The first dosimeter composition studied was 25% Pluronic F-127, 50 mM H_2SO_4 , 0.5 mM FAS, and 0.165 mM XO. The gel was scanned using a laser with a wavelength of 589 nm (orange light). The optical density distributions in the dosimeter scanned 65 min after irradiation, along with the calibration curves, are shown in [Figure 59](#). In the lower dose regions (30-50 mm and 75-95 mm on the X-axis, -95-(-77) mm and -50-(-35) mm on the Y-axis, and 18-25 mm and 55-90 mm), the optical density distribution corresponds to the planned dose distribution ([Figure 10 B](#)). However, in the part of the sample irradiated with the highest doses, artifacts are visible, which in the XY plane take the form of rings, while in the YZ and XZ planes they take the form of vertical stripes. The presence of artifacts is also visible in the optical density profile along the X axis ([Figure 63 A](#)), where in the range of 50-75 mm there are visible fluctuations in optical density, although according to the plan the dose in this area was homogeneous. The sources of ring artifacts are most often CCD matrix defects (dead pixels or a non-uniform pixels response to incident light) or dirt/scratches on the refractive index matching liquid tank or parts of the scanner optics. [133]. In the central part ($X = 64$ mm) of the profile ([Figure 63 A](#)), the optical density of the gel is the lowest for the discussed range of 50-75 mm, and in the XZ and YZ planes in the center of the sample a clearly lighter stripe can be observed. Most likely, this is cupping artifact resulting from too strong light absorption by the dye or light scattering from the used gelling agents [190,191]. A method to overcome the formation of cupping artifacts may be to weaken light absorption by reducing the concentration of the dye in the composition [192]. The optical density distributions in the XY, XZ and YZ planes as well as the calibration curves of the dosimeters containing 0.08 and 0.04 mM XO are presented in [Figure 60](#) and [Figure 61](#), respectively. Despite the reduction of the dye concentration, ring artifacts are still visible in the optical dose distributions. Cupping artifact can be observed in the central part of the gel containing 0.04 mM XO, but is not visible in the images of the sample with 0.08 mM dye. It is likely that further reduction of the XO concentration would be necessary to eliminate visible artifacts, but it should be noted that this may reduce the dose range in which the dosimeter can be used, as there will be too few dye particles in the composition to bind all oxidized iron ions (such a phenomenon could be observed in the optimization studies of Fricke-XO-Pluronic F-127 in cuvettes [142]). Hence, for further optimization experiment the dye concentration of 0.08 mM was chosen and the orange laser light (589 nm) in OCT was changed to red light with a wavelength of 633 nm, which is less absorbed by the dosimeter (maximum absorption at 585 nm [142]). After this change, no ring or cupping artifacts were observed in the optical density distribution images ([Figure 62](#)). This indicates

that the source of the ring artifacts was not a lamp failure or a dead spot on the CCD camera. Most likely the visible rings were caused by a damaged or dirty orange light filter or strong scattering of laser light by the sample. However, further studies should be conducted to explain the origin of the visible artifacts. Due to the significant improvement in the quality of the scans obtained during treatment plan verification using Fricke-XO-Pluronic F-127 (section 5.3.3.), the samples with 0.08 mM XO were scanned with a 633 nm laser.

Analyzing the obtained calibration curves, it can be seen that regardless of the composition and the laser light used, the gels darken intensively after irradiation. The dosimeter darkens most intensively within about the first two hours of irradiation. During this time, the greatest increase in sensitivity (the slope value of the curves) can also be observed, which indicates that most likely at this time reactions induced by ionizing radiation occur. Further darkening of the gel is most likely due to autoxidation of Fe^{3+} ions. For compositions containing 0.04 and 0.08 mM XO in the calibration curves obtained 9 hours after irradiation, the points for the dose of 4.15 Gy deviate from the linear relationship due to too low an optical density value. This may indicate saturation of the dosimeter in this area, or too strong light absorption and the formation of cupping artifact. This phenomenon negatively affects the time regime after irradiation, in which the dose distribution reading from the dosimeter should be performed. The sensitivity of the dosimeter depends on both the dye content and the laser light used. After the first scans performed with orange light, the highest sensitivity was observed for the composition containing 0.08 mM XO, and the lowest for 0.165 mM, however, as a result of changes occurring in the gels, after about 3 hours from irradiation, the composition with 0.04 mM dye showed the lowest sensitivity. The obtained results are contradictory to the observations made during the optimization of the dosimeter composition in the measuring cuvettes [142], where the highest sensitivity was shown by the gel containing 0.165 mM XO. The differences in the observations may result from the presence of artifacts visible in the studies using OCT. The use of light with a wavelength of 633 nm resulted in an approximately three-fold decrease in the sensitivity of the dosimeter, which is due to the weaker absorption of red light by the gel.



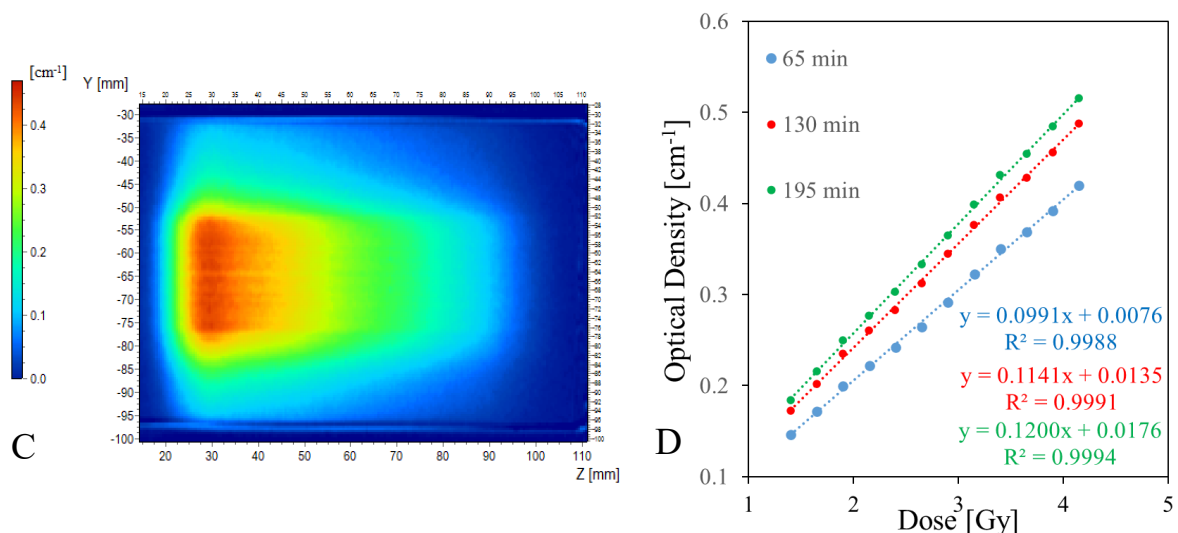


Figure 59. Optical density distributions in the XY (A), XZ (B), and YZ (C) planes. Images were obtained by scanning Fricke-XO-Pluronic F-127 (25% Pluronic, 50 mM H₂SO₄, 0.5 mM FAS, 0.165 mM XO) irradiated according to the calibration plan. The scan was performed using OCT (laser wavelength 589 nm) 65 min after irradiation. Calibration curves obtained from scans performed 65, 130 and 190 min after irradiation are presented in D.

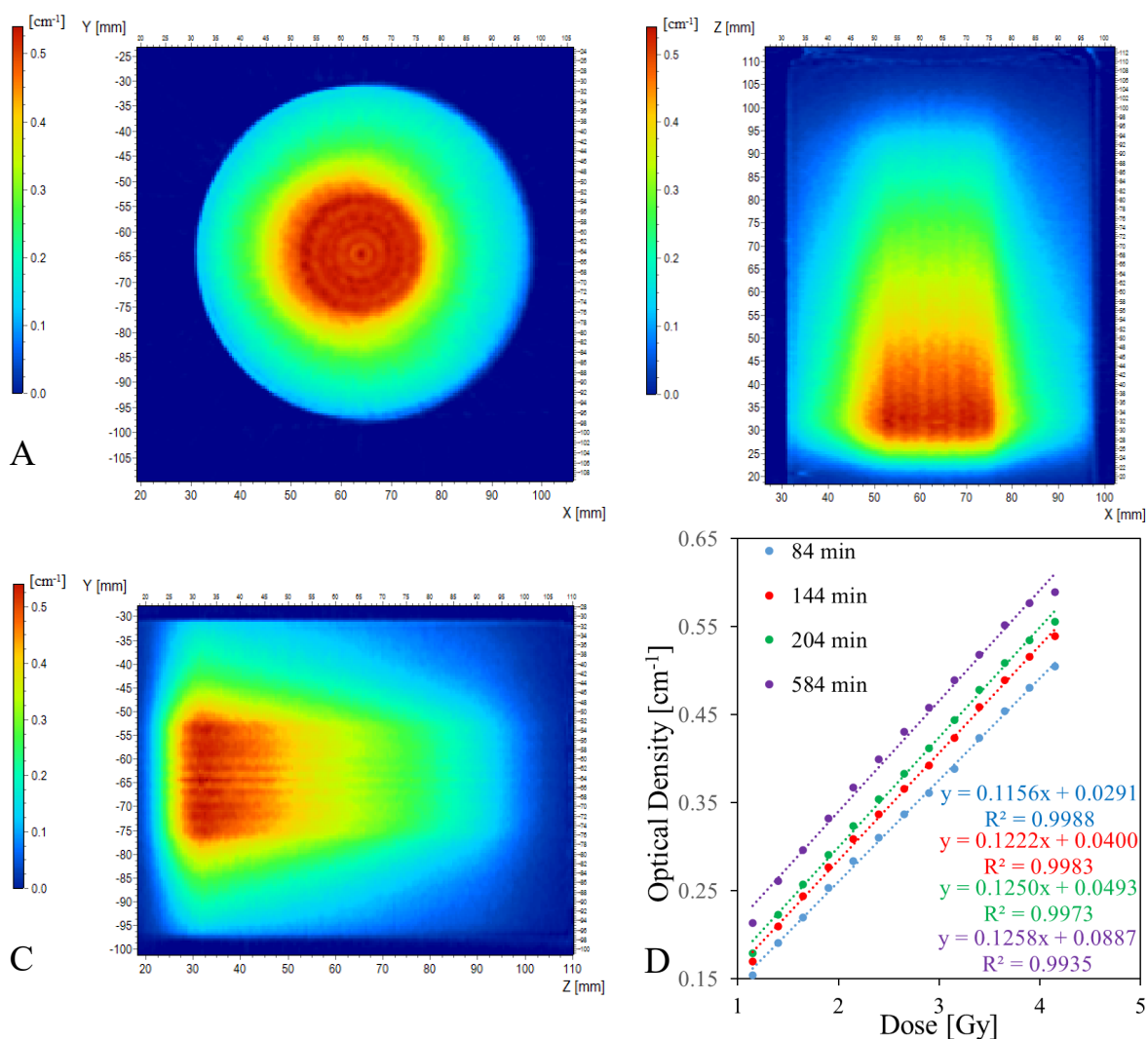


Figure 60. Optical density distributions in the XY (A), XZ (B), and YZ (C) planes. Images were obtained by scanning Fricke-XO-Pluronic F-127 (25% Pluronic, 50 mM H₂SO₄, 0.5 mM FAS, 0.08

mM XO) irradiated according to the calibration plan. The scan was performed using OCT (laser wavelength 589 nm) 84 min after irradiation. Calibration curves obtained from scans performed 84, 144, 204 and 584 min after irradiation are presented in **D**.

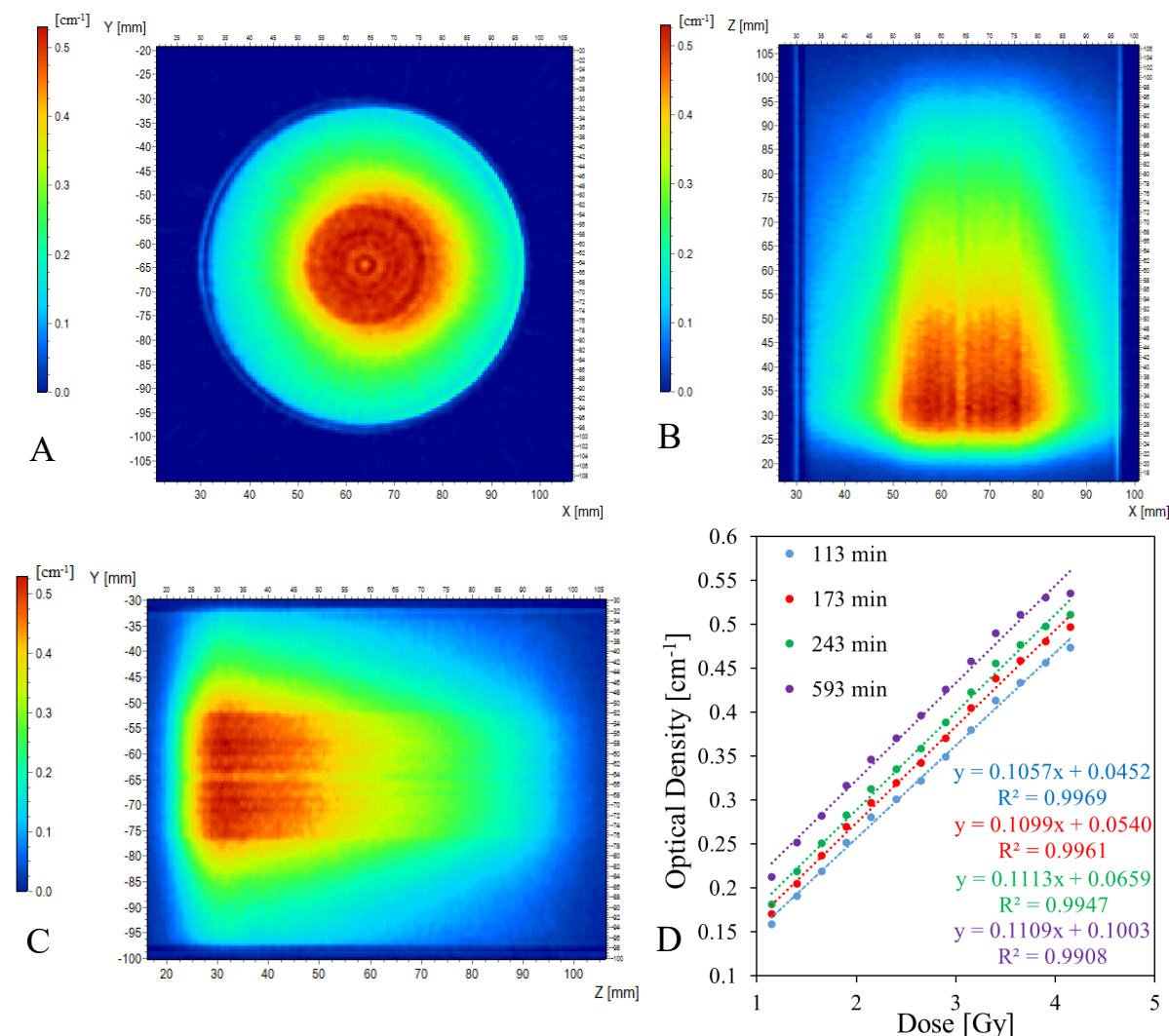


Figure 61. Optical density distributions in the XY (**A**), XZ (**B**), and YZ (**C**) planes. Images were obtained by scanning Fricke-XO-Pluronic F-127 (25% Pluronic, 50 mM H₂SO₄, 0.5 mM FAS, 0.04 mM XO) irradiated according to the calibration plan. The scan was performed using OCT (laser wavelength 589 nm) 113 min after irradiation. Calibration curves obtained from scans performed 113, 173, 243 and 593 min after irradiation are presented in **D**.

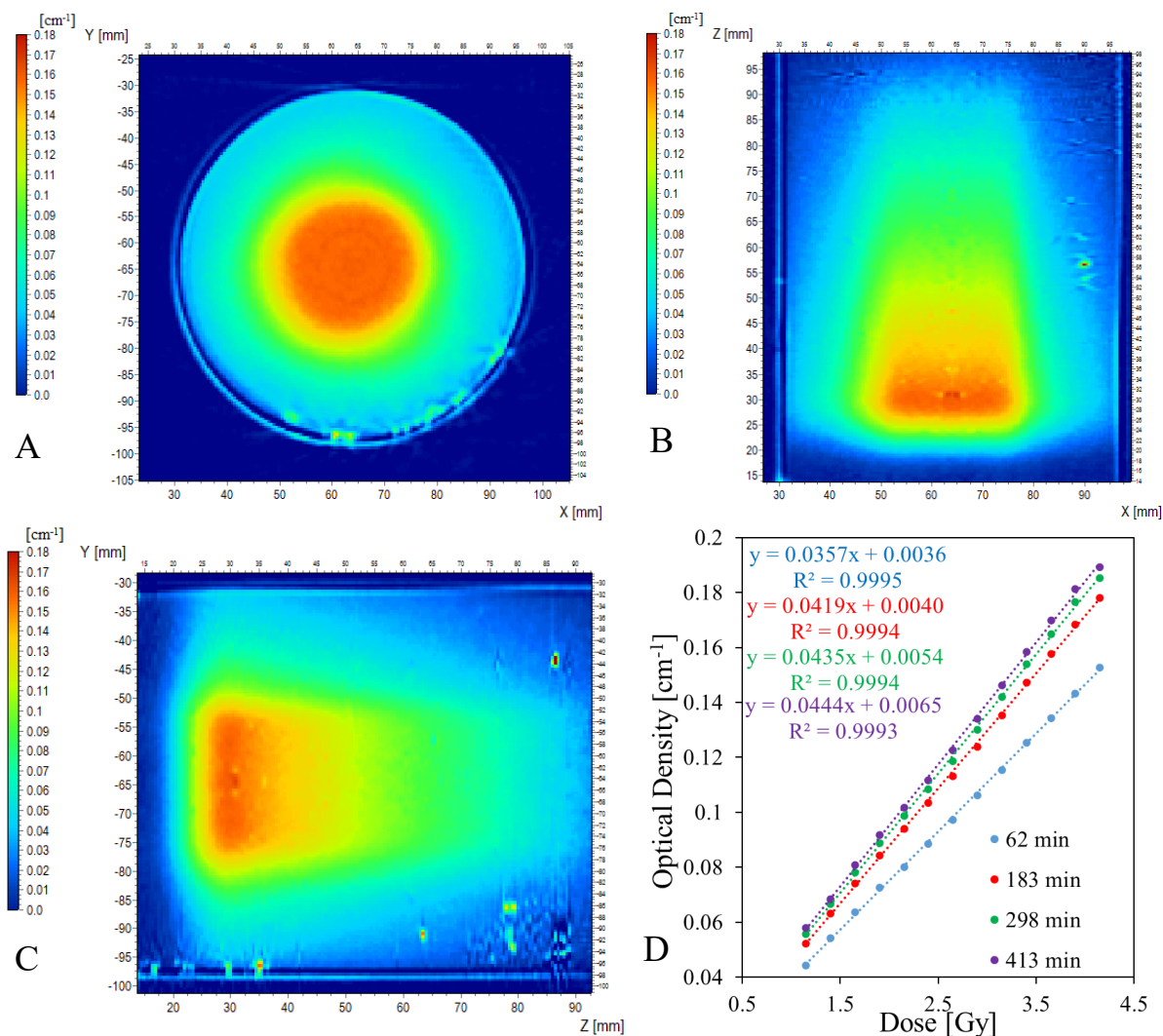


Figure 62. Optical density distributions in the XY (A), XZ (B), and YZ (C) planes. Images were obtained by scanning Fricke-XO-Pluronic F-127 (25% Pluronic, 50 mM H_2SO_4 , 0.5 mM FAS, 0.08 mM XO) irradiated according to the calibration plan. The scan was performed using OCT (laser wavelength 633 nm) 62 min after irradiation. Calibration curves obtained from scans performed 62, 183, 298 and 413 min after irradiation are presented in D.

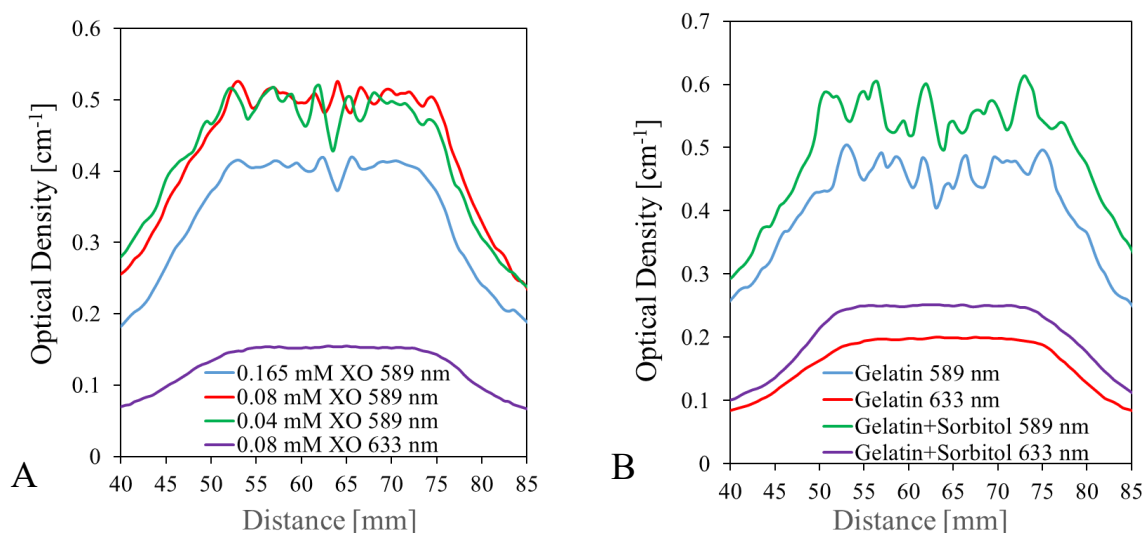


Figure 63. Optical density profiles plotted along the X axis for Fricke-XO-Pluronic F-127 (A), Fricke-XO-Gelatin, and Fricke-XO-Gelatin with sorbitol (B). The profiles were obtained from the scans presented in Figures 59-62 and 65-67.

The optimization studies of Fricke-XO-Gelatin and Fricke-XO-Gelatin with sorbitol were started with a composition containing 8% gelatin, 50 mM H₂SO₄, 0.5 mM FAS and 0.165 mM XO. The composition with sorbitol contained 23% of this compound. Both tested dosimeters were too dark and completely absorbed the laser light (589 nm) and as a result no images of optical density distributions were obtained. Scanning of brighter gels with reduced dye concentration to 0.04 and 0.08 mM was also not successful. Images of optical density distributions were obtained after using a concentration of XO of 0.08 mM and reducing the gelatin content to 4%. The obtained optical density distributions with calibration curves are presented in Figure 64 (Fricke-XO-Gelatin) and Figure 66 (Fricke-XO-Gelatin with sorbitol). Similarly to the Pluronic dosimeter scanned with orange light, clearly visible ring artifacts are visible in the center of the scans of both the gelatin and gelatin-sorbitol compositions. In the profiles along the X axis (Figure 63 B), these artifacts are visible between 50 and 75 mm as optical density fluctuations. Changing the wavelength of laser light in OCT to 633 nm allowed obtaining artifact-free images (Figure 65 and Figure 67). The points on the calibration curves obtained for the samples scanned with orange light (589 nm) are characterized by poor adjustment to the linear relationship (after about 2 h from irradiation, the R² coefficient for the compositions with gelatin and gelatin with sorbitol is 0.9927 and 0.9852, respectively), which is most probably the result of artifacts present in the scans. Moreover, for the dosimeter with gelatin and sorbitol, the optical density value for the highest doses (from 3.8 Gy) does not increase with time from irradiation (in contrast to the areas irradiated with lower doses), and for the dosimeter with gelatin, a decrease in optical density can be observed in the area irradiated with a dose of 4.15 Gy. This most probably indicates the formation of cupping artifacts as a result of gel darkening. Scanning with red light (633 nm) allows obtaining calibration curves with better fit to the linear relationship, which however decreases with time from irradiation due to gel darkening. The changes occurring in the gelatin and gelatin with sorbitol dosimeters are much less intensive than those observed for the Pluronic dosimeters and are most probably caused only by autoxidation of ferric ions. This indicates that most reactions induced by ionizing radiation in compositions with gelatin occur at the latest about 45 minutes after irradiation, while for the Pluronic gel this time is at least about 2 hours. The highest sensitivity of the tested compositions was demonstrated by Fricke-XO-Gelatin with sorbitol. The addition of sorbitol increased the sensitivity by over 26% (one hour after irradiation) compared to

Fricke-XO-Gelatin. The least sensitive to radiation was Fricke-XO-Pluronic F-127. [Table 9](#) presents the optimized dosimeter compositions and measurement conditions using OCT.

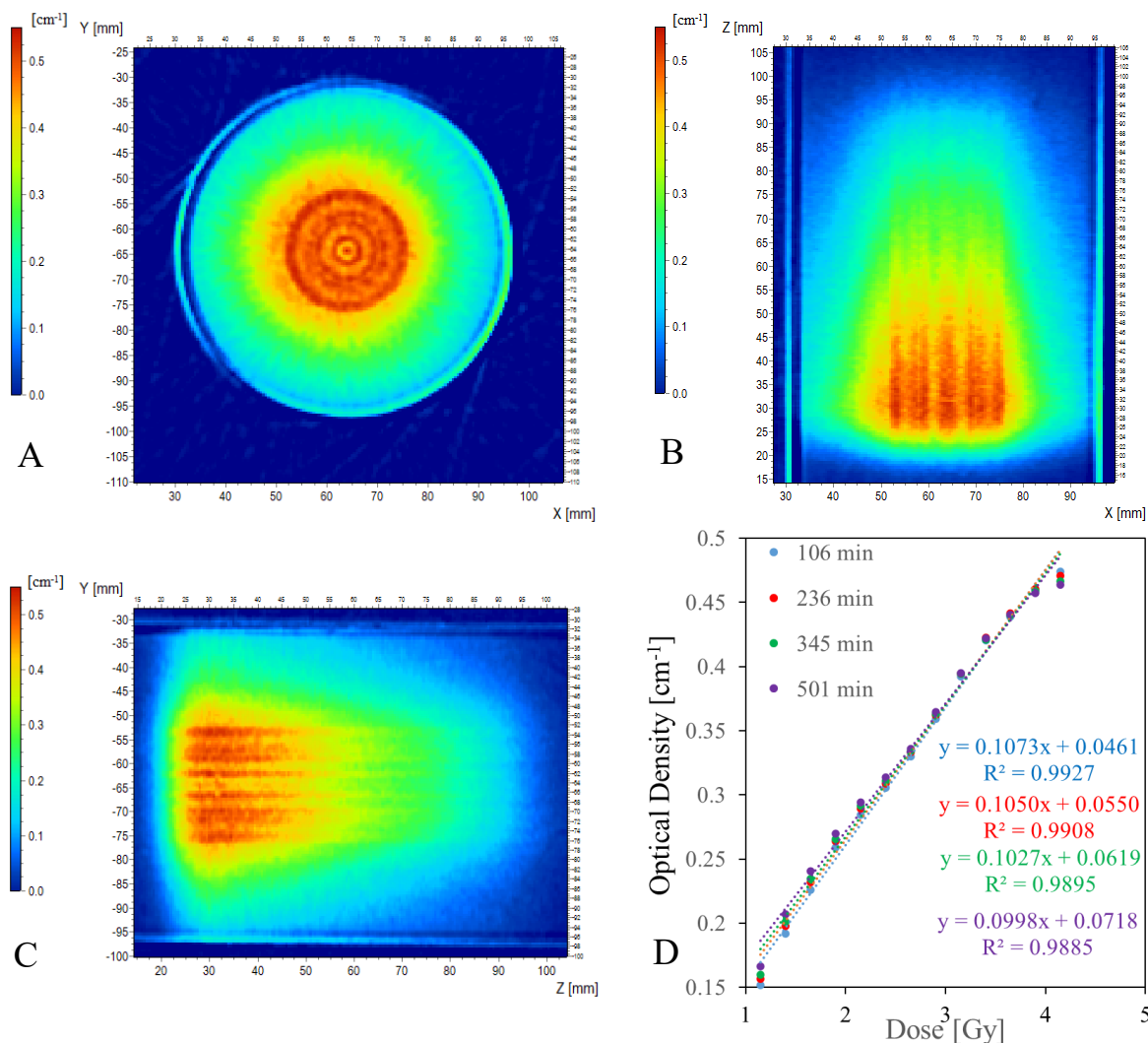


Figure 64. Optical density distributions in the XY (A), XZ (B), and YZ (C) planes. Images were obtained by scanning Fricke-XO-Gelatin (4% Gelatin, 50 mM H_2SO_4 , 0.5 mM FAS, 0.08 mM XO) irradiated according to the calibration plan. The scan was performed using OCT (laser wavelength 589 nm) 106 min after irradiation. Calibration curves obtained from scans performed 106, 236, 345 and 501 min after irradiation are presented in D.

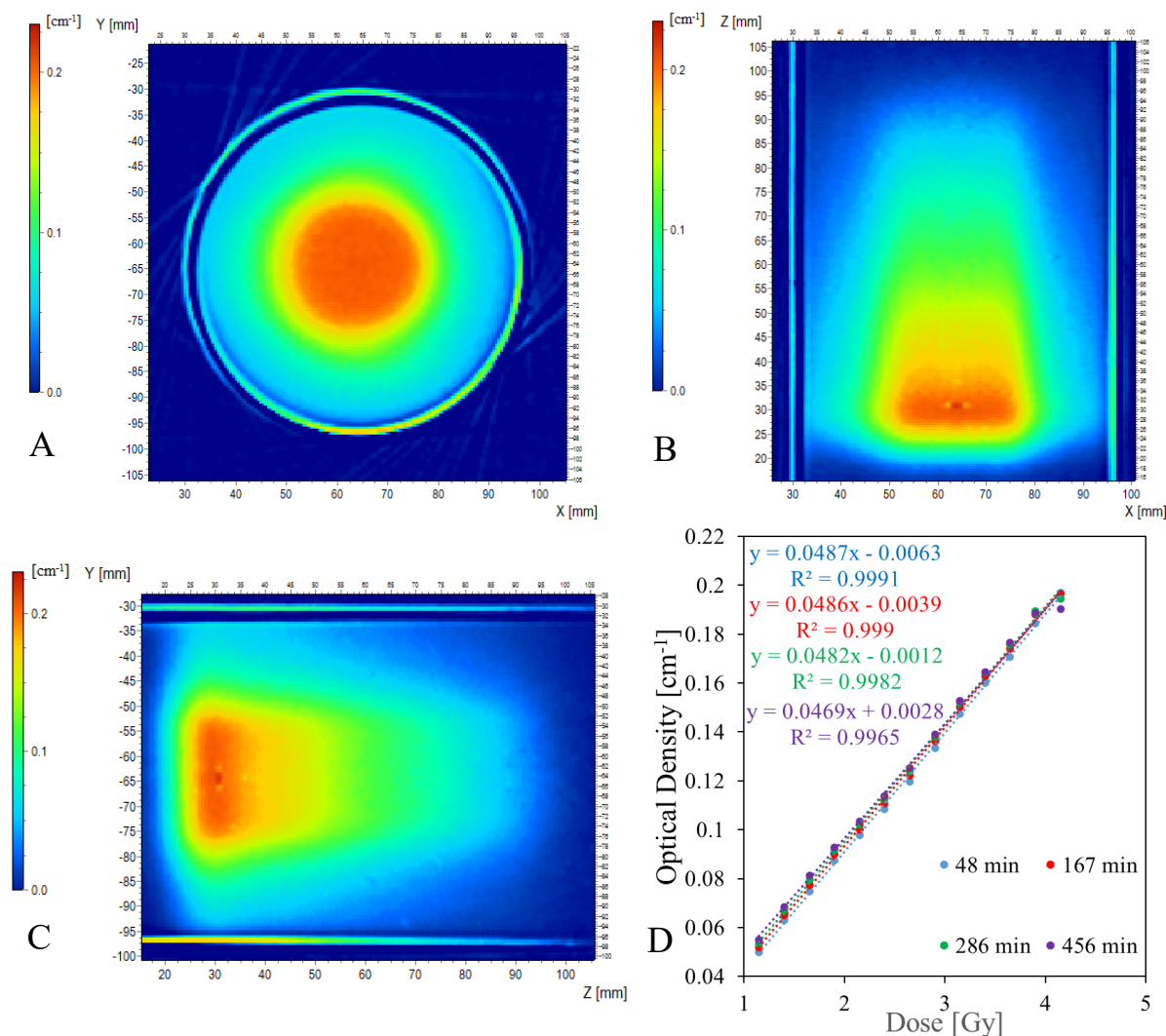
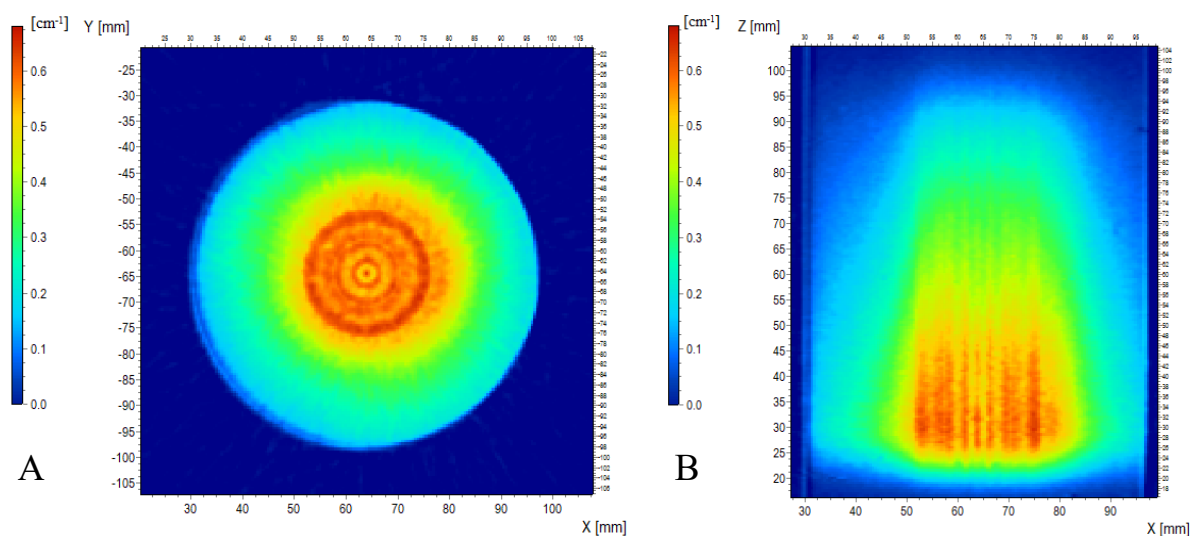


Figure 65. Optical density distributions in the XY (A), XZ (B), and YZ (C) planes. Images were obtained by scanning Fricke-XO-Gelatin (4% Gelatin, 50 mM H₂SO₄, 0.5 mM FAS, 0.08 mM XO) irradiated according to the calibration plan. The scan was performed using OCT (laser wavelength 633 nm) 48 min after irradiation. Calibration curves obtained from scans performed 48, 167, 286 and 456 min after irradiation are presented in D.



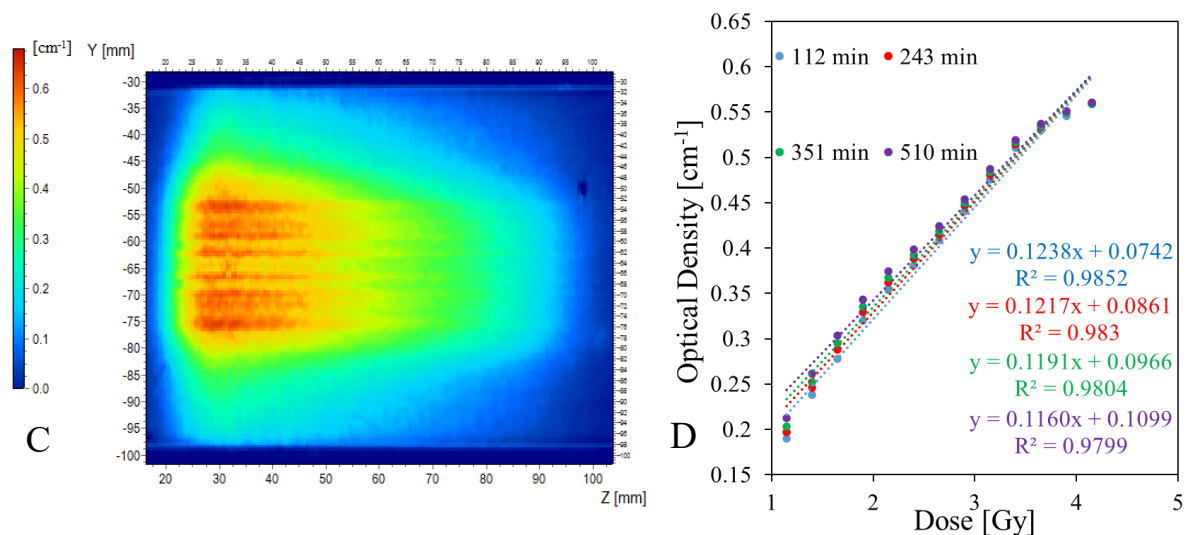


Figure 66. Optical density distributions in the XY (A), XZ (B), and YZ (C) planes. Images were obtained by scanning Fricke-XO-Gelatin with sorbitol (4% Gelatin, 50 mM H_2SO_4 , 0.5 mM FAS, 0.08 mM XO, 23% sorbitol) irradiated according to the calibration plan. The scan was performed using OCT (laser wavelength 589 nm) 112 min after irradiation. Calibration curves obtained from scans performed 112, 243, 351 and 510 min after irradiation are presented in D.

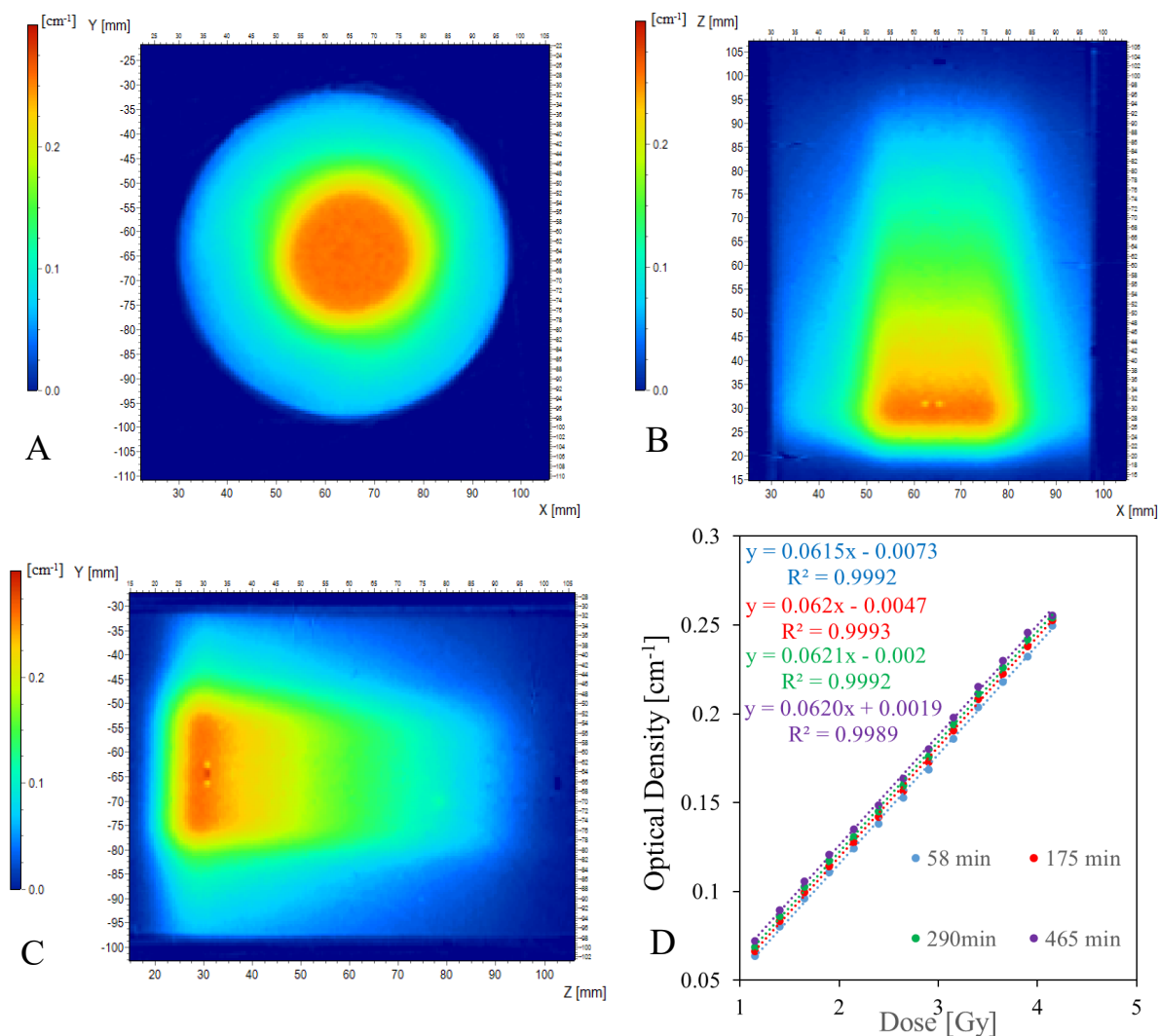


Figure 67. Optical density distributions in the XY (A), XZ (B), and YZ (C) planes. Images were obtained by scanning Fricke-XO-Gelatin with sorbitol (4% Gelatin, 50 mM H_2SO_4 , 0.5 mM FAS,

0.08 mM XO, 23% sorbitol) irradiated according to the calibration plan. The scan was performed using OCT (laser wavelength 633 nm) 58 min after irradiation. Calibration curves obtained from scans performed 58, 175, 290 and 465 min after irradiation are presented in **D**.

Table 9. Optimal dosimeter compositions and OCT measurement conditions.

Composition	Optimal concentrations of dosimeter components						OCT laser wavelength [nm]	Sensitivity (1 hour after irradiation) [Gy ⁻¹ cm ⁻¹]
	H ₂ SO ₄ [mM]	FAS [mM]	XO [mM]	Pluronic F-127 [%]	Gelatin [%]	Sorbitol [%]		
Fricke-XO-Pluronic F-127	50	0.5	0.08	25	0	0	633	0.0357
Fricke-XO-Gelatin	50	0.5	0.08	0	4	0	633	0.0487
Fricke-XO-Gelatin with sorbitol	50	0.5	0.08	0	4	23	633	0.0615

5.3.2. Determination of the diffusion coefficient of Fricke dosimeters

The diffusion coefficient values were determined for Fricke-XO-Pluronic F-127 (25% Pluronic F-127, 0.08 mM XO, scanned with a laser at a wavelength of 589 nm), Fricke-XO-Gelatin (4% gelatin, 0.08 mM XO, scanned with a laser at a wavelength of 633 nm), and Fricke-XO-Gelatin with sorbitol (4% gelatin, 23% sorbitol, 0.08 mM XO, scanned with a laser at a wavelength of 633 nm). Each of the tested compositions contained 50 mM H₂SO₄ and 0.5 mM FAS. In the center of each sample, a cylindrical volume with a base diameter of 6 cm and a height of 1 cm was homogeneously irradiated with a dose of 3 Gy. The base of the cylinder was parallel to the bottom of the vial. The optical density distribution images of the samples in the XZ plane obtained by scanning the samples over time are shown in [Figure 68 A-F](#) (Fricke-XO-Pluronic F-127), [Figure 69 A-F](#) (Fricke-XO-Gelatin) and [Figure 70 A-F](#) (Fricke-XO-Gelatin with sorbitol). In the scans of each dosimeter, it can be seen that the optical density distribution in the irradiated volume is inhomogeneous, which is incongruent with the irradiation plan. The optical density inside the sample is lower than in the external part. This phenomenon is also visible in the optical density distributions in the XY plane ([Figure 71 A, C, E](#)) and in the profiles plotted along the X axis ([Figure 71 B, D, F](#)). It is the result of the formation of the cupping artifacts. Despite the applied dose (3 Gy) being lower than the maximum dose used in the calibration plan (4.15 Gy, section 5.3.1.), due to irradiation along the entire optical path of the sample, the artifacts created are much more visible than in the scans of gels irradiated with the calibration plan. The highest optical density amplitude (about 0.2 cm⁻¹) was observed for Fricke-XO-Pluronic F-127, and the ring artifacts can also be observed in the scans of this gel sample, which is the result of scanning the dosimeter with orange light (589 nm). Although in the part of the work dedicated to the optimization of scanning conditions (section 5.3.1.) red light was determined as more suitable for scanning Fricke dosimeters, the studies determining the diffusion coefficient were conducted in parallel with the optimization studies and the diffusion of the dosimeter with Pluronic was investigated before attempting to read the dose distribution using the red light.

At 530 min post-irradiation, a small volume of high optical density can be seen at the bottom of the scans of the Fricke-XO-Pluronic F-127 sample (indicated by the red arrow in [Figure 68 B](#)). With time after irradiation, this volume significantly enlarges, furthermore, 1680 min after irradiation, another time-increasing volume of higher optical density appears at the bottom of the sample (from 32 mm to

40 mm on the X-axis). These artifacts are the result of autoxidation of Fe^{2+} ions occurring locally faster than in the entire volume of the gel. The cause of their formation is currently unknown; however, as similar artefacts did not appear in dosimeters containing gelatin, it is possible that they originate from the micellar structure of the physical gel created by Pluronic F-127 [193]. In the hydrophobic core of the micelles, there may be a local increase in concentrations of the oxygen or impurities from the vials (artifacts formed at the point of contact between the gel and the vessel), leading to faster oxidation of ferrous ions. Nevertheless, further research is required to fully understand the formation of these artifacts.

The diffusion coefficients of the dosimeters were determined following the method proposed elsewhere [146]. The authors used the Einstein-Smoluchowski equation (33) [194]:

$$\overline{x^2} = 2Dt \quad (33)$$

where $\overline{x^2}$ denotes the mean square of the displacements of particles in one dimension, D is the diffusion coefficient and t is time. To determine the D value for each sample, twelve profiles were plotted along the Z axis of the scans obtained. Due to the presence of cupping artifacts, the profiles were plotted so that they passed through points lying in the XY plane at the same distance from the center of the sample (the position of the points is indicated by the white dashed circles in Figure 71 A, C, E). The maximum values of the profiles obtained in this way were similar despite the observed artifacts. Then, the average profile was calculated from the twelve profiles obtained. Since diffusion in the samples occurred both in the direction of gravity (towards the bottom of the vial) and against it (towards the cap of the vial), the average profile was divided into two (the division axis was a straight line parallel to the ordinate axis and passing through the maximum value of the profile), which enabled the determination of the effect of gravity on the diffusion coefficient of $[\text{Fe-XO}]^{3+}$ complexes. The profiles obtained in this way are shown in Figure 68 G, H (Fricke-XO-Pluronic F-127), Figure 69 G, H (Fricke-XO-Gelatin) and Figure 70G, H (Fricke-XO-Gelatin with sorbitol). The profiles were fitted to the "DoseResp" function equation using Origin software (equation (34), Origin 2021, OriginLab Corporation, USA):

$$y = A1 + \frac{A2 - A1}{1 + 10^{(\log x_0 - x)p}} \quad (34)$$

where y is the optical density, x is the distance, A1 and A2 are the lower and upper asymptotes, respectively, p is the slope factor of the curve and $\log x_0$ is the position of the inflection point of the profile related to the movement of the boundary between the irradiated and non-irradiated parts of the gel. With diffusion, the position of the inflection point changes. According to the equation (33), the slope of the relationship $(\log x_0)^2 = f(t)$ divided by two is equal to D. The determined diffusion coefficients are presented in the Table 9.

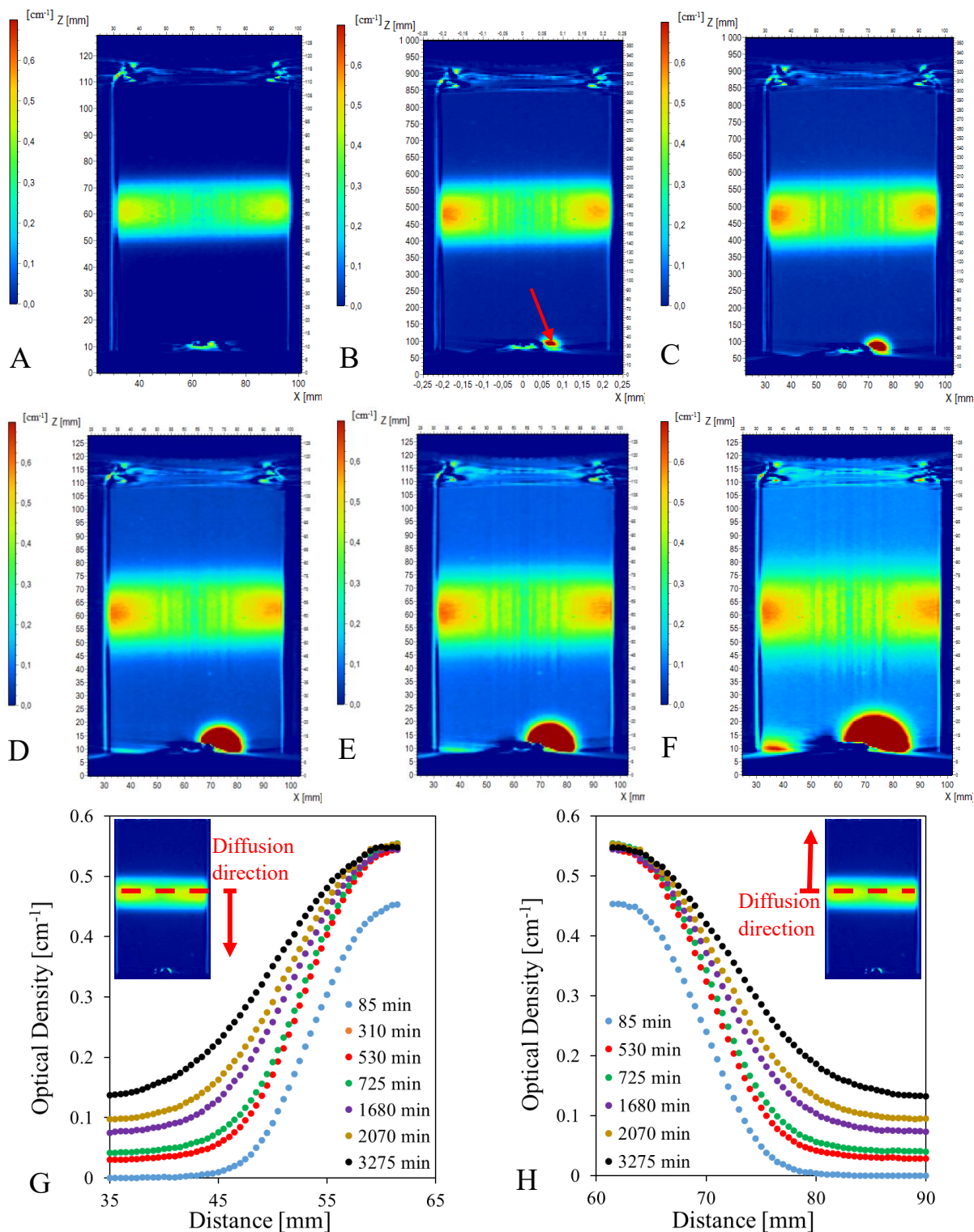


Figure 68. Images of optical density distributions in the XZ plane obtained for Fricke-XO-Pluronic F-127. Based on scans obtained 85 (A), 530 (B), 725 (C), 1680 (D), 2070 (E) and 3275 (F) min after irradiation, profiles were obtained that were used to determine the diffusion coefficient of the dosimeter occurring in the direction of gravity (G) and opposite (H). Due to the at least 2-hour time when the reactions induced by ionizing radiation occur in the gel, the profile obtained 85 min after irradiation was not included in the calculations. The red arrow in B indicates an artifact resulting from autoxidation of Fe^{2+} ions occurring locally faster than in the entire volume of the dosimeter.

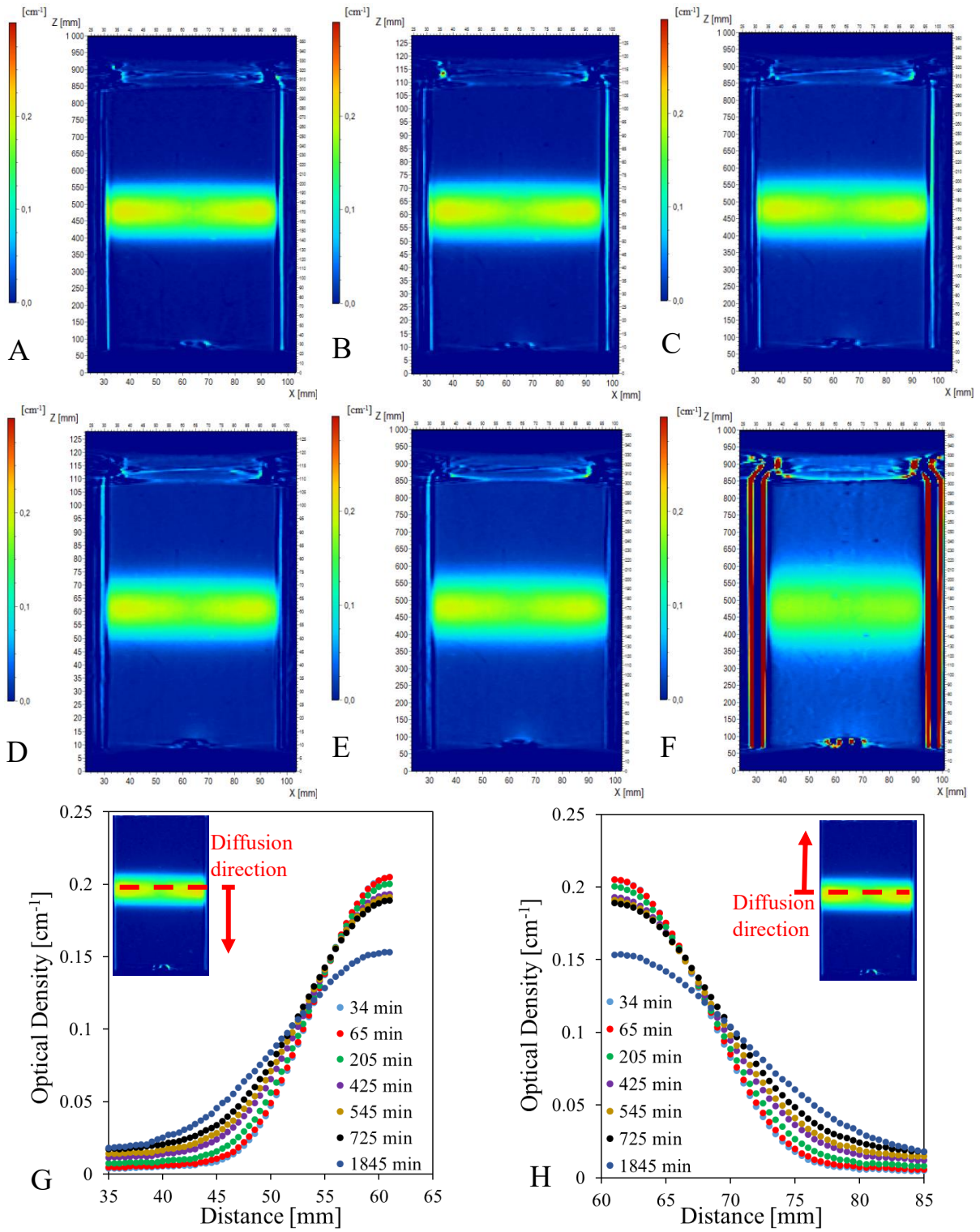


Figure 69. Images of optical density distributions in the XZ plane obtained for Fricke-XO-Gelatin. Based on scans obtained 34 (A), 205 (B), 425 (C), 545 (D), 725 (E) and 1845 (F) min after irradiation, profiles were obtained that were used to determine the diffusion coefficient of the dosimeter occurring in the direction of gravity (G) and opposite (H).

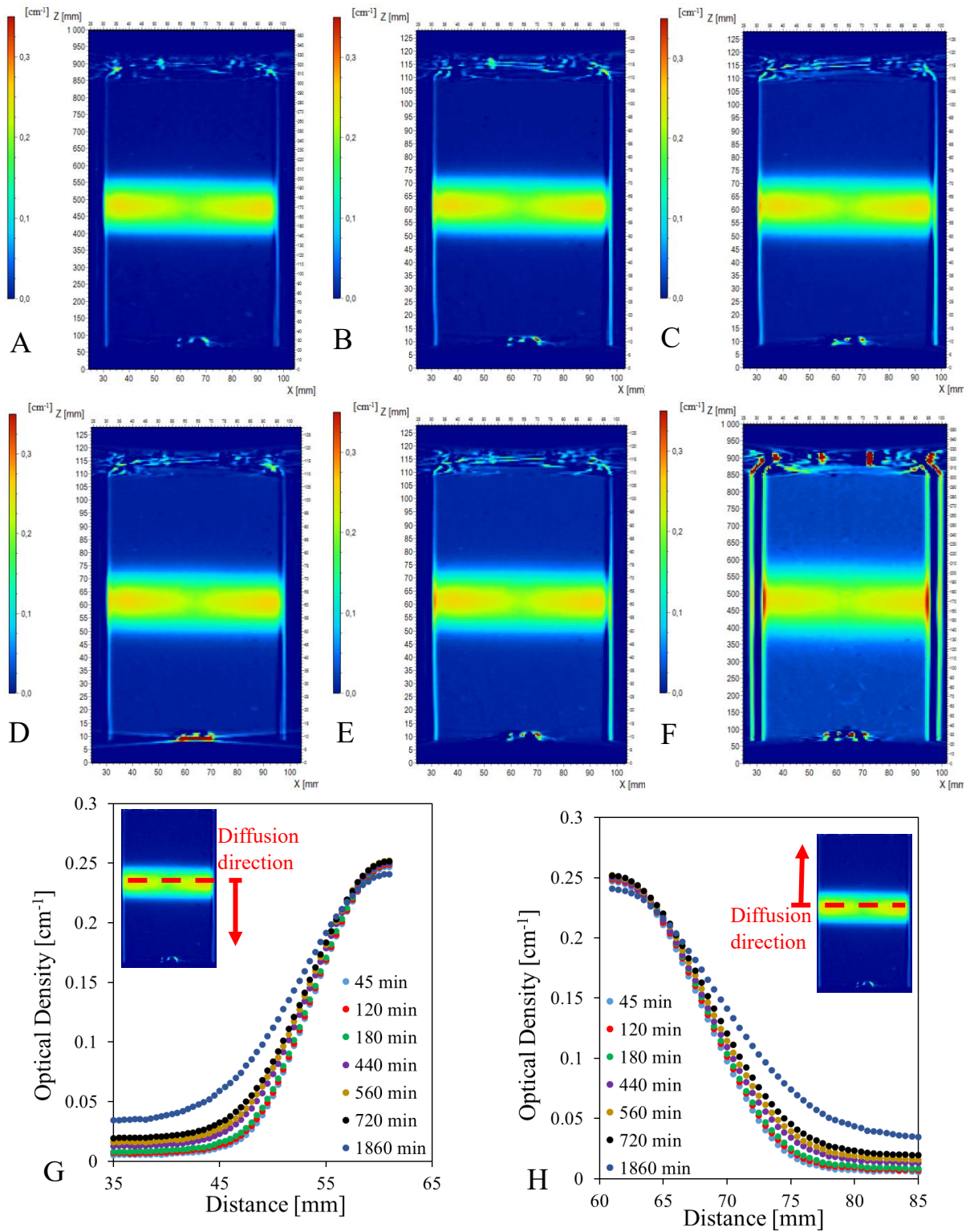


Figure 70. Images of optical density distributions in the XZ plane obtained for Fricke-XO-Gelatin with sorbitol. Based on scans obtained 45 (A), 180 (B), 440 (C), 560 (D), 720 (E) and 1860 (F) min after irradiation, profiles were obtained that were used to determine the diffusion coefficient of the dosimeter occurring in the direction of gravity (G) and opposite (H).

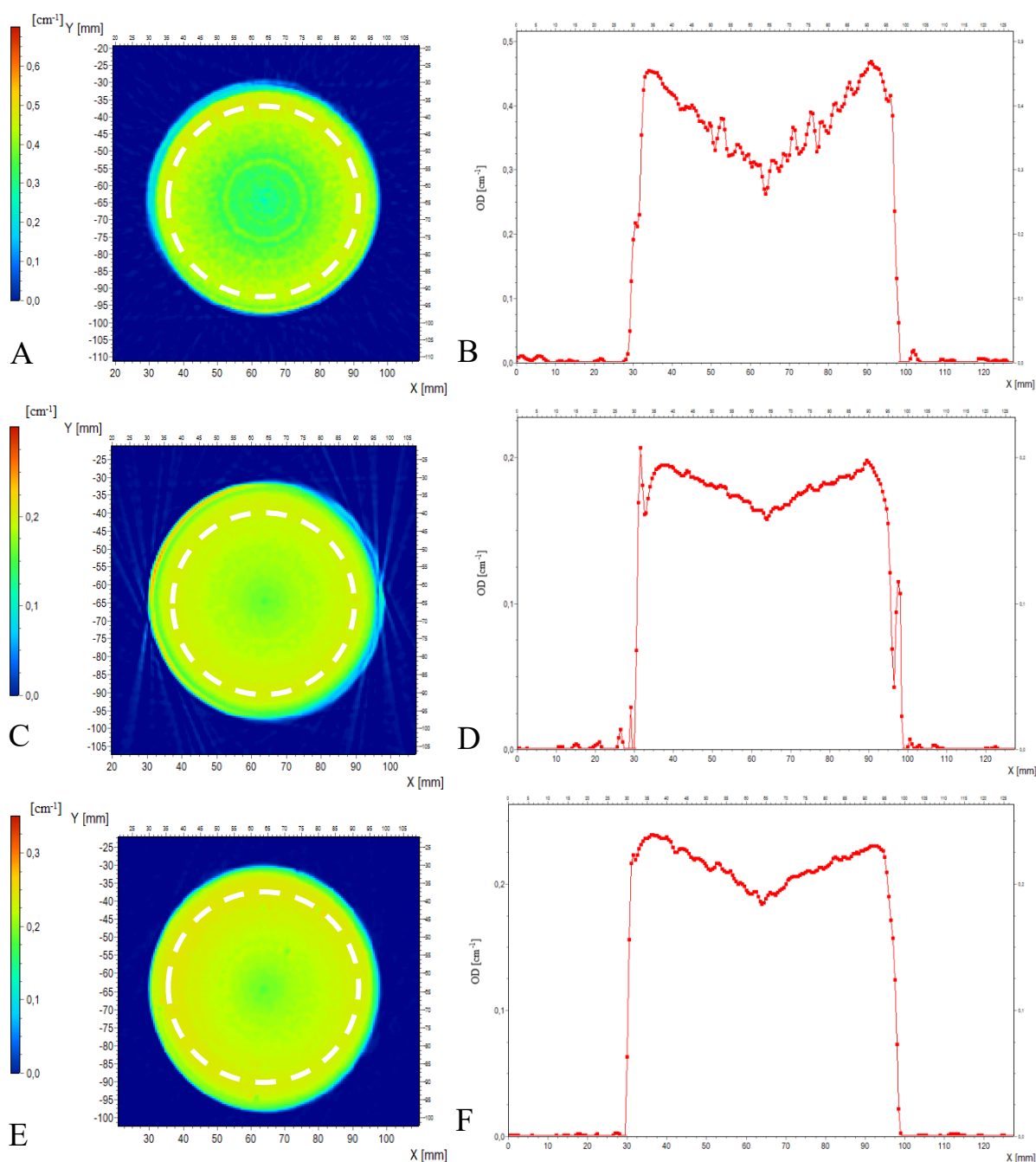


Figure 71. Images of the optical density distributions in the XY plane for Fricke-XO-Pluronic F-127 (A), Fricke-XO-Gelatin (C), and Fricke-XO-Gelatin with sorbitol (E) irradiated for the determination of the diffusion coefficient of these dosimeters. The white dashed circles in the images indicate the distances from the center of the samples at which the profiles along the Z axis passed, from which the mean profiles shown in Figures 68-70 (G, H) were determined. In B, D, and F, the optical density profiles plotted along the X axis of the images shown in A, C, and E, respectively, are shown.

The values of diffusion coefficients of Fricke dosimeters with different matrices and additives presented in the literature are in the range of 0-1.83 mm²h⁻¹ [148]. The values obtained in this part of the work for each of the dosimeters are higher, however, the value of the determined diffusion coefficients may be influenced by a number of factors such as the volume of the dosimeter, the shape of the irradiated area, the applied dose, the method of storing the gel, the 2D/3D imaging method and the calculation method, hence it is suggested to compare the determined values separately for each specific experimental system [148]. In the conducted study, the highest diffusion coefficient in both directions was shown by Fricke-

XO-Gelatin and the lowest by Fricke-XO-Gelatin with sorbitol. The addition of sorbitol resulted in a decrease of the diffusion coefficient value by about two times. Taking into account also the higher sensitivity (section 5.3.1.), better temperature stability and more favourable mechanical properties (sections 5.2.1. and 5.2.2.) it can be stated that the modification of Fricke-XO-Gelatin with the addition of sorbitol allows for significant improvement of the properties of this dosimeter. Fricke-XO-Pluronic F-127 showed a lower diffusion coefficient than Fricke-XO-Gelatin. A similar relation could be observed in the experiment in which the gels contained in measuring cuvettes made of PMMA were irradiated to half with a dose of 30 Gy [148].

Recently, the phenomenon of anisotropic diffusion of Fe^{3+} ions in the Fricke-XO-Pluronic F-127 and Fricke-XO-Gelatin dosimeters has been reported [148]. Samples of both dosimeters in measuring cuvettes (4 cm height, 1 cm optical path) were irradiated to half height with a dose of 30 Gy. Then the cuvettes were stored in a vertical position, but some of them were placed on caps (in this case diffusion occurred in the direction of gravity). It was observed that for both dosimeters the diffusion coefficient depended on its direction and had a higher value when it was in the direction of gravity. A similar phenomenon can be observed by analyzing the values presented in Table 10. The value of the diffusion coefficient occurring in the direction of gravity for Fricke-XO-Pluronic F-127 and Fricke-XO-Gelatin with sorbitol was higher by about 20.6% and 33.6%, respectively, than when the diffusion direction was opposite to gravity. The exception was Fricke-XO-Gelatin, for which a higher value of the diffusion coefficient was determined for Fe^{3+} ions moving against gravity. It should be noted, that the difference in the values of the diffusion coefficients was within the measurement uncertainty limit and was less than 1.6%, which may indicate no effect of gravity on diffusion for this composition. It would be necessary to repeat the experiment to confirm this observation. A thorough understanding of the effect of gravity on iron ion diffusion in Fricke dosimeters may be crucial to the development of the novel approach of Romeo et al [195,196] who use neural networks to predict diffusion progression over time. This may allow the introduction of diffusion correction algorithms for use in verifying treatment plans. Further studies of diffusion anisotropy for different Fricke dosimeter compositions and different experimental conditions are necessary to make such an approach accurate.

Table 10. Diffusion coefficient values (expressed in mm^2h^{-1}) with uncertainties determined for Fricke-XO-Pluronic F-127, Fricke-XO-Gelatin and Fricke-XO-Gelatin with sorbitol. Diffusion coefficients were determined for a composition containing 50 mM H_2SO_4 , 0.5 mM FAS, 0.08 mM XO. Gel matrix concentrations were 25% and 4% for Pluronic F-127 and gelatin, respectively. Sorbitol concentration was 23%.

Direction of the diffusion	Type of dosimeter		
	Fricke-XO-Pluronic F-127	Fricke-XO-Gelatin	Fricke-XO-Gelatin with sorbitol
In the direction of gravity	3.02±0.05	5.06±0.10	2.51±0.09
Against the direction of gravity	2.26±0.04	5.14±0.17	2.08±0.15

5.3.3. Treatment planning verification in 3D: Fricke-XO-Pluronic F-127

For the treatment plan verification process, two vials with a Fricke-XO-Pluronic F-127 dosimeter (the selected dye concentration was 0.08 mM) were prepared and stored in the same conditions until irradiation. One of the dosimeters was irradiated according to the calibration plan (the 3D view of the scanned gel is shown in Figure 72 B) and the other vial was irradiated according to the treatment plan.

During irradiation, both samples were placed in a phantom imitating a human skull filled with water (Figure 10 D in section 4.3.2). After irradiation, both samples were scanned over time. Based on the calibration dosimeter scans, calibration curves (Figure 72 A) were prepared, and their equations were determined. Analyzing the obtained curves, it can be seen that with time the optical density of the irradiated gel increased (the slope and intercept values for the calibration curves increased), but the rate of change decreased (the average increase in optical density between 1 and 2 h after irradiation was 0.015 cm^{-1} (the increase in optical density in the parts irradiated with the lowest and highest doses used in calibration was approximately 18% and 12%, respectively), while between 2 and 4 h after irradiation it was 0.016 cm^{-1} (the increase in optical density in the parts irradiated with the lowest and highest doses used in calibration was approximately 13% and 9%, respectively)), which suggests that the observed changes in optical density were mainly the result of irradiation. A similar phenomenon was observed for the other tested compositions with Pluronic (section 5.3.1.).

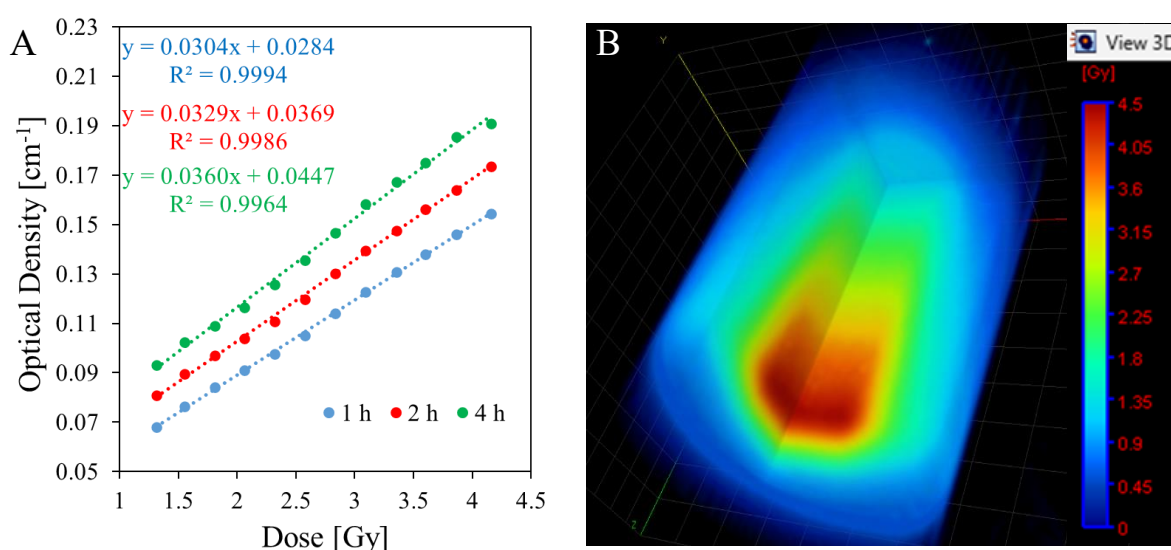
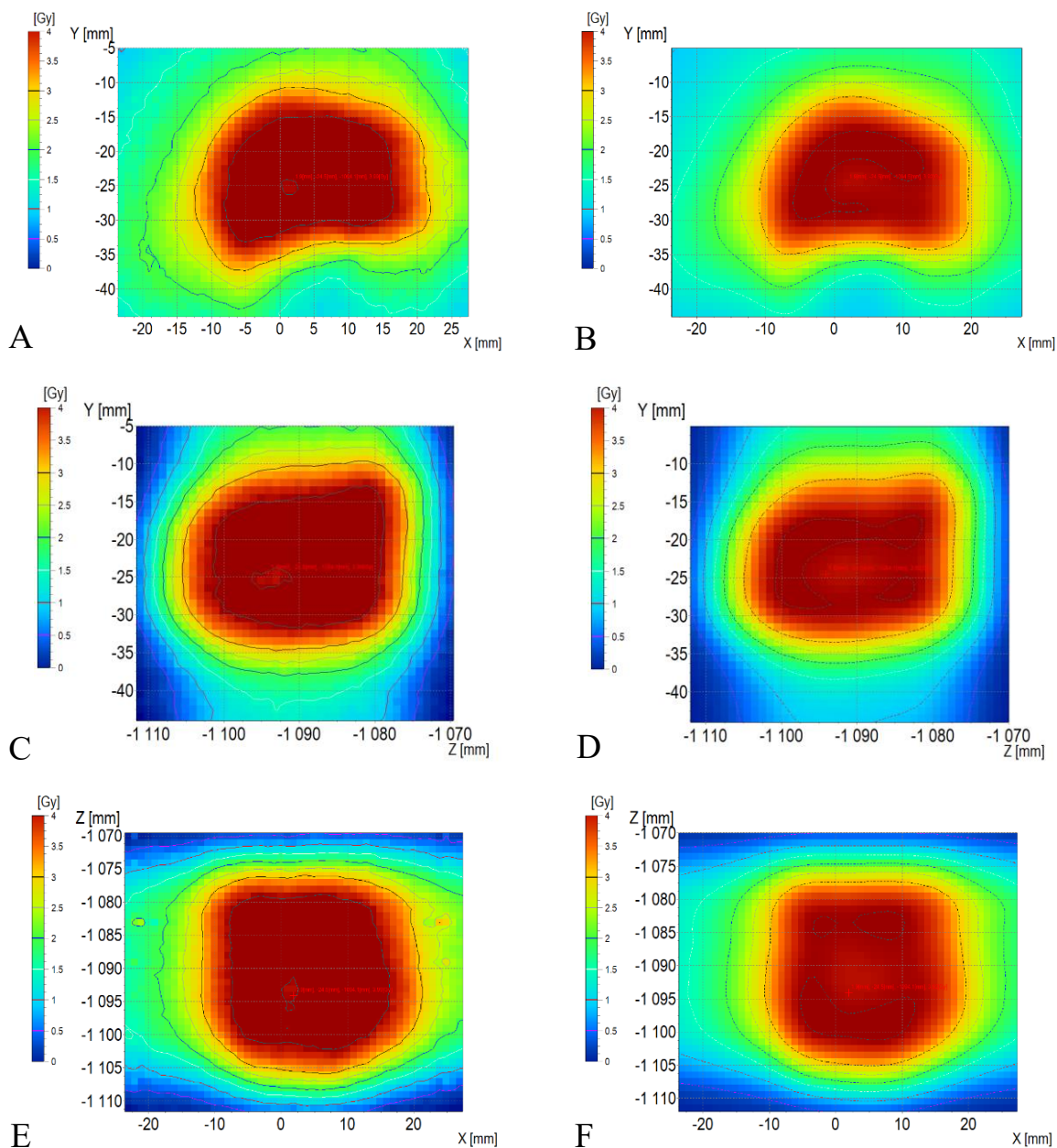


Figure 72. A: Calibration curves of the Fricke-XO-Pluronic F-127 dosimeter obtained about 1, 2 and 4 hours after irradiation. B: 3D view of the scanned calibration sample (scan performed 1 h after irradiation).

The comparison of dose distributions measured using Fricke-XO-Pluronic F-127 (scanned about 1 hour after irradiation) and calculated by TPS is presented in Figure 73 (2D and 3D dose distributions), Figure 74 (profiles and isodoses) and Figure 75 (evaluation of the 3D local gamma index, histograms of 3D dose distribution and 3D local gamma index). Comparing the dose distributions presented in Figure 73, one can see similarities between the measured and calculated dose distributions in the outer part of the irradiated volume, while in its inner part (limited by coordinates -5 mm to 15 mm on the X-axis, -17 mm to -30 mm on the Y-axis and -1100 mm to -1080 mm on the Z-axis) the measured dose is higher than the calculated dose in TPS. While at the central point of the irradiated volume the measured dose is 3.99 Gy and the calculated dose is 3.92 Gy (difference between doses is 0.07 Gy which corresponds to a percentage difference of 1.8% within the required accuracy of $\pm 3\text{-}5\%$ [189]), the average doses measured and calculated from the entire central volume (defined by the coordinates presented above) are 4.28 Gy and 3.95 Gy, respectively. The dose profiles (Figure 74) along the X and Y axes have a similar shape for the dosimeter and TPS, however along the entire length of the profiles the measured dose is higher than the calculated one. The profiles along the Z axis are almost overlapping except for the part from -1092 mm to -1075 mm, where the profile for the dosimeter is up to 0.5 Gy higher than for TPS. The isodoses in Figure 74 have similar shapes (except for the 4 Gy isodose) for the gel and for TPS.

TPS, however they are not overlapped due to differences in dose distributions. Concerning the local gamma index comparison (Figure 75) for the calculated and measured dose distributions almost 20% of the pixels are above 1. This result exceeds the tolerance limits of 0-5% of pixels above 1 [188] which means that the verification cannot be considered successful.



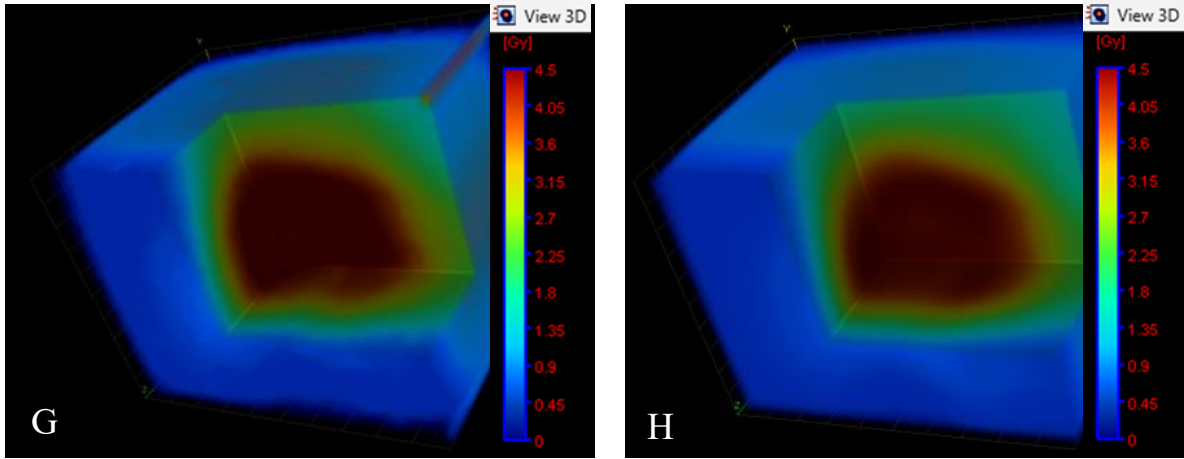
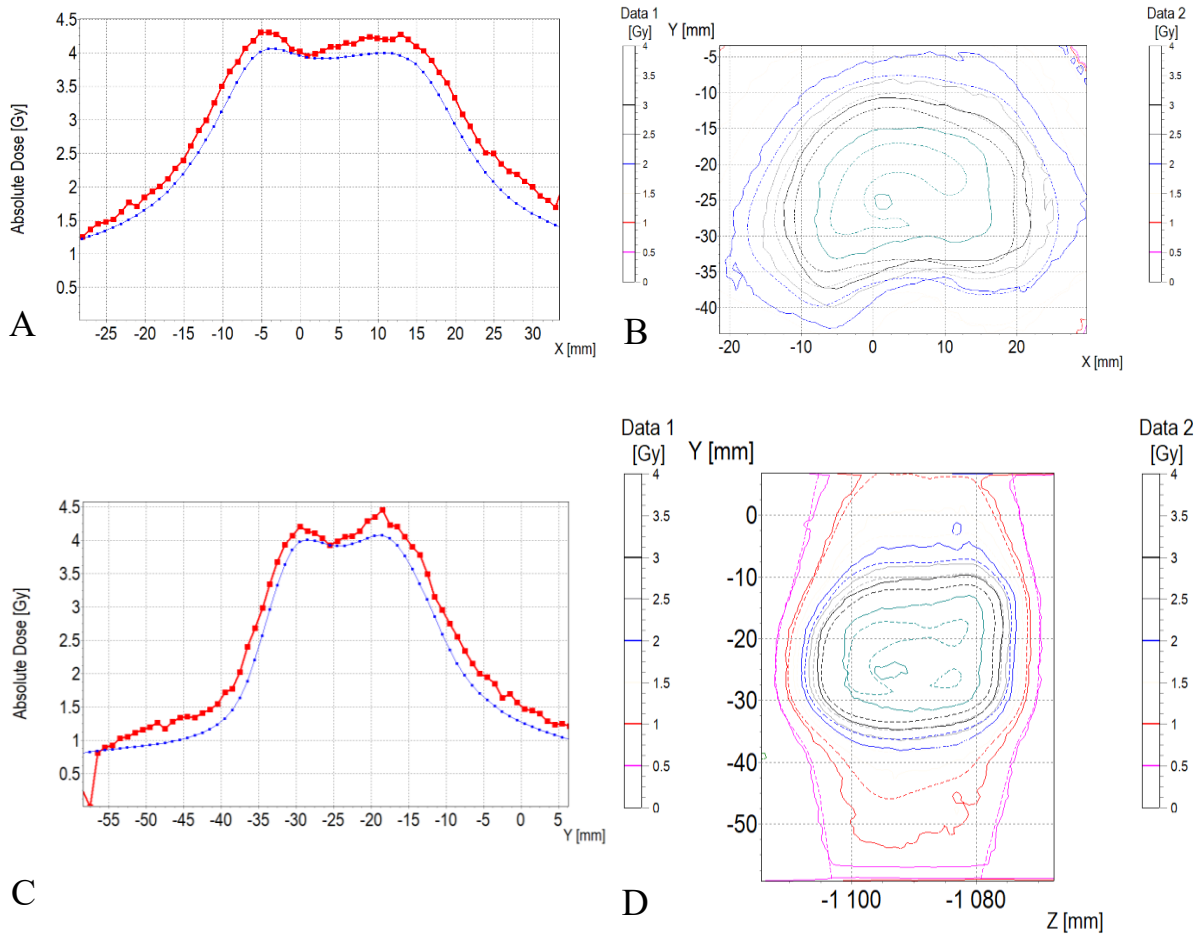


Figure 73. Comparison of 2D dose distributions for Fricke-XO-Pluronic F-127 (A, C, E) and TPS (B, D, F). Fricke-XO-Pluronic F-127 was scanned with an optical computed tomography (OCT) about 1 h after irradiation. 3D dose distributions for Fricke-XO-Pluronic F-127 and TPS are presented in G and H respectively.



C

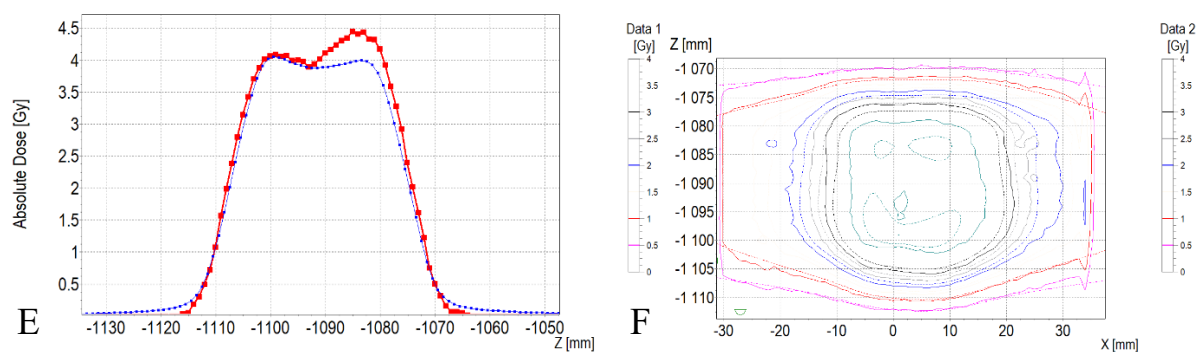


Figure 74. Comparisons of profiles along X (A), Y (C) and Z (E) axes for Fricke-XO-Pluronic F-127 (red points) and TPS (blue points). B, D and F are images with isodoses for Fricke-XO-Pluronic F-127 (Data 1, solid lines) and TPS (Data 2, dashed lines). Fricke-XO-Pluronic F-127 was scanned with an optical computed tomography (OCT) about 1 h after irradiation.

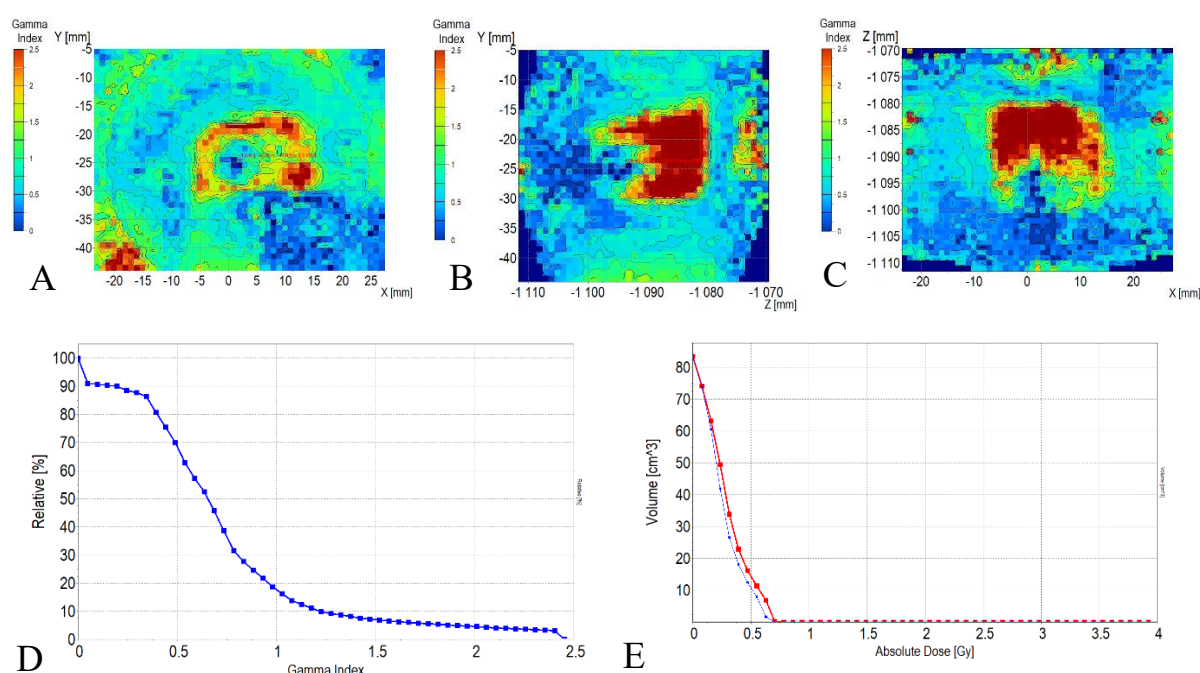


Figure 75. 3D local gamma index for YX (A), YZ (B) and ZX (C) planes (DD=3%, DTA=3mm). Fricke-XO-Pluronic F-127 was scanned with an optical computed tomography (OCT) about 1 h after irradiation. D: 3D local gamma index histogram, E: Histogram for 3D dose distributions for Fricke-XO-Pluronic F-127 and TPS.

The dose distribution measured with the Fricke-XO-Pluronic F-127 dosimeter scanned 4 h after irradiation is presented in Figure 76. Figures 77 and 78 show comparisons of the profiles along the X, Y and Z axes and isodoses between the dosimeter scanned 1 and 4 h after irradiation and between the TPS and the dosimeter (scanned after 4 h after irradiation) respectively. Evaluation of the 3D local gamma index, histograms of 3D dose distribution and 3D local gamma index are presented in Figure 79. The dose distribution measured with the dosimeter scanned 1 and 4 h after irradiation are clearly different. The shapes of the dose profiles (Figure 77 A, C and E) are similar, but the doses read 4 h after irradiation are clearly lower. The greatest differences are visible in the area of the highest doses and reach about 0.6 Gy. The isodoses (Figure 77 B, D and F) for both scans have similar shapes, however, those obtained 1 h after irradiation limit larger areas due to differences in dose distribution. The dose profiles for the TPS and the dosimeter scanned 4 h after irradiation (Figure 78 A, C and E) have similar shapes and overlap in dose regions up to 3 Gy. Above this value, the doses calculated by the TPS are

higher than those measured by the dosimeter. About 15% of the pixels exceed a gamma index value of 1, which is slightly lower than for the comparison of the TPS with the dosimeter scanned 1 h after irradiation, however it is still above the 5% tolerance limit.

The observed differences between the dose distributions calculated and measured, as well as between those measured after different times of irradiation, may be the result to the long time (at least 2 hours) during which changes induced by ionizing radiation occur in the Fricke-XO-Pluronic F-127 dosimeter. Due to the dynamics of changes (an increase in the slope coefficient in the calibration equation by over 8% and the intercept by almost 30% in the time between scans performed 1 and 2 h after irradiation), it is necessary to maintain an almost identical (the exact tolerance should be determined experimentally, but it should most probably not exceed 5 minutes) time between irradiation and the scan of the dosimeters used for calibration and verification of the treatment plan. Due to the limited availability of the accelerator, maintaining a strict time regime within the conducted experiment was impossible. The time between irradiation and scan was approximately 20 minutes longer for the verification sample than for the calibration one, which most likely led to differences between the measured and calculated dose distributions. At the time of scanning, the gel irradiated according to the treatment plan was already darker than the gel used for calibration, which caused the measured dose distribution to be higher than the calculated one. When the dosimeters were scanned 4 h after irradiation, the rate of gel darkening was already lower (an increase in the slope coefficient in the calibration equation by about 9% and the intercept by about 21% in the time between scans performed 2 and 4 h after irradiation), hence the approximately 20-minute difference in time from irradiation to scan between the verification and calibration samples had a smaller impact on the measurement results and thus the calculated and measured dose distributions in the range up to 3 Gy are similar. The difference appears in the central part of the sample irradiated with doses above 3 Gy, where the measured dose is lower than the calculated one. Probably 4 hours after irradiation the gel became so dark that it absorbed the laser light too strongly, which resulted in the formation of cupping artifacts.

Although the verification of the treatment plan using the Fricke-XO-Pluronic F-127 dosimeter was not entirely successful, the obtained results allowed to determine the direction of further research. It is necessary to optimize the verification process, first of all to maintain the same time intervals between irradiation and scanning of the calibration and verification samples. Moreover, the dosimeter should be used to verify plans in which the maximum dose does not exceed 3 Gy to avoid the occurrence of cupping artifacts. To use higher doses, the composition of the dosimeter should be modified by reducing the dye concentration. Currently, the dosimeter can be used, for example, in radiation fields distribution dosimetry or in coincidence tests of the radiation and mechanical isocenter of a medical accelerator. After further optimization, it is possible that it will also find other applications in radiotherapy.

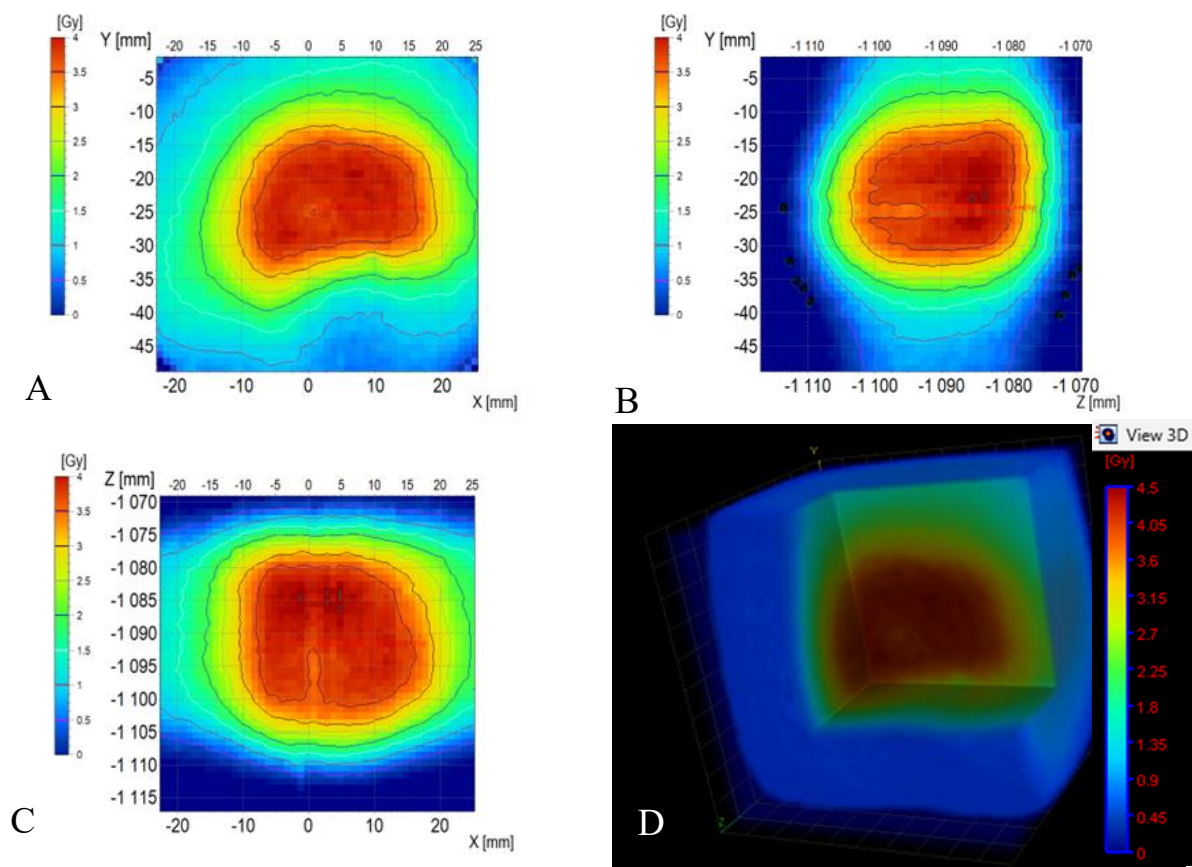
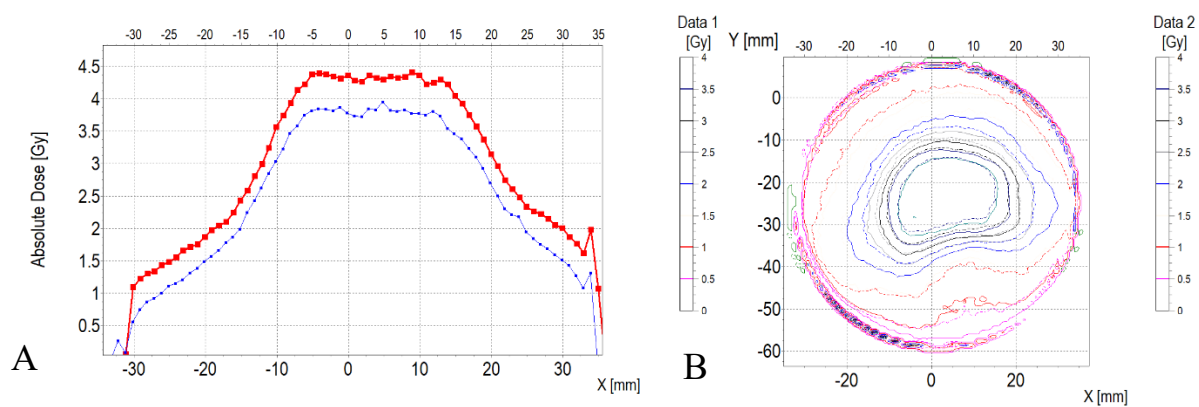


Figure 76. 2D dose distributions (A, B, C) and 3D dose distribution (D) for Fricke-XO-Pluronic F-127 about 4 h after irradiation.



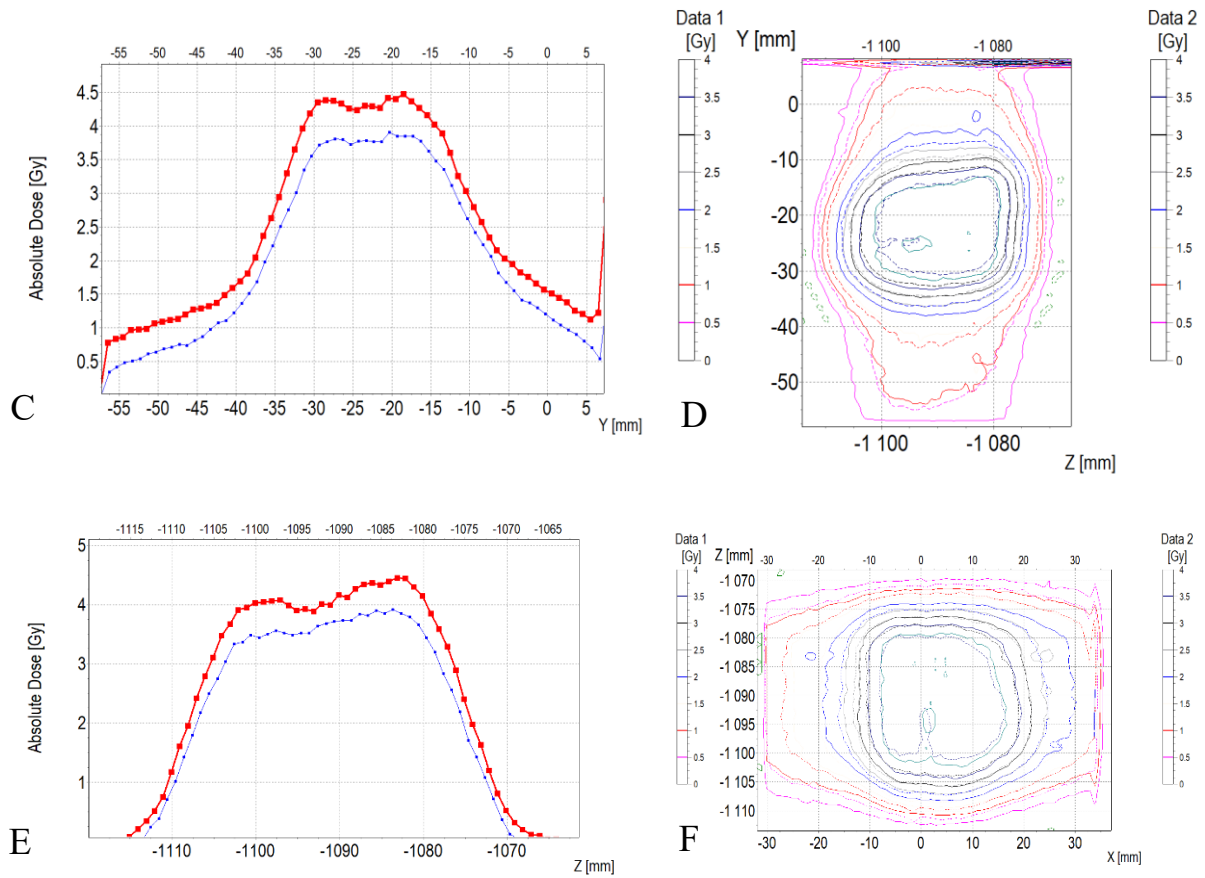
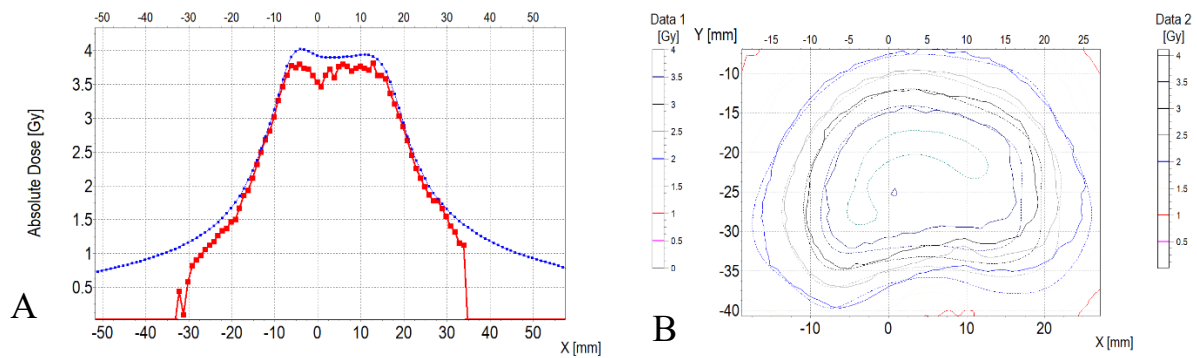


Figure 77. A, C, E: Comparison of profiles for Fricke-XO-Pluronic F-127 measured 1 h (red points) and 4 h (blue points) after irradiation. B, D, F: Comparison of isodoses for Fricke-XO-Pluronic F-127 measured 1 h (Data 1, solid lines) and 4 h (Data 2, dashed lines) after irradiation.



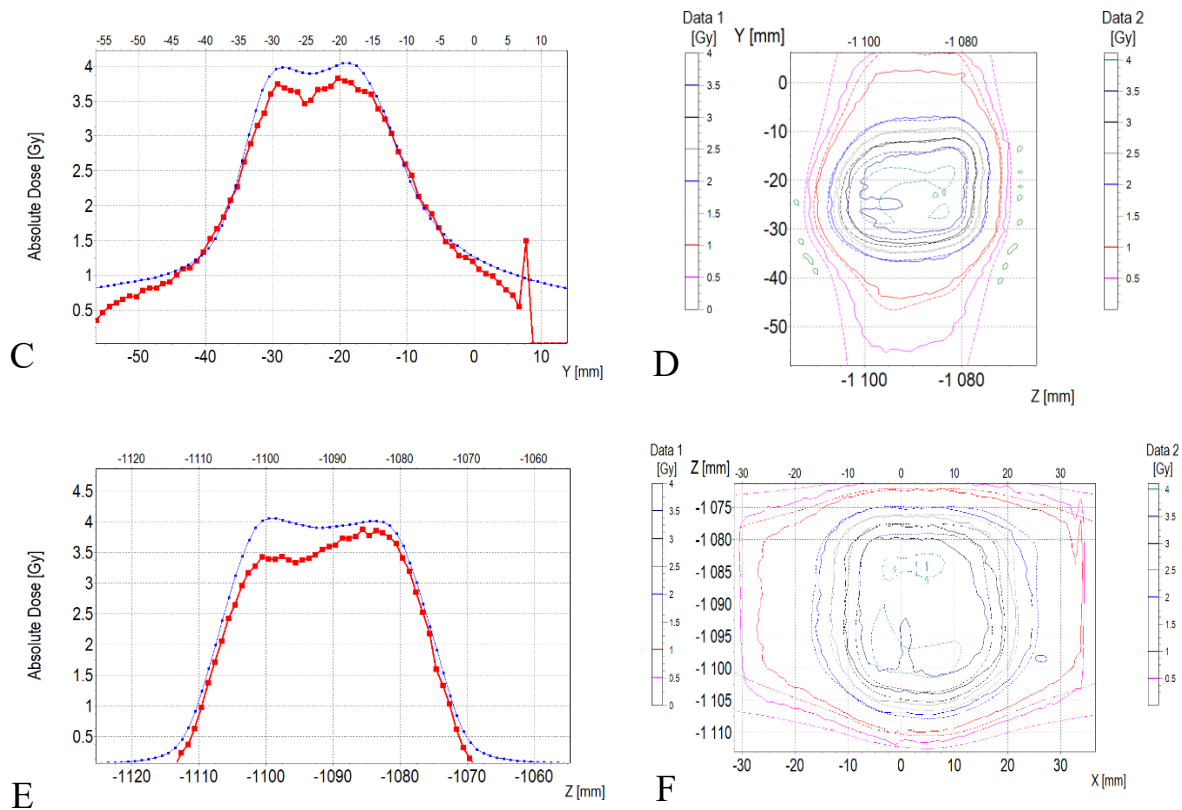


Figure 78. Comparisons of profiles along X (A), Y (C) and Z (E) axes for Fricke-XO-Pluronic F-127 (red points) and TPS (blue points). B, D and F are images with isodoses for Fricke-XO-Pluronic F-127 (Data 1, solid lines) and TPS (Data 2, dashed lines). Fricke-XO-Pluronic F-127 was scanned with an optical computed tomography (OCT) about 4 h after irradiation.

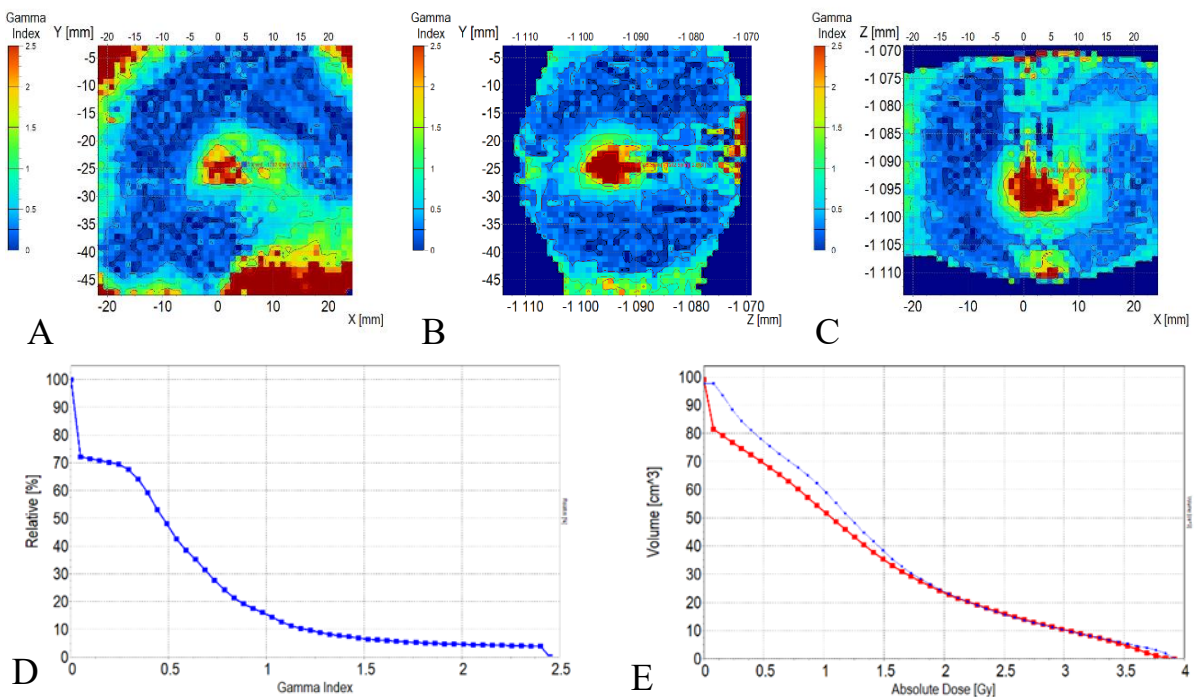


Figure 79. 3D local gamma index for YX (A), YZ (B) and ZX (C) planes (DD=3%, DTA=3mm). Fricke-XO-Pluronic F-127 was scanned with an optical computed tomography (OCT) about 4 h after irradiation. D: 3D local gamma index histogram. E: Histogram for 3D dose distributions for Fricke-XO-Pluronic F-127 and TPS.

5.3.4. Treatment planning verification in 3D: Fricke-XO-Gelatin with sorbitol

The process of treatment plan verification using Fricke-XO-Gelatin with sorbitol was performed analogously to the verification with the Fricke-XO-Pluronic F-127 dosimeter (section 5.3.3). Two vials of gel were prepared, one of which was irradiated for calibration and the other for verification. Samples were scanned 1, 2, and 4 hours after irradiation. Calibration curves (Figure 80 A) were prepared, and their equations were determined. As with the Pluronic dosimeter, the gelatin gel darkens over time after irradiation, but the rate of change is much slower (the average increase in optical density between 1 and 2 h after irradiation was 0.004 cm^{-1} (the increase in optical density in the parts irradiated with the lowest and highest doses used in calibration was approximately 3% and 1.6%, respectively), while between 2 and 4 h after irradiation it was 0.005 cm^{-1} (the increase in optical density in the parts irradiated with the lowest and highest doses used in calibration was approximately 3.5% and 1.5%, respectively)). Figure 80 B shows the 3D view of the scanned calibration gel.

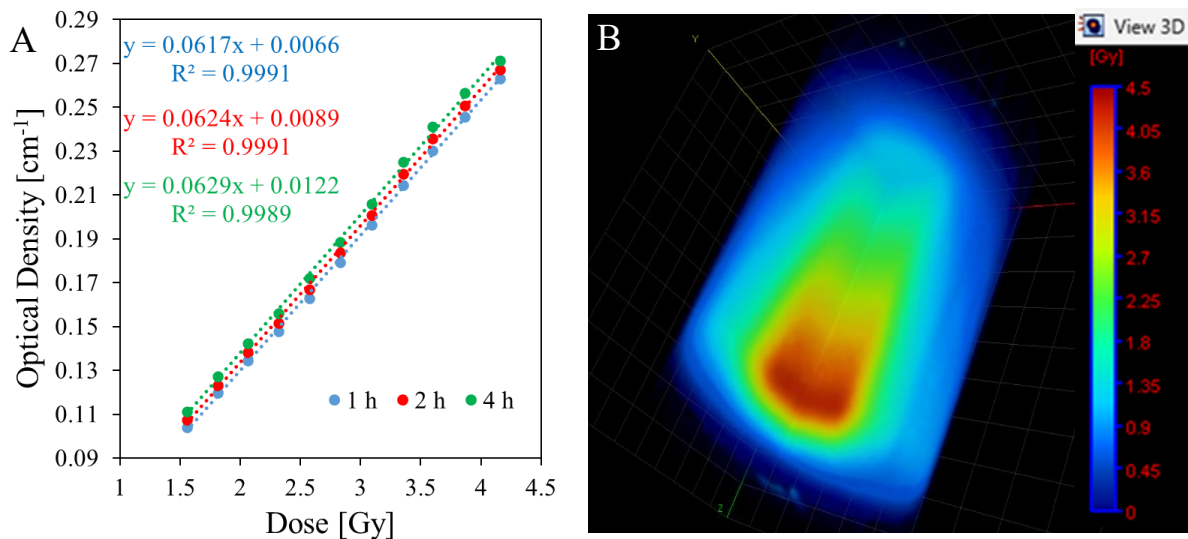
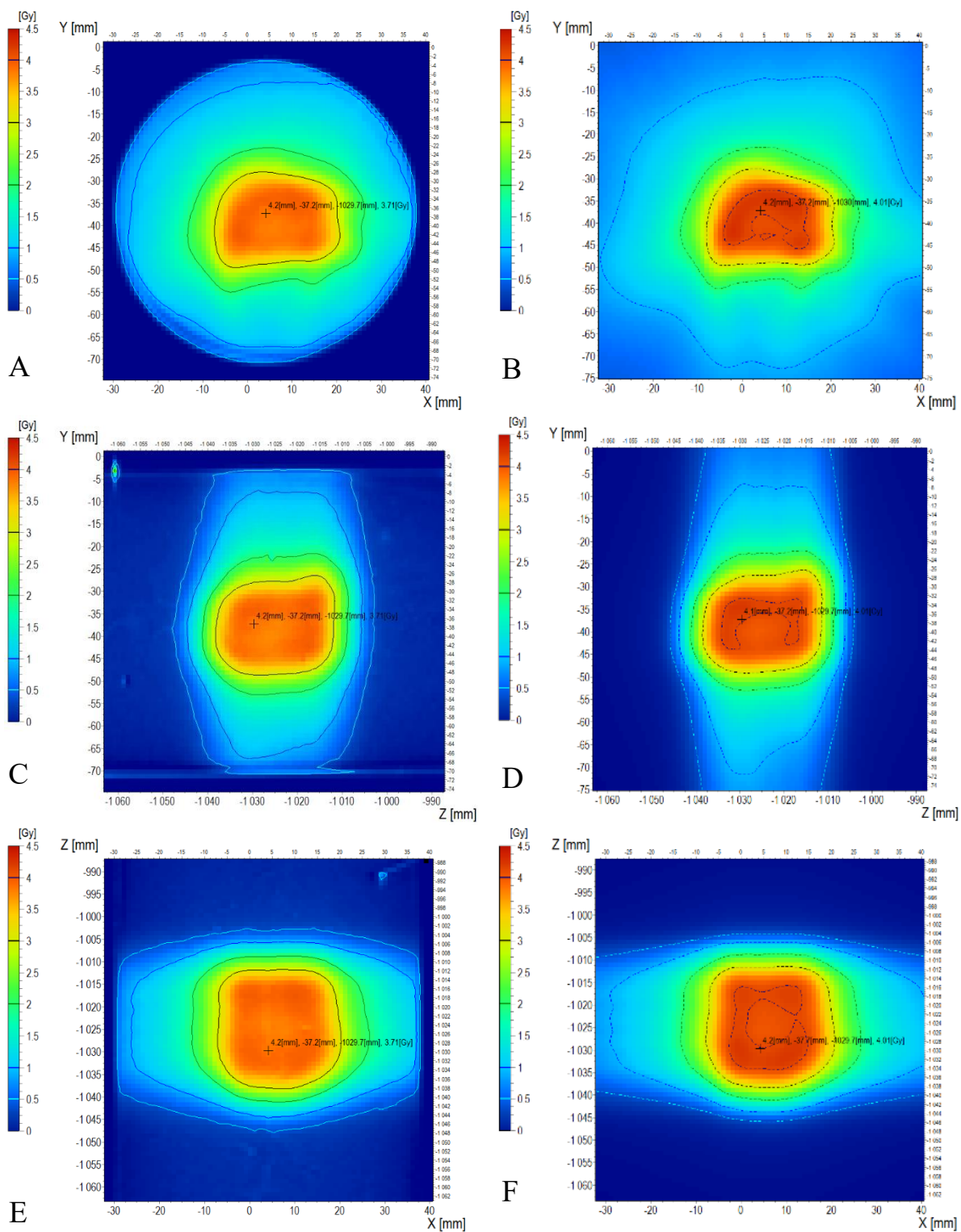


Figure 80. A: Calibration curves of the Fricke-XO-Gelatin with sorbitol obtained about 1, 2 and 4 hours after irradiation. B: 3D view of the scanned calibration sample (scan performed 1 h after irradiation)

The comparison of dose distributions measured using Fricke-XO-Gelatin with sorbitol and calculated by TPS is presented in Figure 81. It is clearly visible that the measured and calculated dose distributions are very similar. The only difference is observed in the center of the irradiated volume, where the measured dose is lower than the planned dose. The dose difference between the gel and TPS at the center point is -0.3 Gy . This value amounts to a percentage dose difference of -7.5% with respect to TPS and does not meet the required accuracy of $\pm 3\text{-}5\%$ [188]. The superimposed isodoses for the dosimeter and TPS (Figure 82 B, D, E) have similar shapes and differ only slightly in some parts, which may result from the occurring diffusion of Fe^{3+} ions and potential inaccuracies of the measuring device. The dose profiles along the X, Y and Z axes have almost identical shapes for both the dosimeter and TPS (Figure 82 A B C). The dose values are also similar except for the central parts of the profiles, where the measured dose is lower than the planned dose. The observed dose differences are probably due to too strong absorption of the tomograph laser light (a phenomenon described in section 5.3.1.). Despite the optimization of the dosimeter composition and measurement conditions, the gel was too dark in the central part of the sample for the applied treatment plan, which led to a partial inconsistency between

the dosimeter and the TPS. To avoid emerging of the artifacts during sample scanning, the gel should be irradiated with doses lower than 4 Gy. When it is necessary to use higher doses, the dosimeter composition can be modified by reducing the dye concentration. Despite the observed dose differences, the gamma index value of 1 is exceeded by less than 5% of the pixels (Figure 83), which is within the tolerance range of 0-5% [188]. Therefore, the verification of the treatment plan using Fricke-XO-Gelatin can be considered successful.



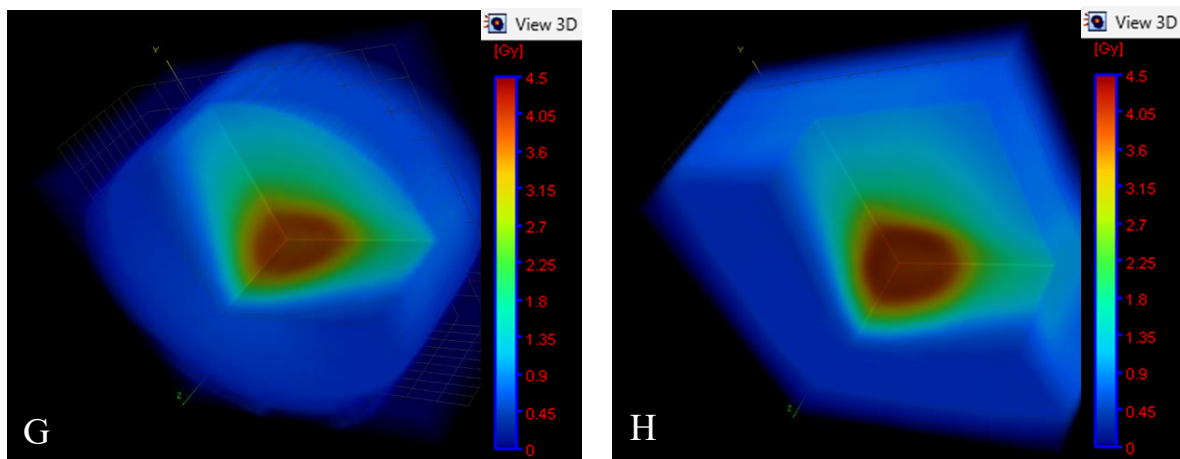
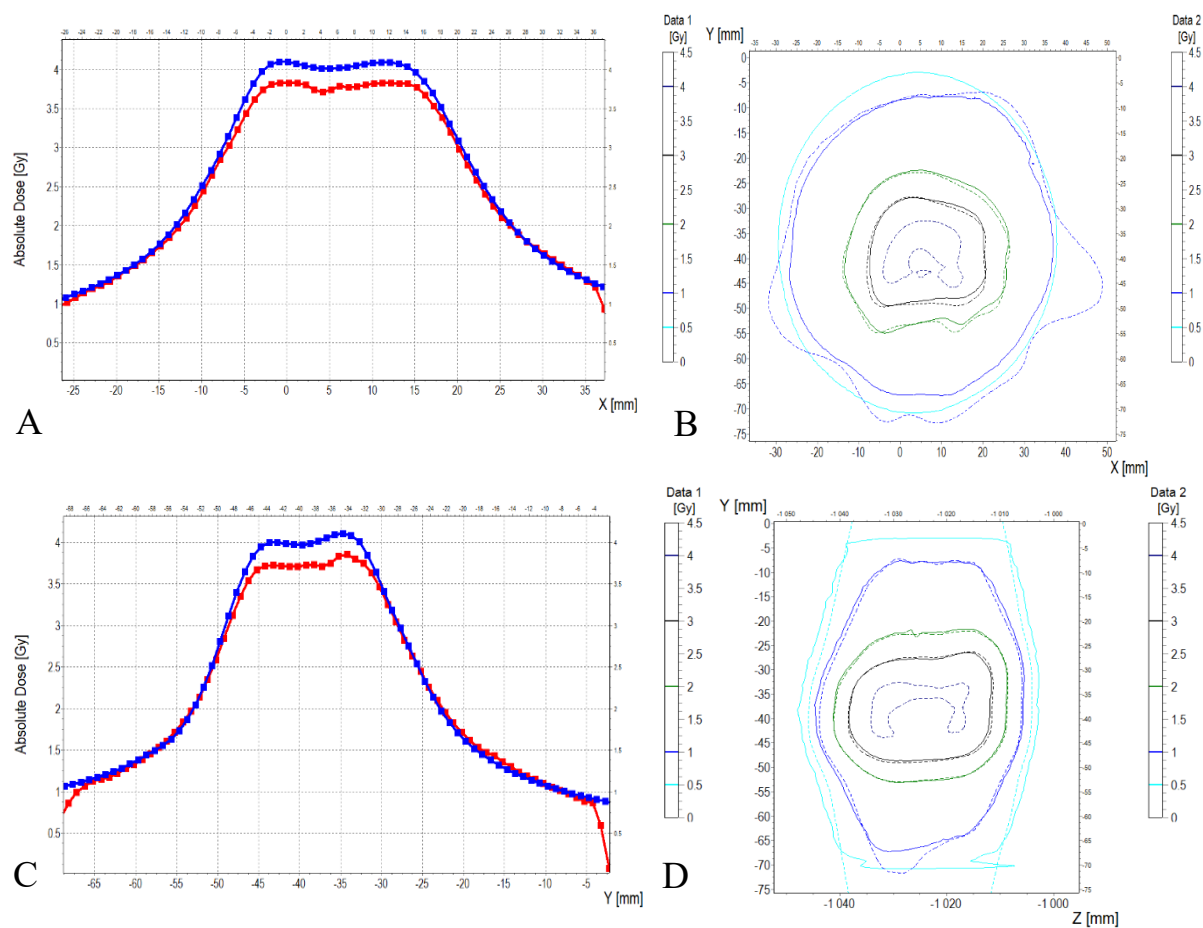


Figure 81. Comparison of 2D dose distributions for Fricke-XO-Gelatin with sorbitol (A, C, E) and TPS (B, D, F). Fricke-XO-Pluronic F-127 was scanned with an optical computed tomography (OCT) about 1 h after irradiation. 3D dose distributions for Fricke-XO-Pluronic F-127 and TPS are presented in G and H respectively.



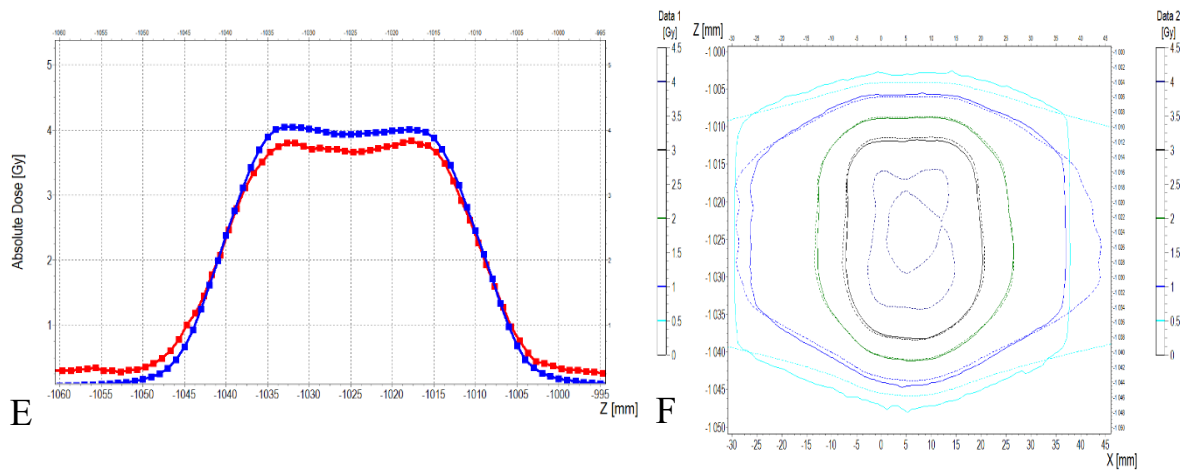


Figure 82. Comparisons of profiles along X (A), Y (C) and Z (E) axes for Fricke-XO-Gelatin (red points) and TPS (blue points). B, D and F are images with isodoses for Fricke-XO-Gelatin (Data 1, solid lines) and TPS (Data 2, dashed lines). The dosimeter was scanned with an optical computed tomography (OCT) about 1 h after irradiation.

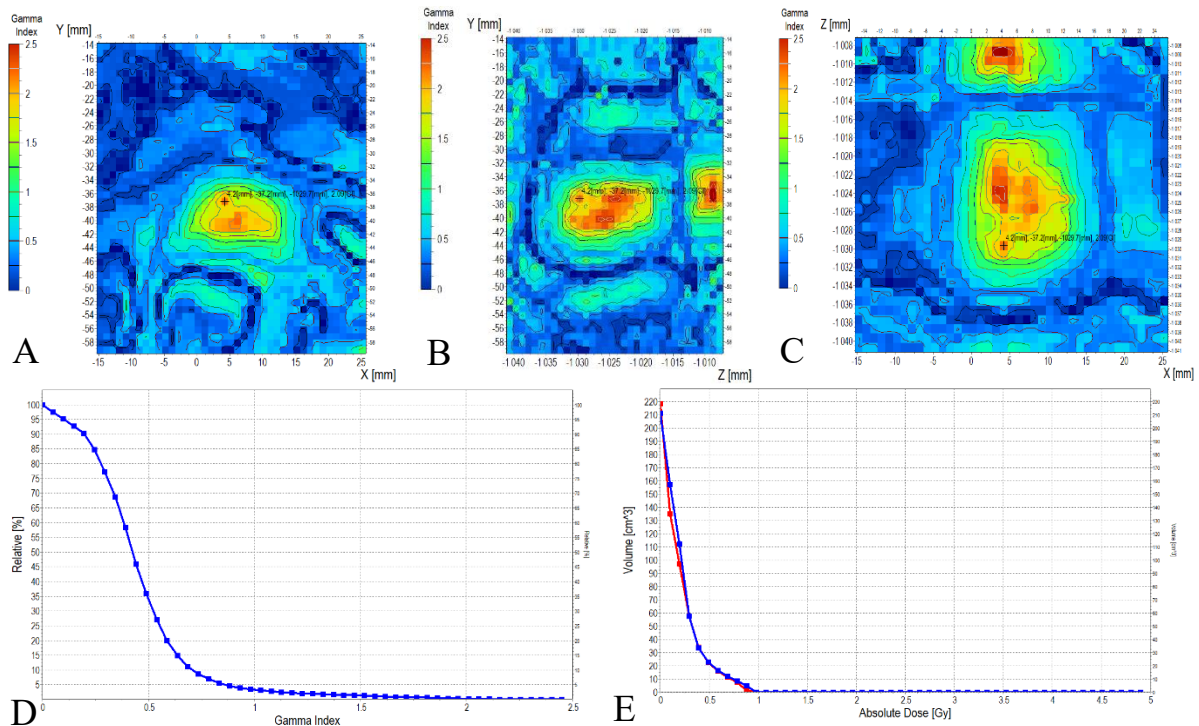
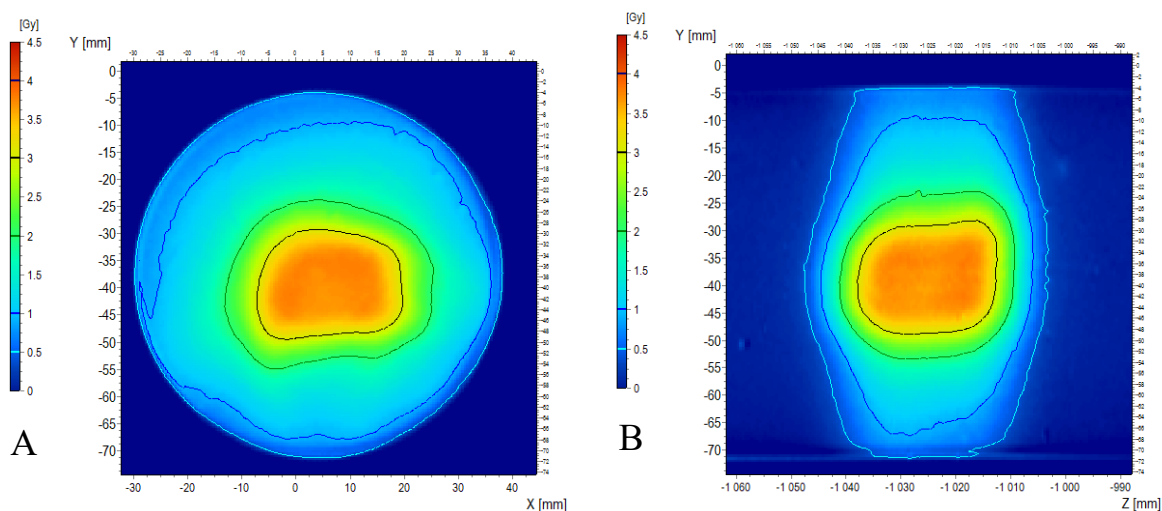


Figure 83. 3D local gamma index for YX (A), YZ (B) and ZX (C) planes (DD=3%, DTA=3mm). Fricke-XO-Gelatin with sorbitol was scanned with an optical computed tomography (OCT) about 4 h after irradiation. D: 3D local gamma index histogram. E: Histogram for 3D dose distributions for Fricke-XO-Gelatin with sorbitol and TPS.

The dose distribution measured with the Fricke-XO-Gelatin with sorbitol scanned 4 h after irradiation is presented in Figure 84. The comparison of profiles and isodoses between the dosimeters scanned after 1 and 4 h after irradiation is presented in Figure 85 A, C, E and Figure 85 B, D, F, respectively. The profiles after 1 and 4 h after irradiation have identical shapes, but the doses measured after 4 h are lower on average by 0.08 Gy. The largest differences can be observed in the central part of the irradiated volume, where the doses for the dosimeter scanned after 4 h are about 0.15 Gy lower. Similarly, in the central part of the sample, the measured doses (scanned after 1 h) were lower than calculated due to too

strong absorption of laser light, which causes cupping artifact. As can be seen on the calibration curves (Figure 80), the gel darkens over time, most likely due to autoxidation of Fe^{3+} ions. The darker the gel, the stronger the laser absorption, as a result of which the dose measured 4 h after irradiation is lower than 1 h after irradiation. The use of lower doses in the treatment plan (up to 3 Gy) should overcome the formation of cupping artifacts. As a result of changes occurring in the gel, compliance with the treatment plan decreased (about 6.5% of pixels exceed the gamma index value equal to 1) hence, according to the adopted criteria, verification after 4 hours after irradiation cannot be considered successful. It should be noted, however, that the decrease in compliance occurring between 1 and 4 hours after irradiation is small and probably, after further optimization of the verification process, the dosimeter reading even after 4 hours after irradiation would allow for effective verification of the treatment plan.

Comparing both dosimeters used to verify the treatment plan, Fricke-XO-Gelatin with sorbitol shows better features than Fricke-XO-Pluronic F-127. The advantages of the composition with gelatin include higher sensitivity, lower diffusion coefficient and significantly shorter time in which changes caused by irradiation occur in the dosimeter (section 5.3.1.). Moreover, no formation of artifacts caused by rapid spontaneous autoxidation of Fe^{2+} ions was observed in the gelatin dosimeter, whereas such artifacts appeared in the Pluronic gel (section 5.3.2.). Taking into account the advantages of Fricke-XO-Gelatin with sorbitol over Fricke-XO-Gelatin (26% higher sensitivity, twice lower diffusion coefficient, better temperature and mechanical properties), it can be stated that the modification of the gelatin matrix with sorbitol made it possible to obtain a dosimeter that may be a promising tool for use in radiotherapy both for the verification of treatment plans and for performing quality tests of medical accelerators.



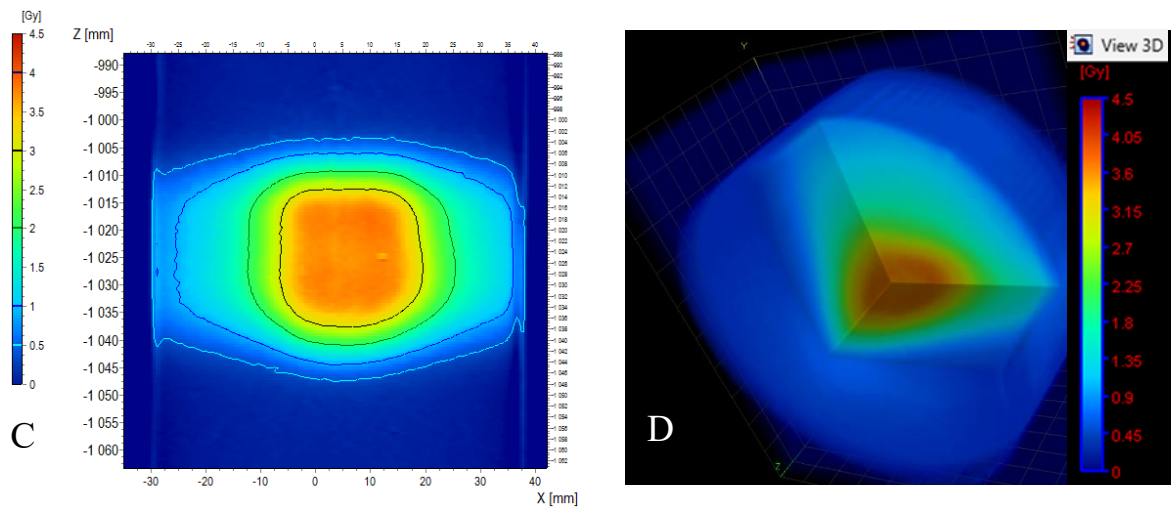
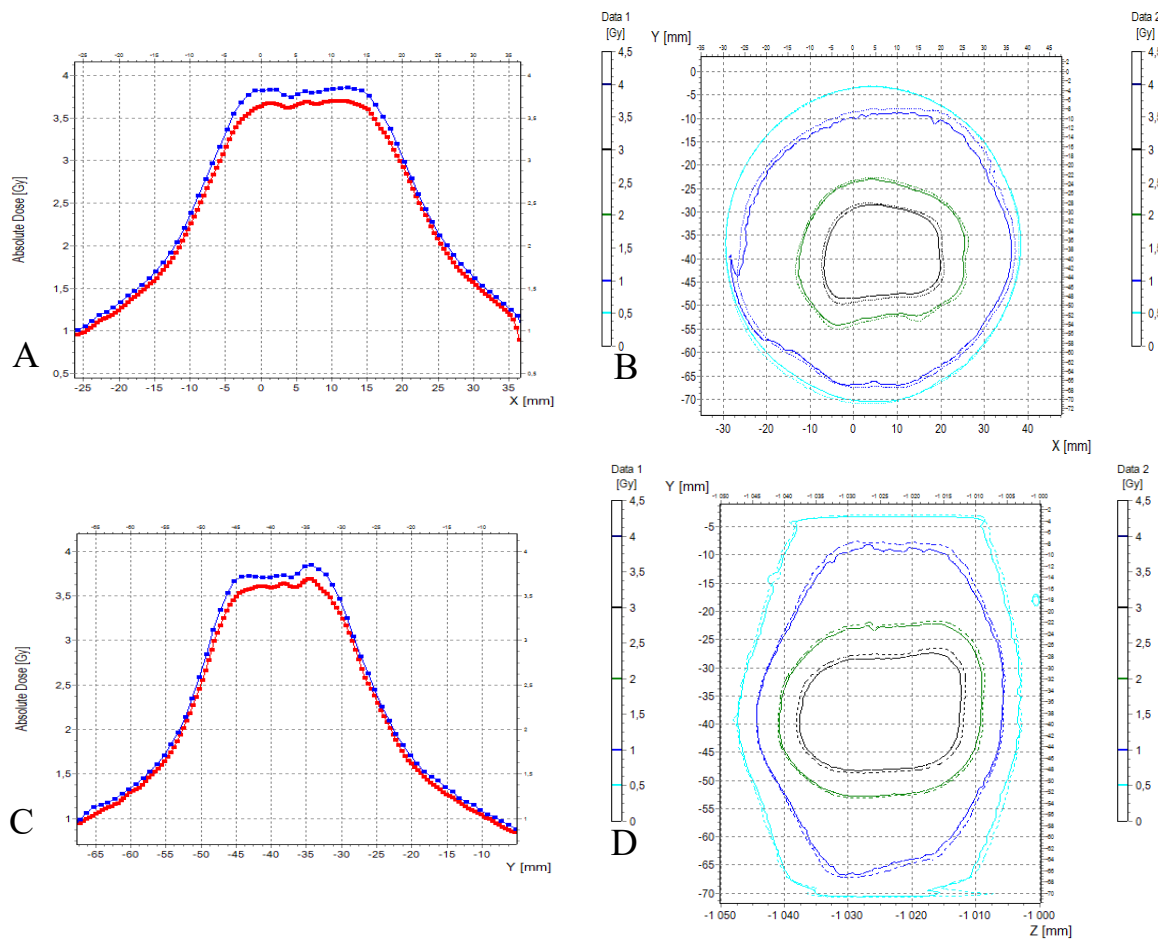


Figure 84. 2D dose distributions (A, B, C) and 3D dose distribution (D) for Fricke-XO-Gelatin with sorbitol about 4 h after irradiation.



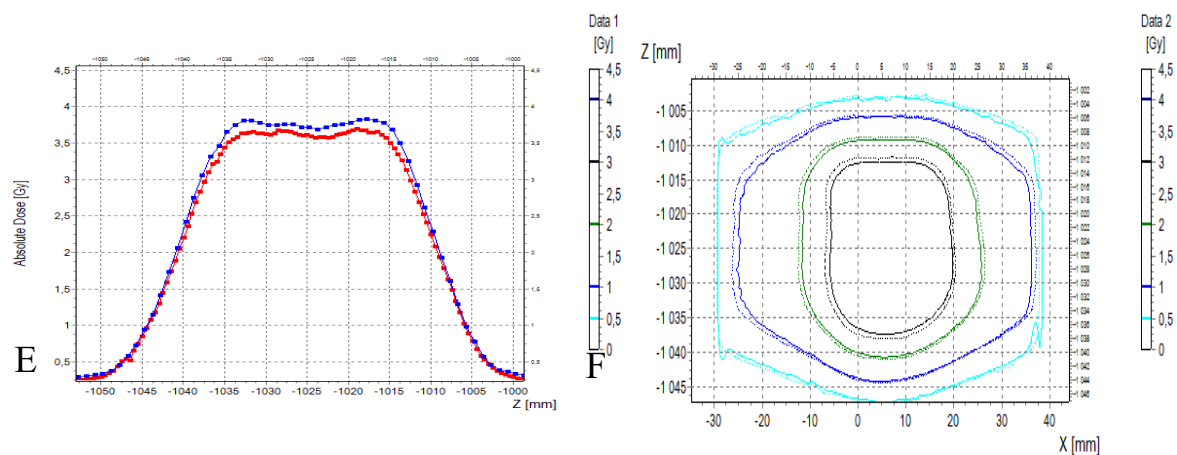


Figure 85. A, C, E: Comparison of profiles for Fricke-XO-Gelatin with sorbitol measured 1 h (blue points) and 4 h (red points) after irradiation. B, D, F: Comparison of isodoses for Fricke-XO-Gelatin with sorbitol measured 1 h (Data 2, dashed lines) and 4 h (Data 1, solid lines) after irradiation.

6. Conclusions

1. Water quality has a significant influence on the stability of ferrous ions. The use of at least double-distilled water or deionized water is recommended in the preparation of the Fricke dosimeter to ensure its highest possible chemical stability.
2. It is possible to obtain macrocapsules by dripping a sodium alginate solution in concentrations of 1.7-3.5% to Fricke's solution with the addition of 0-3.5% calcium chloride. Depending on the type of alginate used and the concentrations of the compounds, the capsules differ in shape and mechanical strength. The best properties of the capsules were obtained using 3.5% sodium alginate and 3.5% calcium chloride. The possibility of obtaining capsules (mechanically weak and irregularly shaped) despite the lack of calcium ions indicates the binding of Fe^{2+} ions to sodium alginate. This is also confirmed by measurements of the metal content using the ICP-OES method, showing that iron is bound to alginate, but in smaller amounts (approx. 7.5 mg/kg of capsules) than calcium (approx. 650 mg/kg of capsules). Most of the unbound metals diffuse from the capsules within 45 minutes of their introduction into water. The dye also diffuses almost completely.
3. Diffusion of the dye and Fe^{3+} ions is also observed after the introduction of the capsule into the gel matrix. When the introduced capsule was previously stored in water for the purpose of diffusion of unbound ferrous ions, no color changes are observed after irradiation. The introduction of capsules into the gel is also accompanied by a change in their diameter. When the gel is Pluronic F-127, the capsules decrease their diameter almost twice, while when the matrix is gelatin, the capsules first shrink by about 5% and then their diameter increases slightly, but does not return to the initial size. Attempts to stop the diffusion and shrink the capsules by increasing the ionic strength of the matrix or coating the capsules with poly-L-lysine were unsuccessful.
4. Attempts have been made to obtain alginate-Fe microgel. Due to the low pH of the solution associated with the presence of 50 mM sulphuric acid, sodium alginate undergoes protonation and precipitates as alginic acid. When sulphuric acid is eliminated from the composition, a rapid color change of the dosimeter occurs due to autoxidation of ferrous ions. Removing the dye from the composition allows slowing down the autoxidation time of iron ions observed as the precipitation of an orange precipitate at the bottom of the vessel. Microscopic observations confirmed the formation of microstructures in sodium alginate and ferrous ion solutions at pH 3.9-4.2, however, further analysis would be necessary to determine the exact chemical composition of these structures, e.g. using TEM microscopy.
5. Considering the complications associated with the addition of sodium alginate to the Fricke dosimeter (precipitation of sodium alginate at the pH optimal for the Fricke dosimeter, potential introduction of impurities with alginate that can accelerate the oxidation of ferrous ions, the need to remove the dye from the composition), it is suggested to search for alternative polymers that can bind ferrous ions. Due to the diffusion of Fe ions from the capsules and the shrinkage of the capsules after the introduction into the matrix, it can be considered that the modification of the Fricke dosimeter with sodium alginate was unsuccessful. Nevertheless, the idea of introducing compounds capable of binding iron in order to obtain both a 3D and 1D dosimeter seems to be right. However, it is necessary to find the right polymer to bind ferrous ions and to develop an optimal methodology for the production of microgels and capsules. Awareness of the phenomena that may accompany the

addition of a polymer to the Fricke dosimeter and the knowledge acquired during the conducted research will be invaluable in further attempts to modify the dosimeter.

6. Sulphuric acid leads to degradation of the gelatin matrix, which results in a decrease in the gel-sol transition temperature and a deterioration in the mechanical properties of the gel. The addition of sorbitol to some extent mitigates the presence of acid, but due to the high concentration of H_2SO_4 the protective effect is insufficient.
7. Fricke-XO-Pluronic F-127 and Fricke-XO-Gelatin with sorbitol are suitable dosimeters for performing the high-accuracy coincidence test of the radiation and mechanical isocenter of the accelerator. Due to its higher chemical stability and slower diffusion, the use of Fricke-XO-Gelatin with sorbitol is recommended.
8. Both thick (bolus like) and thin dosimeters made of Fricke-XO-Gelatin with sorbitol have been proposed for treatment plan verification. The experimental verification showed that the method of producing the dosimeters requires further optimization. It is also suggested to test other gel matrices. Nevertheless, two-dimensional gel detectors may be promising tools for use in radiotherapy as an *in vivo* dosimeter acting as a bolus and a thin dosimeter for the *in vivo* measurements of the dose distribution on the skin.
9. In order to image three-dimensional dosimeters Fricke-XO-Gelatin, Fricke-XO-Gelatin with sorbitol and Fricke-XO-Pluronic F-127 with an optical path of 6 cm using OCT without artifacts, it is necessary to reduce the XO concentration to 0.08 mM and the gelatin concentration to 4%. The optimal concentrations of the remaining ingredients are 50 mM sulphuric acid, 0.5 mM FAS, 23% sorbitol (Fricke-XO-Gelatin with sorbitol) and 25% Pluronic F-127 (Fricke-XO-Pluronic F-127). At the same time, it is recommended to scan the gels with red light (633 nm).
10. The phenomenon of anisotropic diffusion observed earlier in small volumes (measuring cuvettes) was also observed for 100 times larger volumes. The diffusion coefficients for Fricke-XO-Pluronic F-127 and Fricke-XO-Gelatin with sorbitol had higher values when diffusion occurred in the direction consistent with gravity. For Fricke-XO-Gelatin the opposite effect was observed, although the values of the diffusion coefficients in both directions were very similar (difference of 1.5%). It is difficult to explain the discrepancy between the observations for Fricke-XO-Gelatin and the other two gels; hence it is suggested to repeat the measurement to exclude a potential error in the experiment.
11. Fricke-XO-Pluronic F-127 has been proposed for treatment plan verification. The experiments indicated the necessity of further optimization of the verification process so that the time from irradiation to imaging is identical (the potential time tolerance should be determined experimentally) for the calibration and verification samples. Maintaining a strict time regime is of great importance in the case of the Pluronic dosimeter because it has been observed that radiation-induced reactions in the dosimeter occur even up to several hours after irradiation.
12. The verification of the treatment plan using Fricke-XO-Gelatin with sorbitol imaged one hour after irradiation was successful. Nevertheless, further optimization of the gel composition or use of values below 3 Gy in the treatment plans is necessary to obtain even better agreement between the measured

and calculated dose distribution. Probably after further optimization it will be possible to perform successful verification even for a dosimeter scanned 4 h after irradiation.

13. The modification of the Fricke-XO-Gelatin dosimeter with the addition of sorbitol increased its temperature stability and improved its mechanical properties. The gel with sorbitol showed 26% higher sensitivity and more than twice lower diffusion coefficient in OCT measurements. In addition, the verification of the treatment plan using the gel with sorbitol was successful. The dissertation also presents potential new applications of the two-dimensional Fricke gel dosimeter as a thick bolus dosimeter and a thin dosimeter for skin dose measurements, which can be used as *in vivo* dosimeters and a dosimeter for performing quality tests of medical accelerators (e.g. a test of the coincidence of the radiation and mechanical isocenter of the accelerator). The idea of one-dimensional Fricke dosimeters in the form of capsules was also presented. Taking the above into consideration, it can be assumed that the aim of the work has been fulfilled.

Literature

- [1] F. Bray, M. Laversanne, E. Weiderpass, I. Soerjomataram, The ever-increasing importance of cancer as a leading cause of premature death worldwide, *Cancer*, 127 (2021), pp. 3029-3030, <https://doi.org/10.1002/cncr.33587>
- [2] F. Bray, M. Laversanne, H. Sung, J. Ferlay, R.L. Siegel, I. Soerjomataram, A. Jemal, Global cancer statistics 2022: GLOBOCAN estimates of incidence and mortality worldwide for 36 cancers in 185 countries, *CA Cancer J. Clin.*, 74 (2024), pp. 229-263, <https://doi.org/10.3322/caac.21834>
- [3] W. Cao, K. Qin, F. Li, W. Chen, Comparative study of cancer profiles between 2020 and 2022 using global cancer statistics (GLOBOCAN), *J. Natl. Cancer Cent.*, 4 (2024), pp. 128-134, <https://doi.org/10.1016/j.jncc.2024.05.001>
- [4] M. Arruebo, N. Vilaboa, B. Sáez-Geutierrez, J. Lambea, A. Tres, M. Valladares, Á. González-Fernández, Assessment of the Evolution of Cancer Treatment Therapies, *Cancers*, 3 (2011), pp. 3279-3330, <https://doi.org/10.3390/cancers3033279>
- [5] R.B. Mokhtari, T.S. Homayouni, N. Baluch, E. Morgatskaya, S. Kumar, B. Das, H. Yeger, Combination therapy in combating cancer, *Oncotarget*, 8 (2017), pp. 38022-38043, <https://doi.org/10.18632/oncotarget.16723>
- [6] E. Bidram, Y. Esmaeili, H. Ranji-Burachaloo, N. Al-Zaubadi, A. Zarrabi, A. Stewart, D.E. Dunstan, A concise review on cancer treatment methods and delivery systems, *J. Drug. Deliv. Sci. Technol.*, 54 (2019), article 101350, <https://doi.org/10.1016/j.jddst.2019.101350>
- [7] M.D. Hellmann, B.T. Li, J.E. Chaft, M.G. Kris, Chemotherapy remains an essential element of personalized care for persons with lung cancers, *Ann. Oncol.*, 27 (2016), pp. 1829-1835, <https://doi.org/10.1093/annonc/mdw271>
- [8] U. Anand, A. Dey, A.K.S. Chandel, R. Sanyal, A. Mishra, D.K. Pandey, V. De Falco, A. Upadhyay, R. Kandimalla, A. Chaudhary, J.K. Dhanjal, S. Dewanjee, J. Vallamkondu, J.M. Perez de la Lastra, Cancer chemotherapy and beyond: Current status, drug candidates, associated risks and progress in targeted therapeutics, *Genes Dis.*, 10 (2023), pp. 1367-1401, <https://doi.org/10.1016/j.gendis.2022.02.007>
- [9] W.M.C. van den Boogaard, D.S.J. Komninos, W.P. Vermeij, Chemotherapy Side-Effects: Not All DNA Damage Is Equal, *Cancers*, 14 (2022), p. 627, <https://doi.org/10.3390/cancers14030627>
- [10] D.J. Benjamin, The efficacy of surgical treatment of cancer– 20 years later, *Med. Hypotheses*, 82 (2014), pp. 412-420, <http://dx.doi.org/10.1016/j.mehy.2014.01.004>
- [11] S. Tohme, R.L. Simmons, A. Tsung, Surgery for Cancer: A Trigger for Metastases, *Cancer Res.*, 77 (2017), pp. 1548-1552, <https://doi.org/10.1158/0008-5472.CAN-16-1536>
- [12] M. Zeman, M. Czarnecki, A. Chmielarz, A. Idasiak, M. Grajek, A. Czarniecka, Assessment of the risk of permanent stoma after low anterior resection in rectal cancer patients, *World J. Surg. Oncol.*, 18 (2020), p. 207, <https://doi.org/10.1186/s12957-020-01979-5>
- [13] L.L. Gunderson, J.E. Tepper (eds.), *Clinical Radiation Oncology*, third ed., Elsevier, Amsterdam, 2012

- [14] P. Mayles, A. Nahum, J. C. Rosenwald, Handbook Of Radiotherapy Physics. Theory and Practice, Taylor & Francis, Abingdon-on-Thames, 2007
- [15] K.A. Pilonis, C. Vanpouille-Box, S. Demaria, Combination of Radiotherapy and Immune Checkpoint Inhibitors, *Semin. Radiat. Oncol.*, 25 (2015), pp. 28-33, <http://dx.doi.org/10.1016/j.semradonc.2014.07.004>
- [16] S. Tan, D. Li, X. Zhu, Cancer immunotherapy: Pros, cons and beyond, *Biomed. Pharmacother.*, 124 (2020), article 109821, <https://doi.org/10.1016/j.biopha.2020.109821>
- [17] G. Chaput, L. Regnier, Radiotherapy: Clinical pearls for primary care, *Can. Fam. Physician.*, 67 (2021), pp. 753-757, <https://doi.org/10.46747/cfp.6710753>
- [18] E. Miller, A. Nalin, D.D. Pardo, A. Arnett, L. Abushahin, S. Husain, N. Jin, T. Williams, J. Bazan, Stage I Squamous Cell Carcinoma of the Anus: Is Radiation Therapy Alone Sufficient Treatment?, *Cancers*, 4 (2020), p. 3248, <https://doi.org/10.3390/cancers12113248>
- [19] M. Rucińska, Combined radiotherapy and chemotherapy, *Nowotwory J. Oncol.*, 72 (2022), pp. 319-325, <https://doi.org/10.5603/NJO.2022.0051>
- [20] T. Mee, N.F. Kirkby, N.N. Defourny, K.J. Kirkby, N.G. Burnet, *Br. J. Radiol.*, 96 (2023), article 20230334, <https://doi.org/10.1259/bjr.20230334>
- [21] R. Baskar, K.A. Lee, R. Yeo, K.-W. Yeoh, Cancer and Radiation Therapy: Current Advances and Future Directions, *Int. J. Med. Sci.*, 9 (2012), pp. 193-199, <https://doi.org/10.7150/ijms.3635>
- [22] S. Baatout (ed.), *Radiobiology Textbook*, Springer Nature, Basel, 2023
- [23] Y. Jiao, F. Cao, H. Liu, Radiation-induced Cell Death and Its Mechanisms, *Health Phys.*, 123 (2022), pp. 376-386, <https://doi.org/10.1097/HP.0000000000001601>
- [24] N. Ghaderi, J. Jung, S.C. Brünink, A. Subramanian, L. Nassour, J. Peacock, A Century of Fractionated Radiotherapy: How Mathematical Oncology Can Break the Rules, *Int. J. Mol. Sci.*, 23 (2022), p. 1316, <https://doi.org/10.3390/ijms23031316>
- [25] J.R. Hubenak, Q. Zhang, C.D. Branch, S.J. Kronovitz, Mechanisms of injury to normal tissue after radiotherapy: a review, *Plast. Reconstr. Surg.*, 133 (2014), 49e-56e, <https://doi.org/10.1097/01.prs.0000440818.23647.0b>
- [26] J.P. Williams, W. Newhauser, Normal tissue damage: its importance, history and challenges for the future, *Br. J. Radiol.*, 92 (2019), article 20180048, <https://doi.org/10.1259/bjr.20180048>
- [27] G. Mohan, A.T.P. Hamna, A.J. Jijo, S.K.M. Devi, A. Narayanasamy, B. Vellingiri, Recent advances in radiotherapy and its associated side effects in cancer—a review, *JoBAZ*, 80 (2019), p. 14, <https://doi.org/10.1186/s41936-019-0083-5>
- [28] L.F.N. Yit, Y. Li, A Review of the Evolving Role of Radiotherapy in the Treatment of Neuroendocrine Neoplasms, *Neuroendocrinology*, 114 (2024), pp. 856-865, <https://doi.org/10.1159/000538140>
- [29] D. Lahkar, R. Kalita, H. Kashyap, Evolution of Radiotherapy- A Brief Review, *J. Med. Sci. Clin. Res.*, 12 (2024), pp. 5-11, <https://dx.doi.org/10.18535/jmscr/v12i02.02>
- [30] Y. Nishimura, R. Komaki (eds.), *Intensity-Modulated Radiation Therapy*, Springer Nature, Tokyo, 2015
- [31] J.M. Galvin, G. Ezzell, A. Eisbrauch, C. Yu, B. Butler, Y. Xiao, I. Rosen, J. Rosenman, M. Sharpe, L. Xing, P. Xia, T. Lomax, D.A. Low, J. Palta, IMPLEMENTING IMRT IN CLINICAL

PRACTICE: A JOINT DOCUMENT OF THE AMERICAN SOCIETY FOR THERAPEUTIC RADIOLOGY AND ONCOLOGY AND THE AMERICAN ASSOCIATION OF PHYSICISTS IN MEDICINE, *Int. J. Radiat. Oncol. Biol. Phys.*, 58 (2004), pp. 1616-1634, <https://doi.org/10.1016/j.ijrobp.2003.12.008>

- [32] J. ur Rehman, Zahra, N. Ahmad, M. Khalid, H.M. Noor ul Huda Khan Asghar, Z.A. Gilani, I. Ullah, G. Nasar, M.M. Akhtar, M.N. Usmani, Intensity modulated radiation therapy: A review of current practice and future outlooks, *J. Radiat. Res. Appl. Sci.*, 11 (2018), pp. 361-367, <https://doi.org/10.1016/j.jrras.2018.07.006>
- [33] M. Teoh, C.H. Clark, K. Wood, S. Whitaker, A. Nisbet, Volumetric modulated arc therapy: a review of current literature and clinical use in practice, *Br. J. Radiol.*, 84 (2011), pp. 967-996, <https://doi.org/10.1259/bjr/22373346>
- [34] F. Cuccia, S. D'Alessandro, G. Carruba, V. Figlia, A. Spera, D. Cespuglio, G. Mortellaro, G. Iavociello, A. Lo Casto, G. Tringali, G. Craparo, L. Blasi, G. Ferrera, Fractionated Stereotactic Radiotherapy with Helical Tomotherapy for Brain Metastases: A Mono-Institutional Experience, *J. Pers. Med.*, 13 (2023), p. 1099, <https://doi.org/10.3390/jpm13071099>
- [35] T.D. Solberg, P.M. Medin, Quality and safety in stereotactic radiosurgery and stereotactic body radiation therapy: can more be done?, *JRSBRT*, 1 (2011), pp. 13-19
- [36] N. Matuszak, W.M. Suchorska, P. Milecki, M. Kruszyna-Mochalska, A. Misiarz, J. Pracz, J. Malicki, FLASH radiotherapy: an emerging approach in radiation therapy, *RPOR*, 27 (2022), pp. 344-351, <https://doi.org/10.5603/rPOR.a2022.0038>
- [37] K. Śłosarek, FLASH technology – new possibilities of radiotherapy (in Polish), *IFM*, 4 (2022), pp. 279-282
- [38] D.L. Dewey, J.W. Boag, Modification of the oxygen effect when bacteria are given large pulses of radiation, *Nature*, 183 (1959), pp. 1450–1451, <https://doi.org/10.1038/1831450a0>
- [39] J C.D. Town, Radiobiology. Effect of high dose rates on survival of mammalian cells, *Nature*, 215 (1967), pp. 847–848, <https://doi.org/10.1038/215847a0>
- [40] S.C. Bondy, FLASH Radiotherapy Versus Conventional Cancer Therapy: Promises, Paradoxes and Problems, *Int. J. Transl. Med.*, 4 (2024), pp. 559-569, <https://doi.org/10.3390/ijtm4030038>
- [41] G. Pratx, D.S. Kapp, Ultra-high-dose-rate FLASH irradiation may spare hypoxic stem cell niches in normal tissues, *Int. J. Radiat. Oncol. Biol. Phys.* 105 (2019), pp. 190–192, <https://doi.org/10.1016/j.ijrobp.2019.05.030>
- [42] C. Chargari, E. Deutsh, P. Blanchard, S. Gouy, H. Martelli, F. Guerin, I. Dumas, A. Bossi, P. Morice, A.N. Viswanathan, Ch. Haie-Meder, Brachytherapy: An Overview for Clinicians, *CA Cancer J. Clin.*, 69 (2019), pp. 386-401, <https://doi.org/10.3322/caac.21578>
- [43] R. Potter, K. Tanderup, Ch. Kirisits, A. de Leeuw, K. Kirchheiner, R. Nout, L.T. Tan, Ch. Haie-Meder, U. Mahantshetty, B. Segedin, P. Hoskin, K. Bruheim, B. Rai, F. Huang, E. Van Limbergen, M. Shmid, N. Nesvacil, A. Sturdza, L. Fokdal, N.B.K. Jensen, D. Georg, M. Assenholt, Y. Seppenwoolde, Ch. Nomden, I. Fortin, S. Chopra, U. van der Heide, T. Rumpold, J.Ch. Lindegaard, I. Jurgenliemk-Schulz, the EMBRACE Collaborative Group, The EMBRACE II study: The outcome and prospect of two decades of evolution within the GEC-ESTRO GYN working group and the EMBRACE studies, *Clin. Transl. Radiat. Oncol.*, 9 (2018), pp. 48-60, <https://doi.org/10.1016/j.ctro.2018.01.001>

- [44] T. Kron, J. Lehmann, P.B. Greer, Dosimetry of ionising radiation in modern radiation oncology, *Phys. Med. Biol.*, 61 (2016), R167–205, <http://dx.doi.org/10.1088/0031-9155/61/14/R167>
- [45] E.E. Klein, J. Hanley, J. Bayouth, F.F. Yin, W. Simon, S. Dresser, C. Serago, F. Aguirre, L. Ma, B. Arjomandy, C. Liu, C. Sandin, T. Holmes, Task Group 142 report: Quality assurance of medical accelerators, *Med. Phys.*, 36 (2009), pp. 4197–4212, <https://doi.org/10.1118/1.3190392>
- [46] D.H. Choi, J.S. Kim, R. Lee, S.H. Ahn, W.S. Ahn, Dosimetric verification of annual quality assurance for a linear accelerator using a transmission type detector, *Sci. Rep.*, 13 (2023), article 17994, <https://doi.org/10.1038/s41598-023-45114-2>
- [47] G. Gungor, G. Aydin, T.Z. Mustafayev, E. Ozyar, Output factors of ionization chambers and solid state detectors for mobile intraoperative radiotherapy (IORT) accelerator electron beams, *J. Appl. Clin. Med. Phys.*, 20 (2019), pp. 13–23, <https://doi.org/10.1002/acm2.12522>
- [48] Sh. Akter, R. Khatun, F. Uddin, A.N. Monika, M. Rahman, M. Parvej, N. Sultana, A. Hasnat, S. Alim, M.M. Ahasan, Dosimetry Measurement of Medical Linear Accelerator and Assessment the Authentication it with Machine Records, *J. Med. Phys. Appl. Sci.*, 7 (2022), article IPIMP-22-13844, <https://doi.org/10.36648/2574-285x.7.4.19>
- [49] E.B. Podgorsak (ed.), *Radiation Oncology Physics: A Handbook for Teachers and Students*, INTERNATIONAL ATOMIC ENERGY AGENCY, Vienna, 2005
- [50] *Absorbed Dose Determination in External Beam Radiotherapy*, Technical Report Series No. 398, INTERNATIONAL ATOMIC ENERGY AGENCY, Vienna, 2000
- [51] E. Spezi, A.L. Angelini, F. Romani, A. Ferri, Characterization of a 2D ion chamber array for the verification of radiotherapy treatments, *Phys. Med. Biol.*, 50 (2005), pp. 3361–3373, <http://dx.doi.org/10.1088/0031-9155/50/14/012>
- [52] L. de Freitas Nascimento, A. Gasparini, Review of real time 2D dosimetry in external radiotherapy: Advancements and techniques, *Radiat. Meas.*, 180 (2025), article 107344, <https://doi.org/10.1016/j.radmeas.2024.107344>
- [53] F. Horst, Calorimetry as a tool to improve the dosimetric accuracy in novel radiotherapy modalities, *phiRO*, 28 (2023), article 100516, <https://doi.org/10.1016/j.phro.2023.100516>
- [54] J. Vedalgo, Ch.P. Karger, O. Jakel, A review on reference dosimetry in radiation therapy with proton and light ion beams: status and impact of new developments, *Radiat. Meas.*, 157 (2022), article 106844, <https://doi.org/10.1016/j.radmeas.2022.106844>
- [55] A. Subiel, F. Romano, Recent developments in absolute dosimetry for FLASH radiotherapy, *Br. J. Radiol.*, 96 (2023), article 20220560, <https://doi.org/10.1259/bjr.20220560>
- [56] G.A. Bass, D.R. Shipley, S.F. Flynn, R.A.S. Thomas, A prototype low-cost secondary standard calorimeter for reference dosimetry with ultra-high pulse dose rates, *Br. J. Radiol.*, 96 (2023), article 20220638, <https://doi.org/10.1259/bjr.20220638>
- [57] J. Kim, S.M. Nam, H. Jang, J.-P. Chung, J.S. Kim, B.-Ch. Kim, K.J. Chun, W. Lee, Development and application of chip calorimeter as an X-ray detector, *Curr. Appl. Phys.*, 20 (2020), pp. 337–343, <https://doi.org/10.1016/j.cap.2019.11.020>
- [58] J. Cotterill, S. Flynn, R. Thomas, A. Subiel, N. Lee, D. Shipley, H. Palmans, A. Lourenco, Monte Carlo modelling of a prototype small-body portable graphite calorimeter for ultra-high dose rate proton beams, *phiRO*, 28 (2023), article 100506, <https://doi.org/10.1016/j.phro.2023.100506>

- [59] B. Mijnheer, EPIDs and QA of advanced treatments, *J. Phys.: Conf. Ser.*, 1305 (2019), article 012061, <https://doi.org/10.1088/1742-6596/1305/1/012061>
- [60] B.M.C. McCurdy, Dosimetry in radiotherapy using a-Si EPIDs: Systems, methods, and applications focusing on 3D patient dose estimation, *J. Phys.: Conf. Ser.*, 444 (2013), article 012002, <https://doi.org/10.1088/1742-6596/444/1/012002>
- [61] Ch. Arilli, Y. Wandaël, Ch. Galeotti, L. Marazzo, S. Calusi, M. Grusio, I. Desideri, F. Fusi, A. Piermattei, S. Pallotta, C. Talamonti, Combined Use of a Transmission Detector and an EPID-Based In Vivo Dose Monitoring System in External Beam Whole Breast Irradiation: A Study with an Anthropomorphic Female Phantom, *Appl. Sci.*, 10 (2020), article, 7611, <https://doi.org/10.3390/app10217611>
- [62] N. Dogan, B.J. Mijnheer, K. Padgett, A. Nalichowski, Ch. Wu, M.J. Nyflot, A.J. Olch, N. Papanikolaou, J. Shi, Sh.M. Holmes, J. Moran, P.B. Greer, AAPM Task Group Report 307: Use of EPIDs for Patient-Specific IMRT and VMAT QA, *Med. Phys.*, 50 (2023), pp. e865-e903, <https://doi.org/10.1002/mp.16536>
- [63] F.M. Khan (ed), *THE PHYSICS OF RADIATION THERAPY Third Edition*, Lippincott Williams & Wilkins, Philadelphia, 2003
- [64] B. Sadeghi, R. Purimani, M.R. Bayatiani, A. Jafari, F. Seif, Thermoluminescent dosimeters (TLD-100 and GR-200) calibration for dose verification in radiotherapy: Different photon and electron energies, *Radiat. Phys. Chem.*, 230 (2025), article 112590, <https://doi.org/10.1016/j.radphyschem.2025.112590>
- [65] L. Beaulieu, M. Goulet, L. Archambault, S. Beddar, Current status of scintillation dosimetry for megavoltage beams, *J. Phys.: Conf. Ser.*, 444 (2013), 012013, <https://doi.org/10.1088/1742-6596/444/1/012013>
- [66] Ł. Kapłon, G. Moskal, Blue-emitting polystyrene scintillators for plastic scintillation dosimetry, *BAMS*, 17 (2021), pp. 191-197, <https://doi.org/10.1515/bams-2021-0088>
- [67] E. Ciarrocchi, E. Ravera, A. Cavalieri, M. Celentano, D. Del Sarto, F. Di Martino, S. Linsalata, M. Massa, L. Masturzo, A. Moggi, M. Morrocchi, J.H. Pensavalle, M.G. Bisogni, Plastic scintillator-based dosimeters for ultra-high dose rate (UHDR) electron radiotherapy, *Phys. Med.*, 121 (2024), article 103360, <https://doi.org/10.1016/j.ejmp.2024.103360>
- [68] A. Gago-Arias, D.M. Gonzalez-Castano, F. Gomez, E. Peteiro, C. Lodeiro, J. Pardo-Montero, Development of an alanine dosimetry system for radiation dose measurements in the radiotherapy range, *JINST*, 10 (2015), article T08004, <https://doi.org/10.1088/1748-0221/10/08/T08004>
- [69] A.M. Al-Karmi, M.A. Morsy, EPR of gamma-irradiated polycrystalline alanine-in-glass dosimeter, *Radiat. Meas.*, 43 (2008), pp. 1315-1318, <https://doi.org/10.1016/j.radmeas.2008.04.088>
- [70] A. Romanyukha, J. Delzer, Multiple alanine pellet dosimeter: Design and first test results, *Radiat. Meas.*, 176 (2024), article 107201, <https://doi.org/10.1016/j.radmeas.2024.107201>
- [71] K. Schultka, B. Ciesielski, B. Wysocka, In vivo dosimetry in electron beam teletherapy using electron paramagnetic resonance in L-alanine, *Nowotwory J. Oncol.*, 55 (2005), pp. 448-451,
- [72] A. Bourgouin, T. Hackel, M. Marinelli, R. Kranzer, A. Schuller, R.-P. Kapsch, Absorbed-dose-to-water measurement using alanine in ultra-high pulse-dose-rate electron beams, *Phys. Med. Biol.*, 67 (2022), article 205011, <https://doi.org/10.1088/1361-6560/ac950b>

- [73] A.B. Rosenfeld, G. Biasi, M. Petasecca, M.L.F. Lerch, G. Villani, V. Feygelman, Semiconductor dosimetry in modern external-beam radiation therapy, *Phys. Med. Biol.*, 65 (2020), article 16TR01, <https://doi.org/10.1088/1361-6560/aba163>
- [74] S. Pai, I.J. Das, J.F. Dempsey, K.L. Lam, T.J. LoSasso, A.J. Olch, J.R. Palta, L.E. Reinstein, D. Ritt, E.E. Wilcox, TG-69: Radiographic film for megavoltage beam dosimetry, *Med. Phys.*, 34 (2007), pp. 2228-2258, <https://doi.org/10.1118/1.2736779>
- [75] P.L. Roberson, J.M. Moran, R. Kulasekere, Radiographic film dosimetry for IMRT fields in the near surface buildup region, *J. Appl. Clin. Med. Phys.*, 9 (2008), pp. 87-97, <https://doi.org/10.1120/jacmp.v9i4.2782>
- [76] S. Devic, N. Tomic, D. Lewis, Reference radiochromic film dosimetry: Review of technical aspects, *Phys. Med.*, 32 (2016), pp. 541-556, <http://dx.doi.org/10.1016/j.ejmp.2016.02.008>
- [77] R.S. Khandpur, *Compendium of Biomedical Instrumentation*, Volume 2, Wiley, New York, 2020
- [78] S. Devic, Radiochromic film dosimetry: Past, present, and future, *Phys. Med.*, 27 (2011), pp. 122-134, <http://dx.doi.org/10.1016/j.ejmp.2010.10.001>
- [79] A.L. Palmer, D. Nash, Radiochromic film dosimetry in radiotherapy: a survey of current practice in the United Kingdom, *Br. J. Radiol.*, 97 (2024), pp. 646-651, <https://doi.org/10.1093/bjr/tqae008>
- [80] R. Broszkiewicz, *Chemical methods of ionizing radiation dosimetry* (in Polish), Wydawnictwa Naukowo-Techniczne, Warsaw, 1971
- [81] R. Polanek, Z. Varga, E. Fodor, Sz. Brunner, E.R. Szabó, T. Tőkés, K. Hideghéty, Improved FBX chemical dosimeter system with enhanced radiochemical yield for reference dosimetry in radiobiology and radiotherapy research, *Radiat. Phys. Chem.*, 174 (2020), article 108899, <https://doi.org/10.1016/j.radphyschem.2020.108899>
- [82] A. Kuppermann, Theoretical Foundations of Radiation Chemistry, *J. Chem. Educ.*, 36 (1959), pp. 279-285, <https://doi.org/10.1021/ed036p279>
- [83] S. La Caer, Water Radiolysis: Influence of Oxide Surfaces on H₂ Production under Ionizing Radiation, *Water*, 3 (2011), pp. 235-253, <https://doi.org/10.3390/w3010235>
- [84] H. Fricke, S. Morse, The chemical action of Roentgen rays on dilute ferrous sulphate solutions as a measure of radiation dose, *Am. J. Roentgenol. Radium Ther. Nucl. Med.*, 18 (1927), pp. 430-432
- [85] W. Stenström, A. Lohmann, EFFECT OF ROENTGEN RADIATION ON SOLUTIONS OF TYROSINE AND CYSTINE, *J. Biol. Chem.*, 79 (1928), pp. 673-678, [https://doi.org/10.1016/S0021-9258\(20\)79956-4](https://doi.org/10.1016/S0021-9258(20)79956-4)
- [86] T.J. Hardwick, Radiation chemistry investigation of aqueous solutions using P32 and S35 as internal sources. *Can. J. Chem.*, 30 (1952), pp. 17-22, <http://doi.org/10.1139/v52-003>
- [87] K. Sharf, M.R. Lee, Investigation of the spectrophotometric method of measuring the ferric ion yield in the ferrous sulfate dosimeter. *Radiat. Res.*, 16 (1962), pp. 115-124, <http://doi.org/10.2307/3571190>
- [88] F.H. Krenz, H.A. Dewhurst, The Mechanism of Oxidation of ferrous Sulphate by γ -Rays in Aerated Water, *J. Chem. Phys.*, 17 (1949), p. 1337, <https://doi.org/10.1063/1.1747167>

- [89] J.-P. Jay-Gerin, Fundamentals of Water Radiolysis, Encyclopedia, 5 (2025), p. 38, <https://doi.org/10.3390/encyclopedia5010038>
- [90] L.J. Schreiner, Review of Fricke gel dosimeters, J. Phys.: Conf. Ser., 3 (2004), pp. 9-21, <https://doi.org/10.1088/1742-6596/3/1/003>
- [91] T. Kume, H. Tachibana, M. Takehisa, Japan Atomic Energy Research Inst., Fricke dosimetry in low dose range for food irradiation, Tokyo, 1982
- [92] H.A. Dewhurst, Effect of organic substance on the γ -ray oxidation of ferrous sulphate, J. Chem. Phys., 19 (1951), p. 1329, <https://doi.org/10.1063/1.1748051>
- [93] L.S. Del Lama, P.C.D. Petchevist, A. de Almeida, Fricke Xylenol Gel characterization at megavoltage radiation energy, Nucl. Instrum. Methods Phys. Res. B, 394 (2017), pp. 89-96, <http://dx.doi.org/10.1016/j.nimb.2016.12.045>
- [94] R.K. Broszkiewicz, Z. Bulhak, Errors in Ferrous Sulphate Dosimetry, Phys. Med. Biol., 15 (1970), pp. 549-556, <https://doi.org/10.1088/0031-9155/15/3/315>
- [95] Y. De Deene, Radiation dosimetry by use of radiosensitive hydrogels and polymers: mechanisms, state-of-the-art and perspective from 3D to 4D, Gels, 8 (2022), p. 599, <https://doi.org/10.3390/gels8090599>
- [96] A.O. Allen, Hugo Fricke and the Development of Radiation Chemistry: A Perspective View. Radiat. Res., 17 (1962), pp. 255–261, <http://doi.org/10.2307/3571090>
- [97] E.M. Arango, A. Pickler, A. Mantuano, C. Salata, C.D. de Almeida, Feasibility study of the Fricke chemical dosimeter as an independent dosimetric system for the small animal radiation research platform (SARRP), Phys. Med., 71 (2020), pp. 168-175, <https://doi.org/10.1016/j.ejmp.2020.03.006>
- [98] B.L. Gupta, R.M. Bhat, G.R. Narayan, S.R. Nilekani, Chemical dosimetry techniques for various applications under different geometries, Radiat. Phys. Chem., 59 (2000), pp. 81-90, [https://doi.org/10.1016/S0969-806X\(00\)00187-0](https://doi.org/10.1016/S0969-806X(00)00187-0)
- [99] B.L. Gupta, R.M. Bhat, G.R. Narayan, B. Susheela, Acid and xylenol orange effects in the FBX dosimeter, Int. J. Appl. Radiat. Isot., 34 (1983), pp. 887–890. [https://doi.org/10.1016/0020-708x\(83\)90148-5](https://doi.org/10.1016/0020-708x(83)90148-5)
- [100] B.L. Gupta, U.R. Kini, R.M. Bhat, Sensitivity of ferrous sulphate-benzoic acid-xylenol orange dosimeter (FBX system) to $^{10}\text{B}(\text{n}, \alpha)^7\text{Li}$ recoils, Int. J. Appl. Radiat. Isot., 27 (1976), pp. 31–34. [https://doi.org/10.1016/0020-708x\(76\)90165-4](https://doi.org/10.1016/0020-708x(76)90165-4)
- [101] B.L. Gupta, U.R. Kini, R.M. Bhat, Dose-rate and fractionation studies with FBX dosimeter, Int. J. Appl. Radiat. Isot., 32 (1981), pp. 701–704. [https://doi.org/10.1016/0020-708x\(81\)90017-x](https://doi.org/10.1016/0020-708x(81)90017-x)
- [102] B.L. Gupta, G.R. Narayan, R.M. Bhat, U.R. Kini, R.S. Ramaswamy, B. Suseela Use of the FBX dosimeter for the quality assurance of ^{60}Co and high energy teletherapy machines by mail, Phys. Med. Biol., 37 (1992), pp. 2095-2102, <https://doi.org/10.1088/0031-9155/37/11/006>
- [103] C. Baldock, Y. De Deene, S. Doran, G. Ibbott, A. Jirasek, M. Lepage, K.B. McAuley, M. Oldham, L.J. Schreiner, Polymer gel dosimetry, Phys. Med. Biol., 55 (2010), pp. R1–R63, <http://dx.doi.org/10.1088/0031-9155/55/5/R01>
- [104] Y. De Deene, J. Vandecasteele, T. Vercauteren, Low-density polymer gel dosimeters for 3D radiation dosimetry in the thoracic region: A preliminary study, J. Phys.: Conf. Ser., 444 (2013), article 012026, <https://doi.org/10.1088/1742-6596/444/1/012026>

- [105] Y. De Deene, K. Vergote, C. Claeys, C. De Wagter, Three dimensional radiation dosimetry in lung-equivalent regions by use of a radiation sensitive gel foam: Proof of principle, *Med. Phys.*, 33 (2006), pp. 2586-2597, <http://doi.org/10.1118/1.2208939>
- [106] M. Kozicki, M. Bartosiak, P. Maras, R. Wach, S. Kadłubowski, First Combined, Double-Density LCV-Pluronic F-127 Radiochromic Dosimeter Mimicking Lungs and Muscles, *Adv. Mater. Technol.*, 8 (2023), article 2201023, <https://doi.org/10.1002/admt.202201023>
- [107] N. Kumahara, A. Takemura, S. Ishihara, K. Noto, H. Kojima, N. Isomura, H. Yokoyama, I. Goto, Sensitivity of a bone-equivalent polymer gel dosimeter for measuring the dose to bone during radiation therapy, *Radiol. Phys. Technol.*, 16 (2023), pp. 227-234, <https://doi.org/10.1007/s12194-023-00710-9>
- [108] M. Jaszczak-Kuligowska, M. Kozicki, P. Maras, Towards optimisation of the chemical composition of a bone-imitating dosimeter as a potential component of multiphase dosimeters, *J. Phys.: Conf. Ser.*, 2799 (2024), article 012006, <https://doi.org/10.1088/1742-6596/2799/1/012006>
- [109] M. Kozicki, M. Jaszczak-Kuligowska, P. Maras, Measurement of ionising radiation dose absorbed by bones by using a bone-imitating polymer gel dosimeter, *Measurement*, 240 (2025), article 115633, <https://doi.org/10.1016/j.measurement.2024.115633>
- [110] M. Kozicki, P. Maras, M. Jaszczak-Kuligowska, Multiphase 3D dosimeters for radiotherapy, *J. Phys.: Conf. Ser.*, 2799 (2024), article 012001, <https://doi.org/10.1088/1742-6596/2799/1/012001>
- [111] C.J. Niu, W.D. Foltz, M. Velec, J.L. Moseley, A. Al-Mayah, A novel technique to enable experimental validation of deformable dose accumulation, *Med. Phys.*, 39 (2012), pp. 765-776, <https://doi.org/10.1118/1.3676185>
- [112] L.P. Kaplan, E.M. Høye, P. Balling, L.P. Muren, J.B.B Petersen, P.R. Poulsen, E.S. Yates, P.S. Skyt, Determining the mechanical properties of a radiochromic silicone-based 3D dosimeter, *Phys. Med. Biol.*, 62 (2017), pp. 5612-5622, <https://doi.org/10.1088/1361-6560/aa70cd>
- [113] Y. De Deene, P.S. Skyt, R. Hill, J.T. Booth, FlexyDos3D: a deformable anthropomorphic 3D radiation dosimeter: radiation properties, *Phys. Med. Biol.*, 60 (2015), pp. 1543-1563, <https://doi.org/10.1088/0031-9155/60/4/1543>
- [114] E.M. Høye, P.S. Skyt, E.S. Yates, L.P. Muren, J.B.B Petersen, P. Balling, A new dosimeter formulation for deformable 3D dose verification, *J. Phys.: Conf. Ser.*, 573 (2015), article 012067, <https://doi.org/10.1088/1742-6596/573/1/012067>
- [115] J.C. Gore, Y.S. Kang, R.J. Shultz, Measurement of radiation dose distributions by nuclear magnetic resonance (NMR) imaging, *Phys. Med. Biol.*, 29 (1984), pp. 1189-1197, <https://doi.org/10.1088/0031-9155/29/10/002>
- [116] J.C. Gore, Y.S. Kang, R.J. Shultz, Measurement of radiation dose distributions by NMR imaging, *Magn. Reson. Imaging*, 2 (1984), p. 244, [https://doi.org/10.1016/0730-725X\(84\)90033-X](https://doi.org/10.1016/0730-725X(84)90033-X)
- [117] A. Appleby, E.A. Christman, A. Leghrouz, Imaging of spatial radiation dose distribution in agarose gels using magnetic resonance, *Med. Phys.*, 14 (1987), pp. 382-384, <https://doi.org/10.1118/1.596052>

- [118] C. Duzenil, L. Sloboda, D. Robinson, A spin-spin relaxation rate investigation of the gelatin ferrous sulphate NMR dosimeter, *Phys. Med. Biol.*, 39 (1994), pp. 1577-1592, <https://doi.org/10.1088/0031-9155/39/10/005>
- [119] L.E. Olsson, S. Petersson, L. Ahlgren, S. Mattson, Ferrous sulphate gels for determination of absorbed dose distributions using MRI technique: basic studies, *Phys. Med. Biol.*, 34 (1989), pp. 43-52, <https://doi.org/10.1088/0031-9155/34/1/004>
- [120] M.A. Bero, W.B. Gilboy, P.M. Glover, Radiochromic gel dosimeter for three-dimensional dosimetry, *Radiat. Phys. Chem.*, 61 (2001), pp. 433-435, [https://doi.org/10.1016/S0969-806X\(01\)00289-4](https://doi.org/10.1016/S0969-806X(01)00289-4)
- [121] G.M. Liosi, D. Dondi, D.A. Vander Griend, S. Lazzaroni, G. D'Agostino, M. Mariani, Fricke-gel dosimeter: overview of Xylenol Orange chemical behavior, *Radiat. Phys. Chem.*, 140 (2017), pp. 74-77, <https://doi.org/10.1016/j.radphyschem.2017.01.012>
- [122] T.V. Pedersen, D.R. Olsen, A. Skretting, Measurement of the ferric diffusion coefficient in agarose and gelatine gels by utilization of the evolution of a radiation induced edge as reflected in relaxation rate images, *Phys. Med. Biol.*, 42 (1997), pp. 1575-1585, <https://doi.org/10.1088/0031-9155/42/8/008>
- [123] C. Baldock, P.J. Harris, A.R. Piercy, B. Healy, Experimental determination of the diffusion coefficient in two dimensions in ferrous sulphate gels using the finite element method, *Australas. Phys. Eng. Sci. Med.*, 24 (2001), pp. 19-30, <https://doi.org/10.1007/BF03178282>
- [124] S.J. Doran, The history and principles of optical computed tomography for scanning 3D radiation dosimeters: 2008 update, *J. Phys.: Conf. Ser.*, 164 (2009), article 012020, <https://doi.org/10.1088/1742-6596/164/1/012020>
- [125] A.V.S. Alves, W.S. de Almeida, E.M. Sussuchi, L. Lazzeri, F. d'Errico, S.O. de Souza, Investigation of chelating agents/ligands for Fricke gel dosimeters, 150 (2018), pp. 151-156, <https://doi.org/10.1016/j.radphyschem.2018.04.031>
- [126] M. Lepage, K. Jordan, 3D dosimetry fundamentals: gels and plastics, *J. Phys.: Conf. Ser.*, 250 (2010), article 012055, <https://doi.org/10.1088/1742-6596/250/1/012055>
- [127] W.I. Rae, C.A. Willemse, M.G. Lötter, J.S. Engelbrecht, J.C. Swarts, Chelator effect on ion diffusion in ferrous-sulfate-doped gelatin gel dosimeters as analyzed by MRI, *Med. Phys.*, 23 (1996), pp. 15-23, <https://doi.org/10.1118/1.597787>
- [128] J.P. Fernandes, B.F. Pastorello, D.B. de Araújo, O. Baffa Formaldehyde increases MAGIC gel dosimeter melting point and sensitivity, *J. Phys.: Conf. Ser.* 164 (2009), article 012004, <https://doi.org/10.1088/0031-9155/53/4/n04>
- [129] A. Songur, O.A. Ozen, M. Sarsilmaz, The toxic effects of formaldehyde on the nervous system, *Rev. Environ. Contam. Toxicol.*, 203 (2010), pp. 105-18, https://doi.org/10.1007/978-1-4419-1352-4_3
- [130] K. Jordan, M. Sekimoto, Effects of adding glycerol and sucrose to ferrous xylenol orange hydrogel, *J. Phys. Conf. Ser.*, 250 (2010), Article 012048, <https://doi.org/10.1088/1742-6596/250/1/012048>
- [131] T. Maeyama, N. Fukunishi, K.L. Ishikawa, T. Furuta, K. Fukasaku, S. Takagi, S. Noda, R. Himeno, S. Fukuda, A diffusion-free and linear-energy-transfer-independent nanocomposite Fricke gel dosimeter, *Radiat. Phys. Chem.*, 96 (2014), pp. 92-96, <http://dx.doi.org/10.1016/j.radphyschem.2013.09.004>

- [132] M.M. Eyadeh, K.A. Rabaeh, T.F. Hailat, F.M. Aldweri, Evaluation of ferrous Methylthymol blue gelatin gel dosimeters using nuclear magnetic resonance and optical techniques, *Radiat. Meas.*, 108 (2018), pp. 26-33, <https://doi.org/10.1016/j.radmeas.2017.11.004>
- [133] K.I. Penev, K. Mequanint, Controlling sensitivity and stability of ferrous–xylenol orange–gelatin 3D gel dosimeters by doping with phenanthroline-type ligands and glyoxal, *Phys. Med. Biol.*, 58 (2013), pp. 1823–1838, <http://dx.doi.org/10.1088/0031-9155/58/6/1823>
- [134] N.A. Silva, P. Nicolucci, O. Baffa, Spatial resolution of magnetic resonance imaging Fricke-gel dosimetry is improved with a honeycomb phantom, *Med. Phys.*, 30 (2003), pp. 17-20, <https://doi.org/10.1118/1.1527039>
- [135] K. Jordan, M. Sekimoto, Development of a radiochromic ferric oligomer hydrogel, *J. Phys. Conf. Ser.*, 250 (2010), Article 012030, <https://doi.org/10.1088/1742-6596/250/1/012030>
- [136] K.C. Chu, K.J. Jordan, J.J. Battista, J. Van Dyk, B.K. Rutt, Polyvinyl alcohol-Fricke hydrogel and cryogel: Two new gel dosimetry systems with low Fe^{3+} diffusion, *Phys. Med. Biol.*, 45 (2000), pp. 955–969, <https://doi.org/10.1088/0031-9155/45/4/311>
- [137] F. d’Errico, L. Lazzeri, D. Dondi, M. Mariani, M. Marrale, S.O. Souza, S. Gambarini, Novel GTA-PVA Fricke gels for three-dimensional dose mapping in radiotherapy, *Radiat. Meas.*, 106 (2017), pp. 612-617, <https://doi.org/10.1016/j.radmeas.2017.07.003>
- [138] A. Marini, L. Lazzeri, M.G. Cascone, R. Ciolini, L. Tana, F. d’Errico, Fricke gel dosimeters with low-diffusion and high-sensitivity based on a chemically cross-linked PVA matrix, *Radiat. Meas.*, 106 (2017), pp. 618-621, <http://dx.doi.org/10.1016/j.radmeas.2017.02.012>
- [139] M.M. Eyadeh, K.A. Rabaeh, T.F. Hailat, M.Y. Al-Shorman, F.M. Aldweri, H.M. Kanan, S.I. Awad, Investigation of a novel chemically cross-linked fricke-Methylthymol blue-synthetic polymer gel dosimeter with glutaraldehyde cross-linker, *Radiat. Meas.*, 118 (2018), pp. 77-85, <https://doi.org/10.1016/j.radmeas.2018.09.013>
- [140] K.A. Rabaeh, M.M. Eyadeh, T.F. Hailat, B.G. Madas, F.M. Aldweri, A.M. Almomani, S.I. Awad, Improvement on the performance of chemically cross-linked Fricke methylthymol-blue radiochromic gel dosimeter by addition of dimethyl sulfoxide, *Radiat. Measur.*, 141 (2021), Article 106540, <https://doi.org/10.1016/j.radmeas.2021.106540>
- [141] M.M. Eyadeh, K.A. Rabaeh, L.S. Alshomali, K.R. Diamond, A.A. Oglat, Evaluation of a novel physically cross-linked fricke-xylenol orange-polyvinyl alcohol radio-chromic gel dosimeter for radiotherapy, *Radiat. Meas.*, 177 (2024), Article 107263, <https://doi.org/10.1016/j.radmeas.2024.107263>
- [142] M. Piotrowski, P. Maras, S. Kadłubowski, M. Kozicki, Study of the Optimal Composition and Storage Conditions of the Fricke–XO–Pluronic F–127 Radiochromic Dosimeter, *Materials*, 15 (2022), Article 984, <https://doi.org/10.3390/ma15030984>
- [143] P. Alexandridis, T.A. Hatton, Poly(ethylene oxide)-poly(propylene oxide)-poly(ethylene oxide) block copolymer surfactants in aqueous solutions and at interfaces: Thermodynamics, structure, dynamics, and modelling, *Colloids Surf. A*, 96 (1995), pp. 1–46, [https://doi.org/10.1016/0927-7757\(94\)03028-X](https://doi.org/10.1016/0927-7757(94)03028-X)
- [144] H. Almeida, M.H. Amaral, P. Lobão, J.M.S. Lobo, Pluronic F–127 and Pluronic lecithin organogel (PLO): Main features and their applications in topical and transdermal administration of drugs, *J. Pharm. Pharm. Sci.*, 15 (2012), pp. 592–605, <https://doi.org/10.18433/J3HW2B>

- [145] I.M. Diniz, C. Chen, X. Xu, S. Ansari, H.H. Zadeh, M.M. Marques, S. Shi, A. Moshaverinina, A. Pluronic F-127 hydrogel as a promising scaffold for encapsulation of dental-derived mesenchymal stem cells, *J. Mater. Sci. Mater. Med.*, 26 (2015), Article 153, <https://doi.org/10.1007/s10856-015-5493-4>
- [146] M. Kozicki, K. Kwiatos, S. Kadlubowski, M. Dudek, TTC-Pluronic 3D radiochromic gel dosimetry of ionizing radiation, *Phys. Med. Biol.*, 62 (2017), pp. 5668–5690, <https://doi.org/10.1088/1361-6560/aa77eb>
- [147] M. Piotrowski, P. Maras, R. Wach, S. Kadlubowski, M. Kozicki, Impact of Salt on Thermal Stability and Dose Response of the Fricke-XO-Pluronic F-127 3D Radiotherapy Dosimeter, *Materials*, 15 (2022), Article 5223, <https://doi.org/10.3390/ma15155223>
- [148] M. Dudek, M. Piotrowski, P. Maras, M. Jaszczak, M. Kozicki, Anisotropic diffusion of Fe ions in Fricke-XO-Pluronic F-127 and Fricke-XO-Gelatine 3D radiotherapy dosimeters, *Phys. Med. Biol.*, 66 (2021), Article 155005, <https://doi.org/10.1088/1361-6560/ac101e>
- [149] M.J. Maryanski, J.C. Gore, R.P. Kennan, R.J. Schulz: NMR relaxation enhancement in gels polymerized and cross-linked by ionizing radiation: a new approach to 3D dosimetry by MRI, *Magn. Reson. Imaging*, 11, (1993), pp. 253–258. [https://doi.org/10.1016/0730-725X\(93\)90030-H](https://doi.org/10.1016/0730-725X(93)90030-H)
- [150] M.J. Maryanski, R.J. Schulz, G.S. Ibbott, J.C. Gatenby, J. Xie, D. Horton, J.C. Gore, Magnetic resonance imaging of radiation dose distributions using a polymer-gel dosimeter, *Phys. Med. Biol.*, 39 (1994), pp. 1437-1455, <https://doi.org/10.1088/0031-9155/39/9/010>
- [151] M.J. Maryanski, R.J. Schulz, J.C. Gore, Three dimensional detection, dosimetry and imaging of an energy field by formation of a polymer in a gel US Patent No. 5,321,357, 1994a
- [152] M. Hilts, C. Audet, C. Duzenli, A. Jirasek, Polymer gel dosimetry using x-ray computed tomography: a feasibility study, *Phys. Med. Biol.* 45 (2000), pp. 2559–71, <https://doi.org/10.1088/0031-9155/45/9/309>
- [153] M.L. Mather, A.K. Whitakker, C. Baldock, Ultrasound evaluation of polymer gel dosimeters *Phys. Med. Biol.* 47 (2002) 1449–58, <http://dx.doi.org/10.1088/0031-9155/47/9/302>
- [154] P.M. Fong, D.C. Keil, M.D. Does, J.C. Gore: Polymer gels for magnetic resonance imaging of radiation dose distributions at normal room atmosphere, *Phys. Med. Biol.*, 46 (2001), pp. 3105–3113, <https://doi.org/10.1088/0031-9155/46/12/303>
- [155] Y. De Deene, C. Hurley, A. Venning, K. Vergote, M. Mather, B.J. Healy, C. Baldock, A basic study of some normoxic polymer gel dosimeters, *Phys. Med. Biol.*, 19 (2002), pp. 3441-3463, <https://doi.org/10.1088/0031-9155/47/19/301>
- [156] M. Kozicki, M. Jaszczak, K. Kwiatos, P. Maras, S. Kadlubowski, R. Wach, M. Dudek, Three-dimensional radiochromic and polymer gel dosimeters with Pluronic F-127 matrix – a review of current research, *J. Phys.: Conf. Ser.*, 1305 (2019), article 012035, <https://doi.org/10.1088/1742-6596/1305/1/012035>
- [157] M. Kozicki, P. Maras, M. Jaszczak-Kuligowska, 3D Polymer Gel Dosimeters with iCBCT 3D Reading and polyGeVero-CT Software Package for Quality Assurance in Radiotherapy, *Materials*, 17 (2024), article 1283, <https://doi.org/10.3390/ma17061283>
- [158] K. Jordan, N. Avvakumov, Radiochromic leuco dye micelle hydrogels: I. Initial investigation, *Phys. Med. Biol.*, 54 (2009), pp. 6773-6789, <https://doi.org/10.1088/0031-9155/54/22/002>

- [159] K. Kouvatı, M. Jaszczak, P. Papagiannis, S. Kadłubowski, R. Wach, P. Maras, M. Dudek, M. Kozicki, Leuco crystal violet-Pluronic F-127 3D radiochromic gel dosimeter, *Phys. Med. Biol.*, 64 (2019), article 175017, <https://doi.org/10.1088/1361-6560/ab2f5d>
- [160] K. Kwiatos, P. Maras, S. Kadłubowski, Z. Stempień, M. Dudek, M. Kozicki, Tetrazolium salts-Pluronic F-127 gels for 3D radiotherapy dosimetry, *Phys. Med. Biol.*, 63 (2018), article 095012, <https://doi.org/10.1088/1361-6560/aabbb6>
- [161] S. Hayashi, K. Ono, K. Fujino, S. Ikeda, K. Tanaka, Novel radiochromic gel dosimeter based on a polyvinyl alcohol-Iodide complex. *Radiat. Meas.* 131 (2020), article 106226 <http://doi.org/10.1016/j.radmeas.2021.106674>
- [162] J.E. Tano, C.A.B. Gonzales, A. Saito, T. Wada, Y. Nagata, H. Yasuda, Annealing properties of the PVA-GTA-I gel dosimeter. *Radiat. Meas.*, 149 (2021), article 106674, <http://doi.org/10.1016/j.radmeas.2021.106674>
- [163] M. Kozicki, M. Jaszczak, P. Maras, S. Kadłubowski, Measurement of the radiation dose and radiation isocenter of the TrueBeam accelerator using 3D polymer gel dosimeters from the VIPAR family with different chemical history, *Measurement*, 221 (2023), article 113452, <https://doi.org/10.1016/j.measurement.2023.113452>
- [164] P. Maras, M. Kozicki, Fast isocenter determination using 3D polymer gel dosimetry with kilovoltage cone-beam CT reading and the polyGeVero-CT software package for linac quality assurance in radiotherapy, *Materials*, 15 (2022), article 6807, <https://doi.org/10.3390/ma15196807>
- [165] M. Kozicki, P. Maras, A.C. Karwowski, Software for 3D radiotherapy dosimetry. Validation, *Phys. Med. Biol.*, 59 (2014), article 4111, <https://doi.org/10.1088/0031-9155/59/15/4111>
- [166] D.N. Makris, E.P. Pappas, E. Zoros, N. Papanikolaou, D.L. Saenz, G. Kalaitzakis, K. Zourari, E. Efstathopoulos, T.G. Maris, E. Pappas, Characterization of a novel 3D printed patient specific phantom for quality assurance in cranial stereotactic radiosurgery applications, *Phys. Med. Biol.*, 64 (2019), article 105009, <https://doi.org/10.1088/1361-6560/ab1758>
- [167] M. Piotrowski, A. Pawlaczyk, M.I. Szykowska-Jóźwik, P. Maras, M. Kozicki, Radiation Sensitive Nano-, Micro-, Macro-Gels and Polymer Capsules for the Use in Radiotherapy Dosimetry, *IJMS*, submitted 10.06.2025
- [168] O.D. Frent, L.G. Vicas, N. Duteanu, C.M Morgovan, T. Jurca, A. Pallag, M.E. Muresan, S.M. Filip, R.-L. Lucaciu, E. Marian, Sodium Alginate—Natural Microencapsulation Material of Polymeric Microparticles, *Int. J. Mol. Sci.* 23 (2022) 121018. <https://doi.org/10.3390/ijms232012108>
- [169] J.-J. Chuang, Y.-Y. Huang, S.-H. Lo, T.-F. Hsu, W.-Y. Huang, S.-L. Huang, Y.-S. Lin, Effects of pH on the Shape of Alginate Particles and Its Release Behavior, *Int. J. Polym. Sci.* 2017 (2017) 3902704. <https://doi.org/10.1155/2017/3902704>
- [170] C. Ferradini, J. Jay-Gerin, The effect of pH on water radiolysis: A still open question—A minireview, *Res. Chem. Intermed.* 26 (2000) 549-565. <https://doi.org/10.1163/156856700X00525>
- [171] B. Morgan, O. Lahav, The effect of pH on the kinetics of spontaneous Fe(II) oxidation by O₂ in aqueous solution— basic principles and a simple heuristic description, *Chemosphere* 68 (2007) 2080-2084. <https://doi.org/10.1016/j.chemosphere.2007.02.015>

- [172] W. Stumm, G.F. Lee, Oxygenation of Ferrous Iron, *Ind. Eng. Chem.* 53 (1961), 143-146. <https://doi.org/10.1021/ie50614a030>
- [173] H.E. Irianto, G. Giyatmi, D. Fransiska, A. Nuraelah, Physical and Chemical Characteristics of Alginate Extracted from *Sargassum* sp, *IOP Conf. Ser.: Earth Environ. Sci.* 1177 (2023) 012029. <https://doi.org/10.1088/1755-1315/1177/1/012029>
- [174] L. Kong, Copper Requirement and Acquisition by Marine Microalgae, *Microorganisms* 10 (2022) 1853. <https://doi.org/10.3390/microorganisms10091853>
- [175] W. Zhang, K. Wang, Y. Zeng, X. Hu, X. Zhang, S. Chang, H. Zhang, Low-Diffusion Fricke Gel Dosimeters with Core-Shell Structure Based on Spatial Confinement, *Materials* 14 (2021) 3992. <https://doi.org/10.3390/ma14143932>
- [176] M. Piotrowski, P. Maras, M. Kozicki, On the Use of the Fricke-Pluronic F-127 Gel Dosimeter for Radiation Isocenter Testing of a Medical Linear Accelerator, *Materials*, 17 (2024), Article 1521, <https://doi.org/10.3390/ma17071521>
- [177] M. Piotrowski, P. Maras, Z. Stempień, R. Wach, M. Kozicki, Deformable Fricke-XO-Gelatin radiochromic dosimeter of ionising radiation and its applications in quality assurance tests for radiation therapy, *Materials*, submitted 03.06.2025
- [178] H. Dai, X. Li, J. Du, L. Ma, Y. Yu, H. Zhou, T. Guo, Y. Zhang, Effect of interaction between sorbitol and gelatin on gelatin properties and its mechanism under different citric acid concentrations, *Food Hydrocolloids*, 101 (2020), article 105557, <https://doi.org/10.1016/j.foodhyd.2019.105557>
- [179] R. Wang, R.W. Hartel, Citric acid and heating on gelatin hydrolysis and gelation in confectionery gels, *Food Hydrocolloids*, 129 (2022), article 107642, <https://doi.org/10.1016/j.foodhyd.2022.107642>
- [180] J.F. Martucci, R.A. Ruseckaite, Tensile Properties, Barrier Properties, and Biodegradation in Soil of Compression—Molded Gelatin-Dialdehyde Starch Films, *J. Appl. Polym. Sci.*, 112 (2009), pp. 2166-2178, <https://doi.org/10.1002/app.29695>
- [181] S. Rivero, M.A. Garcia, A. Pinotti, Correlations between structural, barrier, thermal and mechanical properties of plasticized gelatin films, *Innov. Food Sci. Emerg. Technol.*, 11 (2010), pp. 369-375, <https://doi.org/10.1016/j.ifset.2009.07.005>
- [182] Y. Lu, J. Song, X. Yao, M. An, Q. Shi, X. Huang, 3D Printing Polymer-based Bolus Used for Radiotherapy, *Int. J. Bioprint.*, 7 (2021), article 414, <https://doi.org/10.18063/ijb.v7i4.414>
- [183] M.A. Bero, I. Abukassem, Detection of Ultraviolet Radiation Using Tissue Equivalent Radiochromic Gel materials, *J. Phys.: Conf. Ser.*, 164 (2009), article 012064, <https://doi.org/10.1088/1742-6596/164/1/012064>
- [184] M. Zhang, S-M. Zhou, T. Qu, What Do We Mean When We Talk about the Linac Isocenter?, *Int. J. Med. Phys. Clin. Eng. Radiat. Oncol.*, 4 (2015), pp. 233-242, <https://doi.org/10.4236/ijmpcero.2015.43028>
- [185] P. Rowshanfarzad, M. Sabet, D.J. O'Connor, P.B. Greer, Isocenter verification for linac-based stereotactic radiation therapy: review of principles and techniques, *J. Appl. Clin. Med. Phys.*, 12 (2011), pp. 185-195, <https://doi.org/10.1120/jacmp.v12i4.3645>
- [186] E.E. Klein, J. Hanley, J. Bayouth, F.F. Yin, W. Simon, S. Dresser, C. Serago, F. Aguirre, L. Ma, B. Arjomandy, C. Liu, C. Sandin, T. Holmes, Task Group 142 report: Quality assurance of medical accelerators, *Med. Phys.*, 36 (2009), pp. 4197-4212, <https://doi.org/10.1118/1.3190392>

- [187] UNIQUE Linear Accelerator Installation Product Acceptance (IPA-LE-UNIQUE-K), December 2021, Varian, Palo Alto, USA
- [188] M. Stock, B. Kroupa, D. Georg, Interpretation and evaluation of the γ index and the γ index angle for the verification of IMRT hybrid plans, *Phys. Med. Biol.*, 50 (2005), pp. 399-411, <https://doi.org/10.1088/0031-9155/50/3/001>
- [189] D. Thwaites, Accuracy required and achievable in radiotherapy dosimetry: have modern technology and techniques changed our views?, *J. Phys.: Conf. Ser.*, 444 (2013), article 012006, <https://doi.org/10.1088/1742-6596/444/1/012006>
- [190] K. Hayashi, H. Gotoh, Prediction of the presence of cupping artifacts for gel dosimeter based on considerations of scattered light in optical computed tomography measurements, *Radiat. Meas.*, 138 (2020), article 106437, <https://doi.org/10.1016/j.radmeas.2020.106437>
- [191] T. Takanashi, K. Hayashi, M. Nemoto, H. Kawamura, S. Hayashi, H. Gotoh, Cause of cupping artifacts from radiochromic micelle gel dosimeters used in optical CT scanner measurement, *J. Phys.: Conf. Ser.*, 1305 (2019), article 012020, <https://doi.org/10.1088/1742-6596/1305/1/012020>
- [192] P.V.S. Tavares, R.E. Diniz, O. Rodrugies Jr., L.L. Campos, Attenuation images of optical CT using Fricke xylenol orange gel for dose mapping in radiotherapy, *Radiat. Phys. Chem.*, 224 (2024), article 112016, <https://doi.org/10.1016/j.radphyschem.2024.112016>
- [193] L.C.E. da Silva, A.C. Borges, M.G. de Oliveira, M.A. de Farias, Visualization of supramolecular structure of Pluronic F127 micellar hydrogels using cryo-TEM, *MethodsX*, 7 (2020), 101084, <https://doi.org/10.1016/j.mex.2020.101084>
- [194] A. Einstein, On the movement of small particles suspended in stationary liquids required by the molecular-kinetic theory of heat (in German), *Ann. Phys., Lpz.*, 17 (1905), pp. 549-60, <https://doi.org/10.1002/andp.19053220806>
- [195] M. Romeo, G. Cottone, M.C. D'Oca, A. Bartolotta, R. Miraglia, R. Gerasia, C. Gagliardo, F. d'Errico, M. Marrale, Deep learning approach for diffusion correction in Fricke hydrogel dosimeters, *Radiat. Meas.*, 175 (2024), article 107171, <https://doi.org/10.1016/j.radmeas.2024.107171>
- [196] M. Romeo, G. Cottone, M.C. D'Oca, A. Bartolotta, S. Gallo, R. Miraglia, R. Gerasia, G. Milluzzo, F. Romano, C. Gagliardo, F. Di Martino, F. d'Errico, M. Marrale, Diffusion Correction in Fricke Hydrogel Dosimeters: A Deep Learning Approach with 2D and 3D Physics-Informed Neural Network Models, *Gels*, 10 (2024), article 565, <https://doi.org/10.3390/gels10090565>

Publications

Publications related to the doctoral dissertation

1. M. Piotrowski, P. Maras, M. Kozicki, On the Use of the Fricke-Pluronic F-127 Gel Dosimeter for Radiation Isocenter Testing of a Medical Linear Accelerator, *Materials*, 17 (2024), Article 1521, <https://doi.org/10.3390/ma17071521>, IF=3.1, MEiN=140
2. M. Piotrowski, P. Maras, M. Kozicki, Sorbitol to reduce Fe diffusion in a Fricke gel dosimeter and enhance its resistance to elongation, *J. Phys.: Conf. Ser.*, 2799 (2024), article 012008, <https://doi.org/10.1088/1742-6596/2799/1/012008>, MEiN=40

Submitted manuscripts related to the doctoral dissertation

1. M. Piotrowski, A. Pawlaczyk, M.I. Szykowska-Jóźwik, P. Maras, M. Kozicki, Radiation Sensitive Nano-, Micro-, Macro-Gels and Polymer Capsules for the Use in Radiotherapy Dosimetry, *IJMS*, submitted 10.06.2025, IF=4.9, MEiN=140
2. M. Piotrowski, P. Maras, Z. Stempień, R. Wach, M. Kozicki, Deformable Fricke-XO-Gelatin radiochromic dosimeter of ionising radiation and its applications in quality assurance tests for radiation therapy, *Materials*, submitted 03.06.2025, IF=3.1, MEiN=140

Other publications

1. M. Piotrowski, P. Maras, R. Wach, S. Kadłubowski, M. Kozicki, Impact of Salt on Thermal Stability and Dose Response of the Fricke-XO-Pluronic F-127 3D Radiotherapy Dosimeter, *Materials*, 15 (2022), Article 5223, <https://doi.org/10.3390/ma15155223>, IF=3.1, MEiN=140
2. M. Piotrowski, P. Maras, S. Kadłubowski, M. Kozicki, Study of the Optimal Composition and Storage Conditions of the Fricke-XO-Pluronic F-127 Radiochromic Dosimeter, *Materials*, 15 (2022), Article 984, <https://doi.org/10.3390/ma15030984>, IF=3.1, MEiN=140
3. M. Dudek, M. Piotrowski, P. Maras, M. Jaszczak, M. Kozicki, Anisotropic diffusion of Fe ions in Fricke-XO-Pluronic F-127 and Fricke-XO-Gelatine 3D radiotherapy dosimeters, *Phys. Med. Biol.*, 66 (2021), Article 155005, <https://doi.org/10.1088/1361-6560/ac101e>, IF=3.3, MEiN=100

Conferences

1. M. Piotrowski, P. Maras, M. Kozicki, Sorbitol to reduce Fe diffusion in a Fricke gel dosimeter and enhance its resistance to elongation, poster presentation, 13th International Conference on 3D dosimetry (IC3DDose 2024), 17-19 June 2024, Aarhus, Denmark
2. M. Piotrowski, P. Maras, M. Kozicki, 2D Fricke gel bolus dosimeter (in Polish), poster presentation, Symposium on the occasion of the 55th anniversary of the OŁ-PTBR – Historia i Perspektywy, 11 May 2024, Łódź, Poland
3. M. Piotrowski, Fricke-XO-Pluronic F-127 radiochromic gel dosimeter (in Polish), oral presentation (awarded with distinction), X National Conference of Medical Physics Students "Fizyka dla Medyka", 15-16 April 2023, online conference